Report Title:

Computation Modeling and Assessment of Nanocoatings for Ultra Supercritical Boilers: Final Report

Type of Report: Final Technical Report
Reporting Period: Start Date: 8/14/2007 - End Date: 6/21/2011

Principle Authors:
J. Shingledecker – EPRI
D. Gandy – EPRI
N .Cheruvu – SwRI
R. Wei – SwRI
K. Chan – SwRI

DOE Award Number:
DE-FC26-07NT43096

Submitting Organization:
Electric Power Research Institute
3420 Hillview Avenue
Palo Alto, CA 94304

.

[THIS PAGE INTENTIONALLY LEFT BLANK]

CITATIONS

This final report was prepared by:

Electric Power Research Institute
1300 West WT Harris Blvd.
Charlotte, NC 28262

Principle Investigator
J. Shingledecker

Southwest Research Institute®
6220 Culebra Road
San Antonio, TX 78238-5166

Principal Investigators
N. Cheruvu
R. Wei
K. Chan

The authors and project managers would like to acknowledge the guidance and support of Vito Cedro III, NETL project manager and Patricia Rawls, former project manager.

ABSTRACT

Forced outages and boiler unavailability of coal-fired fossil plants is most often caused by fire-side corrosion of boiler waterwalls and tubing. Reliable coatings are required for Ultrasupercritical (USC) application to mitigate corrosion since these boilers will operate at a much higher temperatures and pressures than in supercritical (565° C @ 24 MPa) boilers.

Computational modeling efforts have been undertaken to design and assess potential Fe-Cr-Ni-Al systems to produce stable nanocrystalline coatings that form a protective, continuous scale of either Al_2O_3 or Cr_2O_3. The computational modeling results identified a new series of Fe-25Cr-40Ni with or without 10 wt.% Al nanocrystalline coatings that maintain long-term stability by forming a diffusion barrier layer at the coating/substrate interface. The computational modeling predictions of microstructure, formation of continuous Al_2O_3 scale, inward Al diffusion, grain growth, and sintering behavior were validated with experimental results.

Advanced coatings, such as MCrAl (where M is Fe, Ni, or Co) nanocrystalline coatings, have been processed using different magnetron sputtering deposition techniques. Several coating trials were performed and among the processing methods evaluated, the DC pulsed magnetron sputtering technique produced the best quality coating with a minimum number of shallow defects and the results of multiple deposition trials showed that the process is repeatable.

The cyclic oxidation test results revealed that the nanocrystalline coatings offer better oxidation resistance, in terms of weight loss, localized oxidation, and formation of mixed oxides in the Al_2O_3 scale, than widely used MCrAlY coatings. However, the ultra-fine grain structure in these coatings, consistent with the computational model predictions, resulted in accelerated Al diffusion from the coating into the substrate. An effective diffusion barrier interlayer coating was developed to prevent inward Al diffusion.

The fire-side corrosion test results showed that the nanocrystalline coatings with a minimum number of defects have a great potential in providing corrosion protection. The coating tested in the most aggressive environment showed no evidence of coating spallation and/or corrosion attack after 1050 hours exposure. In contrast, evidence of coating spallation in isolated areas and corrosion attack of the base metal in the spalled areas were observed after 500 hours. These contrasting results after 500 and 1050 hours exposure suggest that the premature coating spallation in isolated areas may be related to the variation of defects in the coating between the samples. It is suspected that the cauliflower-type defects in the coating were presumably responsible for coating spallation in isolated areas. Thus, a defect free good quality coating is the key for the long-term durability of nanocrystalline coatings in corrosive environments. Thus, additional process optimization work is required to produce defect-free coatings prior to development of a coating application method for production parts.

EXCUTIVE SUMMARY

Fire-side corrosion of boiler waterwalls continues to be the number one issue resulting in forced outages and boiler unavailability for conventional coal-fired fossil power plants. Several types of coatings and weld overlays have been used to extend the service life of boiler tubes. These traditional coatings and weld overlays offer protection for only a limited time, 1 to 8 years in subcritical boilers. Accelerated and severe fire-side corrosion in ultra-supercritical (USC) boiler waterwalls is anticipated to be a primary concern since these boilers operate at a much higher temperature and pressure (up to 760° C @ 35 MPa) then subcritical (538° C @ <22 MPa) or supercritical (565° C @ 24 MPa) boilers. Improved coatings or claddings are needed by the industry to reduce/eliminate waterwall damage by mitigating fire-side corrosion. As such, highly reliable coatings are desirable for USC alloys to mitigate corrosion while maintaining the improved strength.

The MCrAl-type coatings have been successfully used for oxidation and sulfidation protection of hot section components of gas turbines that operate at a much higher temperature. These coatings exhibit excellent oxidation and corrosion resistance at the operating metal temperatures up to at least 950° C. The performance of the MCrAl coatings can be significantly enhanced by depositing the coatings using advanced processing techniques that produce nanoscale microstructure. The results published in the literature show that the corrosion and oxidation resistance of nanocrystalline coatings is significantly better than the conventional coatings with the same chemical composition. For a given Cr or Al concentration, nanoscale coatings exhibit 5 to 10 times longer life than the conventional coatings since the critical Cr or Al concentration required for the formation of a protective oxide layer, chromia (Cr_2O_3) or alumina (Al_2O_3), is expected to be significantly lower in the nanocrystalline coatings as compared to the conventional coatings. However, the chemical composition and processing parameters need to be optimized for these advanced coatings either by the trial and error method or using computational methods. Since the trial and error method is costly and time consuming, it is appropriate to use computer simulation methods to speed up the nanocrystalline coating development.

Computational modeling efforts have been undertaken to design and assess potential Fe-Cr-Ni-Al systems to produce stable nanocrystalline coatings that form a protective, continuous scale of Al_2O_3 or Cr_2O_3. Phase diagram computation was performed using Thermo-Calc® software to generate pseudo-ternary phase diagrams for the design of Fe-Cr-Ni-Al nanocrystalline coatings. The computational results identified a new series of Fe-Cr-Ni-Al nanocrystalline coatings that maintain long-term stability by forming a diffusion barrier layer at the coating/substrate interface.

Under Task 2, long-term cyclic oxidation tests were performed on Fe-18Cr-8Ni-xAl (where x = 0, 4, 10 wt.%) and Ni-20Cr-xAl (where x = 4, 7, 10 wt.%) coated and uncoated samples. The Fe-18Cr-8Ni-xAl nanocrystalline coatings were applied on 304 L stainless steel and P91 steel samples and Ni-20Cr-xAl coatings were applied on 304 SS and Haynes 230 substrate samples. The Fe-based coatings were tested at a peak temperature of 750° C, while the Ni-based coatings were tested at two peak temperatures, 750°C and 1010°C. The results of these

tests demonstrated that nanocrystalline coatings showed significant improvement in cyclic oxidation resistance. Following cyclic oxidation testing, metallurgical analysis results showed that for long-term durability, the nanocrystalline coatings should contain at least 7 wt.% Al and the fine grain structure, consistent with the computational model predictions, accelerated the kinetics of inward Al diffusion from the coating into the substrate, suggesting that a diffusion barrier interlayer coating is required to increase the durability of these coatings.

In the initial stages of Task 3, the emphasis was placed on understanding the influence of the deposition parameters on the microstructure of the coating. The critical parameters for the deposition included the deposition time, magnetron power for each target, worktable bias voltage (ion energy delivered to the film surface), worktable bias current (ion flux), and discharge current. A set of experiments were conducted and the coated samples coated were evaluated for microstructure, coating adhesion, and toughness. Based on these results, optimum process parameters were selected for deposition of advanced coatings.

For diffusion barrier coating development, three ceramic coatings, TiN, TiSiCN and AlN, were selected for evaluation. Long-term cyclic oxidation tests were performed at 750º and 1010º C on the Ni-20Cr-10Al and Fe-18Cr-8Ni-10Al coated samples and the results showed that the thermal cycling did not lead to interlayer coating spallation. However long-term thermal exposure resulted in disintegration of AlN interlayer. In contrast, the TiN and the TiSiCN showed no degradation after long-term exposure at both temperatures. Among the three interlayer coatings evaluated, the TiN inter layer coating was the optimum one for both iron and nickel base coating systems.

Considering the computation model results and the reliable MCrAl type coatings used for the hot section parts of a gas turbine, two iron base (Fe-Cr-Ni), a nickel base (Ni-Cr-Co), and a cobalt base (Co-Cr-Ni) MCr systems with 10 wt.% Al were selected for further evaluation. The advanced coatings were deposited after applying a diffusion barrier interlayer coating (TiN) using the selected process parameters. Detailed metallurgical evaluations of as-coated samples revealed coating defects, cracks and “cauliflower–type” nodules with interface delamination. A new deposition method, High Power Impulse Magnetrons Sputtering (HIPIMS), was used to investigate whether this process produces crack free dense coatings. This process produced crack free coatings, but the coatings were found to be extremely brittle. Several coating trials were conducted by controlling the process parameters of plasma enhanced magnetron sputtering process (PEMS). These deposition trials showed that crack free coatings can be produced using low deposition rates, but coatings exhibited a larger number of cauliflower –type defects. Several coating trails were also conducted using DC- pulsed magnetron system. Among the different processing techniques evaluated, the use of DC-pulsed magnetron sputtering system coupled with intermittent Ar sputter cleaning resulted in best quality coatings which were free from cracks and had a minimum number of cauliflower-type defects. To ensure the reproducibility of this deposition process, ten coating trials were conducted and the results showed that the process is reproducible. Using this optimized process, nano-coatings were deposited on the Haynes 230 coupons for 2000 cyclic oxidation and 1000 hours fire-side corrosion testing.

The NiCoCrSiAl and Ni20Cr10Al coated samples with TiN interlayer were cycled between a peak temperature of 1010º C and room temperature. The mass of the nanocrystalline coatings was essentially unchanged following the initial weight gain throughout the entire oxidation testing for over 2100 cycles, indicating that the scale on the nanocrystalline coatings is extremely stable and the kinetics of scale spallation are almost negligible if not zero. With respect to oxide scale spallation, formation of non-Al oxides, and oxidation attack, the nanocrystalline coatings showed better oxidation resistance than the conventional plasma sprayed NiCoCrAlY and PWA 286 coatings that are widely used on the hot section components of gas turbines. The results also showed that the TiN interlayer is effective in shutting off inward diffusion of Al diffusion. Since these coatings offer excellent oxidation resistance at 1050º C, it was concluded that oxidation is not a concern for these coatings at the USC boiler operating temperature of 750º C.

The fire-side corrosion test results showed that the nanocrystalline coatings with a minimum number of defects have a great potential in providing corrosion protection. The coating tested in the most aggressive environment showed no evidence of coating spallation and/or corrosion attack after 1050 hours exposure. In contrast, evidence of coating spallation in isolated areas and corrosion attack of the base metal in the spalled areas were observed after 500 hours. These contrasting results after 500 and 1050 hours exposure suggest that the premature coating spallation in isolated areas may be related to the variation of defects in the coating between the samples. It is suspected that the cauliflower-type defects in the coating were presumably responsible for coating spallation in isolated areas. Thus, a defect free good quality coating is the key for the long-term durability of nanocrystalline coatings in corrosive environments. Additional process optimization work is required to produce defect-free coatings prior to development of coating application methods for production parts.

For model validation, microstructure, formation of continuous scale formation, inward diffusion of Al, grain growth, and pore sintering in nanocrystalline-Fe-Ni-Cr-Al (304 SS + 10Al) coatings were considered and the model predictions were compared against the experimental results. The model predictions of continuous Al_2O_3 scale formation and accelerated Al inward diffusion are in agreement with the experimental results. Grain growth modeling indicated that the columnar grain structure in the nanocrystalline Fe-18Cr-8Ni Al coatings is stable and resistant to growth and the model prediction is in agreement with the experimental results. In contrast, the columnar grain structures in the nanocrystalline Ni20Cr-xAl (x = 4, 7 and 10 wt.%) Al coatings are not stable and the grains have substantially coarsened after thermal cycling exposure. Consistent with Fe-Cr-Ni-Al, the columnar grain structure in the nanocrystalline Ni-Co-Cr-Si-Al coating is also stable. The grain growth model indicated that the activation energies for Ni-based coatings could vary substantially. The grain growth model results indicated that a lower activation energy is responsible for the grain growth of Ni-20Cr-xAl coatings. Thus, the stability of the grain structure depends on the coating chemistry and grain boundary misorientation. Hence, a systematic research effort is required to understand the factors (including coating chemistry) affecting the grain growth kinetics in the Ni-based nanocrystalline coatings. Sintering modeling indicated that the initial relative density of the as-processed coatings must be greater than 98% in order to achieve full density in less than two days of thermal exposure at 750º C.

Finite element and one-dimensional calculations agree that the effect of a very thin (20-30 μm) corrosion/oxidation resistant nanocrystalline coating has a little effect on the thermal properties of a boiler tube. While a full boiler analysis would include temperature changes in the internal fluid as well at the bending of the boiler tube within the firebox, this model gives a clear indication that the total impact of the coating on heat transfer is negligible.

CONTENTS

LIST OF FIGURES

LIST OF TABLES

1.
BACKGROUND

Fire-side corrosion of waterwalls continues to be the number one issue resulting in forced outages and boiler unavailability for conventional coal-fired fossil power plants. The rate of wall thickness corrosion wastage of fire-side waterwalls in fossil fired boilers has been a concern for many years. With the introduction of nitrogen oxide (NOx) emission controls with the staged burners systems, increased waterwall wastage rates of 120 mils (3 mm) a year have been reported [1-1]. The cause of accelerated corrosion rates of waterwall tubes made of carbon and low alloy steels is the reducing environment produced by the low NOx combustion process. The extent of corrosion attack is shown in Figure 1-1. Improved coatings or claddings to mitigate fire-side corrosion are needed by the industry to reduce/eliminate waterwall damage in sub-and supercritical boilers.

Figure 1-1
Photographs of waterwall and a cross section of tubes showing the extent of corrosion and wall-thickness wastage.

Several types of iron (FeCr) and nickel (NiCr) alloys have been used as coatings or weld overlays to extend the service life of boiler tubes coal-fired sub- and supercritical boilers with limited success [1-2,1-3]. These coatings or weld overlays offered protection for only a limited time, 1 to 8 years, in subcritical or supercritical boilers [1-4]. Severe fire-side corrosion is anticipated in USC boiler waterwalls since these boilers operate at a much higher temperature than sub- or supercritical boilers. Hence, highly reliable coatings are desirable for USC alloys to mitigate corrosion.

Iron-aluminum alloys with and without Cr have been considered as coatings or weld overlays [1-5-1-9] for the USC boilers because these alloys exhibit excellent corrosion resistance in a wide range of high temperature environments. The test results showed that a minimum of 12 wt.% Cr is required for the onset of corrosion rate reduction, and the corrosion loss becomes almost negligible when the Cr content in the steel is in the 20-25 wt.% range [1-2].

The addition of the required Cr of 25 wt.% to the Fe-based systems would make the coating(s) susceptible to service-induced embrittlement: as a result, it is not possible to add the required levels of Cr to these coating systems. However, higher amounts of Cr can be added to a Ni-base system. Increased Cr concentration promotes the formation of a pure Cr_2O_3 protective layer without the presence of oxides of other elements (*e,g*., Fe, Ni, or Co, *etc*.). The pure Cr_2O_3 has a very low solubility in the molten phase.

The performance of MCrAl coatings can be significantly enhanced by depositing the coatings using advanced processing techniques such as plasma enhanced magnetron sputtering (PEMS) that produce a nanoscale microstructure. It has been shown that the oxidation and corrosion resistance of nanocrystalline coatings are significantly better than conventional coatings [1-10-1-12]. The critical Cr or Al concentration required for the formation of a protective Cr_2O_3 and Al_2O_3 layer is significantly lower for nanoscale coatings as compared to conventional coatings [1-10- 1-13].

A U. S. Department of Energy program (Contract No. DE-FC26-07NT43096) with cost-share from the Electric Power Research Institute (EPRI) was initiated in 2007 to evaluate advanced nanocrystalline MCrAl (where M is Fe, Ni, or Co) coatings for coal-fired ultra supercritical (USC) boiler tube application to mitigate fire-side corrosion. The overall objective of the project was to develop and demonstrate advanced nanocrystalline coatings using computational modeling methods that will significantly improve oxidation and the corrosion performance of USC boilers. The following five tasks have been performed to achieve the goals of this project:

Task 1. Computational Modeling of MCrAl Systems

Task 2. Establishment of Baseline Coating Data

Task 3. Process Advanced MCrAl Nanocoating Systems

Task 4. Fire-side Corrosion Testing

Task 5. Computational Modeling and Validation

This final report presents a summary of the results of these tasks (additional details are presented in References 1-14 through 1-17), additional work performed completing Tasks 3 and 4, and final conclusions based on the project findings.

1.1. References

1-1. *Weld Overlay of Waterwall Tubing, Alternate Materials and Distortion*. Electric Power Research Institute, Palo Alto, CA: 1999. Report TR-112643.

1-2. *Long-Term Testing of Protective Coatings and Claddings at Allegheny Energy Supply's Ferry #2 Boiler*. Electric Power Research Institute, Palo Alto, CA: 2000. Report 1000186.

1-3. M.A. Uusitalo, P.M.J. Vuoristo and TA. Mäntylä, "High Temperature Corrosion of Coatings and Boiler Steel in Reducing Chlorine-Containing Atmosphere," *Surface & Coatings Technology*. Vol. 161, Nos. 2-3, p. 275 (2002).

1-4. *State of Knowledge Assessment for Accelerated Corrosion with Low NOx Burners*. Electric Power Research Institute, Palo Alto, CA: 1997. Report TR-1007775.

1-5. K.N. Strafford and R. Manifold, "The Effects of Aluminum Alloying Additions on the Sulfidation Behavior of Iron," *Oxidation of Metals*. Vol. 5, No, 2, p. 85 (1972).

1-6. J.H. DeVan, and P.F. Tororelli, "The Oxidation-Sulfidation Behavior of Iron Alloys Containing 16-40 AT% Aluminum." *Corrosion Science*. Vol. 35, Nos. 5-8, p. 1065 (1993).

1-7. S.W. Banovic, J.N. Dupont, and A. R. Marder, "Evaluation of Low Aluminum Fe-Al Alloys for Use as Weld Overlay Coatings in Reducing Environments," presented at the Proceedings of Materials Solution Conference 99 on Joining of Advanced and Specialty Materials, 193, ASM International, Metals Park, OH, (November 1999).

1-8. UT-Battelle, LLC for the U.S. Department of Energy, Oakridge National Laboratory. *Fe-Al Weld Overlay Oxy-Fuel Thermal Spray Coatings for Corrosion Protection of Waterwalls in Fossil Fired Plants with Low NOx Burners: January 2002*. ORNL Final Report ORNL/Sub/95-SU604/04 and *Weldability of Fe-Al-Cr Overlay Coatings for Corrosion Protection in Oxidizing/Sulfidizing Environments*: March 2003. ORNL Final Report ORNL/Sub/95-SU604/05.

1-9. J.T. Murphy, J.R. Marder, R.M. Deacon, and A.R. Marder, "High Temperature Corrosion Resistance of Candidated FeAlCr Coatings in Low NOx Environments," presented at the 19th Annual Conference on Fossil Energy Material, Knoxville, TN (May 2005).

1-10. Z. Liu, W. Gao, and Y. He, "Oxidation Behaviour of Nanocrystalline Fe-Ni-Cr-Al Alloy Coatings," *Materials Science and Technology*. Vol. 15, No. 12, p. 1447 (1999).

1-11. Z. Liu, W. Gao, K.L. Dahm, and F. Wang, "Improved Oxide Spallation Resistance of Microcrystalline Ni-Cr-Al Coatings," *Oxidation of Metals*. Vol. 50, Nos. 1-2, p. 51 (1998).

1-12. F. Wang, H. Lou, S. Zhu, and W. Wu, "The Mechanism of Scale Adhesion on Sputtered Microcrystallized CoCrAl Films," *Oxidation of Metals*. Vol. 45, Nos. 1-2, p. 39 (1996).

1-13. S. Geng, F. Wang, S. Zhu, and W. Wu, "Hot Corrosion Resistance of a Sputter K38G Nanocrystalline Coating in Molten Sulfate at 900º C," *Oxidation of Metals*. Vol. 57, Nos. 5-6, p. 549 (2002).

1-14. U.S. Department of Energy. Office of Fossil Energy. *Computational Modeling and Assessment of Nanocoatings for Ultra Supercritical Boilers, Technical Report, Reporting Period: August 2007 thru June 2008 (Tasks 1 & 2).* Report FC26-07NT43096-01 OSTI ID: 933025. Washington, DC.

1-15. U.S. Department of Energy. Office of Fossil Energy. *Computational Modeling and Assessment of Nanocoatings for Ultra Supercritical Boilers, Task 3 Technical Report, Processing of Advanced MCrAl Nanocoating Systems: 2009*. Report FC26-07NT43096-02 OSTI ID: 962674. Washington, DC.

1-16. U.S. Department of Energy. Office of Fossil Energy. *Computational Modeling and Assessment of Nanocoatings for Ultra Supercritical Boilers, Task 4 Technical Report: Fireside Corrosion Testing: 2010*. Report FC26-07NT43096-03 OSTI ID: 974655. Washington, DC.

1-17. Computational Modeling and Assessment of Nanocoatings for Ultra Supercritical Boilers, Task 5 Technical Report: Computational Modeling and Validation. In press, 2011

2.
TASK 1: COMPUTATIONAL MODELING OF MCrAl SYSTEMS

2.0 Introduction

Several computational modeling efforts were undertaken in the first year to assess potential coating systems that might be considered for this project. The alloy system selected for the computational modeling phase of the project was the Fe-Cr-Ni-Al system. Computational modeling of this system was targeted at producing a stable nanocrystalline coating that produces a protective, continuous scale of alumina or chromia. The computational efforts included (1) the use of Thermo-Calc® software and database [2-1,2-2] for computing pseudo-ternary phase diagrams for the design of nanocrystalline-coatings; (2) the use of grain growth model, sintering model, and interface toughness model for optimizing microstructural stability and interface integrity; and (3) the use of DICTRA diffusion code [2-3] for maximizing the long-term stability of the nanocrystalline coatings. The modeling results are presented in References 1-14 and 2-4.

2.1 Computational Design of Coating Compositions

One of the goals of the phase diagram computation was to identify the minimum amounts of Al addition required to suppress σ-phase formation in Fe-Cr-Ni-Al alloys. To achieve this goal, several the pseudo-ternary phase diagram calculations were performed for Fe-Cr-Ni-Al as a function of Al content at different temperatures. The computational results indicated that a 4 wt.% Al addition or greater suppresses the formation of σ phase in the Fe-Cr-Ni-Al as illustrated in Figure 2-1. The amount of Al addition required to suppress the formation of σ phase decreases with increasing temperature. The microstructure of Fe-Ni-Cr-Al contains ferrite (bcc), austenite (fcc), or a combination of ferrite + austenite. Al is a bcc stabilizer that expands the bcc phase field, but diminishes the σ phase and austenite (fcc) phase fields in Fe-Ni-Cr-Al. These computational results are presented in detail in Ref. [2-4]. The microstructures of Fe-18Cr-8Ni-xAl coatings were investigated at several Al contents [2-6,2-7]. Without Al additions, the microstructure of the Fe-18Cr-8Ni (304 SS) coating, in the as-deposited condition consisted of predominantly metastable bcc ferrite (α) with σ phase, as shown in Figure 2-2. The σ-phase formation was suppressed by an Al addition as low as 4 wt.% and on the other hand, the microstructure of Fe-18Cr-8Ni-4Al contained mostly ferrite (bcc). Thermal exposure at elevated temperature resulted in transformation of σ and α phases into austenite, γ (fcc). These experimental findings are in agreement with phase-diagram computations obtained via Thermo-Calc [2-1].

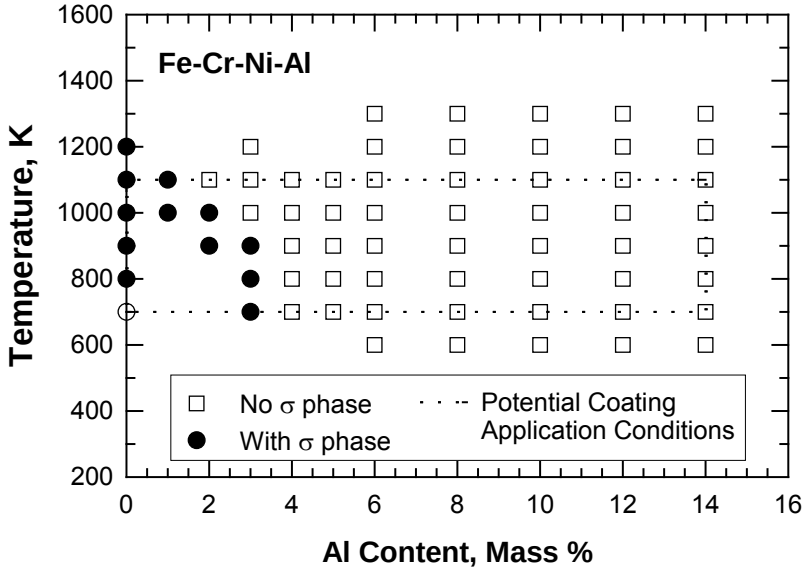

Figure 2-1
Computational results of Al contents required to suppress σ-phase formation in Fe-Cr-Ni-Al at a temperature in the range of 600-1300K [2-4].

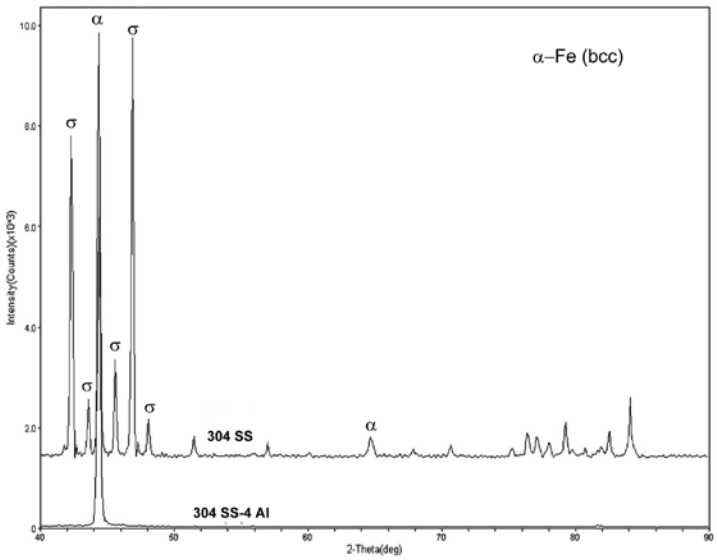

Figure 2-2
XRD patterns of Fe-18Cr-8Ni (304 SS) and Fe-18Cr-8Ni-4Al (304 SS+4Al) as-deposited coatings showing the presence of σ phase in 304 SS and the absence of σ phase in Fe-18Cr-8Ni-4Al [2-7].

Al contents that have been reported to produce alumina scale formation on Fe-Ni-Cr-Al alloys [2-8-2-14] are summarized in Figure 2-3. It has been reported that a minimum of 6 wt.% Al is required to form a continuous alumina scale on coatings with a normal grain size (≈1-10 μm). The critical Al content is reduced from 5 wt.% to 3.5 wt.% Al for nanocrystalline coatings with grain size of ≈60 nm because of a greater Al diffusion kinetics through grain boundaries [2-15]. To ensure a sufficient Al source for long-term service, 10 wt.% Al was selected as the desired Al content for the Fe-Ni-Cr-Al nanocrystalline coating compositions.

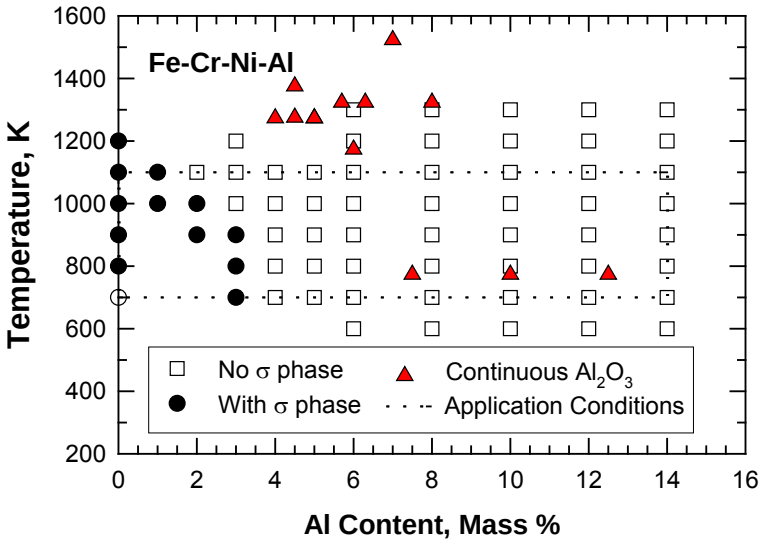

Figure 2-3
Minimum Al content for the formation of a continuous Al_2O_3 scale on Fe-Cr-Ni-Al alloys at various temperatures. Experimental data (triangles) are from the literature [2-8-2-14].

For corrosion resistance, a continuous Cr_2O_3 film must form on the coating without pores, defects or microcracks. The critical Cr content may also vary with the Ni content [2-16,2-17]. For maximum resistance against type II fireside corrosion, the minimum Cr content required is 25 wt.% Cr [2-18, 2-19]. Based on these considerations, Cr contents in the range of 18 wt.% to 25 wt.% were selected for the candidate nanocrystalline coatings.

The microstructural stability of a coating on a particular substrate during long-term high-temperature exposures was evaluated by performing interdiffusion computations, on several coating/substrate systems, treating the coating and the substrate as a diffusion couple. Interdiffusion computation was performed using DICTRA Version 24 [2-3] with TCFE5 [2-2] thermodynamic database and MOB2 mobility database. In these computations, only interdiffusion due to chemical gradients was considered, but outward diffusion due to oxidation was ignored. These results of the interdiffusion of Al, Cr, and Ni were computed for Fe-18Cr-8Ni-10Al coating on 304 SS substrate at 750° C for exposure times of 625, 825, 1250, 2500, and 8760 hours. The results showed that inward diffusion of Al occurred fairly rapidly and the Al concentration deceased from 10 wt.% in the as-deposited condition to about 4.1 wt.% after 625 hours and to 2 wt.% after 8760 hours (1 year), suggesting that these coatings have limited service life and a diffusion barrier interlayer coating is required to shut-off inward diffusion of Al. Consistent with these results a significant reduction of Al content in the Ni-20Cr-10Al nanocrystalline coating was observed in the first few hundred cycles of thermal exposure [2-20].

These results of the interdiffusion computation highlighted three important points, which were: (1) inward diffusion may be an important high-temperature degradation mechanism for Fe-Cr-Ni and Fe-Cr-Ni-Al coatings, (2) a diffusion barrier can be induced to form at the coating/substrate interface that can significantly limit inward diffusion and enhance coating resistance against oxidation and corrosion, thereby extending coating lives, and (3) compositions of coating and substrate may be optimized through thermodynamic and diffusion computations to identify diffusion barrier formation at the coating/substrate interface and to provide a new strategy for coating design.

Diffusion computations revealed that Fe-18Cr-8Ni-10Al and Fe-25Cr-25Ni-10Al would not have good oxidation resistance at 750° C because of excessive loss of Al to the substrate by inward diffusion due to high diffusivity of Al in the bcc phase. A possible remedy is to increase the Ni content to 40 wt.%, leading to a coating composition of Fe-25Cr-40Ni-10Al. With the increased Ni content, the coating is predominantly fcc. Computational modeling identified two coating compositions (Fe-25Cr-40Ni and Fe-25Cr-40Ni-10Al), as shown in Table 2-1, as candidate coatings on the basis of their abilities to maintain a high Cr or Al content during high-temperature exposure. Fe-25Cr-40 Ni forms a σ-phase diffusion barrier layer and Fe-25Cr-40Ni-10Al forms a γ-phase layer at the coating/substrate interface that significantly reduces inward diffusion.

Table 2-1
Summary of candidate nanocrystalline-coating compositions suggested by interdiffusion computations using DICTRA [2-3].

Material	Composition in Weight%					Microstructure
	Cr	Ni	Fe	Mo	Al	
Fe-Cr-Ni-Al	20-30	30-50	Balance	0	0-10	bcc + fcc + σ (depending on Al content)
Fe-25Cr-40Ni	25	40	Balance	0	0	100 mole% fcc; σ phase at coating/substrate interface
Fe-25Cr-40Ni-10Al	25	40	Balance	0	10	bcc + fcc; > 90 mole% fcc

2.2 References

2-1 A. B. Thermo-Calc® Software, Thermo-Calc for Windows Version 4, Thermo-Calc Software AB, Stockholm, 2007.

2-2 A. B. Thermo-Calc Software, TCFE5, Version 5, Thermo-Calc Software AB, Stockholm, 2007.

2-3 A. B. Thermo-Calc Software, DICTRA, Version 24, Thermo-Calc Software AB, Stockholm, 2007.

2-4 N.S. Cheruvu, R. Wei, M.R. Govindaraju, and D.W. Gandy, "Evaluation of Nanocrystalline Coatings for Coal-Fired Ultrasupercritical Boiler Tubes," *ASME Journal of Pressure Vessel Technology*. Vol. 132, No. 6, p. 061403-1-9 (2010).

2.-6 "Nanostructured Coatings by Pulsed Plasma Processing for Alloys used in Coal-fired Environments," Department of Energy, Small Business Technology Transfer (STTR) Program, DE-FG02-5ER 86249

2-7 N.S. Cheruvu, R. Wei, M.R. Govindaraju, and D.W. Gandy, "Microstructure and Oxidation Resistance of Nanocrystalline 304 SS-Al Coatings," *Surface & Coatings Technology*. Vol. 204, Nos. 6-7, p. 751 (2009).

2-8 I.G. Wright, P.A. Pint, L.M. Hall, and P.F. Tortorelli, in *Lifetimes Modeling of High-Temperature Corrosion Processes,* M. Schutze, W. J. Quadakkers, and J. R. Nicholls, eds., EFC Publications No. 34, Maney Publishing, 2001, pp. 339-358.

2-9 T. Murphy, J.R. Marder, R.M. Deacon, and A.R. Marder, "High Temperature Corrosion Resistance of Candidated FeAlCr Coatings in Low NOx Environments," presented at the 19th Annual Conference on Fossil Energy Material, Knoxville, TN (May 2005).

2-10 J.C. Pivin, D. Delaunay, C. Roques-Carmes, A.M. Huntz, and P. Lacombe, *Corrosion Science,* Vol. 20, 1980, pp. 351-373.

2-11 T.T. Huang, R. Richter, Y.L.Chang, and E. Pfender, *Metall. Trans. A.*, Vol. 16A, 1985, pp. 2051-2059.

2-12 M. Karaminezhaad, E. Kordzadeh, and M.R. Bateni, *J. of Corrosion Sci. and Eng.*, Vol. 7, Paper 4, 2004.

2-13 Z. Liu, W. Gao, and Y. He, "Oxidation Behaviour of Nanocrystalline Fe-Ni-Cr-Al Alloy Coatings," *Materials Science and Technology*. Vol. 15, No. 12, p. 1447 (1999).

2-14 S. Yamada, H. Tadashi, Y. Kawamura, and T. Saburi, *J. of High-Temperature Society,* Vol. 26, No. 3, 2000, pp. 131-137 (in Japanese).

2-15 W. Gao, Z. Liu, and Z. Li, *Advanced Materials,* Vol. 13, No. 12-13, 2001, pp. 1001-1004.

2-16 H.E. Evans, A.T. Donaldson, and T. C. Gilmour, *Oxidation of Metals,* Vol. 52, No. 5/6, 1999, pp. 379-402.

2-17 R. Peraldi and B. A Pint, *Oxidation of Metals,* Vol. 61, No. 5/6, 2004, pp. 463-483.

2-18 P. Castello, V. Guttmann, N. Farr, and G. Smith, *Materials and Corrosion,* Vol. 51, 2000, pp. 786-790.

2-19 H. Hack and G. Stanko, Presented at the 31st Int. Technical Conference on Coal Utilization & Fuel Systems, May 1-26, 2006, Sand Key Island, Florida.

2-20 N.S. Cheruvu, R. Wei, and D.W. Gandy, "Oxidation Behavior of Sputter Deposited Nanocrystalline and Conventional Plasma Sprayed MCrAl(Y) Coatings," Paper GT2010-22645, presented at the Proceedings of the ASME Turbo Expo, 2010, ASME Gas Turbine Technical Congress & Exposition, Glasgow, UK (June 2010).

3.
TASK 2: ESTABLISHMENT OF BASELINE COATING DATA

3.0 Introduction

Thermal spray Fe and Ni-based coatings have been widely used for many years to extend the service life of both sub- and supercritical boiler tubes. These coating materials typically contain one or more elements of the three known protective oxide formers Al, Cr, and Si. These elements form protective oxide scales, Al_2O_3, or Cr_2O_3, and/or SiO_2 when the coating is exposed to hot flue gas. The protective-oxide scale separates the boiler tubes from contacting the hot corrosive gases and thus, prolongs the service life of both sub- and supercritical boilers. The field test results have shown that these coatings exhibited a relatively short life, ranging 1 to 8 years in subcritical boilers [1-4]. The post-service metallurgical evaluations of the coated boiler tubes showed the coating failure was due to sulfidation attack penetration into the substrate that led to coating debonding/spallation. No durable coatings are available for the advanced supercritical and ultra supercritical (USC) boilers. Thus, there is a need to develop reliable coatings for the long-term service life for the USC boilers.

Over the past two decades there has been considerable research on the development of coatings with finer microstructures approaching nanometer scale. Nanocrystalline coatings are harder, tougher, and more resistant to high-temperature oxidation and corrosion than their counterpart conventional coatings [1-10- 1-13]. Short-term, 50 to 150 one-hour thermal cycle test results showed that the protective oxide layer formed on the nanocrystalline coating exhibited excellent spallation resistance. However, the long-term stability and oxidation and hot corrosion behavior of these nanocrystalline coatings at elevated temperatures are still unknown. Without knowledge of the long-term stability of the microstructure and the durability of the nanocrystalline coatings under high temperature oxidation/hot hot corrosion conditions, it is difficult to predict the suitability of these coatings for boiler applications. A series of experiments were conducted to characterize the oxidation behavior and to determine the microstructural stability of nanocrystalline Fe-18Cr-8Ni-xAl (where x = 0, 4 and 10 wt.%) and Ni-20Cr-yAl (where y = 3, 7, and 10 wt.%) coatings.

3.1 Experimental Procedure

Nanocrystalline Fe-Cr-Ni-xAl and Ni-Cr-xAl coatings were applied using a plasma enhanced magnetron sputtering (PEMS) deposition process on different 304 SS and Haynes 230 samples utilizing MCr (either 304 SS, or 310 SS or Ni-20Cr) and Al targets. The coating application details are given in Reference 1-14. The microstructure of the coatings was examined in optical and scanning electron microscopy (SEM). The chemical composition of the coatings, in the as-deposited and exposed conditions, and the oxide scale on the exposed samples was determined using energy dispersive x-ray spectroscopy (EDS). The grain sizes of the coatings in the as deposited and exposed conditions are measured by x-ray diffraction and orientation image microscopy (OIM) techniques.

Thermal cycling tests were performed on the uncoated and coated samples. The 304 SS samples were tested at a peak temperature of 750º C, while the Haynes 230 samples were tested at peak temperatures of 750º C and/or 1010º C. The coated and uncoated specimens were thermal cycled in a programmable, automated, and bottom drop furnace. The specimens were inserted into the furnace which was maintained at the desired peak temperature and held at that temperature for 50 minutes. After soaking the specimens at the peak temperature, the specimens were then removed from the furnace for forced air cooling for 10 minutes to room temperature, which constituted one thermal cycle and the samples were then reinserted back into the furnace for another 60-minute cycle. The thermal cycling testing was interrupted at predetermined intervals to weigh the specimens.

3.2 As-Deposited Coating Microstructure, Composition, and Grain Size

Typical microstructures of the as-deposited Fe-Cr-Ni-xAl and Ni-20-xAl coatings are shown in Figures 3-1 through 3-4. The coating thickness on the samples varied from 20 to 32 µm. It is evident from these micrographs that the as deposited coating exhibited columnar grain structure. The density and thickness of the coating seems to vary with the chemical composition of the coating. The chemical composition of the coatings is presented in Tables 3-1 and 3-2.

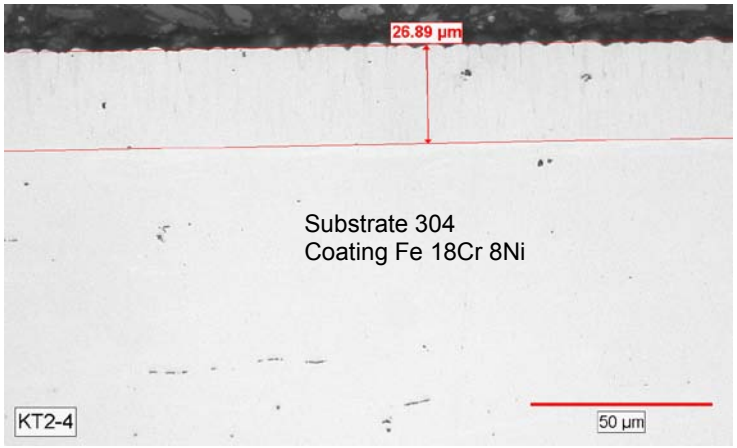

a)

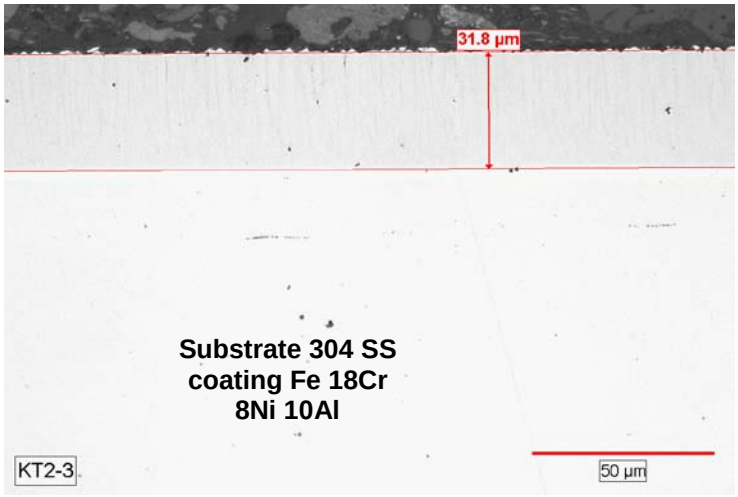

b)

Figure 3-1
Optical micrographs of as-deposited a) Fe-18Cr-8Ni (304 SS) and b) Fe-18Cr-8Ni-10Al (304 SS-10Al) coatings showing coating thickness.

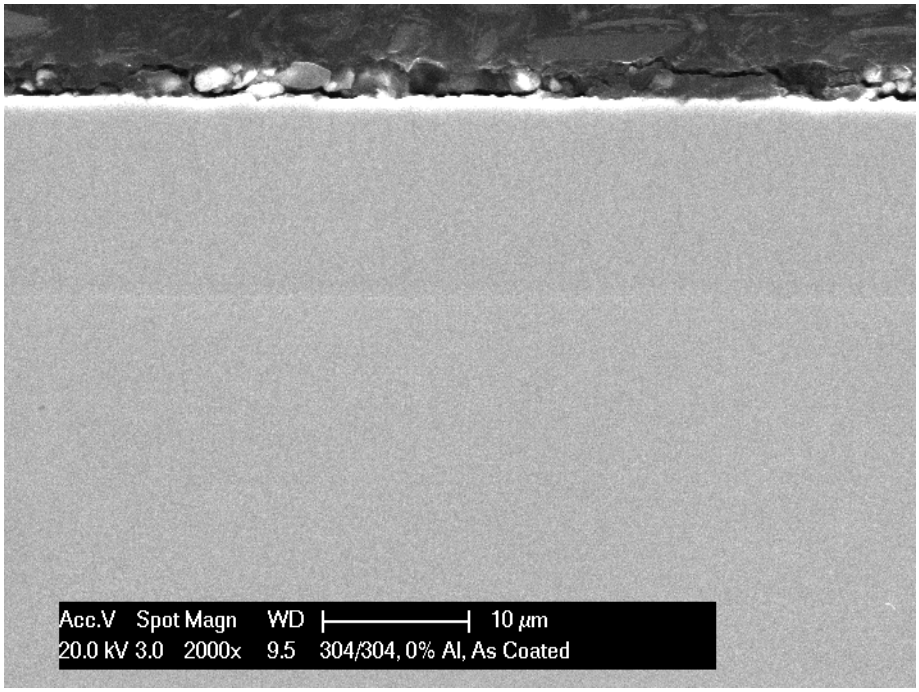

a)

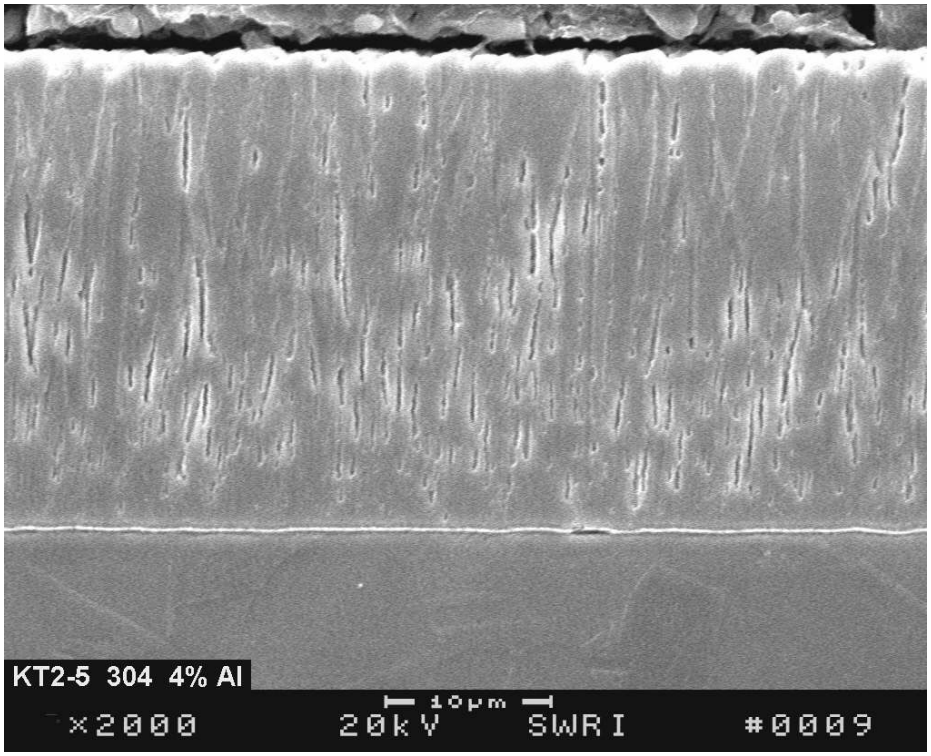

b)

Figure 3-2
SEM micrographs of the as-deposited a) Fe-18Cr-8Ni and b) Fe-18Cr-8Ni-4Al coatings showing columnar grain structure.

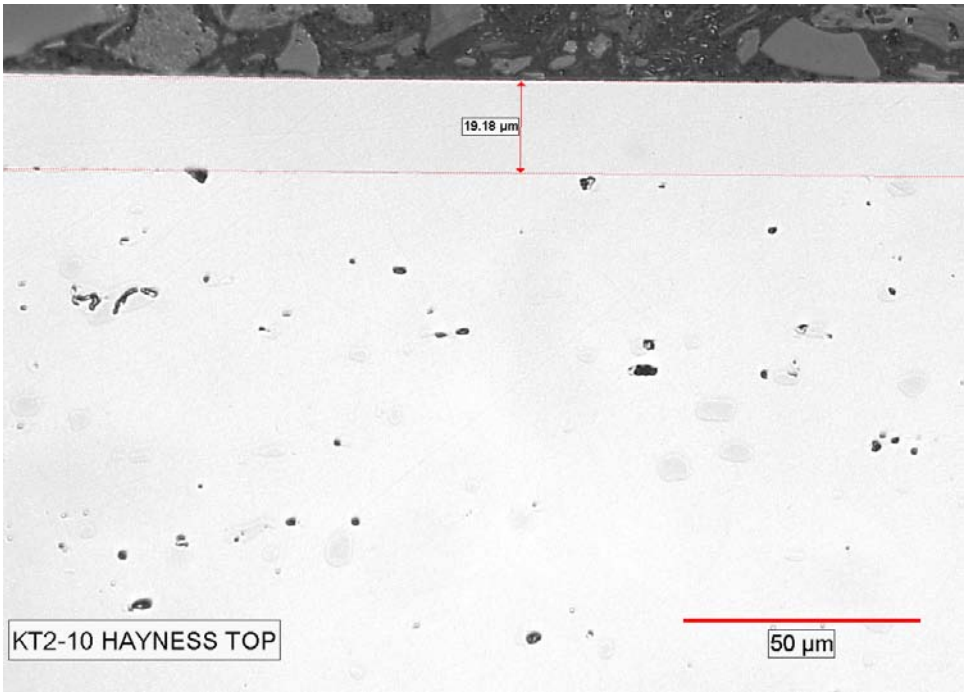

a)

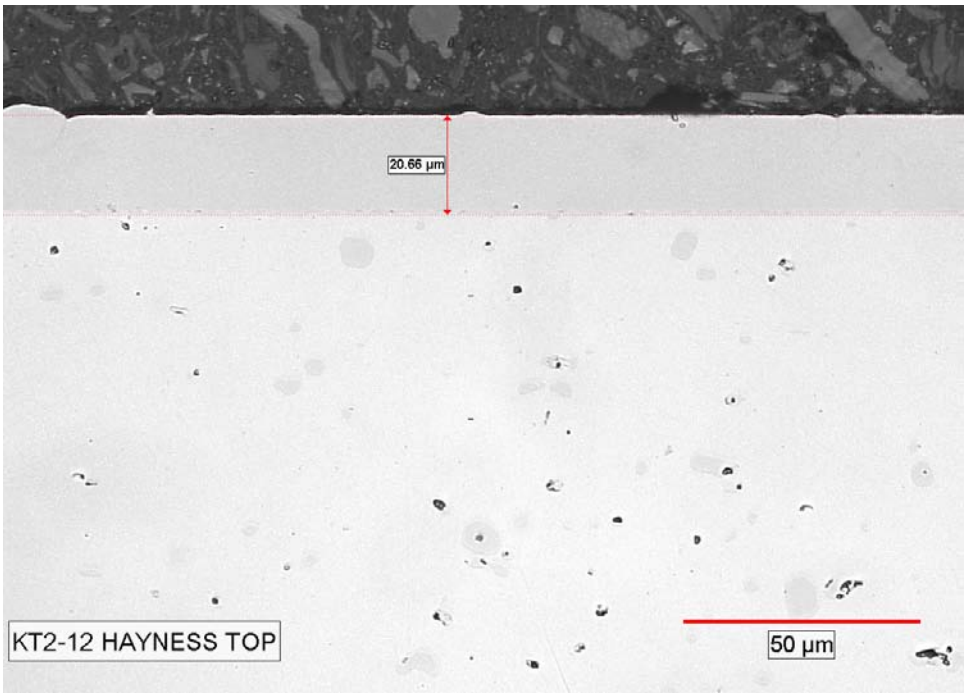

b)

Figure 3-3
Optical micrographs of the as-deposited a) Ni-20Cr 4% Al and b) Ni-20Cr-10% Al showing coating thickness

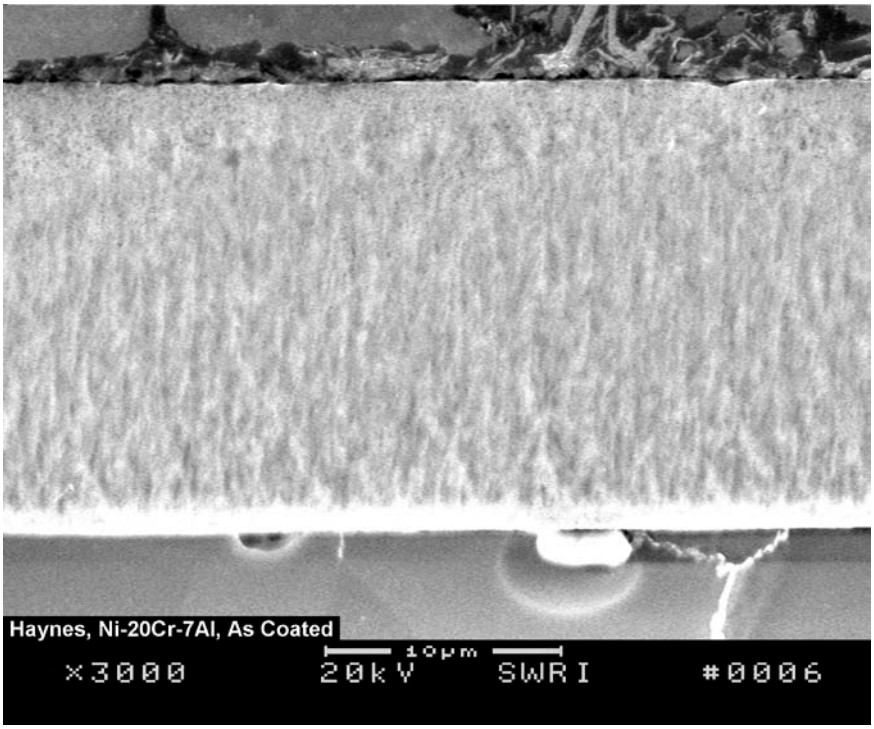

a)

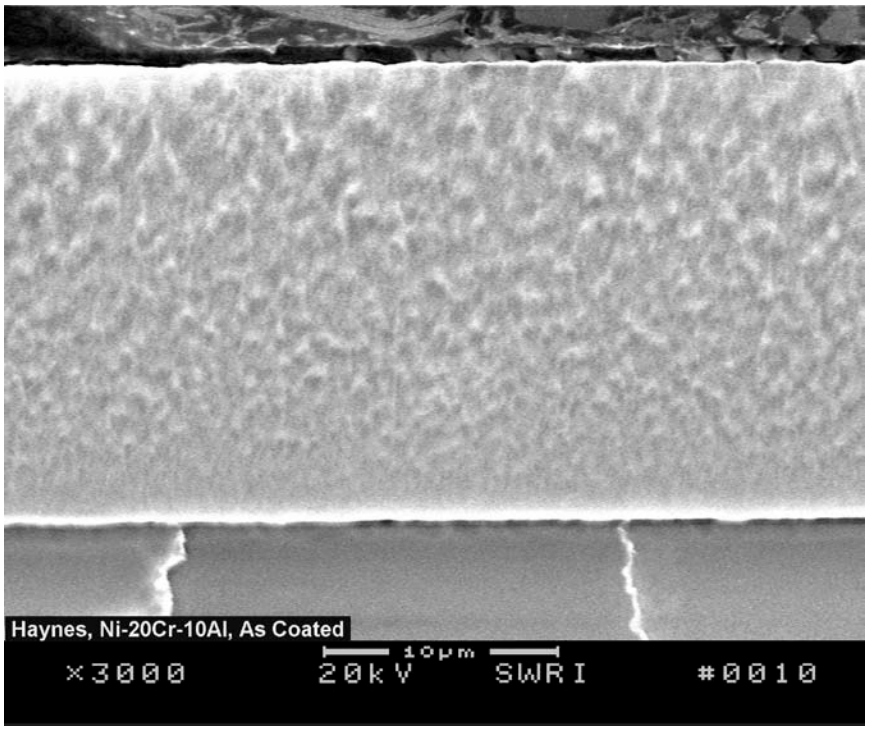

b)

Figure 3-4
SEM micrographs of the as-deposited a) Ni-20Cr-7Al and b) Ni-20Cr-10Al coatings showing a dense and fine columnar grain structure.

Table 3-1
Semi-quantitative chemical composition of the as-deposited Fe-Cr-Ni-xAl coatings, wt.%.

Coating	Si	Cr	Ni	Al	Mn	Fe
304 SS	0.4	20.1	7.3	ND	0.9	Balance
310 SS	0.2	31.2	.4	—	0.4	Balance
304 SS-4Al	0.5	19.1	6.84	4.1	0.8	Balance
304 SS-10Al	0.4	18.4	6.3	10.3	0.9	Balance

Table 3-2
Semi-quantitative chemical composition of the as-deposited Ni-20Cr-xAl coatings, wt.%.

Coating	Al	Cr	Ni	Fe	W
Ni-20Cr-4Al	3.8	20.7	Balance	0.2	0.3
Ni-20Cr -7Al	7.5	20.0	Balance	0.2	0.4
Ni-20Cr -10Al	10.6	19.4	Balance	0.23	0.4

Though both 304 SS and 310 SS target sample, as expected, are austenitic (γ-fcc), the XRD of the as-deposited 304 SS coating revealed the presence of σ phase in a matrix of metastable ferrite (α-bcc). The metastable bcc phase coexisted with austenite (γ-fcc) in the as-deposited 310 SS coating, as illustrated in Figure 3-5. Rapid cooling, in general, promotes formation of metastable phases. The addition of Al to Fe-Cr-Ni (304 SS) suppressed the formation of σ and the microstructure of the as-deposited Fe-18Cr-8Ni-10Al coating was essentially α-bcc, as shown in Figure 3-6, which is consistent with the fact that Al is a bcc stabilizer. The XRD spectra obtained from the Ni-20Cr-4Al, Ni-20Cr-7Al and Ni-20Cr-10Al coatings exhibited primarily a Ni-rich phase [1-14].

The grain size of the coatings was determined using the width of the most intense peak of the XRD spectra obtained from the as-coated specimens. As an example, the most intense peak used to measure the coating grain size is shown in Figure 3-6 (b). The grain size of the as-deposited Fe-18Cr-8Ni-4Al and 10 Al coatings was determined to be 54 and 24 nm, respectively. The grain size for the Fe-18Cr-8Ni coating without Al was not determined since the XRD spectrum from the coating exhibited several intense peaks. The grain size of the as-deposited Ni-20Cr-4Al, Ni-20Cr-7Al, and Ni-20Cr-10Al coatings were determined to be 14.7, 13.2, and 8.7 nm, respectively.

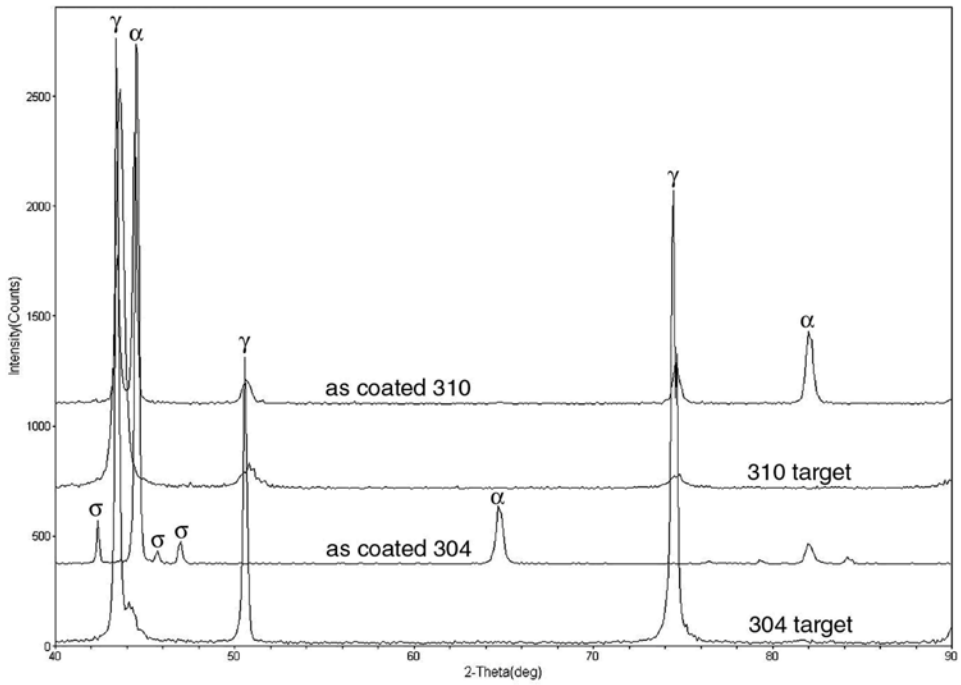

Figure 3-5
Comparison of the XRD patterns of the as-deposited 304 SS and 310 SS nanocrystalline coatings with the corresponding samples removed from the targets.

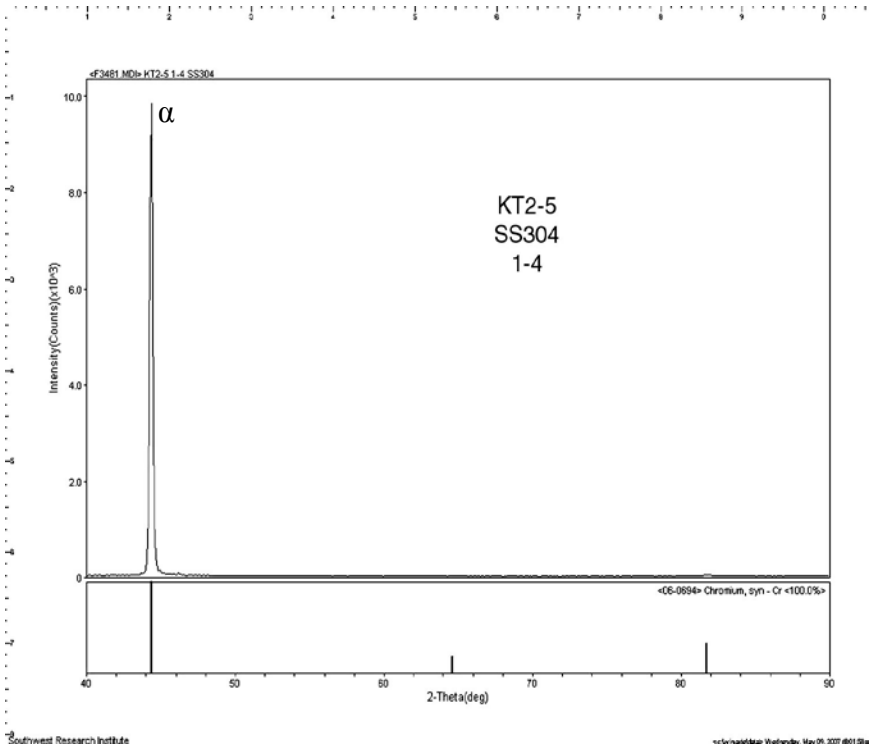

a)

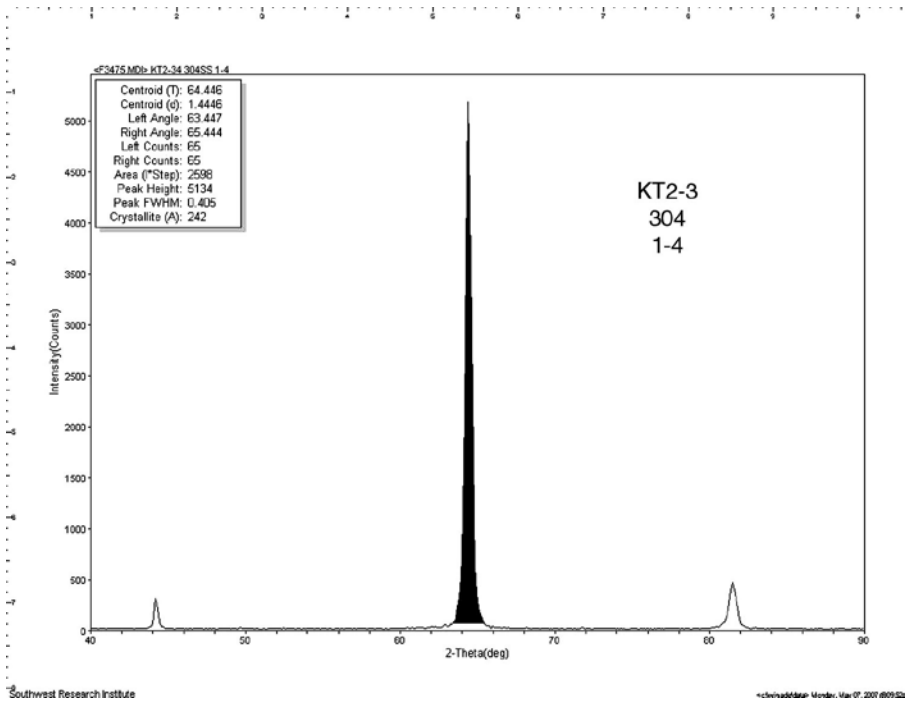

b)

Figure 3-6
XRD spectrum obtained from the as-deposited a) Fe-18Cr-8Ni-4Al (304 SS-4Al) and b) Fe-18Cr-8Ni-10Al (304 SS-10Al) coating showing the most intense peak used to measure the grain size.

The grain size on a plane normal to the columnar growth direction of the Fe-18Cr-8Ni- 10Al coating was also measured using Orientation Image Microscopy (OIM). The OIM results indicated that the average grain size of the coating is 1.23 µm, as shown in Figure 3-7, with a standard deviation of 0.43 µm. Thin foils for transmission electron microscopy (TEM) were also prepared to determine the grain size of the Fe-18Cr-8Ni- 10Al coating. Typical grain-size variation coating is presented in Figure 3-8. Consistent with the OIM results, the average grain size of the as-deposited coating was measured to be 1.2 µm. The OIM and TEM results clearly show that the XRD grain-size measurements were not accurate and significantly underestimate the grain size. The detailed TEM microstructural results, Fe and Ni-based coatings are presented in Appendix A.

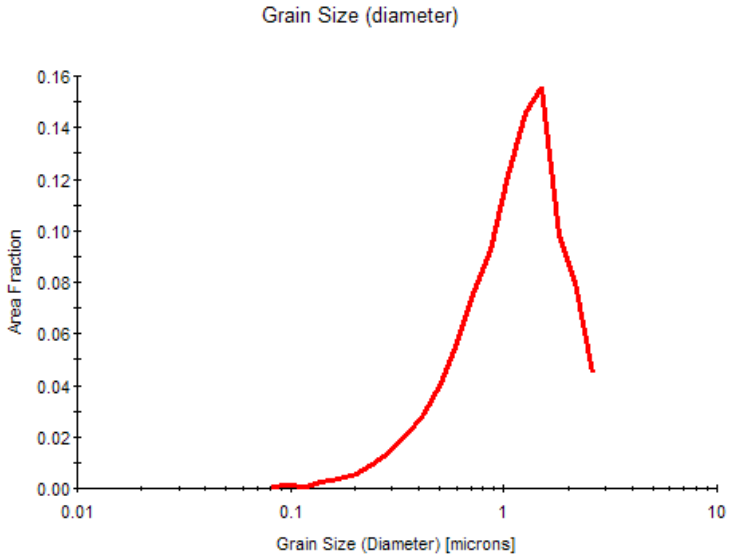

Figure 3-7
OIM Grain diameter distribution for Fe-18Cr-8Ni-10Al nanocrystalline coating in the as-coated condition.

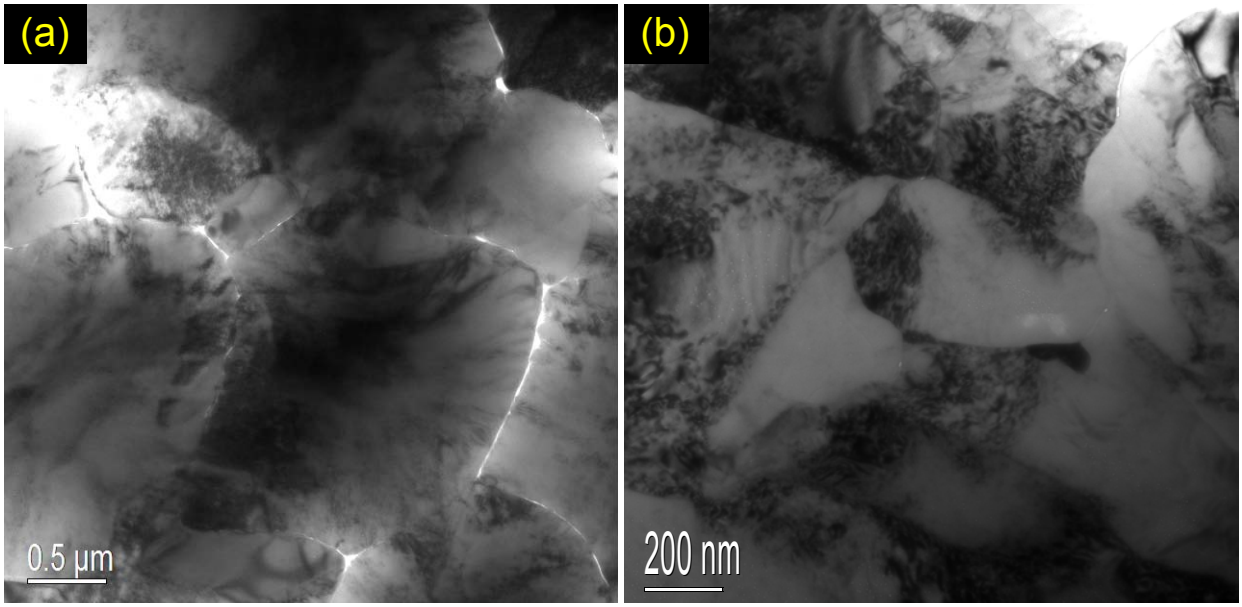

Figure 3-8
Typical grain structure of the as-deposited Fe-18Cr-8Ni-10Al nanocrystalline coating on the plane normal to the columnar grain growth direction.

3.3 Cyclic Oxidation Behavior of Nanocrystalline Coatings

The cyclic oxidation behavior of the uncoated 304 SS and nanocrystalline 304 SS and 310 SS coatings is compared in Figure 3-9. The effect of addition of Al to the nanocrystalline 304 SS (Fe-Ni-Cr) coating on the cyclic oxidation behavior is shown in Figures 3-10. Overall the Fe-based nanocrystalline coatings exhibited excellent oxidation resistance. After the initial gain, the weight of Fe-18Cr-8Ni-xAl and 310 SS-coated samples remained almost unchanged with the thermal cycles. The kinetics of oxide spallation is significantly lower for the nanocrystalline coatings. The results showed that the scale formed on these coatings is more resistant to spallation compared to the scale on the uncoated specimens. The addition of Al to the Fe-Ni-Cr coating further enhanced the oxide spallation resistance.

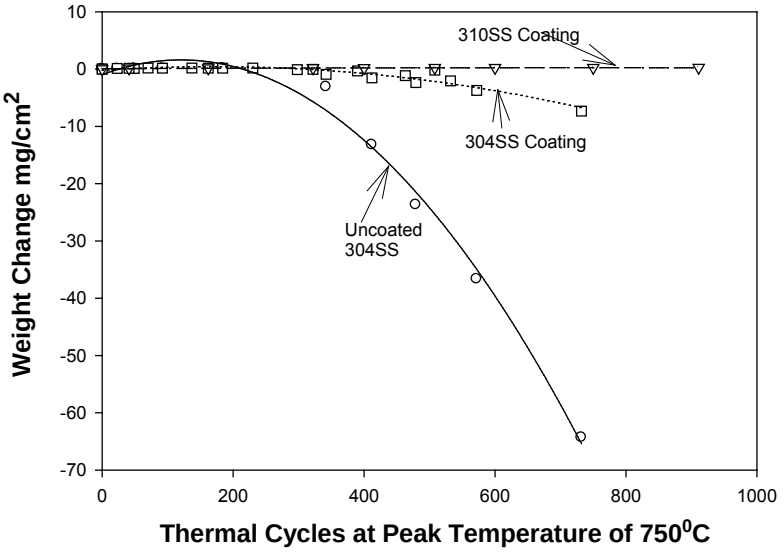

Figure 3-9
Comparison of weight change of uncoated 304 SS and nanocrystalline 304 SS and 310 SS coatings.

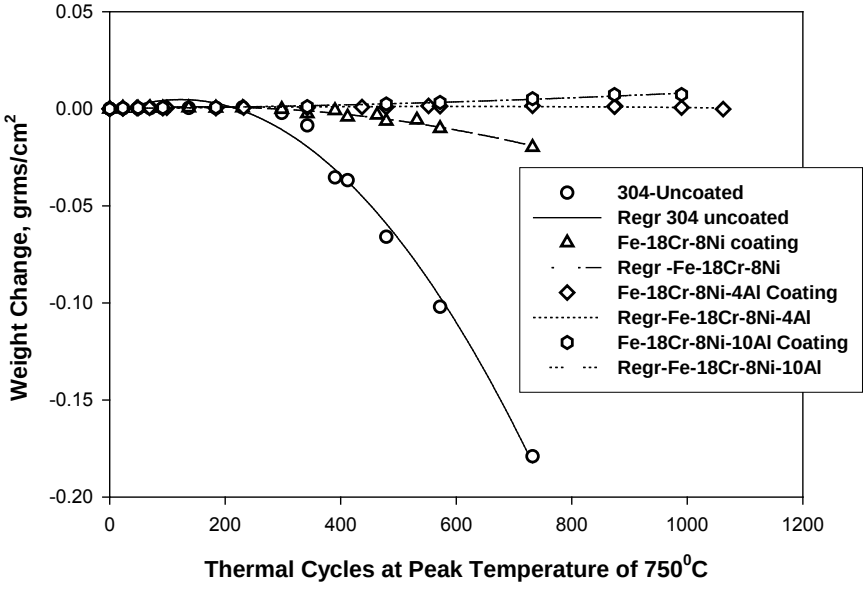

Figure 3-10
Comparison of weight change results of the uncoated and sputter-deposited Fe-18Cr-8Ni (304 SS) with 0 wt.%, 4 wt.%, and 10 wt.% Al on 304 SS substrate samples at the peak temperatures of 750º C.

Examination of the cross sections of an uncoated 304 SS sample showed two or three layers of mixed oxide scale, as shown in Figure 3-11. Analysis of the oxides by EDS revealed that the top layer was predominantly Fe-rich oxide and the second layer was a mixed oxide of Cr- Fe-Ni. The internal oxides were mixed oxides of Fe-Cr-Ni. The nanocrystalline 304 SS and 310 SS coated samples revealed a continuous Cr_2O_3, as illustrated in Figure 3-12. The EDS analysis confirmed a high Cr content (83 wt.%) in the external oxide layer, suggesting that the scale that had formed on the 304 SS and 310 SS coatings during thermal cycling exposure was Cr_2O_3. Examination of the cross section of a 304 SS-4 wt.% Al-coated specimen after 990 cycles exposure showed an external oxide layer on the surface of the coating. The EDS analysis of the external scale showed high Al content (65 wt.%) confirming that Al_2O_3 had formed during thermal exposure, as shown in Figure 3-13. These results showed that the external oxide scale formed during thermal exposure varied from Fe-rich oxide to Cr_2O_3, and to Al_2O_3 on the uncoated 304 SS and coated 304 SS, 310 SS, and 304 SS-4-Al samples, suggesting that the nanocrystalline grain structure promoted selective oxidation of Cr, in the absence of Al and Al. Consistent with these results, the presence of 4 wt.% Al in the Ni-20Cr nanocrystalline coating also resulted in formation of a continuous Al_2O_3scale after thermal exposure at 750º C and 1010º C [1-14,3-2,3-3].

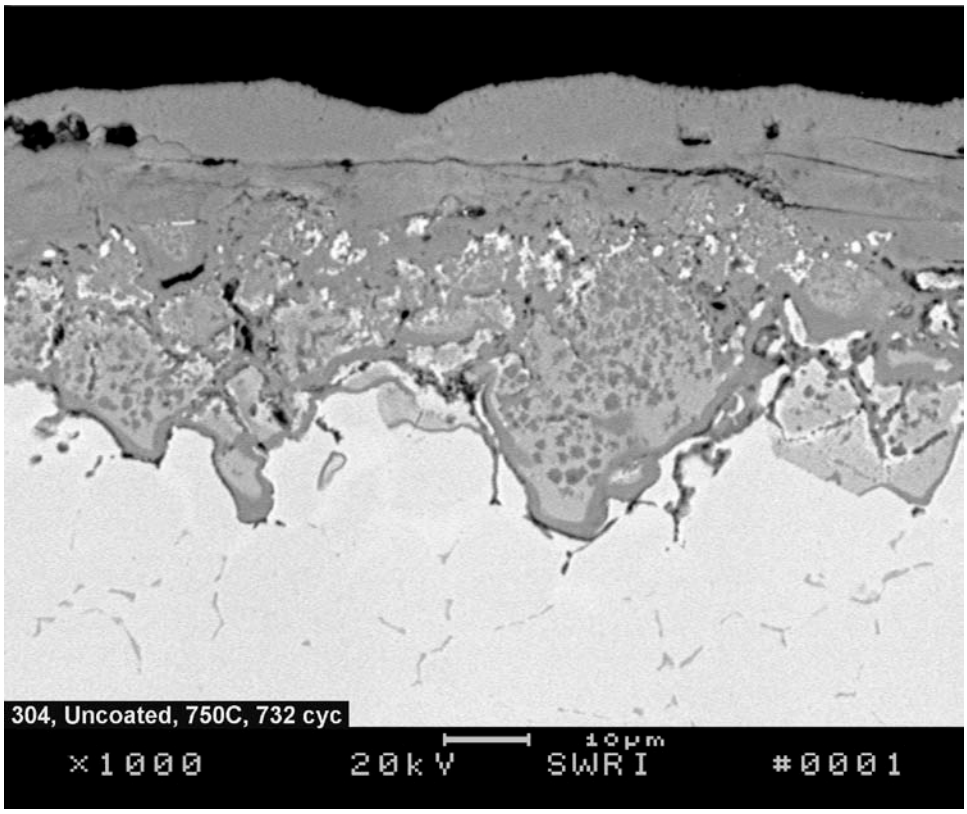

Figure 3-11
SEM micrograph of the cross section of an uncoated 304 SS after 732 thermal cycles exposure at 750° C showing multiple layers of different oxides.

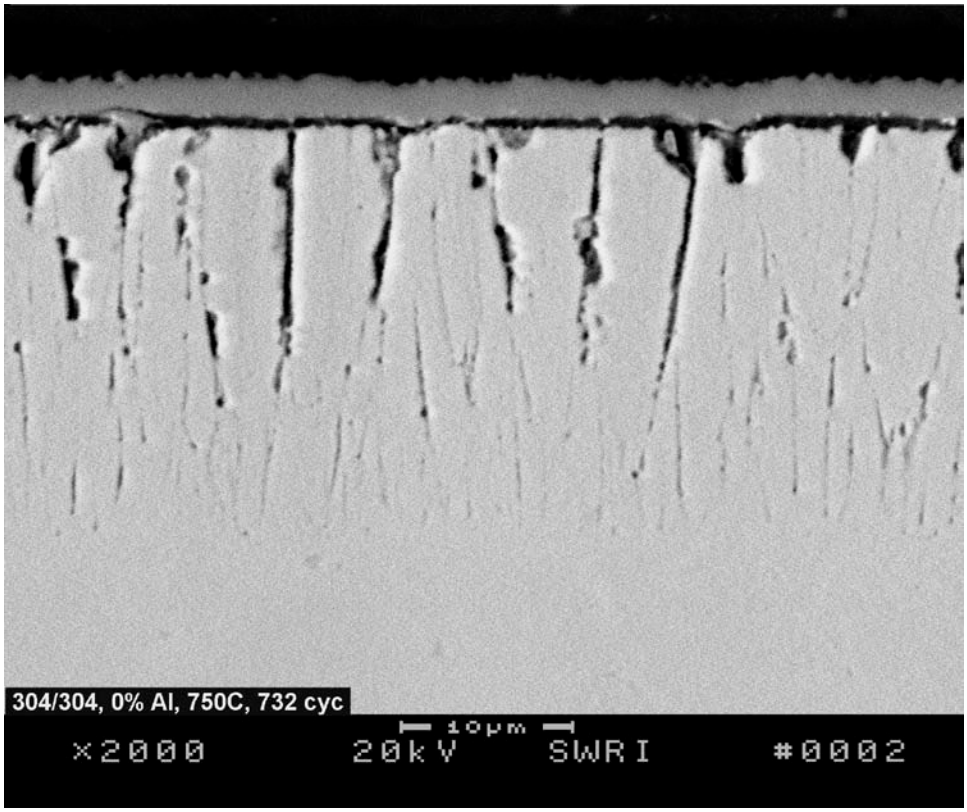

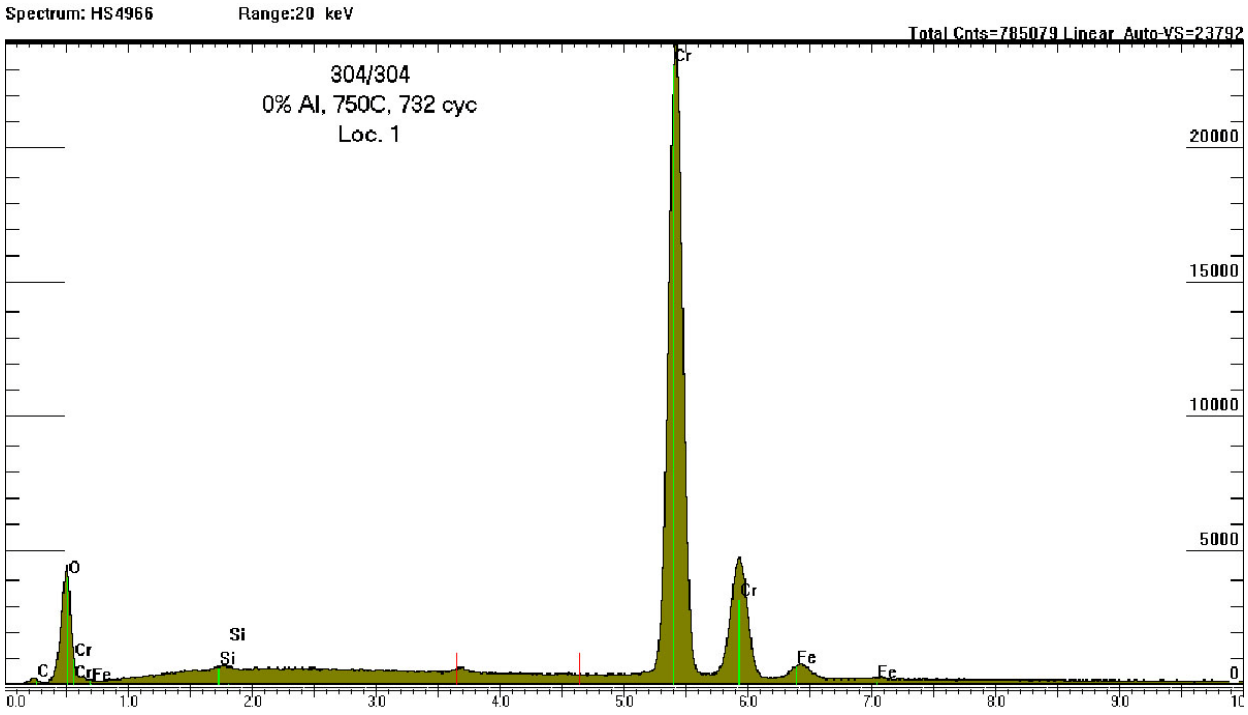

EDS spectrum obtained from the external oxide scale

Figure 3-12
SEM micrograph of the cross section of a nanocrystalline 304 SS coated sample after 732 thermal cycles exposure at 750° C and the EDS obtained from the external oxide scale.

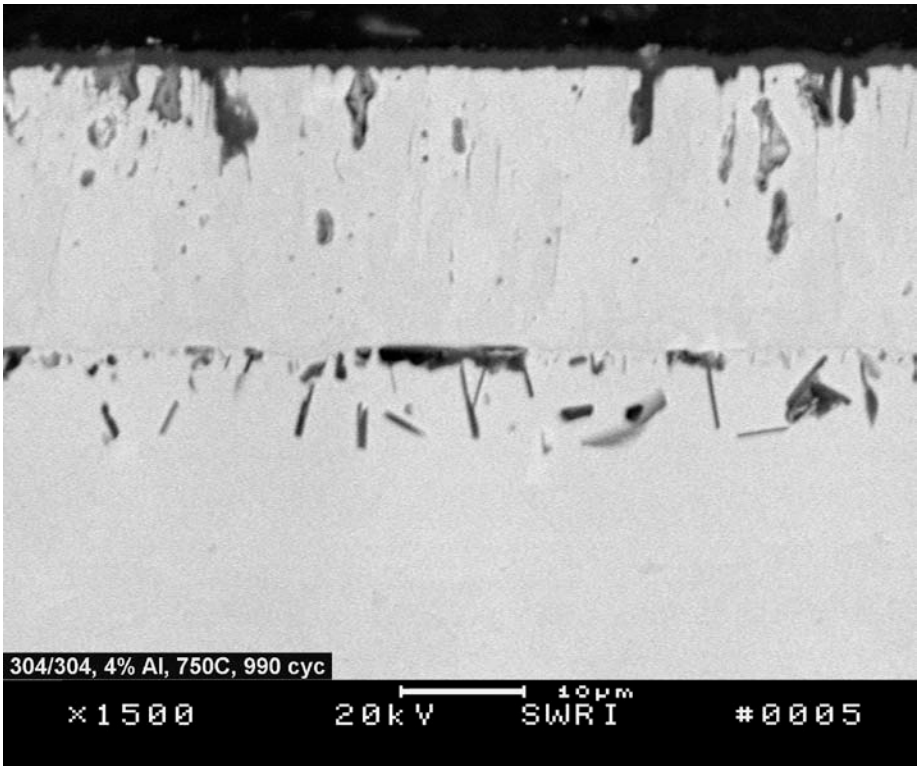

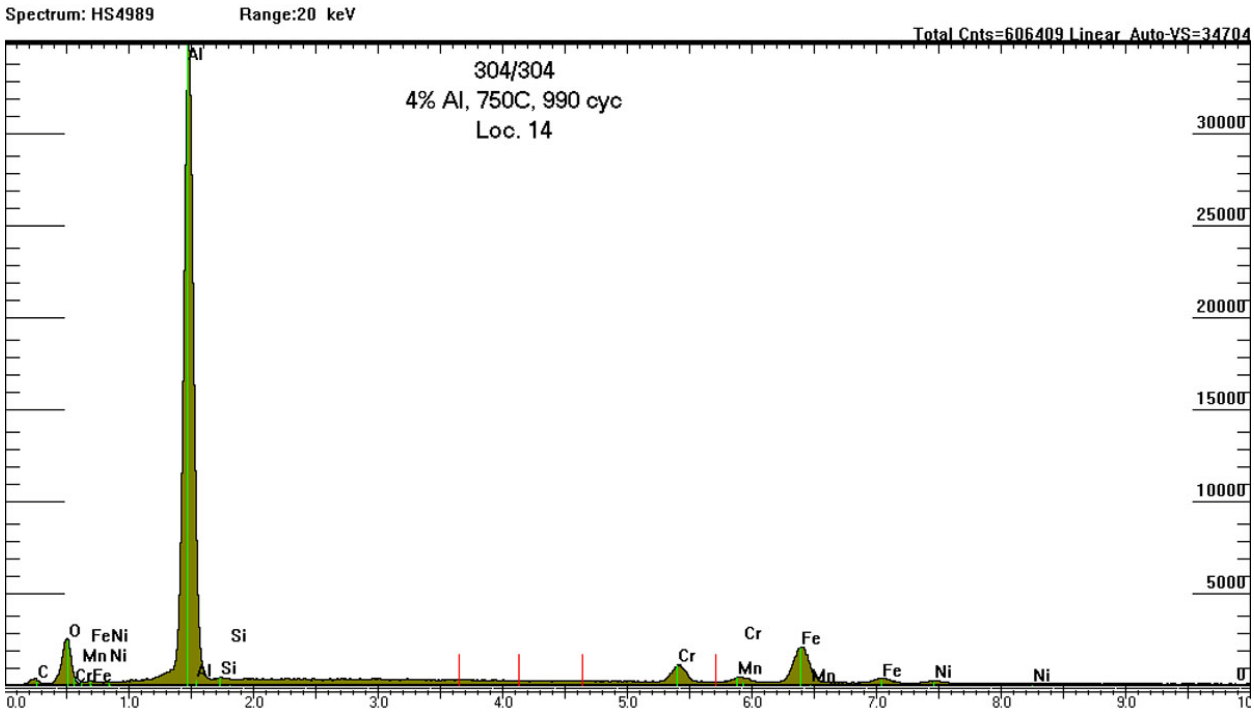

Figure 3-13
SEM micrograph of the cross section of a nanocrystalline 304 SS-coated sample after 732 thermal cycles exposure at 750°C and the EDS obtained from the external oxide scale.

Thermal exposure resulted in precipitation of FeAl particles in the 304 SS substrate below the Fe-Cr-Ni-Al coating/substrate interface in the interdiffusion zone, as shown in Figure 3-14. The interdiffusion zone width increased from 18 to 60 μm as the Al content in the coating increased from 4 to 10 wt.% after 990 cycles exposure at the peak temperature of 750º C. The inward diffusion of Al from the coating into the substrate is responsible for precipitation of these particles. Consistent with FeAl precipitation, the Al content in the coating dropped 4.2 and 10.5 wt.% in the as-deposited condition to 1.8 and 3.7 wt.%, respectively, after thermal exposure [1-14] suggesting that the nanocrystalline grain structure accelerated diffusion of Al from the coating into the substrate. Accelerated diffusion of Al was also noted in the Ni-20Cr-xAl coatings after thermal exposure at 750º C [1-14]. The Al content in these coatings after exposure at 750º C and 1010º C is given in Table 3-3. The accelerated diffusion of Al is considered to limit the long-term durability of these nanocrystalline coatings for USC boiler application. Consistent with computational model predictions, a diffusion barrier interlayer coating is required to minimize or shutoff Al diffusion from the coating into the substrate.

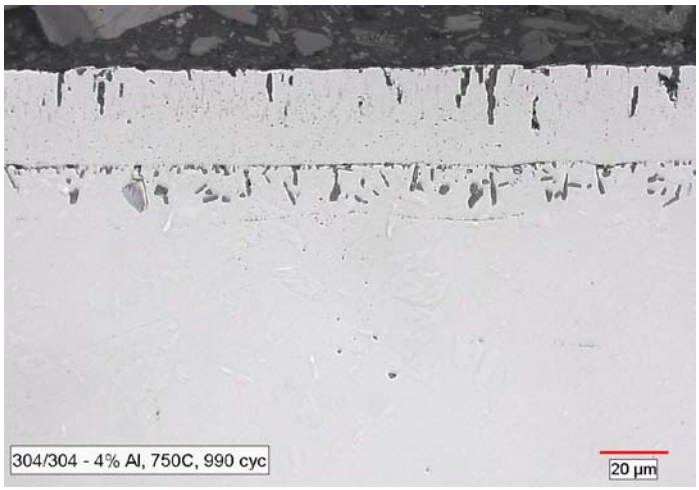

a)

b)

Figure 3-14
Optical micrographs of cross sections of exposed samples at 750°C showing the condition of the coating and FeAl particles in the substrate below the a) Fe-18Cr-8Ni-4Al and b) Fe-18Cr-8Ni-10Al nanocrystalline coatings.

Table 3-3
Al content in the Ni-20Cr-xAl after thermal exposure, wt.% [1-14, 3-2],

Coating	After 2070 cycle at 750º C, by wt.%	After 1472 cycle at 1010º C, by wt.%
Ni-20Cr-4Al	1.6	0.2
Ni-20Cr-7Al	4.8	0.5
Ni-20Cr-10Al	6.5	0.7

3.4 Oxidation Behavior of Nanocrystalline and Conventional MCrAl (Y) Coatings

The mass change results of the nanocrystalline Ni-Cr-10Al coating as a function of thermal cycles at 1010° C are compared with conventional plasma sprayed NiCoCrAlY and PWA coatings in Figure 3-15 [2-20]. These conventional coatings have been widely used on the hot section components of gas turbines for decades. Following the initial mass gain, conventional plasma sprayed coatings showed significant weight loss due to domination of scale spallation with increasing thermal cycles throughout the cyclic oxidation testing; however, the nanocrystalline coating showed little or no weight loss. The kinetics of oxide scale spallation is significantly lower for the nanocrystalline coating and the scale on the coating is highly resistant to spallation.

Examinations of the cross sections of the nanocrystalline coated samples after 347 and 1472 cycles exposure showed a continuous dense Al_2O_3 scale on the external surface of the coating, as illustrated in Figures 3-16 and 3-17 [2-20]. It is evident from these micrographs that the Al_2O_3 scale on the nanocrystalline coating was free from cracks and/or mixed oxides. In contrast, the conventional plasma sprayed coatings revealed mixed oxides (Al_2O_3 and Cr_2O_3) in localized areas and "pitting-like" oxidation attack in both NiCoCrAlY and PWA coated samples after 1500 thermal cycles exposure (Figure 3-18). With respect to internal oxidation and/or localized oxidation attack, the nanocrystalline coatings exhibited better oxidation resistance than the conventional coatings that are successfully used for protecting hot section components in gas turbines that operate at a higher temperature than the ultra supercritical boilers. Hence, the oxidation of these nanocrystalline coatings is not a concern at the USC boiler operating temperatures of 750° C.

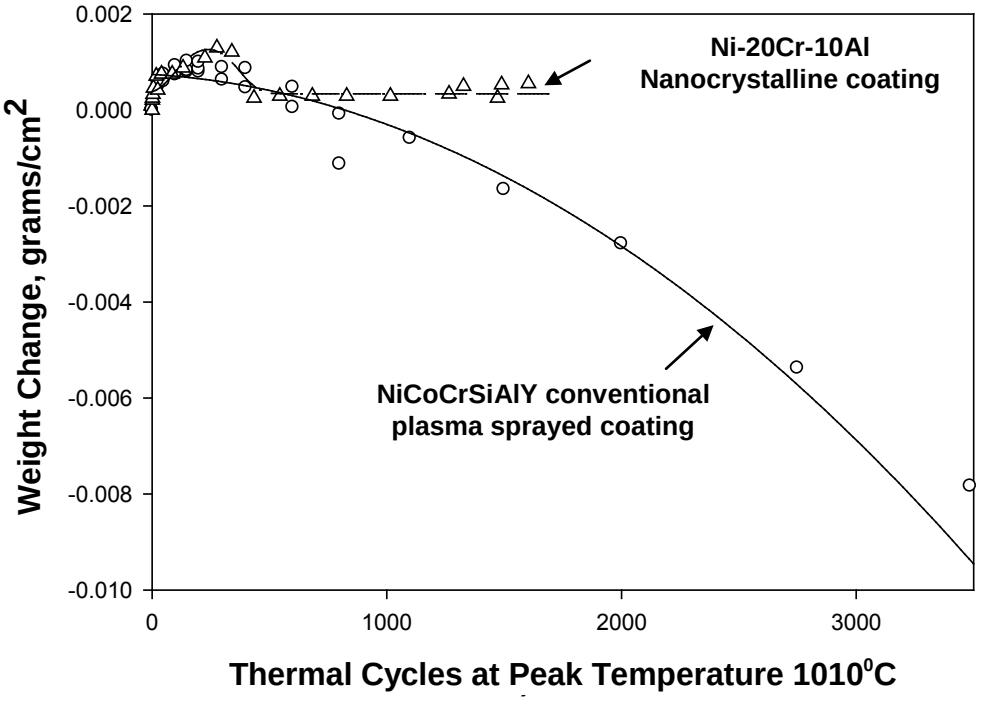

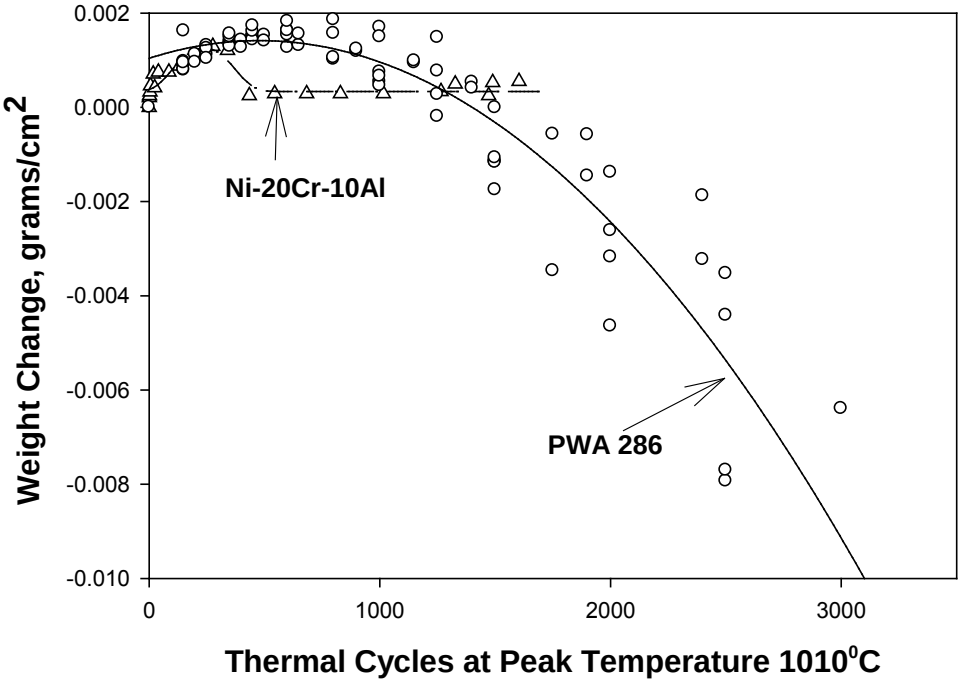

b)

Figure 3-15
Comparison of the cyclic oxidation behavior of nanocrystalline Ni-20Cr-10Al and plasma sprayed a) NiCoCrAlY b) PWA 286 coatings at the peak temperature of 1010º C.

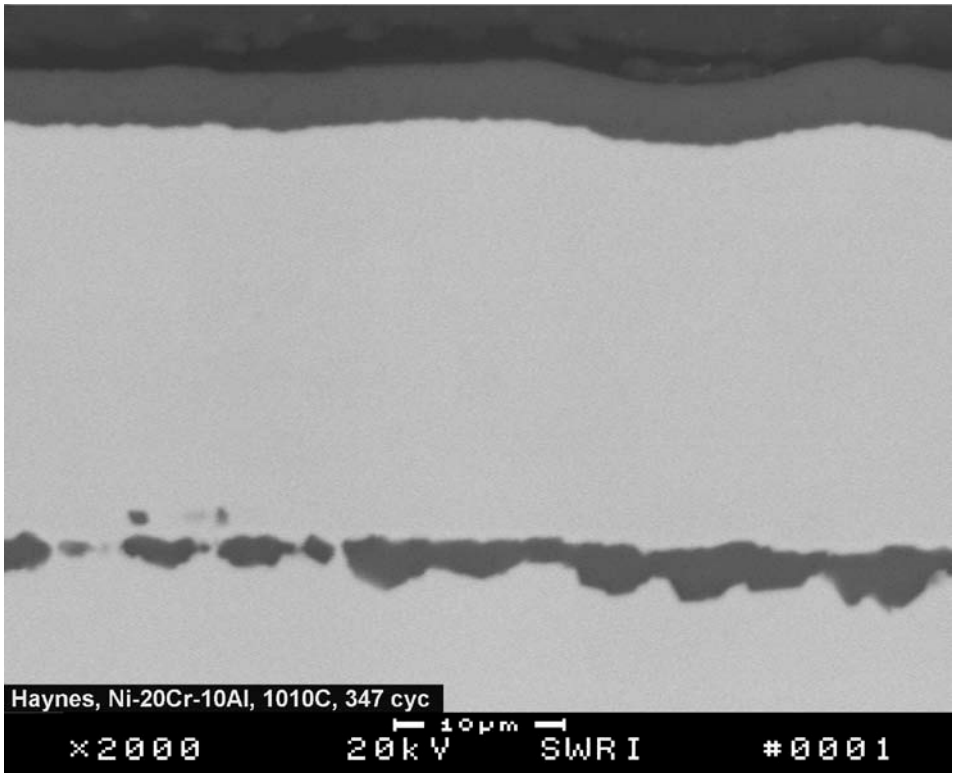

a) after 347 thermal cycles

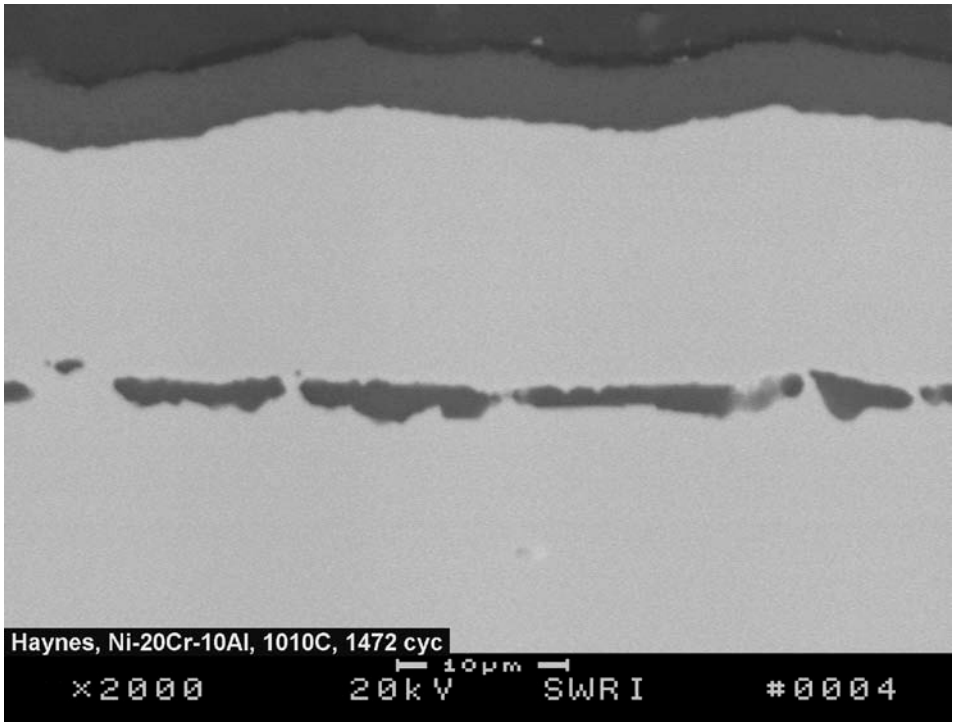

b) after 1472 thermal cycles

Figure 3-16
SEM micrographs of cross sections of nanocrystalline Ni-20Cr-10Al, a) after 347 thermal cycles and b) after 1472 thermal cycles exposure at 1010 C showing Al_2O_3 scale and Al-rich precipitate at the coating/substrate interface.

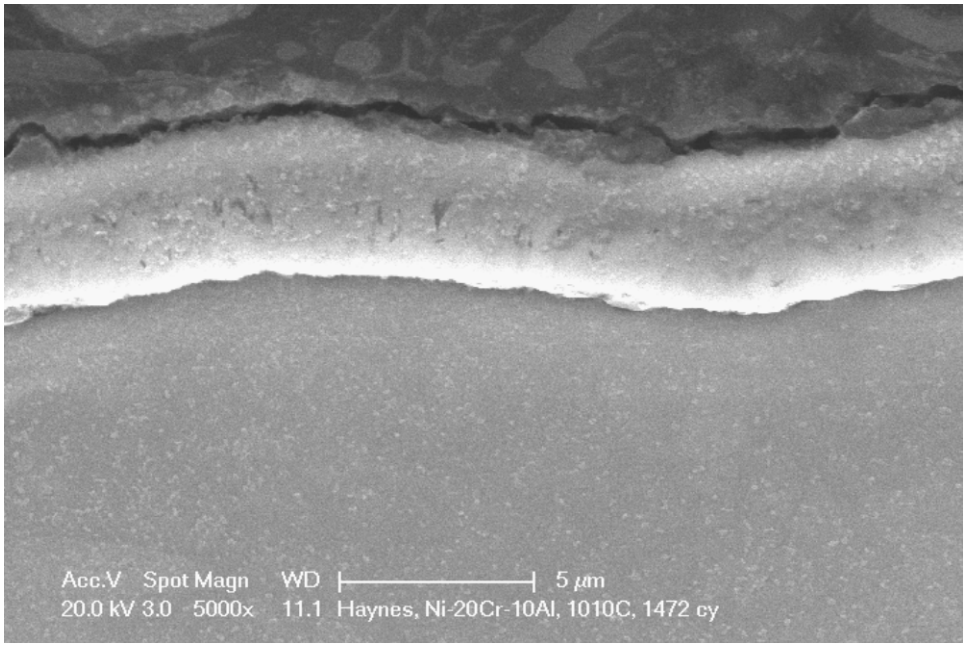

Figure 3-17
SEM micrograph showing a continuous dense Al_2O_3 scale on the nanocrystalline coating after 1472 cycles exposure at 1010º C.

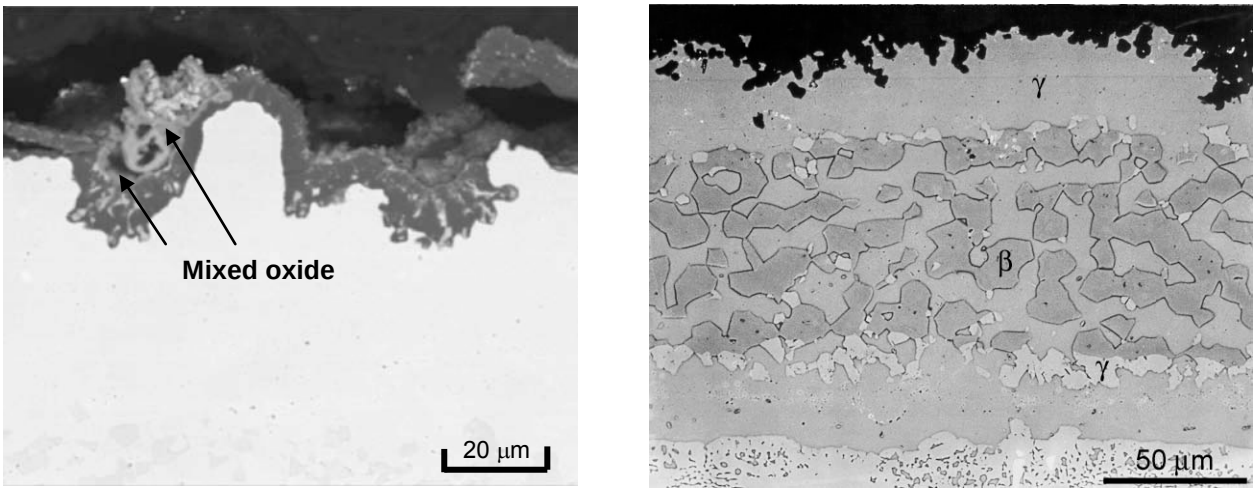

a) NiCoCrAlY **b) PWA 286**

Figure 3-18
Micrographs of cross sections of a) plasma sprayed NiCoCrAlY and b) PWA 286-coated samples after 1500 thermal cycles exposure at 1010 C showing variation of coating oxidation and mixed oxides.

The cross section of the nanocrystalline coated samples also exhibited coarse precipitate particles along the coating/substrate interface. These precipitates at the interface appeared to form in a relatively short time, within 347 thermal cycles (Figure 3-16a). However, formation of these interface precipitates did not lead to coating spallation upon subsequent thermal cycling from 347 to 1472 thermal cycles (Figure 3-16b). The results of the EDS analysis of the precipitates revealed that these were Al-rich (Al-Cr-Ni) particles and showed no oxygen peak, as illustrated in Figure 3-19, indicating that these are not oxide particles. The Al content among the precipitate particles analyzed varied from 50 to 87 wt.%. In addition, the cross section of an exposed sample following indentation hardness test, using 150 kg force, showed no evidence of interface precipitate cracking and/or coating delamination in the vicinity of the indentation, as shown in Figure 3-20, suggesting that the interface precipitates were not a brittle phase.

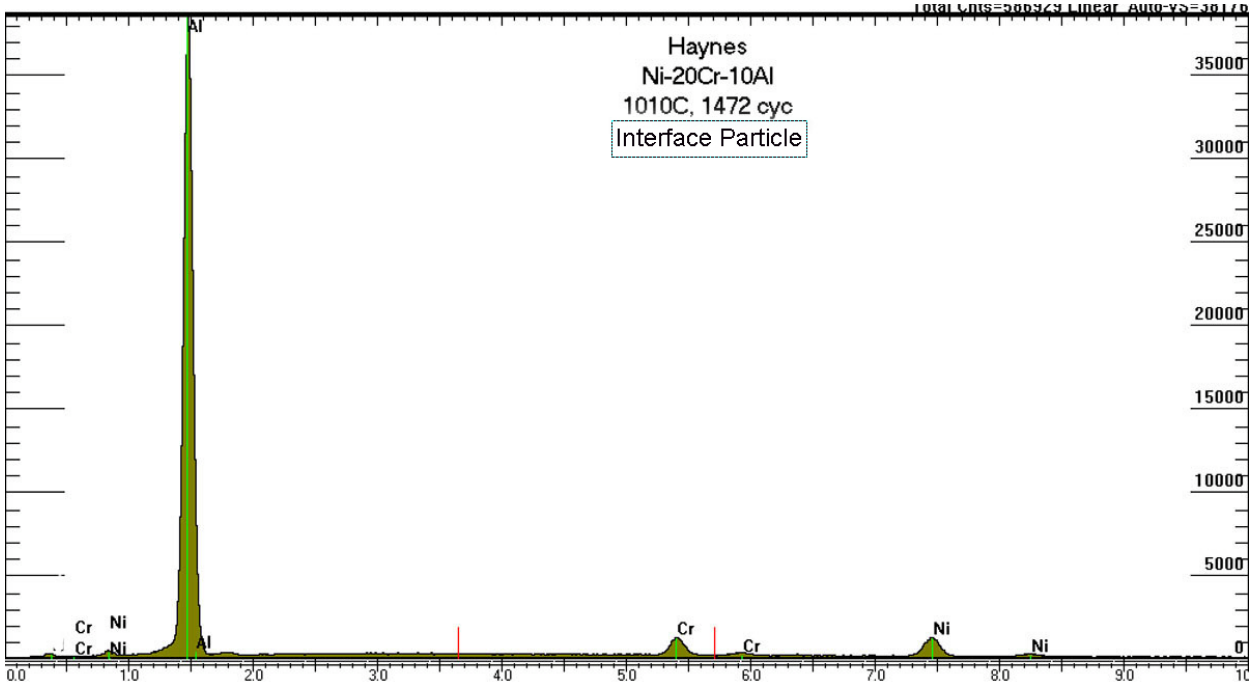

Figure 3-19
Typical EDS spectrum obtained from an interface precipitate particle showing the absence of oxygen peak, suggesting that the interface precipitates are not oxide particles.

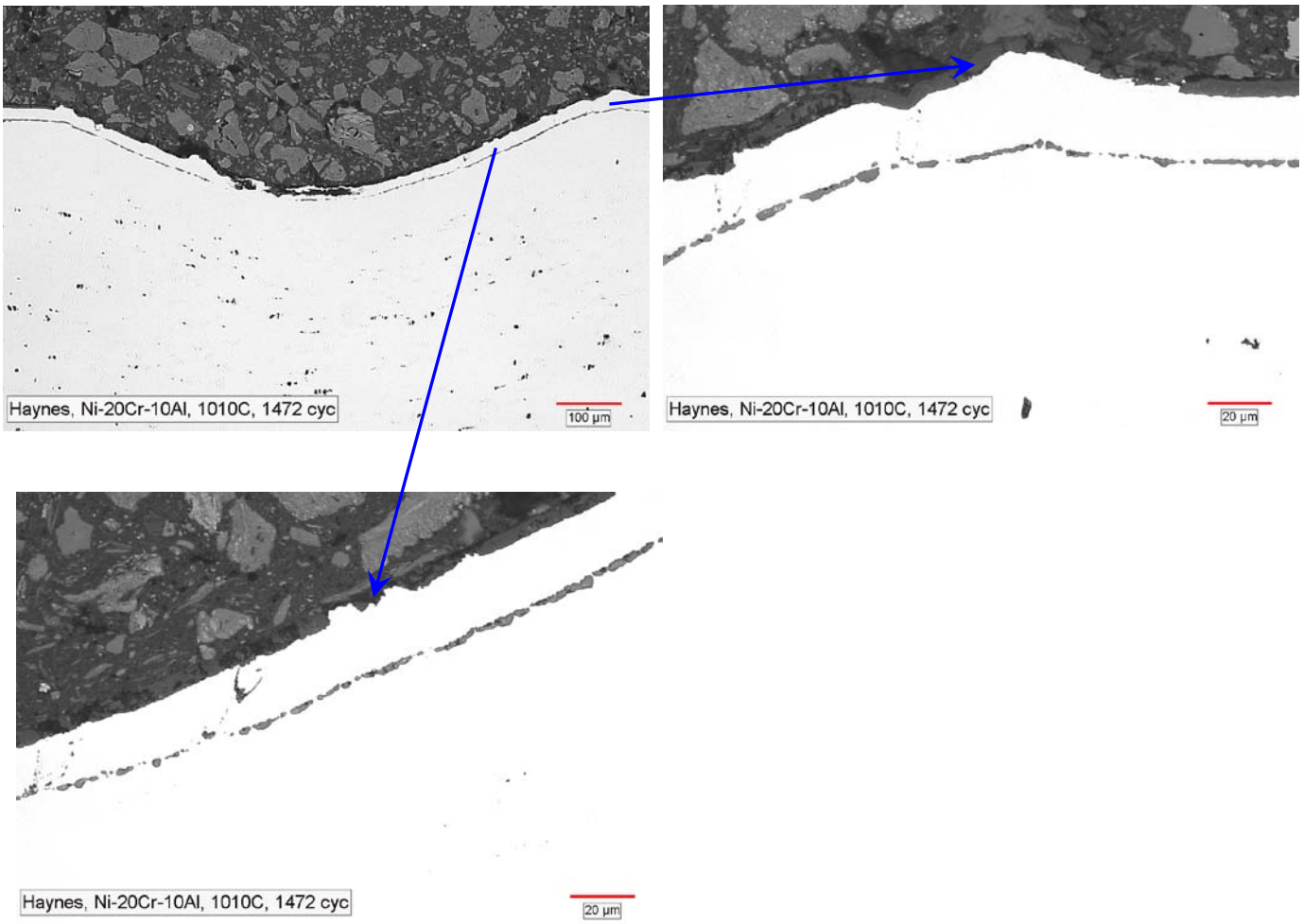

Figure 3-20
Optical micrographs of cross section of the coating through the hardness indention showing absence of cracking in the interface Al rich precipitates at the coating substrate interface [2-20].

The Al content, as a function of thermal cycles, in the nanocrystalline Ni-20Cr-10Al and the plasma sprayed NiCoCrAlY and PWA 286 coatings is compared in Figure 3-21. The Al in the nanocrystalline coating depleted exponentially with thermal cycles, while the Al consumption rate in both conventional plasma sprayed coatings was significantly lower. The Al content in the nanocrystalline coating dropped from 12 wt.% in the as-deposited condition to 1.7% after 347 cycles and to 0.7wt.% after 1472 cycles, respectively due to inward and outward diffusion of Al. A significant amount of Al, more than 85%, was consumed in the first few hundred cycles during the initial weight gain stage suggesting that inward diffusion of Al from the coating into the substrate is primarily responsible for the initial accelerated Al loss. The accelerated rate of Al depletion in the nanocrystalline coating is due to enhanced grain-boundary inward diffusion resulting from the ultra-fine structure of the coating. The accelerated rate of Al consumption limits the durability of the nanocrystalline coatings and a diffusion barrier interlayer between the nanocrystalline coating and the substrate is required to shut-off inward diffusion of Al from the coating into the substrate.

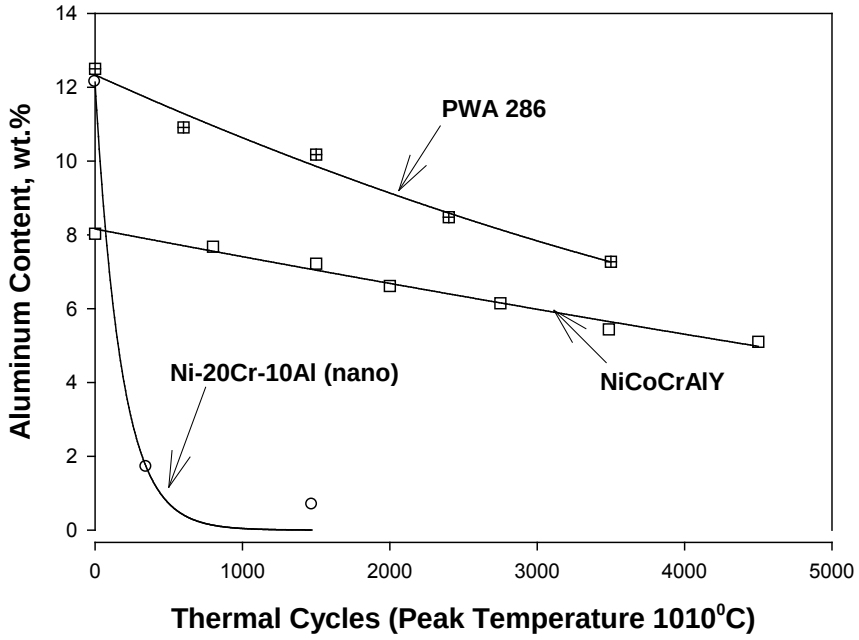

Figure 3-21
Comparison of Al depletion in the nanocrystalline Ni-20Cr-10Al and plasma sprayed NiCoCrAlY and PWA coating at the peak temperature of 1010° C [2-20].

3.5 References

3-1. N.S. Cheruvu, R. Wei, and D.W. Gandy, "Influence of Thermal Exposure on the Stability of Metastable Microstructures of Sputter Deposited Nanocrystalline 304 and 310 Stainless Steel Coatings," *Surface & Coatings Technology*. Vol. 205, No. 5, p. 1211 (2010).

3-2. N. S. Cheruvu, R. Wei, M. R. Govindaraju, and D.W. Gandy, "Evaluation of Nanocrystalline Coatings for Coal-Fired Ultrasupercritical Boiler Tubes," *ASME Journal of Pressure Vessel Technology*. Vol. 132, No. 6, p. 061403-1-9 (2010).

4.

TASK 3: PROCESS ADVANCED MCrAl NANOCOATING SYSTEMS

4.0 Introduction

The computational model results showed that 30 to 50% wt. Ni is required in a Fe-based nanocrystalline coating to maintain a high Cr or Al content during high temperature exposure (see Table 4-1). The model identified Fe-25Cr-40Ni coating with or without 10 wt.% Al as a potential coating. These coatings are expected to form a diffusion barrier interlayer between the coating and the substrates that significantly reduces inward diffusion of elements such as Cr and Al.

Considering the computation model results and the reliable MCrAl-type coatings used for the hot section parts of gas turbines, two iron base (Fe-Cr-Ni), a nickel base (Ni-Cr-Co), and a cobalt base (Co-Cr-Ni-W), MCr systems, with and without 10 wt.% Al were selected for further evaluation. For deposition of these advanced coatings, four different MCr (310SS, Haynes 120, Haynes 160, and Haynes 188) targets were procured. The composition of Hayes 120 is close to the composition identified by the model. The nominal compositions of the MCr target materials are given in Table 4-1. For deposition of the baseline 304-10 wt.% Al and Ni-20Cr-10 wt.% Al coatings, 304 SS and Ni-20Cr targets were used.

Table 4-1
Chemical composition of targets selected for deposition of advanced and baseline coatings.

Coating Type	Fe	Ni	Cr	Co	Si	W
310 SS	**Balance**	**20**	**25**	**—**	**0.6**	**—**
Haynes 120	**Balance**	**37.1**	**24.7**	**0.8**	**0.5**	**< 0.1**
Haynes 160	**0.5**	**Balance**	**28**	**30**	**4**	**< 0.1**
Haynes 188	**1.7**	**23**	**22**	**Balance**	**0.5**	**14**
304 SS	**Balance**	**8**	**18**	**—**	**0.4**	**—**
Ni-20Cr	**—**	**80**	**20**	**—**	**—**	**—**

4.1 Advanced MCrAl Coating Process Development

A PEMS deposition technique was used for the deposition of nanocrystalline coatings. Figure 4-1 shows the PEMS system. The process details are given in Reference 1-15. Two magnetrons, one for Al and the other for MCr, were used for the deposition of MCrAl. By adjusting the power for the MCr and Al targets, the required Al content of approximately 10 wt.% in the coating was obtained.

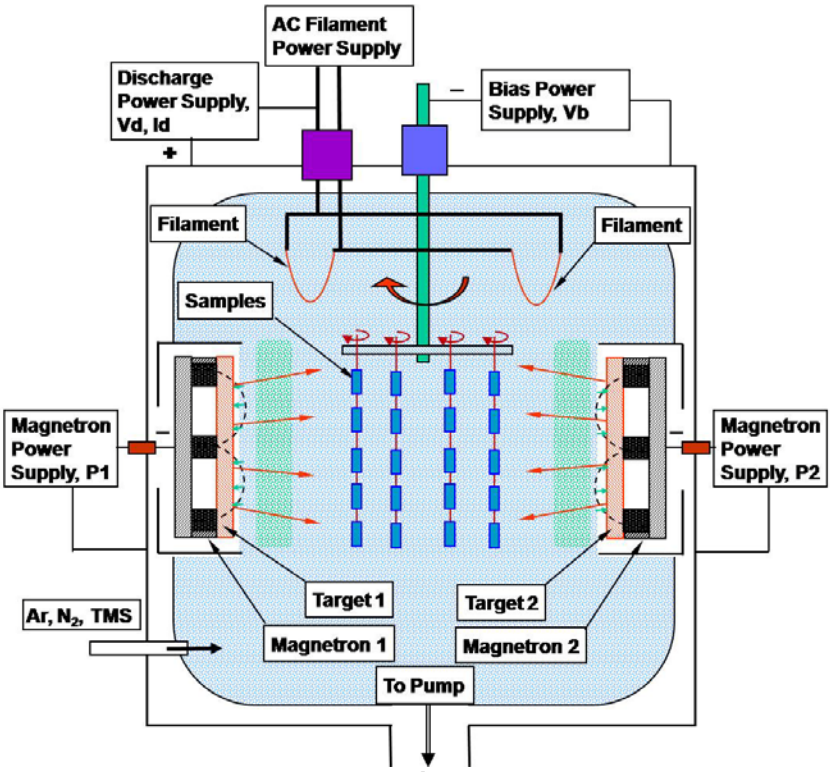

a)

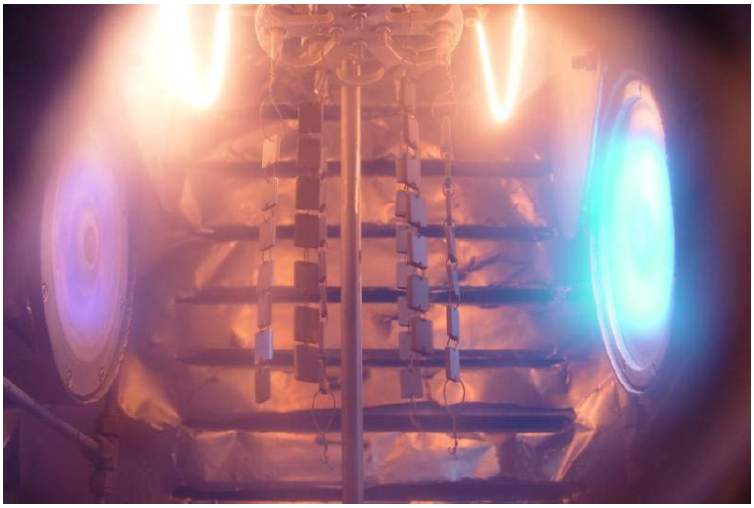

b)

Figure 4-1
(a) SwRI two magnetron PEMS system schematic and (b) a photograph of the PEMS process.

In the project's early stages, a process optimization study was conducted to identify the processing parameters that would produce a defect free dense coating. The critical parameters include the deposition time, magnetron power for each target, worktable bias voltage (ion energy delivered to the film surface), and discharge current and the worktable bias current (both for the ion flux). These parameters were varied and the processing variables considered for this study are shown in Table 4-2. Following deposition, the samples were sectioned and examined in a SEM to assess the coating surface morphology, the coating quality, and microstructure. The results showed that

the coating on the DE-3 samples exhibited the densest microstructure, free from defects, and good toughness among the all the samples processed utilizing different parameters. The typical structure of the coating on a DE-3 sample is shown in Figure 4-2. The quality of the coating on the DE-1 samples was almost comparable to that of DE-3. The metallurgical evaluation results showed that coatings were free cracks and the results were presented in detail in Reference 1-15. The parameters used for DE-3 sample were selected for processing advanced MCr and MCrAl coatings for fire-side corrosion testing.

Table 4-2
Summary of process variables investigated and the properties of the coatings applied using different process variables.

Sample No.	Deposit Time (h)	T1 Matl	T1 Pm1 (kW)	T2 Matl	T2 Pm2 (kW)	V bias (V)	I bias (A)	I disch (A)	Thick-ness (μm)	Al (wt%)	Grain Size (nm)	Microstructure
310SS+Al												
DE-1	4	Al	1.1	310SS	4	100	0.11	0	33.8	14.0	9.9	Dense
DE-2	4	Al	1.1	310SS	4	40	0.80	10	35.3	13.6	15.7	Columnar
DE-3	5	Al	1.1	310SS	5	60	1.28	15	38.5	11.6	21.7	Dense
DE-4	9	Al	0.55	310SS	2	40	0.85	10	37.4	12.9	10.1	Columnar
DE-5	8	Al	0.55	310SS	2	60	1.38	15	29.7			Coating dense, interface defects
DE-6	4	Al	1.1	310SS	4	100	0.14	0	29.8			Columnar
DE-7	4	Al	1.1	310SS	4	0	0.00	0	33.1			Columnar
DE-8	2	Al	1.1	310SS	4	150	0.15	0	13.1			
Ni20Cr+Al												
DE-9	4	Al	1.1	Ni20Cr	4	100	0.14	0	35.1	11.0	9.5	Columnar
DE-10	4	Al	1.1	Ni20Cr	4	60	1.38	15	27.8	8.9	24.1	Dense
DE-11	8	Al	0.55	Ni20Cr	2	60	1.30	15	32.2	10.1	14.9	Coating dense, interface defects
304SS+Al												
DE-12	4	Al	1.1	304SS	5	100		0	41.0			
DE-13	4	Al	1.1	304SS	5	60		15	36.3			

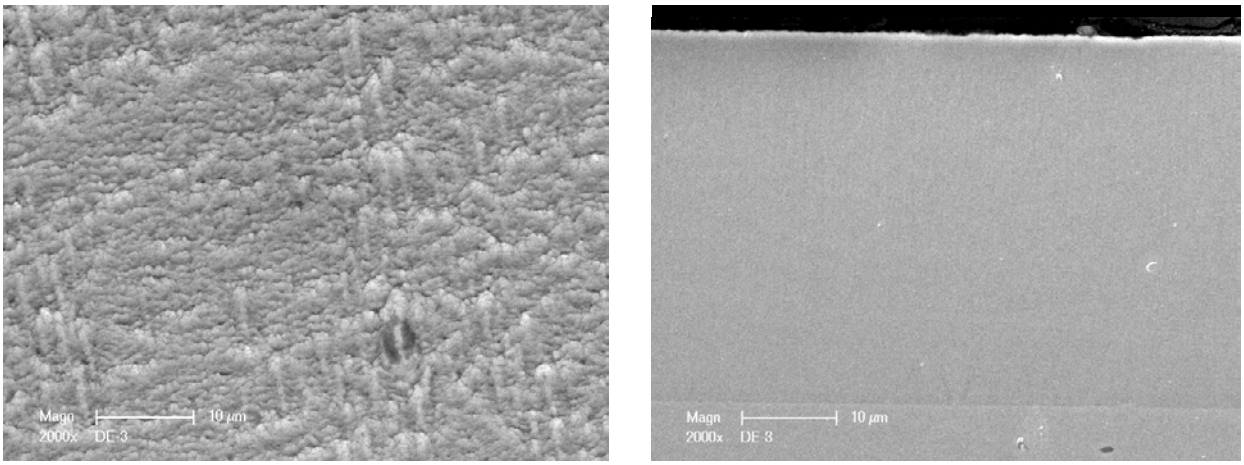

a) **b)**

DE-3 process parameters: Vb = 60V, Ib = 15A

Figure 4-2
Morphological a) and cross-sectional b) SEM images of 310 SS + 10 wt.% Al coating.

4.1.1 Application of Advanced Coatings

Three substrate materials, 304 SS, P91 steel, and Haynes 230 alloys were selected for application of advanced MCrAl and baseline coatings. The coatings with or without 10 wt.% Al were applied using the parameters specified for DE-3 in Table 4-2. The iron based coatings were not deposited on the nickel base Haynes 230 substrate. The samples to be coated were cleaned first using Ar-plasma ions for about 90 minutes to remove oxide scale. To vary the aluminum content from 0 to 10 wt.% in the advanced coatings, the target power for Al deposition was varied from 0 to 1.3 kW. The power for the MCr target was maintained at 4.0 kW. For comparison the baseline 304 SS-10 wt.% Al and N-20Cr-10 wt.% Al coatings were also applied on the substrate alloys.

4.1.2 Metallurgical Evaluation of As-Deposited MCrAl Coatings

Following application of the coating, the chemical composition measurements were conducted on a sample from each set of coating using EDS and the results were given in Tables 4-3 and 4-4. In contrast to the results of DE-1 through DE-3, metallographic examination of the as-coated samples revealed cracks in the coatings containing Al on all three substrate materials. Some of these cracks extended through the thickness of the coating. Typical morphology of cracks in the coating is illustrated in Figure 4-3. The coatings without Al showed no cracks, but exhibited coating defects such droplets, or nodules ("cauliflower" or "kennels").

Table 4-3
Semi-quantitative chemical composition of advanced coatings, wt.%.

Coating ID	Substrate	Al	Si	Ti	Cr	Fe	Co	Ni	W
DE-16, 310-10 Al	304	11.28	0.58	—	25.15	47.92	—	15.07	—
DE-16, 310-10 Al	P91	9.56	0.49	—	25.41	49.46	—	15.09	—
DE-18, H160-10 Al	304	9.53	2.45	0.5	27.43	0.40	28.29	31.40	—
DE-18, H160-10 Al	Haynes 230	10.56	2.71	0.42	27.23	0.32	27.78	30.96	—
DE-19, H120-10 Al	304	10.02	0.50	—	25.48	34.07	—	29.93	—
DE-19, H160-10 Al	P91	11.0	0.55	—	25.33	33.72	—	29.40	—
DE-20, H188-10 Al	304	10.76	—	—	23.87	1.8	35.71	19.60	8.11
DE-20, H188-10 Al	Haynes 230	11.52	—	—	22.91	1.30	35.34	19.96	8.36
DE-21, H188	304	—	—	—	25.33	1.97	40.34	21.70	9.49
DE-21, H188	Haynes 230	—	—	—	25.64	1.94	40.65	22.13	9.49
DE-24, H120	304	—	0.27	—	27.72	37.33	—	34.68	—
DE-24, H120	P91	—	0.28	—	28.15	37.42	—	34.16	—
DE-27, H160	304	—	1.64	0.45	30.28	0.67	32.33	34.63	—
DE-27, H160	P91	—	1.80	0.46	29.96	0.65	32.46	34.66	—

Table 4-4
Semi-quantitative chemical composition of baseline nanocrystalline coatings, wt.%.

Coating ID	Substrate	Al	Si	Cr	Fe	Ni
DE-14, 304-10 Al	304	7.42	0.54	18.44	Balance	6.26
DE-14, 304-10 Al	P91	8.54	0.47	18.26	Balance	6.51
DE-15, Ni-20Cr-10 Al	Haynes 230	7.66	0.18	18.93	0.44	Balance

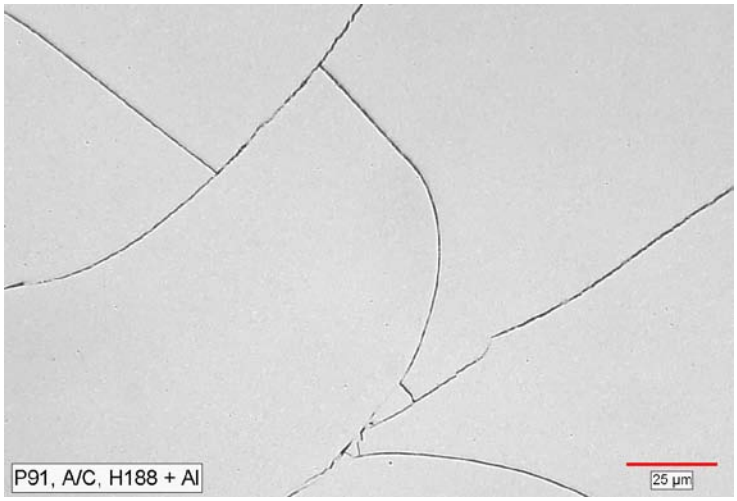

a)

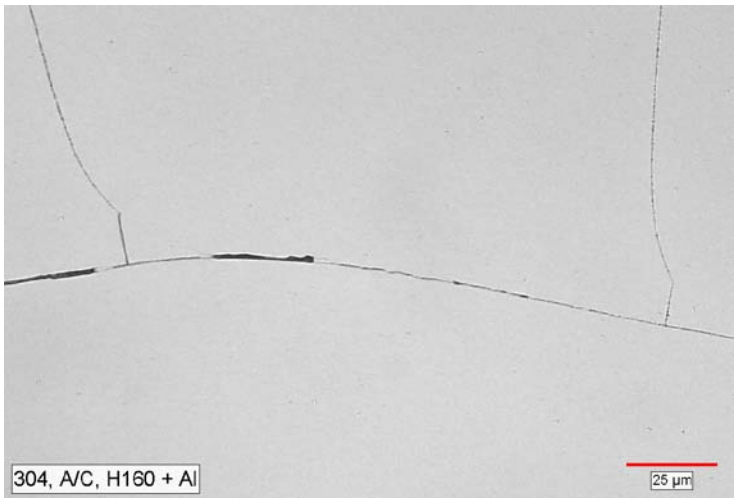

b)

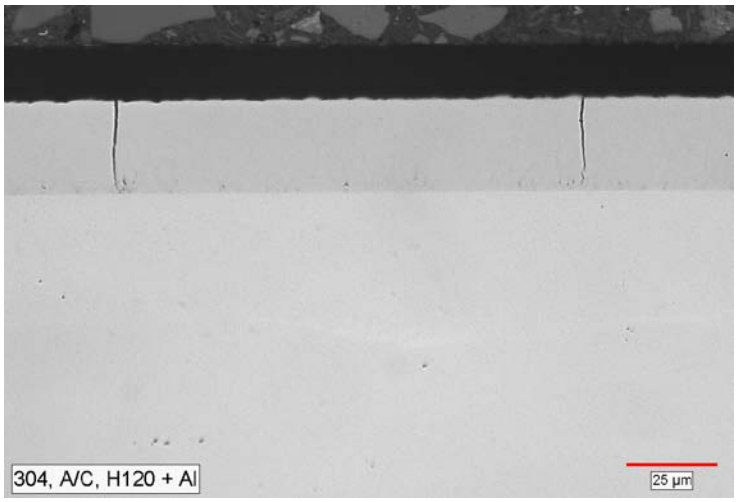

c)

Figure 4-3
Optical micrographs of the top view of coated samples a) Haynes 188-10 wt.% Al on P 91, b) Haynes 160-10 wt.% Al on 304 SS, and c) H120-10 wt.% Al on 304 SS.

4.2 Development of Diffusion Barrier Interlayer Coating

Three ceramic coatings, TiN, TiSiCN, and AlN, were selected as the barrier coating for the preliminary evaluation. The first two Ti-based coatings were prepared prior to depositing the top coating of MCrAl. However, from the process point-of-view, AlN is a preferred barrier coating because both AlN and MCr + 10 wt.% Al can be deposited in the same batch without breaking the vacuum. After application of the interlayer coating, 304 SS + 10 wt.% Al and Ni-20Cr Al coatings were applied on 304 SS and Haynes 230 samples, respectively. Processing details and metallurgical characterization results can be found in Reference 1-15. A typical microstructure of the Ni-20Cr-10Al coating over a diffusion barrier interlayer is shown in Figure 4-4. Cyclic oxidation testing was performed on the 304 SS + 10 wt.% Al and Ni-20Cr Al-coated samples at 750º C and 1010º C, respectively. Consistent with the results shown in the previous section (Figures 3-10 and 3-13), the nanocrystalline coatings showed little or no weight loss following the initial mass gain. The mass change results for the nanocrystalline Ni-20Cr-10Al coating with three diffusion interlayer barrier coatings are shown in Figure 4-5 as a function of thermal cycles at 1010° C. Absence of mass change after the initial gain also suggests that little or no loss of Al occurs in the nanocrystalline coatings after formation of the stable oxide scale. The examination of the cross sections of the specimens with three different interlayer coatings revealed that the TiN-interlayer coating was the best performer on both the 304 SS and Haynes230 alloys. The Al consumption rates for the nanocrystalline coating with and without TiN interlayer and conventional plasma sprayed coatings are presented in Figure 4-6. The Al consumption rates for nanocrystalline coating with TiN interlayer and conventional coatings are comparable and the interlayer is effective in minimizing or preventing inward diffusion of Al.

Consistent with this, the examination of the specimens' cross sections showed that a significant amount of Al is left in both 304 SS + 10 wt.% Al and Ni-20Cr Al-coated samples, as shown in Figures 4-5 b and 4-7 b. The absence of FeAl particles in the 304 SS substrate below the TiN interlayer (Figure 4-7 a) also suggests that the interlayer coating was effective in preventing inward diffusion of Al from the coating into the substrate.

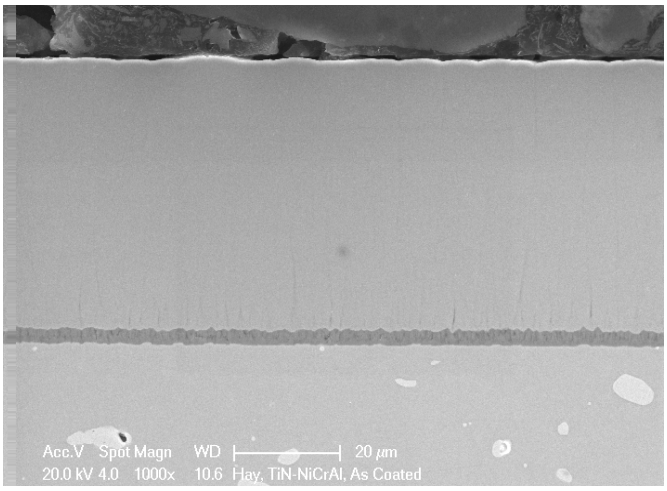

Figure 4-4
Cross section of the as-deposited Ni-Cr-Al coating with a TiN-diffusion barrier Interlayer.

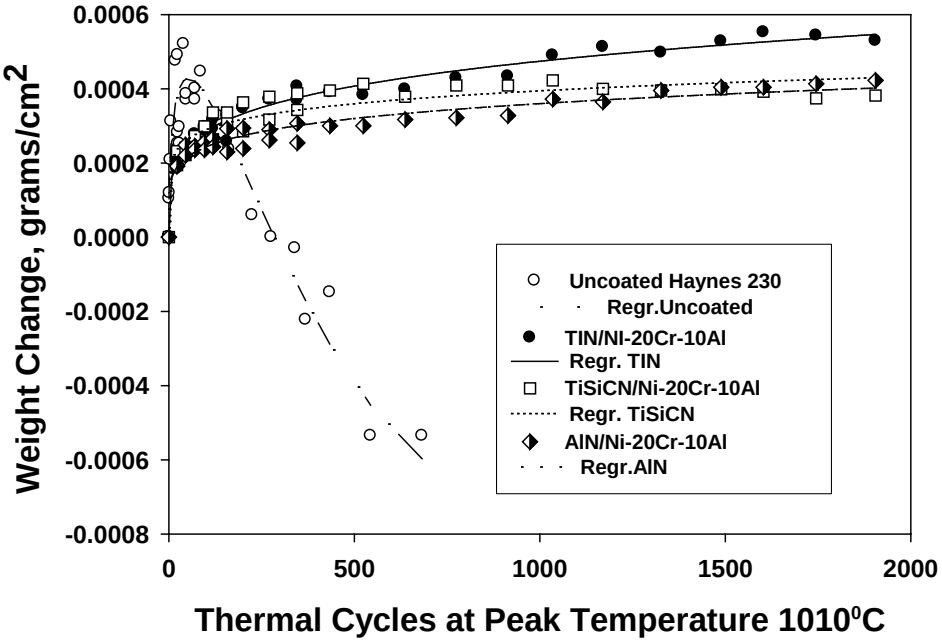

a)

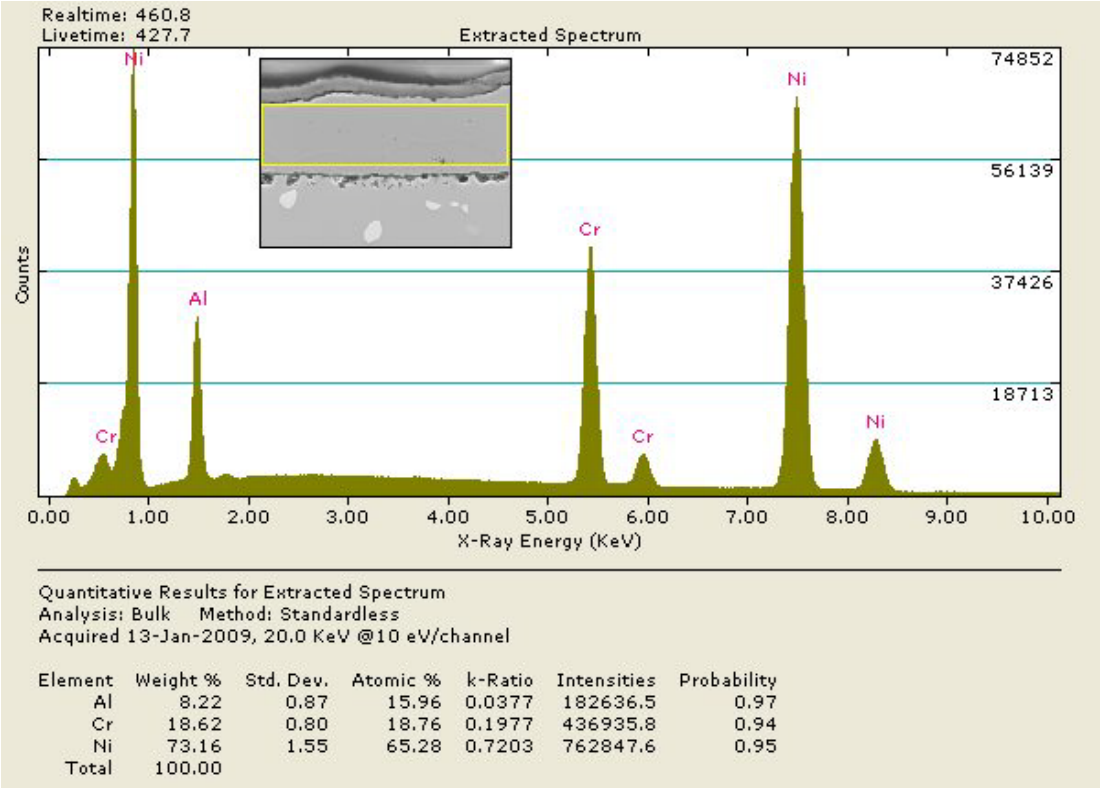

b)

Figure 4-5
Influence of the diffusion barrier interlayer on a) cyclic oxidation behavior of Ni-20Cr-Al and b) EDS spectrum obtained from the coating showing 8.2 wt.% Al after 2100 cycles exposure at a maximum temperature of 1010° C with an insert of the cross section of the coated samples after exposure.

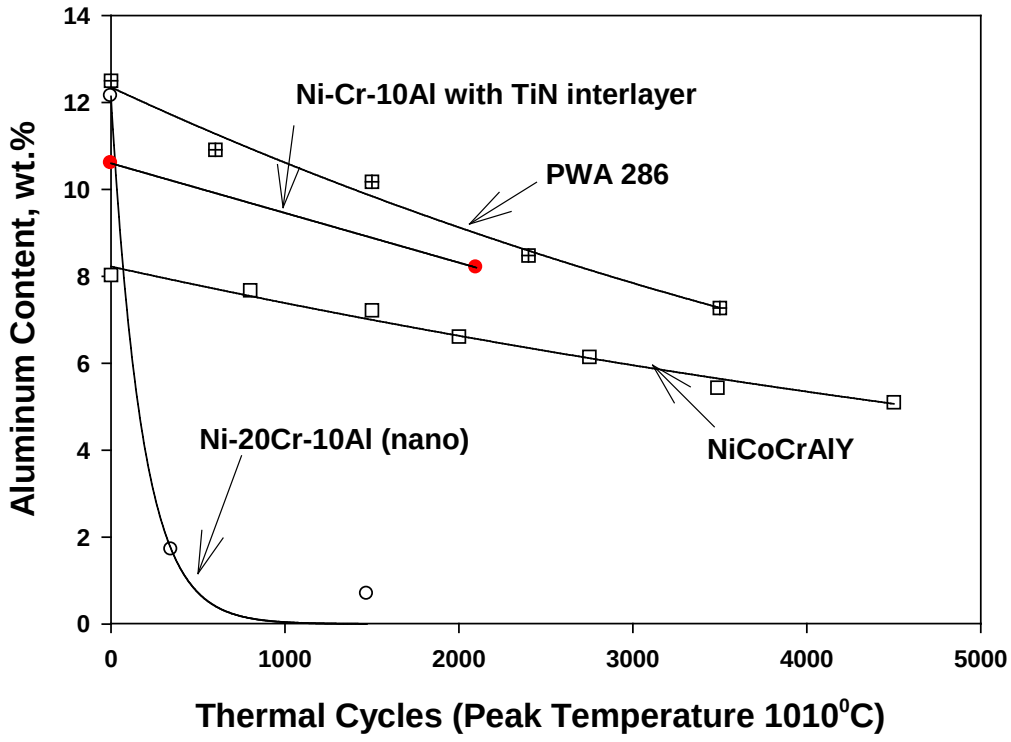

Figure 4-6
Comparison of the Al depletion in the nanocrystalline Ni-20Cr-10Al coating with and without the TiN interlayer and plasma sprayed NiCoCrAlY and PWA coatings at the peak temperature of 1010º C.

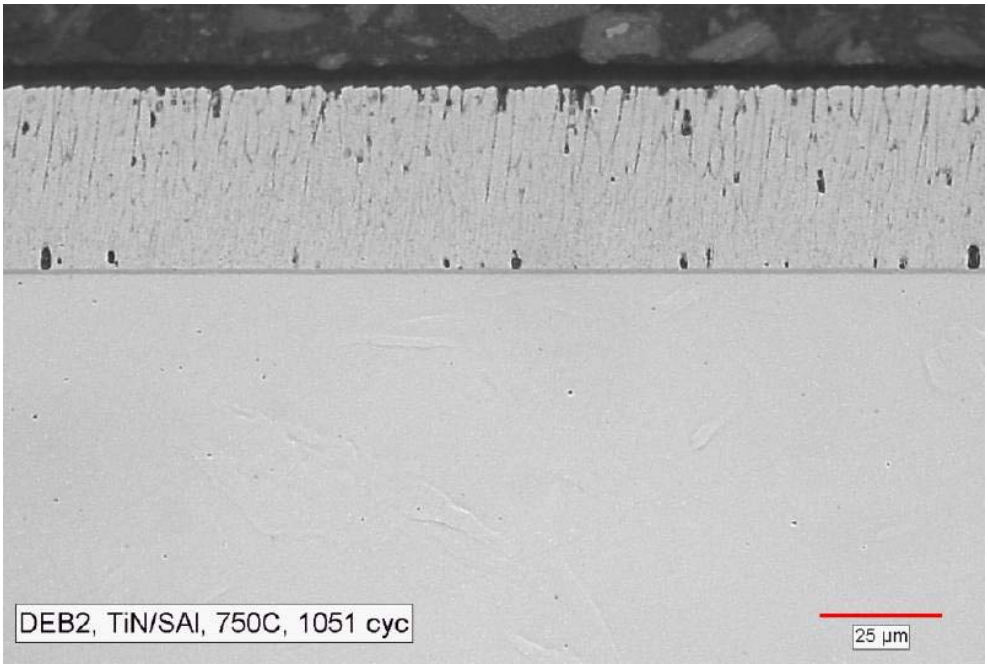

a)

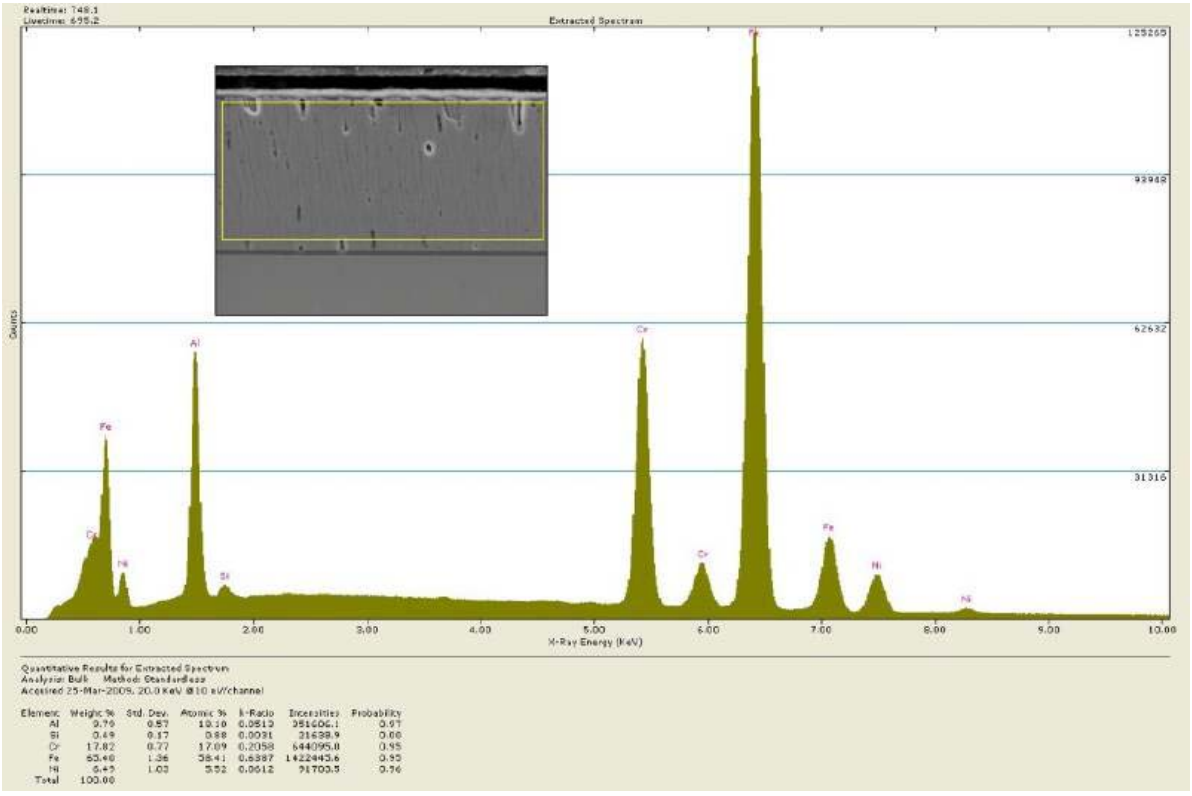

b)

Figure 4-7
SEM micrograph of the cross section of the 304 SS-10Al coating after 1051 cycles exposure at the maximum temperature of 750° C showing the absence of FeAl particles in the 304 SS substrate below the TiN interlayer and b) EDS spectrum obtained from the coating showing 9.8 wt.% Al.

4.2.1 Optimization of TiN-Interlayer Coating Deposition Process

The morphology of the TiN-interlayer coating played a crucial role for the overall structure of the TiN/MCrAl coating. The goal of this study was to reduce the defects (droplets or "cauliflowers") in the TiN coating so that the number of defects in the MCrAl coating could be reduced. A large number of coating deposition trials was conducted to optimize the process parameters for the TiN-interlayer deposition. The typical morphology of a TiN coating deposited using the optimum process parameters is shown in Figure 4-8. It is evident from the micrographs that the outer surface of the TiN coating was smooth and free from cracking. The coating exhibited only a few or "cauliflower" defects. The TiN layer showed good adhesion, as illustrated in Figure 4-9.

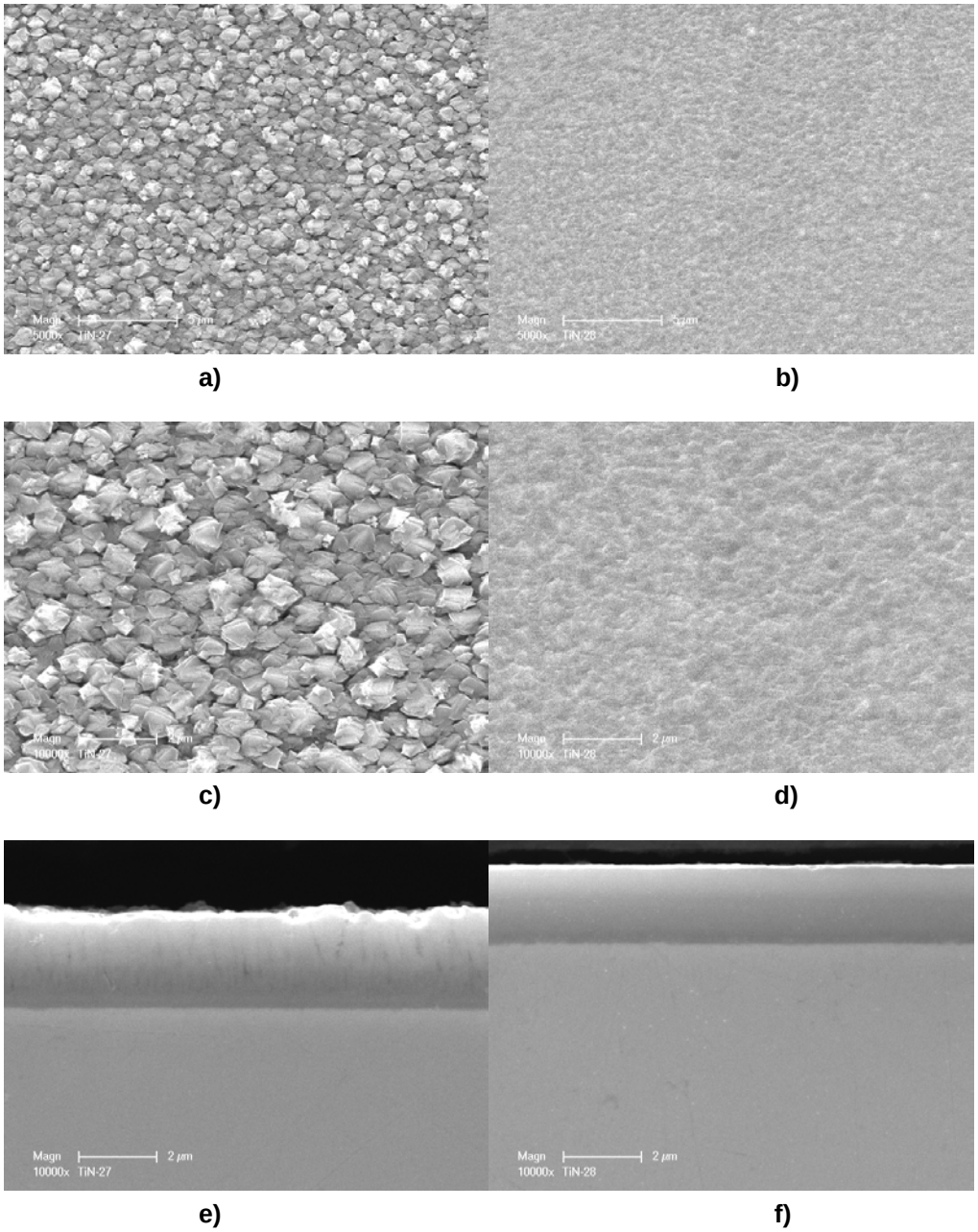

Figure 4-8
SEM images of morphological (a, b, c, and d) and cross-sectional (e and f) views of TiN 27 (left) and TiN 28 (right).

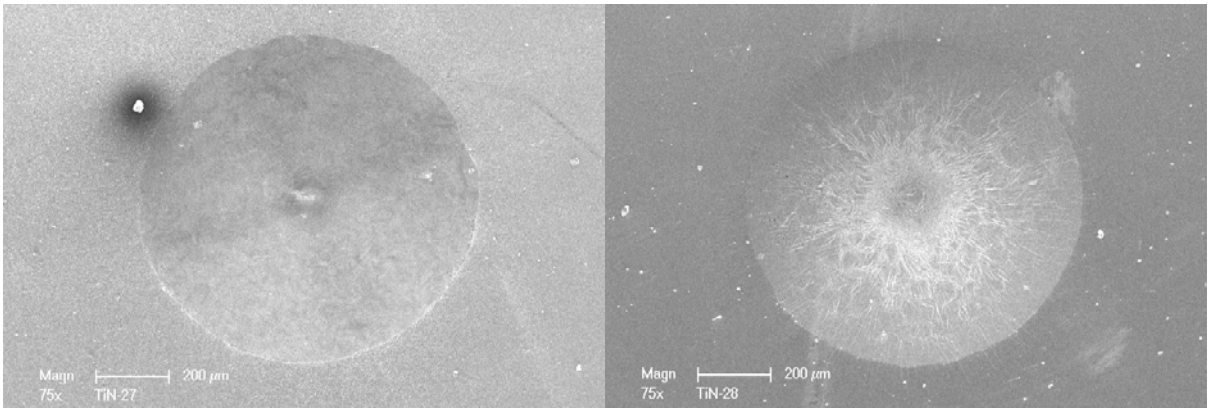

Figure 4-9
SEM images of Rc indents for TiN 27 (left) and TiN 28 (right).

4.3 Process Optimization for MCrAl Deposition Over a Diffusion Barrier Coating

Several coating trails were conducted by a) fine tuning the process parameters of DE-1 and DE-3 and b) increasing sputter cleaning time before coating deposition for improving the quality of the coating. The effect of stress relieving the samples prior to coating application was also investigated. Visual examination of the samples showed a few crack-free samples and these were used for the initial fire-side corrosion testing at Foster Wheeler after coating deposition. Metallurgical examination of the samples revealed kernels (cauliflower type) defects and cracks. The typical defects found in the metallurgical examination are shown in Figure 4-10. The quality of the coatings varied from trial to trial and sample to sample in a given trial, suggesting that a systematic research effort is required to minimize the defects in these coatings. New processing techniques such as a) high power impulse magnetron sputtering, b) processing coatings with four magnetrons, and c) pulsed DC magnetron sputtering were considered to improve the density and quality of the advanced MCrAl coating over the TiN interlayer. These results are presented in the following sections.

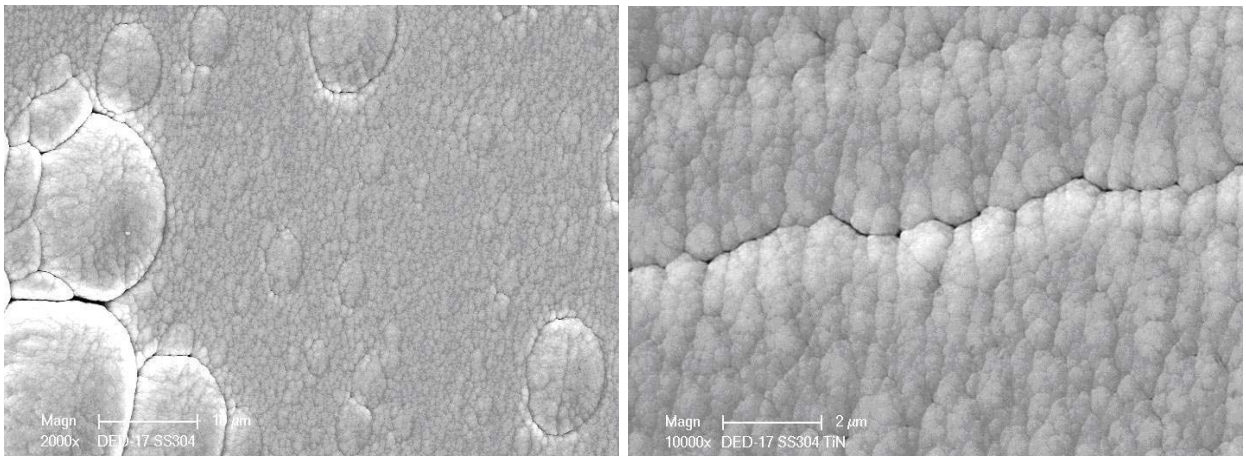

a) **b)**

Figure 4-10
SEM micrographs of top-view of coated samples showing a) kernels or cauliflower type defects and b) crack.

4.3.1 Deposition Process using High Power Impulse Magnetron Sputtering (HIPIMS)

This method utilizes pulsed DC power at a high frequency up to 500 Hz and pulse width of about 200 µs to accomplish the sputtering of a target material. The high pulsed voltage of 1000 volts, (versus ~500volts for the DC magnetron), helps ionize all metal particles and thus, improves density of the coating in the HIPIMS process. In contrast, only a small fraction of the metallic particles (1 to 2 wt.%) are ionized in the DC magnetron sputtering process. The high power supply was used for the Al target and the DC power supply was used for the MCr target. After a number of trials, the best combination of the power to the Al and the MCr (Fe, Ni, and Co-based targets) were established. The final deposition parameters were used for the deposition of the Haynes 120-10Al, Haynes 160-10Al, and Haynes 188 coatings on the AlN and TiN/AiN-coated samples. After the MCrAl coating deposition, a transverse section was removed from an each type of coated sample for SEM examination. Examination of the samples showed that the coating was dense with no macro-cracks. However, a few cauliflower type defects were observed in the as-deposited coatings. Fine delamination was observed around the cauliflower/matrix interface, as illustrated in Figure 4-11. The coatings exhibited poor adhesion. The HIPIMS process seems to generate a higher coating stress, which was considered to be responsible for the coating delamination and poor adhesion. Comparison of the similar coatings, prepared using only DC magnetron sputtering, revealed that the HIPIMS deposited coatings seem to be more brittle. Consequently, the HIPIMS method is not considered to be suitable for the deposition of the MCrAl coatings for structural components.

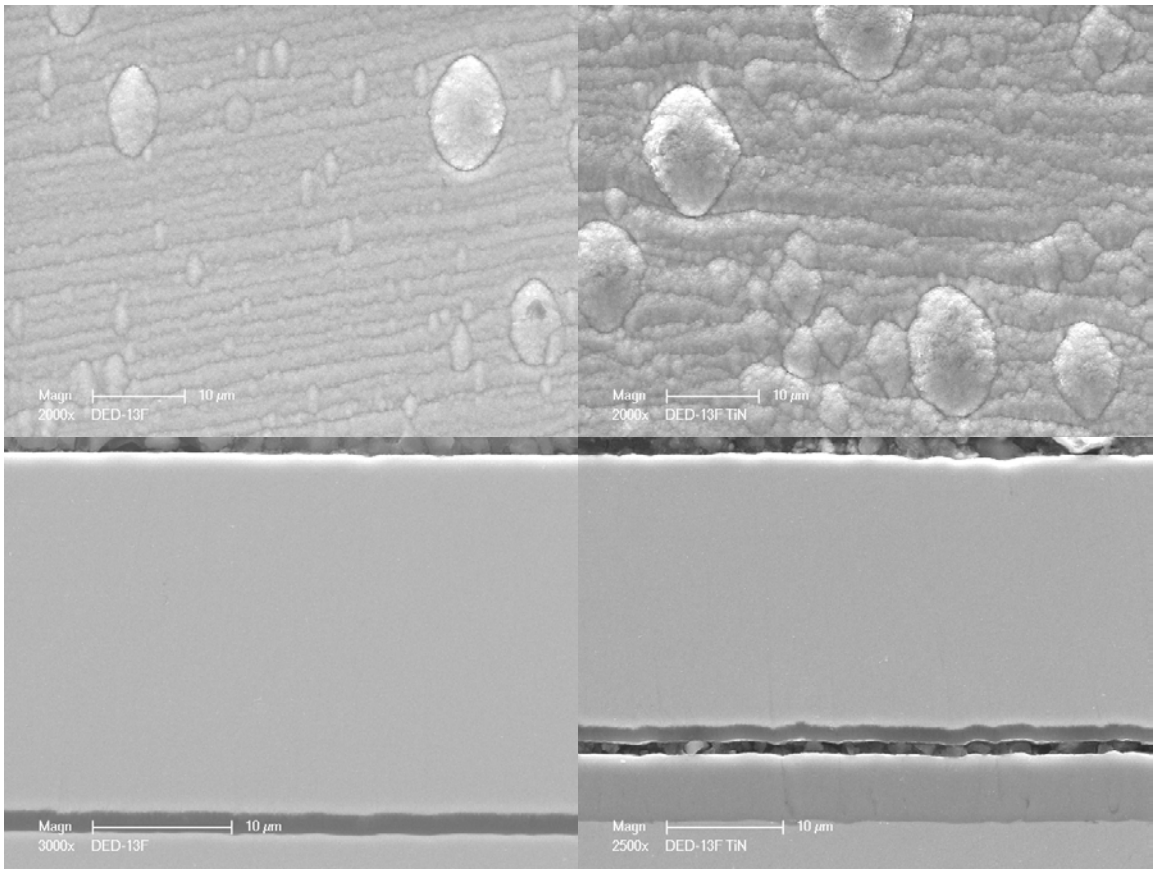

Figure 4-11
Morphological views (top photographs) and cross-sectional view (bottom photograph) of 304 SS + 10 wt.% Al coating on AlN/304 SS (left) and AlN/TiN/304 SS (right).

4.3.2 Plasma Enhanced Magnetron Sputtering (PEMS) Process Using Four Magnetrons

In the previous MCrAl deposition trials, the coating was deposited utilizing a two-step process with two magnetrons. In these trials, first TiN was deposited on the samples using Ti targets and the targets were replaced with the MCr and the Al targets after venting the vacuum chamber. Then MCrAl coating was deposited. It was suspected that this process may have caused the oxide scale formation on the surface of the TiN coating, which later resulted in the poor adhesion of the MCrAl. To avoid this, it was decided to use the SwRI's large deposition chamber with four magnetrons (Figure 4-12). One magnetron hosted the Ti target for the TiN deposition, one magnetron was used for the Al, and two magnetrons were used for the MCr targets. With this procedure the TiN and MCrAl depositions can be handled in one batch without venting the vacuum chamber. Four deposition trials on the 304 SS samples were conducted using different parameters, as illustrated in Table 4-5. The deposition parameters were explored to obtain the desired 10 wt.% Al in the MCrAl coating in the first two trials. Finally, two more tests were conducted to examine the microstructures and adhesion. The morphological (a, b, c, and d) and cross-sectional (e and f) SEM images of DEL 3 (left) and DEL 4 (right) are presented in Figure 4-13. The coating on both samples was free cracks and delamination. However, a few "cauliflowers" were seen on the coating outer surface. SEM images of the Rc indents on DEL3 and DEL4 coating samples are shown in Figure 4-14. It is clear form these images that the single-layered coating with very fine multi-layers, showed excellent adhesion, while the multi-layered coating showed evidence of coating spallation.

Table 4-5
Deposition conditions for samples DEL 3-4 from the four magnetron system.

Sample No.	Coating	Process Step	Process Time (min)	Mag 1 Mat'l/Pwr (kW)	Mag 2 Mat'l/Pwr (kW)	Mag 3 Mat'l/Pwr (kW)	Mag 4 Mat'l/Pwr (kW)	V bias (V)	I bias (A)	I disch (A)	Press (mT)	Ar (sccm)	N2 (sccm)	Thick. (μm)	Depo Rate (μm/h)	Comments
DEL1	Sputter Cleaning	1	200	-	-	-	-	120	0.40	5	3	100	-			
	TiN	2	70	-	-	-	Ti/4	100	0.34	5			50			
	304ss+TiN	3	10	304SS/4	-	304SS/4	Ti/4		0.41	5			50			
	304ss+Al	4	240	304SS/4	Al/2	304SS/4	-		0.46	5						
DEL2	Sputter Cleaning	1	190	-	-	-	-	120	0.33	5	3	100	-			
	TiN	2	120	-	-	-	Ti/4	100	0.32	5			50			
	304ss+Al+TiN	3	10	304SS/4	-	304SS/4	Ti/4		0.37	5			50			
	304ss+Al	4	362	304SS/4	Al/2	304SS/4	-		0.41	5						
DEL3	Sputter Cleaning	1	240	-	-	-	-	120	0.35	5	3	100	-			
	TiN	2	90	-	-	-	Ti/6	100	0.22	5			75			
	304ss+Al+TiN	3	10	304SS/6	-	304SS/6	Ti/6		0.38	5			75			
	304ss+Al	4	242	304SS/6	Al/3	304SS/6	-		0.44	5				25.8	6.4	
DEL4	Sputter Cleaning	1	180	-	-	-	-	120	0.35	5	3	100	-			TiN was a multi-layer (Ti/TiN, 5min/25min) deposition. SS+Al was a multilayer deposition (Al/(SS+Al), 5min/25min)
	TiN	2	90	-	-	-	Ti/6	100	0.44	5			75			
	304ss+TiN	3	10	304SS/6	-	304SS/6	Ti/6		0.4	5			75			
	304ss+Al	4	330	304SS/6	Al/2.7	304SS/6	-		0.44	5				22.8	4.1	

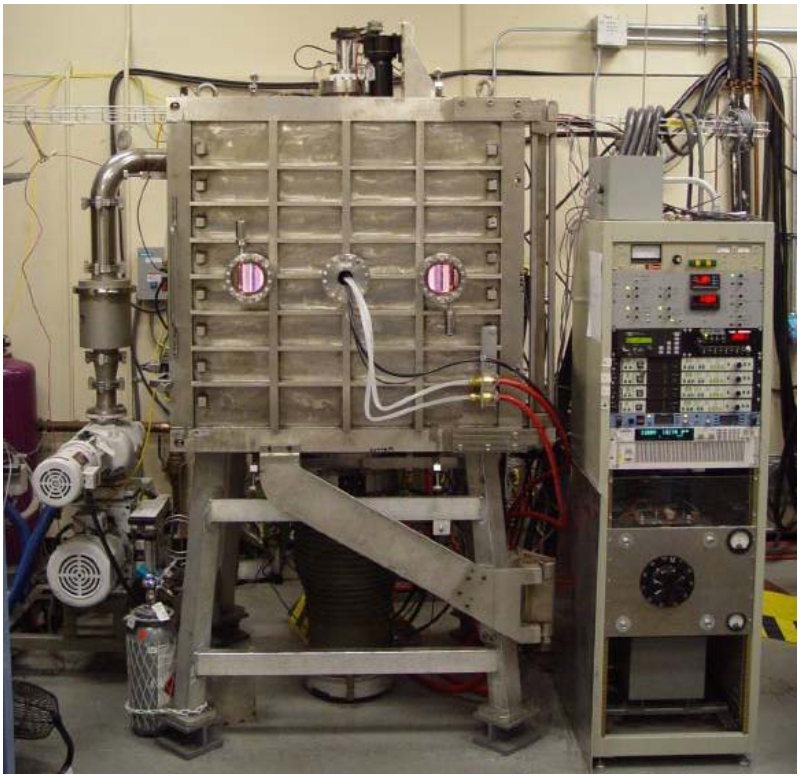

a)

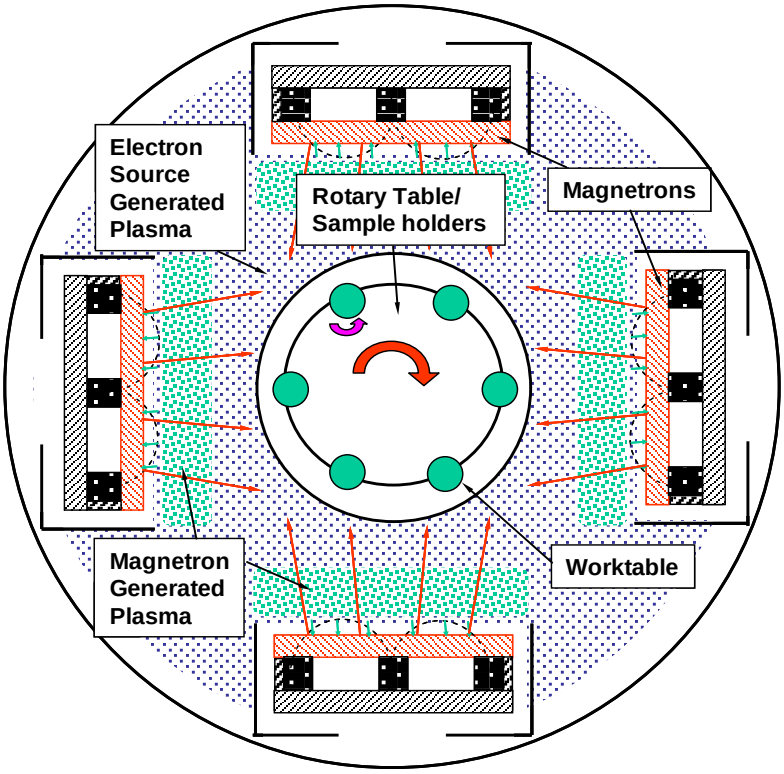

b)

Figure 4-12
(a) Photograph of SwRI's large (1 M^3) four magnetron PEMS system and b) schematic of the process.

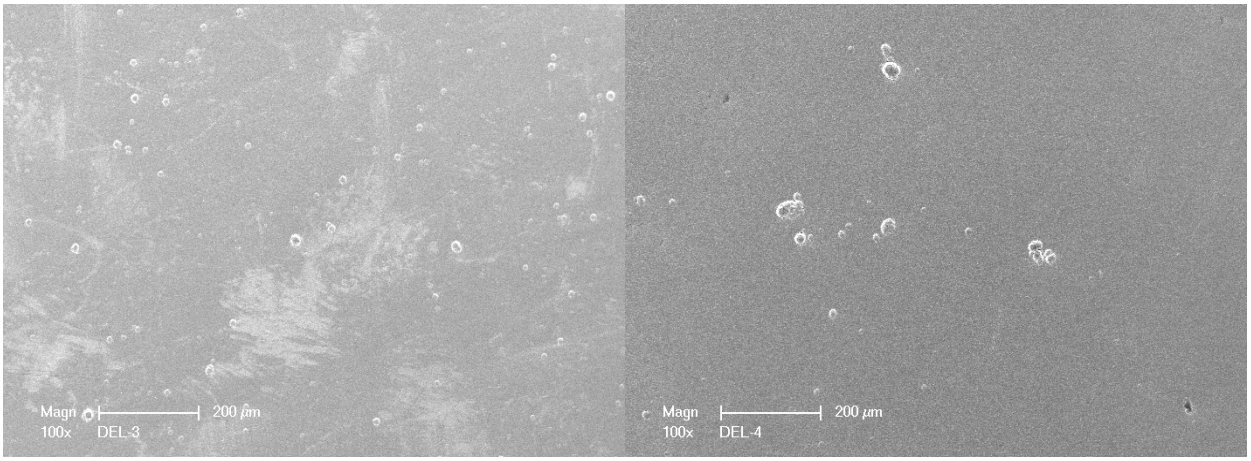

a) b)

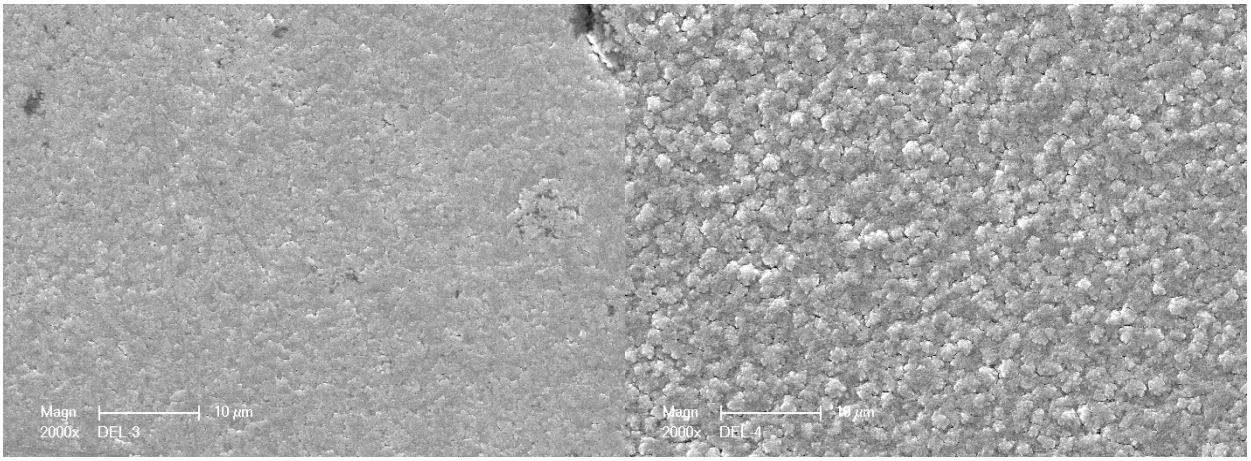

c) d)

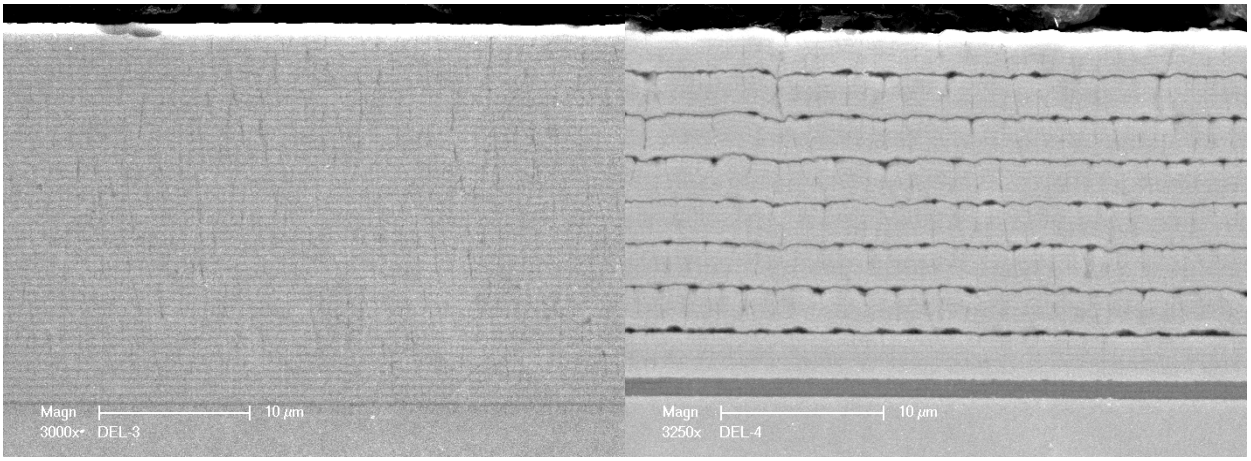

e) f)

Figure 4-13
SEM images of the morphological (a, b, c, and d) and cross-sectional (e and f) views of the DEL3 (left) and DEL4 (right).

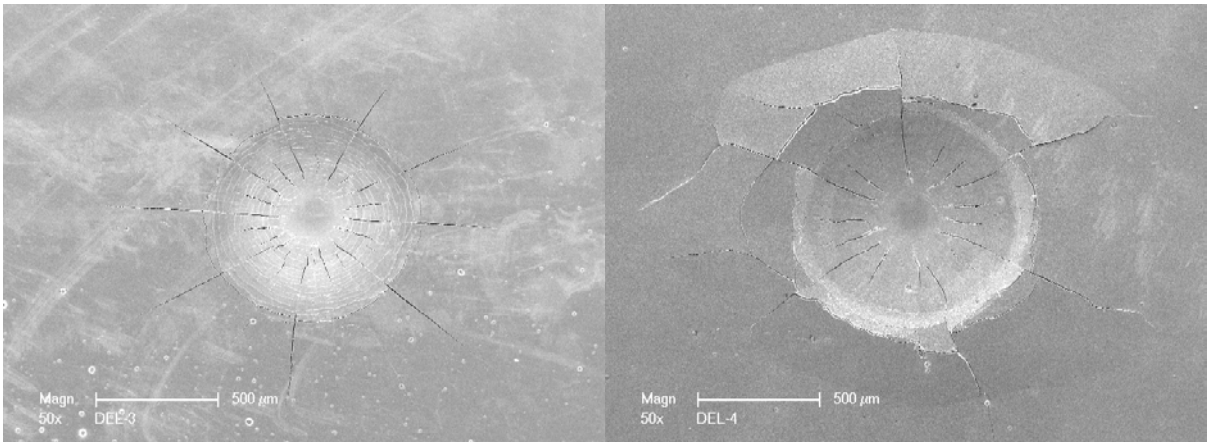

Figure 4-14
SEM images of Rc indents for DEL 3 (left) and DEL 4 (right).

After evaluation of the preliminary results, 24 deposition runs were conducted using the 304 SS, Ni20Cr, H160, 310 SS, and H120 targets, together with an Al target, to form various MCrAl coatings. These coating trials were conducted on a small number of samples for each coating type. The purpose of these multiple tests was to identify the optimum conditions that would eliminate, or minimize cauliflower defects in the coating. The coating morphology and composition were checked after each coating trial and the process parameters were adjusted accordingly for the second deposition run. After determining the process parameters that would produce the desired quality of the coating, 304 SS-Al, 310 SS-Al, Ni-20Cr-Al, H 160-Al, and H120 Al-coatings were deposited on several samples using the large chamber. Metallurgical examination of these samples showed s a significant variability in the quality of the coatings and cauliflower-type defects and fine crack were observed in the coatings. It appears that formation of cauliflower defects is inherent to the process and as a result, it is difficult to eliminate these defects in these coatings. These results showed that this process is not reproducible and a systematic study is required on the coating quality variability.

4.4 Pulsed DC Magnetron Sputtering Process

Advanced Coatings and Surface Engineering Laboratory of Colorado School of Mines (CSM) was contacted for depositing the TiN and 160 + Al coatings on the Haynes 230 and 304 SS samples using with, and without, pulse DC supply. In order to select the process parameters, 6 to 8 µm thick H160 + Al coating was first applied on the 304 SS using pulse DC with 1.0 kW and 1.5 kW power for the Al target. The details of the coating application system, process parameters, and metallurgical examination results are given in Appendix B. The thin and thick coated samples were also examined at SwRI® and the examination results are as follows.

4.4.1 Thin MCrAl Coating

Optical metallographic examination of the samples showed that the quality of the coating was excellent. The coating on both samples showed no cracks and exhibited a few shallow cauliflowers, indicating that the quality of the coating was independent of the DC power of 1 to 1.5 kW to the Al target. Typical micrographs of the coatings are shown in Figures 4-15 and 4-16.

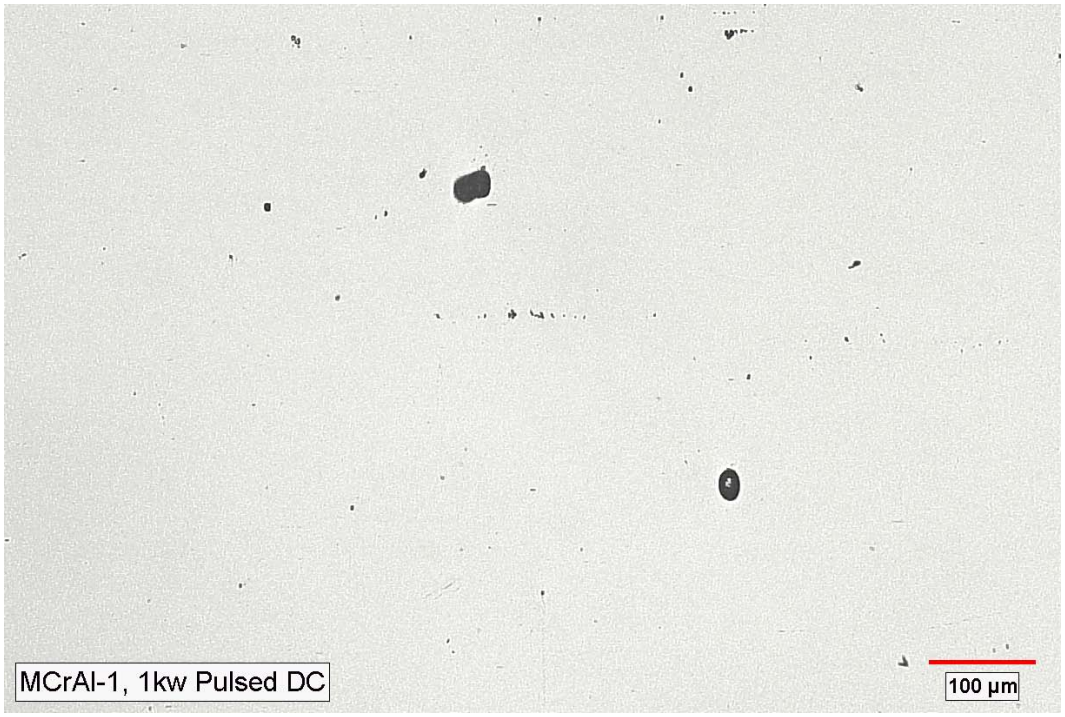

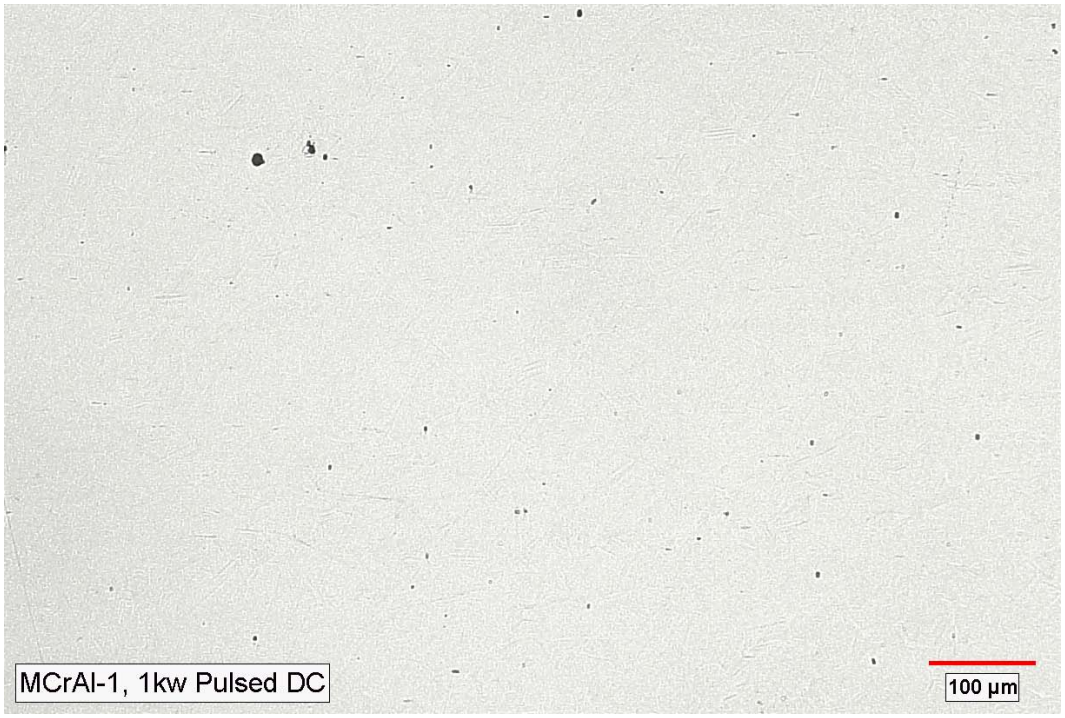

Figure 4-15
Optical micrographs of the pulse DC coated samples (top view) using 1.0 kW power to the Al target.

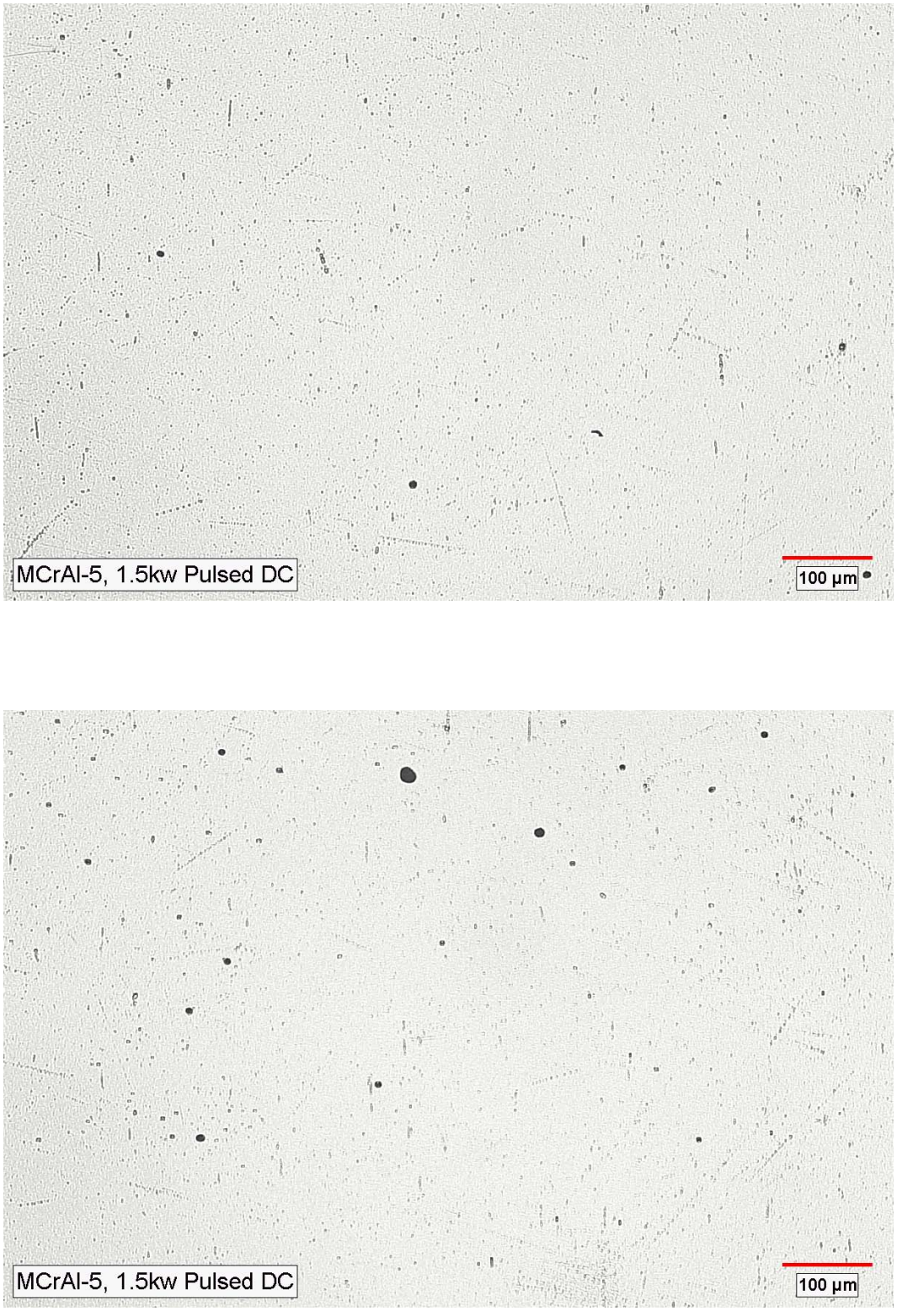

Figure 4-16
Optical micrographs of the pulse DC coated samples (top view) using 1.5 kW power to the Al target.

Chemical composition measurements were made on the outer surface of the coated samples using EDS. The results showed that Al content in the coating increased from 6.02 wt.% to 10.99 wt.% as the power for the Al target increased from 1 to 1.5 kW.

A Rockwell C Hardness Test using 150 kg. load was performed on the coating to determine the coating adhesion. The SEM images of the Rc indents on the H160 + Al coating are shown in Figures 4-17 and 4-18. The coating applied using 1.5 kW exhibited localized spallation at the edges of the Rc indention, while the other coating showed no spallation. This variation in coating spallation can be attributed, in part, to the variation of Al content between the two coatings.

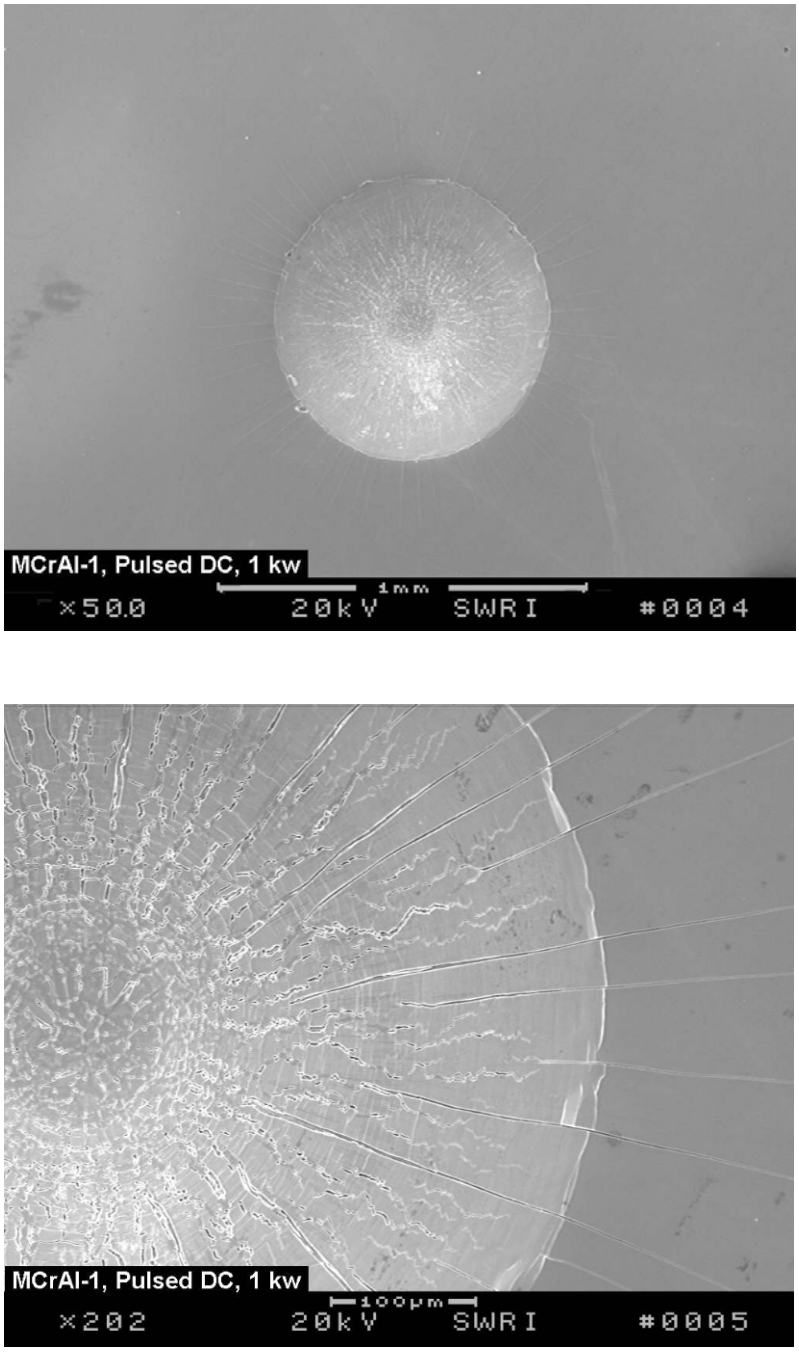

Figure 4-17
SEM images of Rc indentation on the H160 + Al coating deposited using 1 kW power.

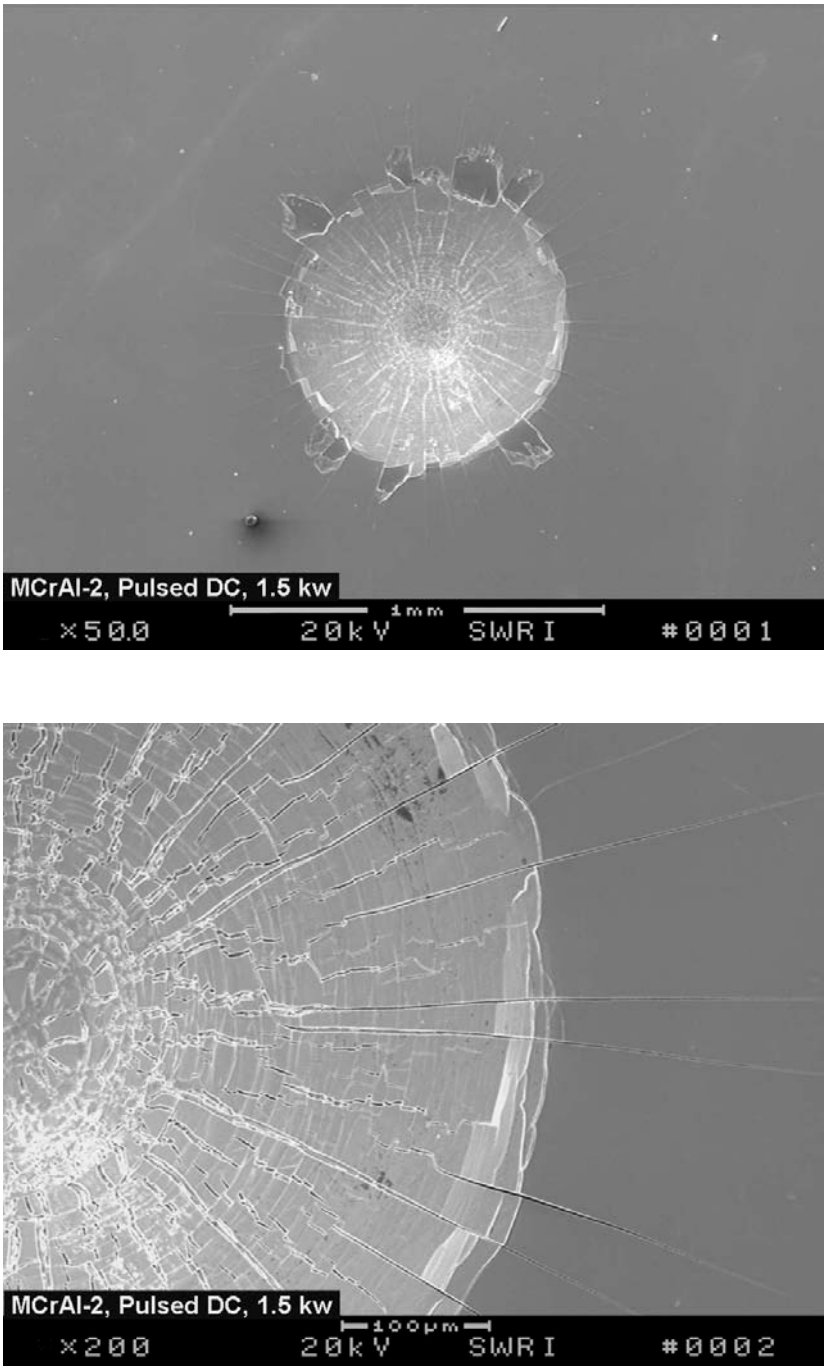

Figure 4-18
SEM images of Rc indentation on the H160 + Al coating deposited using 1.5 kW power.

A transverse section was removed from each of the two coated samples deposited using 1.0 and 1.5 kW power. The two sections were mounted and polished using the standard metallographic techniques and the mounts were examined in an optical light microscope and SEM for coating quality. The metallographic examination showed that the coating on both samples was dense and free from cracks. The coating/substrate interface was clean and showed no evidence of delamination, as illustrated in Figures 4-19 and 4-20. The thickness of the coating deposited using 1.0 and 1.5kW power was 5.85 and 7.95 µm, respectively.

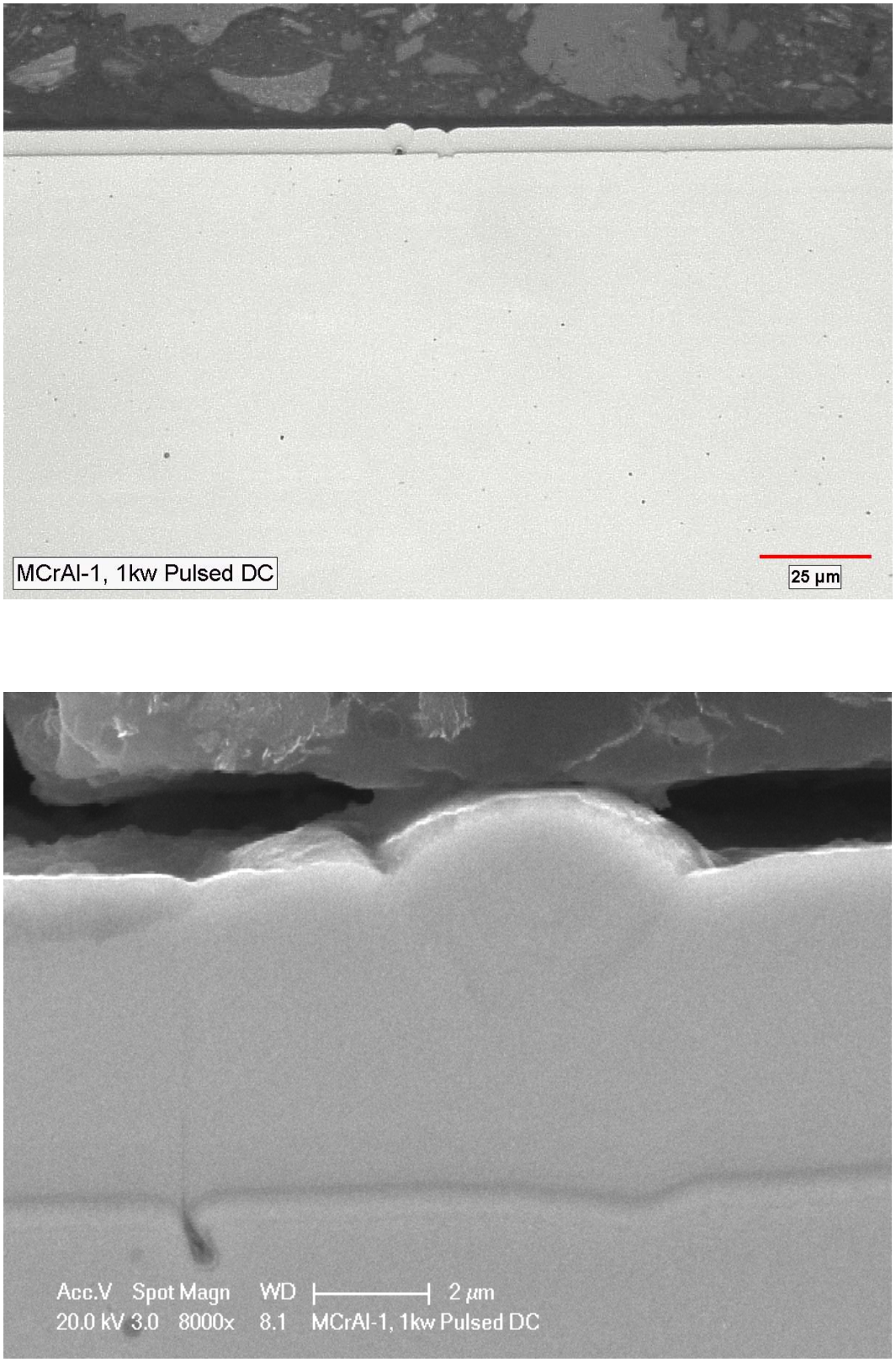

Figure 4-19
Optical and SEM micrographs of transverse sections H160 + Al coating deposited using 1.0 kW power.

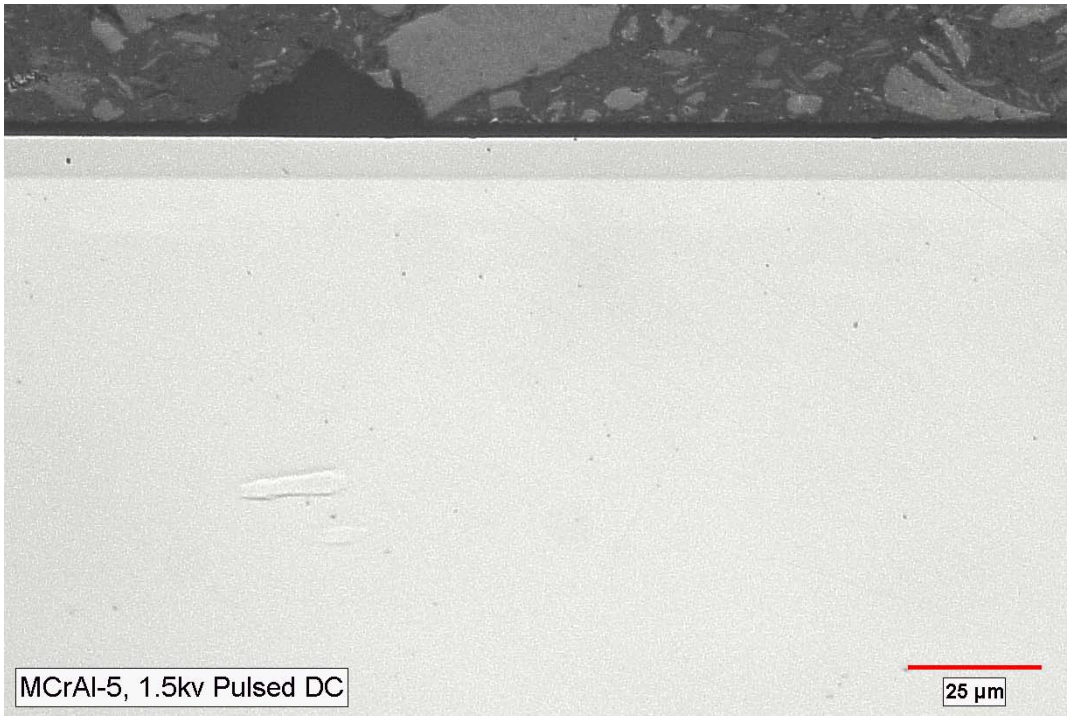

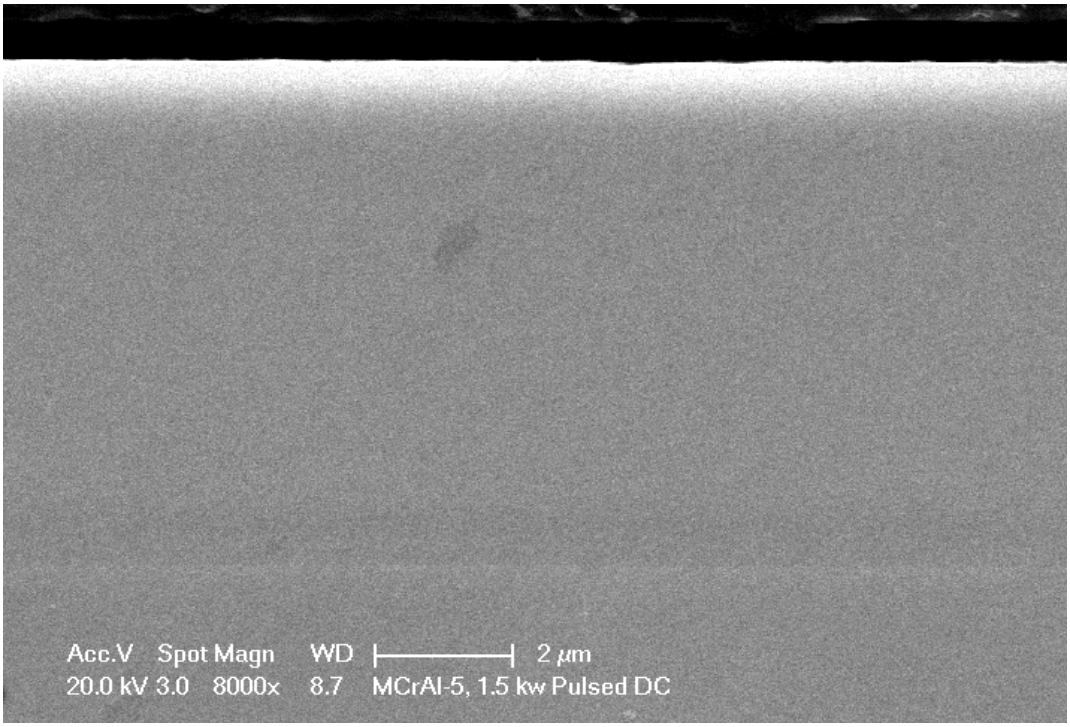

Figure 4-20
Optical and SEM micrographs of transverse sections H160 + Al coating deposited using 1.5 kW power

4.4.2 Thick MCrAl Coating

Following the evaluation of thin coatings, a 30 µm thick H160 + 10 Al coating was deposited on the 304 SS and Haynes 230 samples with and without utilizing the pulse DC supply. For the coating deposition, the magnetron power for H160 and Al targets was set at 2 kW and 1.5 kW. For the pulse DC process, a pulsing parameter of 100 KHz/2.5 µs was used. Following the coating application, metallurgical analysis was conducted on the coated samples to determine the quality of the coating.

Optical metallographic examination of the samples showed several cauliflower-type defects in the coating applied using the pulse DC process as shown in Figure 4-21. The coating deposited using the conventional DC magnetron process exhibited a relatively lower number of defects. Comparison of these micrographs revealed that the coating applied on the 304 SS sample, using the DC magnetron process, showed only a few defects as shown in Figure 1-8 (b). The Al content in the coating varied from about 11.5 to 13.5 wt.% among the 20 samples analyzed.

To improve the quality of the coating, and to minimize the cauliflower defects in thick coatings, the effects of Ar-ion bombardment cleaning at the predetermined intervals and deposition of multilayer coating (MCrAl/Al) for depositing the 20 µm thick coating were considered and the results are presented in the following section.

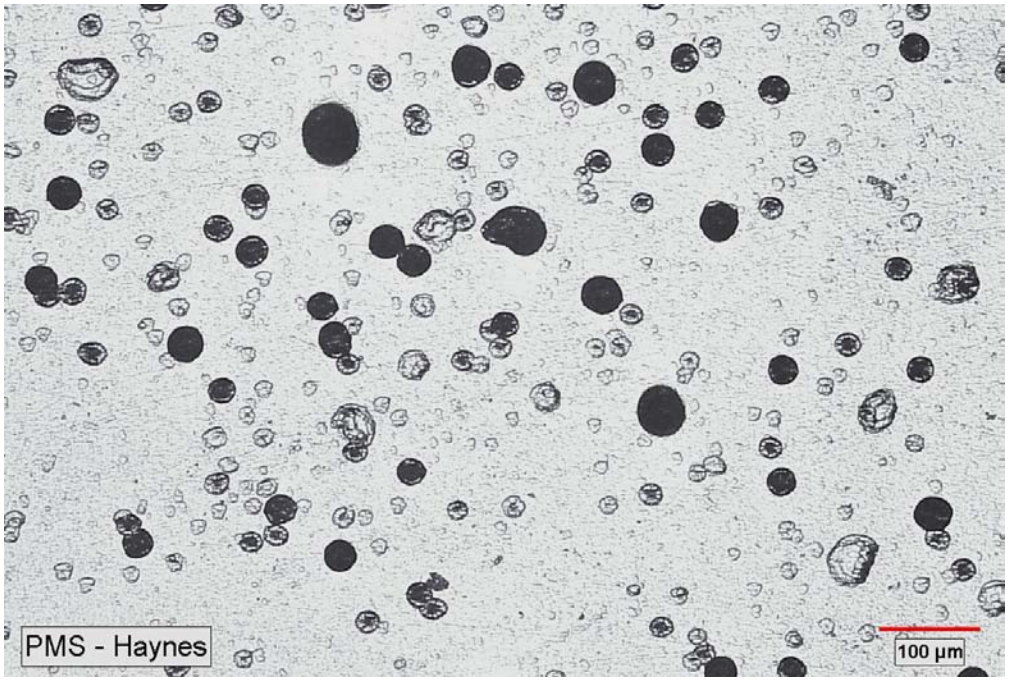

a)

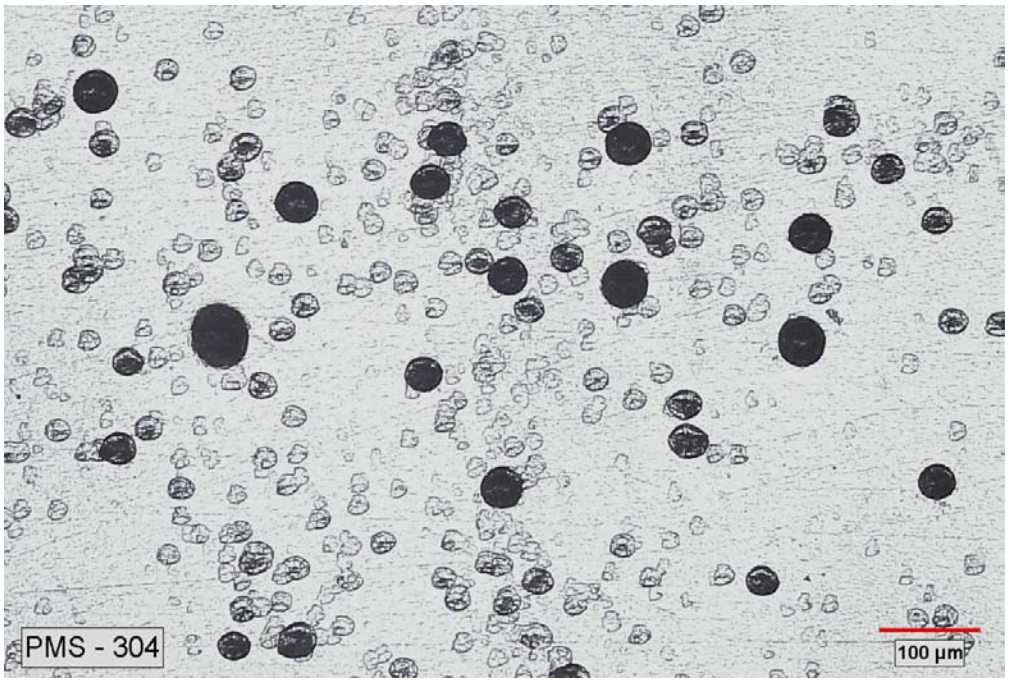

b)

Figure 4-21
Optical micrographs of the pulse DC coating (top view) on a) Haynes 230 and b) 304 SS samples.

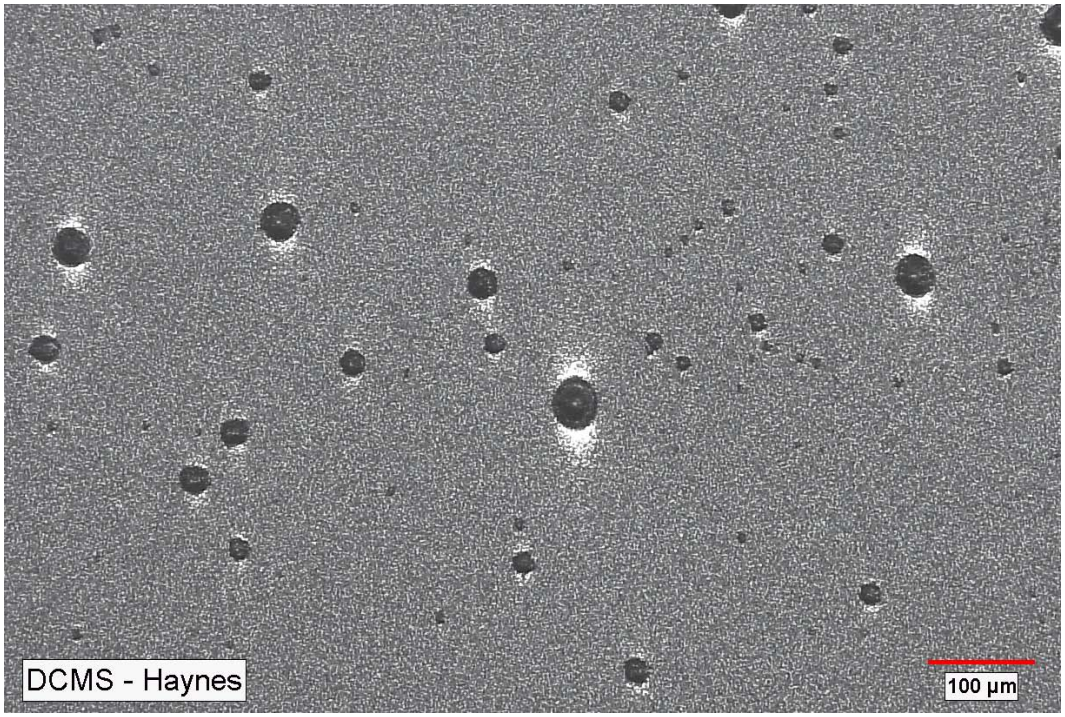

a)

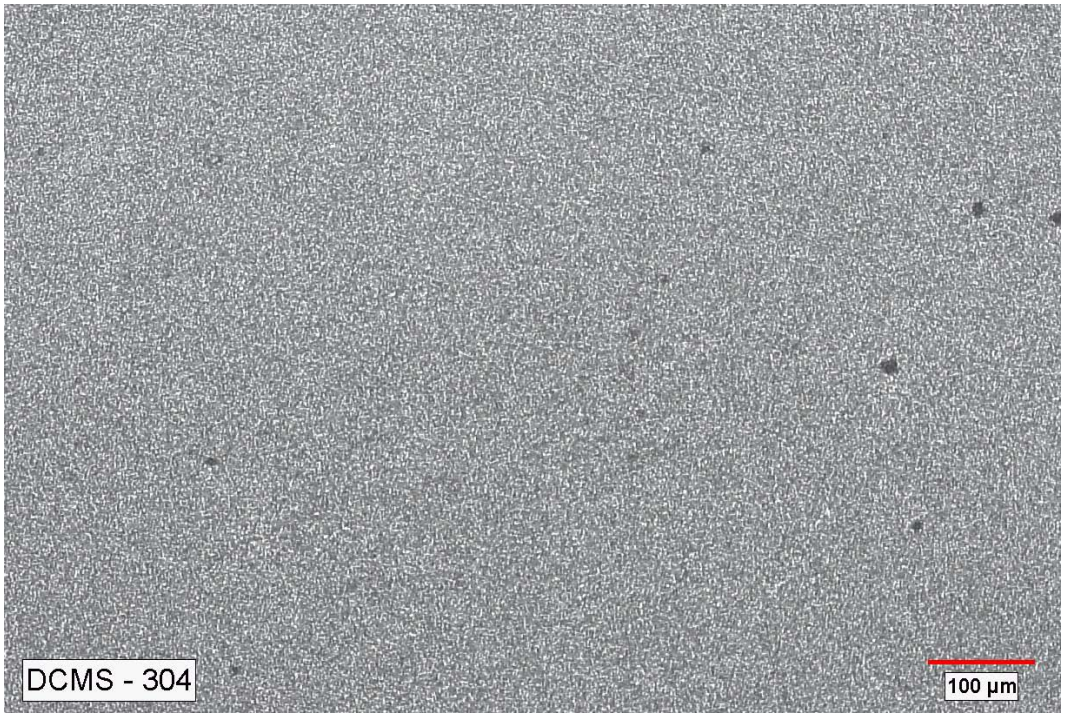

b)

Figure 4-22
Optical micrographs of pulse DC coating (top view) on a) Haynes 230 and b) 304 SS samples.

4.4.3 Coating Process Optimization For Thick Coating

CSM conducted five coating deposition trials. The coating parameters for the first three trials are given in the attached CSM Report (see Table 1, Appendix B). In the first three trials (CSM-1 through 3), the MCrAl coating was applied on the TiN-coated samples. The TiN coating on all samples was approximately 2 μm in thickness. In the first deposition trial, the MCrAl coating was continuously deposited without any interruption. The second trial, the MCrAl coating application process was interrupted after every 80 minutes of deposition for Ar-sputter cleaning for 5 min. The Ar-sputter cleaning was performed at a -500 volts bias and an 8 mTorr working pressure. In the third trail, the power for the MCr targets was turned off for 1 min. after every 20 minutes of deposition to produce a multilayer coating consisting of alternate MCrAl and Al-coating layers.

Examination of the samples showed a few cauliflower-type defects and some of these defects appeared to be shallow, as shown in Figure 4-23. Based on the number and size of the defects, the quality of the coating was considered to be good. Compositional measurements were made at selected locations on the coating using energy dispersive x-ray spectroscopy (EDS). The results showed that the Al content in the CSM-2 and CSM-1 coatings was 4.5 and 7 wt.%, respectively. The Al content in these coatings was significantly lower than the targeted value of 10 wt.% Al, while the CSM-3, multilayer coating exhibited 13 wt.% Al. After generating these results, the coating system was examined to determine the cause for the lower levels Al observed in the CSM-1 and CSM-2 samples. The examination of the coating system revealed that the Al target was not mounted properly, which resulted in lower Al in the CSM-1 and CSM-2 coatings, and a leak was found in the vacuum system which was caused by a roughing valve malfunction.

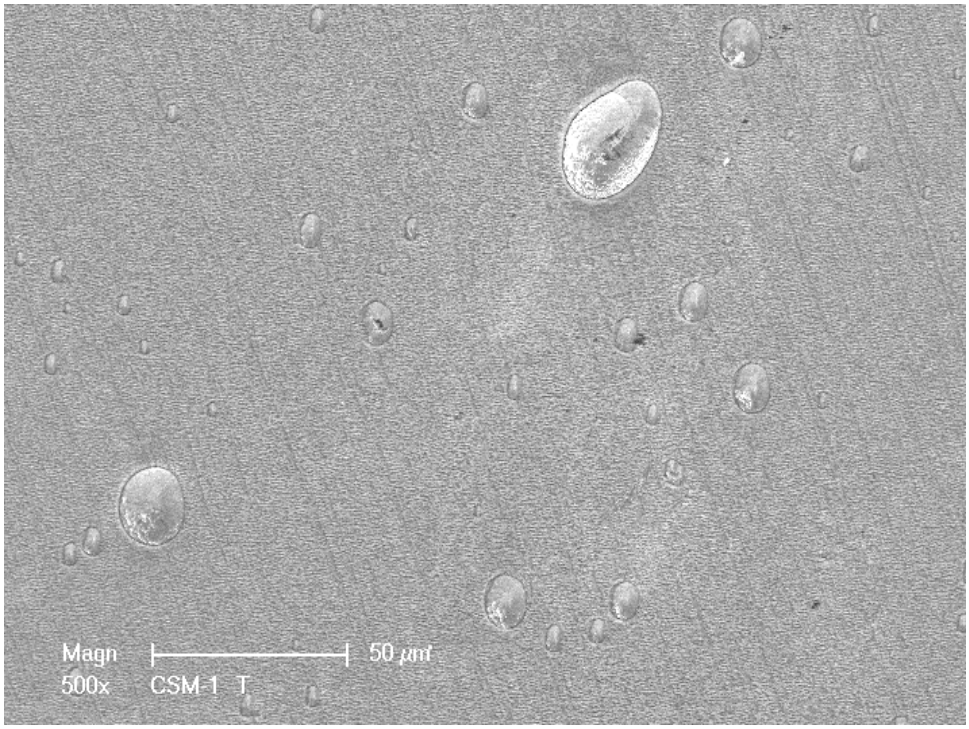

Figure 4-23
Optical micrograph (top view) of the CSM-1 coating showing a few cauliflower defects.

A transverse section was removed from a 304 SS sample deposited in each of the first three coating trials. Metallurgical mounts were prepared from these sections using standard metallographic procedures and the mounts were examined in optical and scanning electron microscopes. Examinations of the mounts showed that the coating was dense and free from cracks. However, the coating delamination was observed at the TiN and substrate interface, as illustrated in Figure 4-24. It is evident from the micrograph that the contamination particles were present between the TiN interlayer and substrate. The leak in the vacuum system is considered to be responsible for the observed contamination at the TiN/substrate interface. The multilayer coating exhibited ultra-fine voids, or pores, parallel to the coating/substrate interface, between the MCAl and Al-coating layers, as shown in Figure 4-25; however, no cracks through the coating thickness were observed. The oxidation and corrosion resistance of the coating would not be adversely affected by the presence of the pores between the coating layers.

Two coating deposition trials, CSM-4 and CSM-5, were conducted using the same deposition parameter as CSM-1 (a single-layer MCrAl coating) with and without the TiN interlayer to assess the TiN/substrate interface delamination. The cross section of the CSM-4 samples with TiN interlayer showed that the coating had a few cauliflower defects on both the 304 SS and Haynes 230 samples, as shown in Figure 4-26. The coating on both 304 SS and Haynes 230 samples exhibited a dense structure as illustrated in Figure 4-27. Delamination at the TiN/substrate was only observed in couple of isolated locations on Haynes 230 samples. A few coating trails were conducted to optimize the TiN coating thickness for preventing localized delamination. The results of these trials showed that reduction of TiN thickness from 2 to 1 μ showed no localized delamination.

Metallurgical examination of the cross sections of the CSM 4 samples without the TiN interlayer showed the coating exhibited a few cauliflower defects on both 304 SS and Haynes 230 samples, as shown in Figure 4-28. The cross section of the coating on both 304 SS and Haynes 230 samples exhibited a dense structure with no evidence of delamination of the coating, as shown in Figure 4-28. The overall quality of the coating on both 304 SS and Haynes 230 samples was excellent.

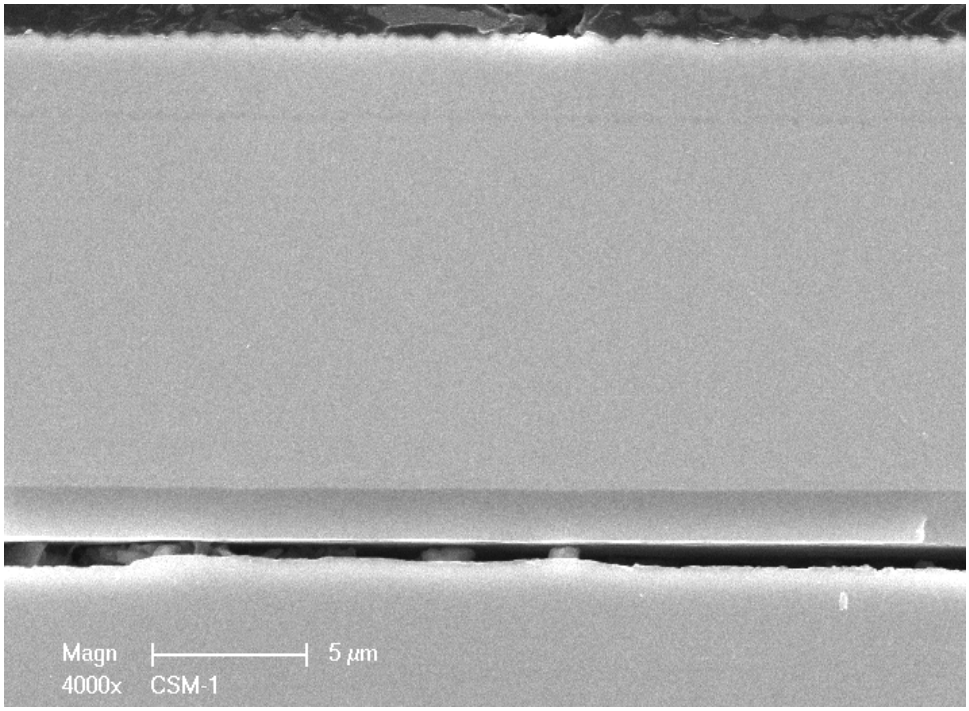

Figure 4-24
SEM micrograph of the cross section of a CSM-1 sample showing delamination at the TiN/substrate interface. Particles are evident between the TiN coating and the substrate.

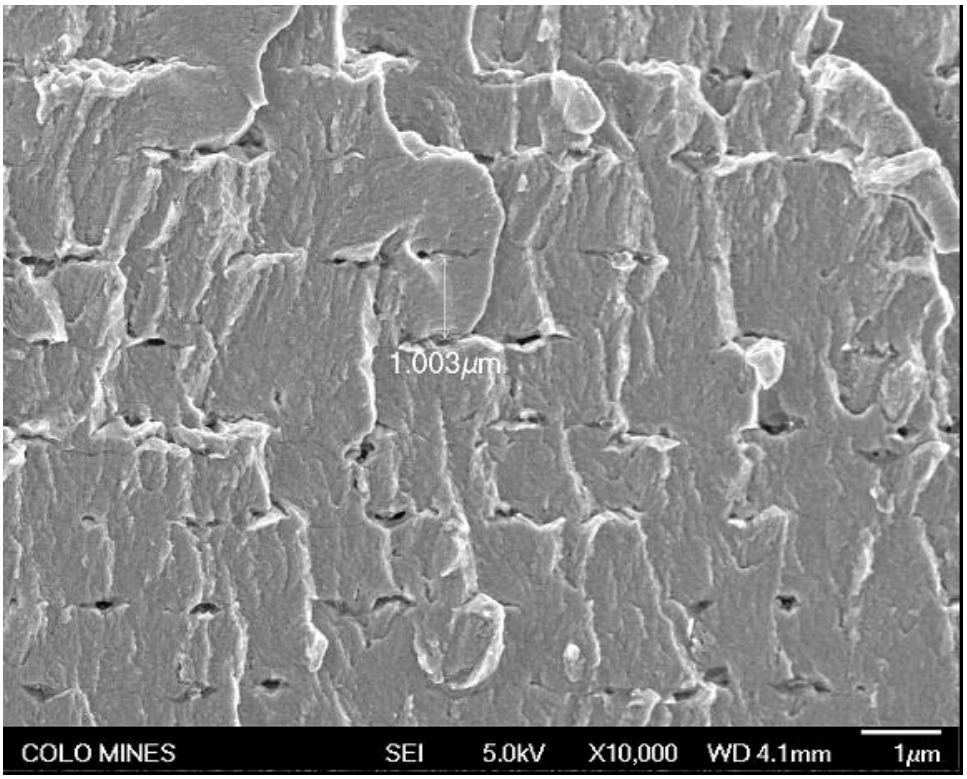

Figure 4-25
SEM micrograph of the cross-section, multilayered coating (CSM-3) showing microvoids between the layers.

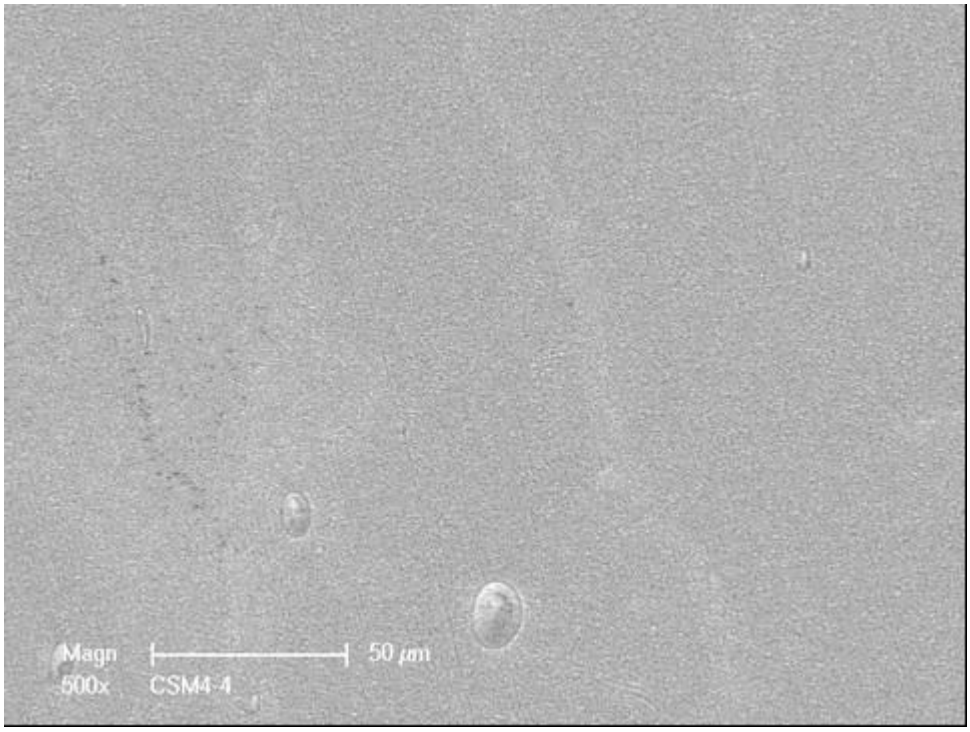

a)

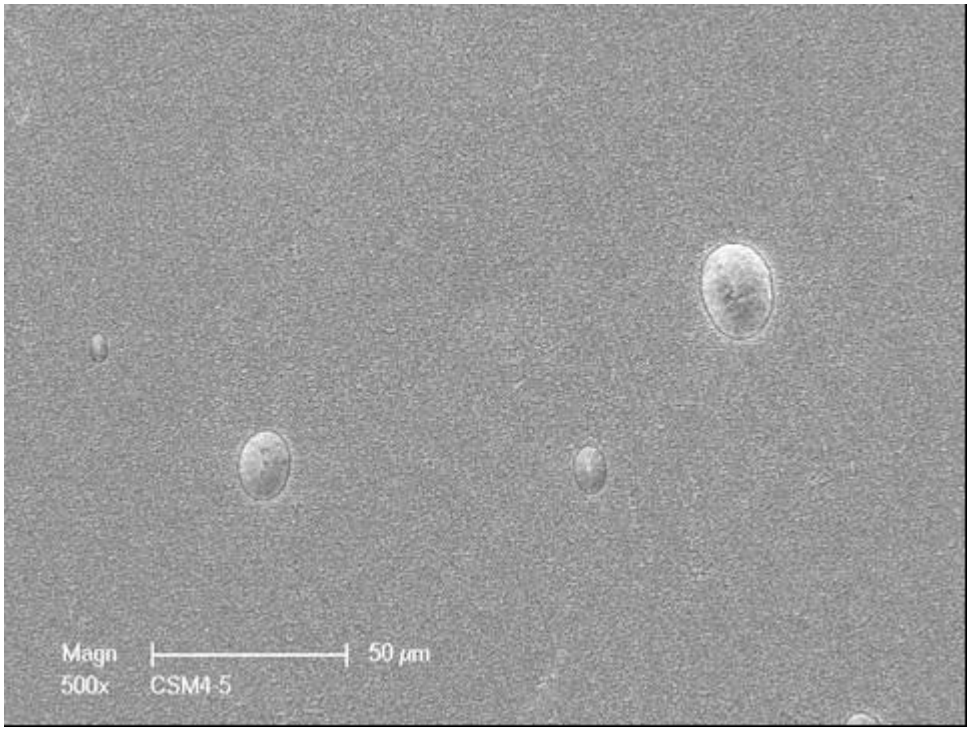

b)

Figure 4-26
Optical micrographs of the top view of the CSM-4 coating on a) 304 SS and b) Haynes 230 samples showing a few cauliflower defects.

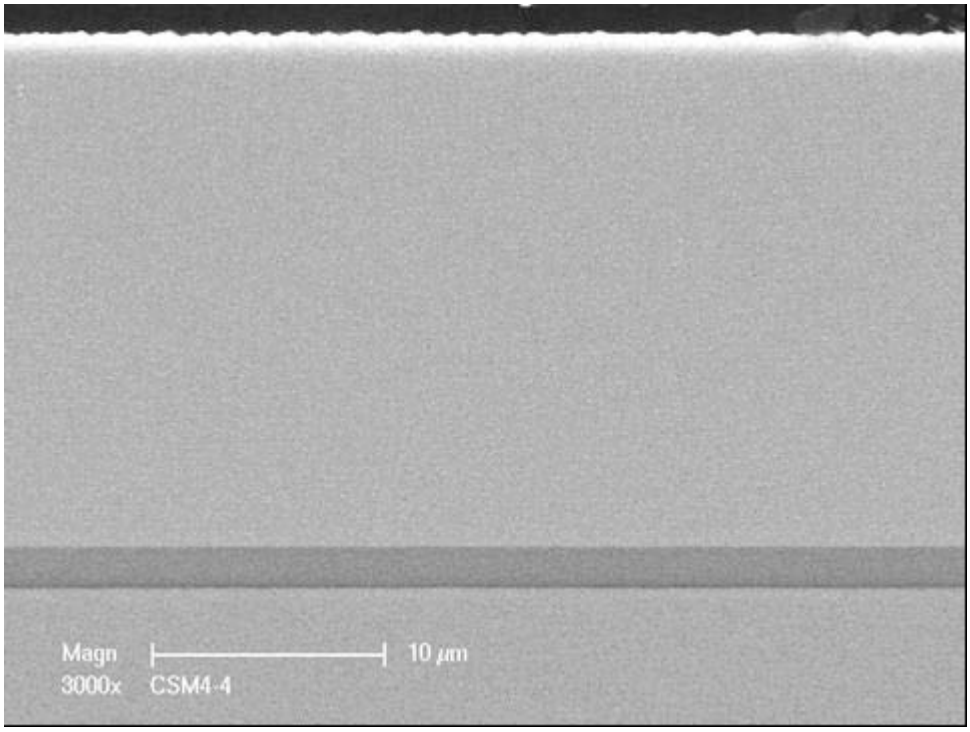

a)

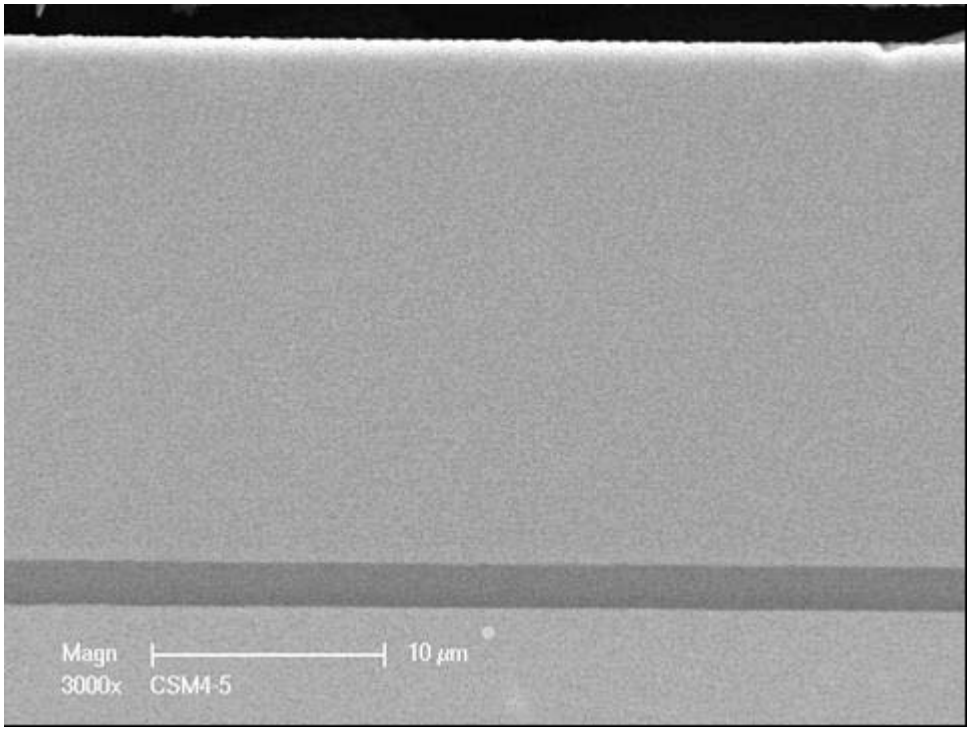

b)

Figure 4-27
SEM micrographs of the cross section of the CSM-4 coating on a) 304 SS and b) Haynes 230 samples showing a dense coating.

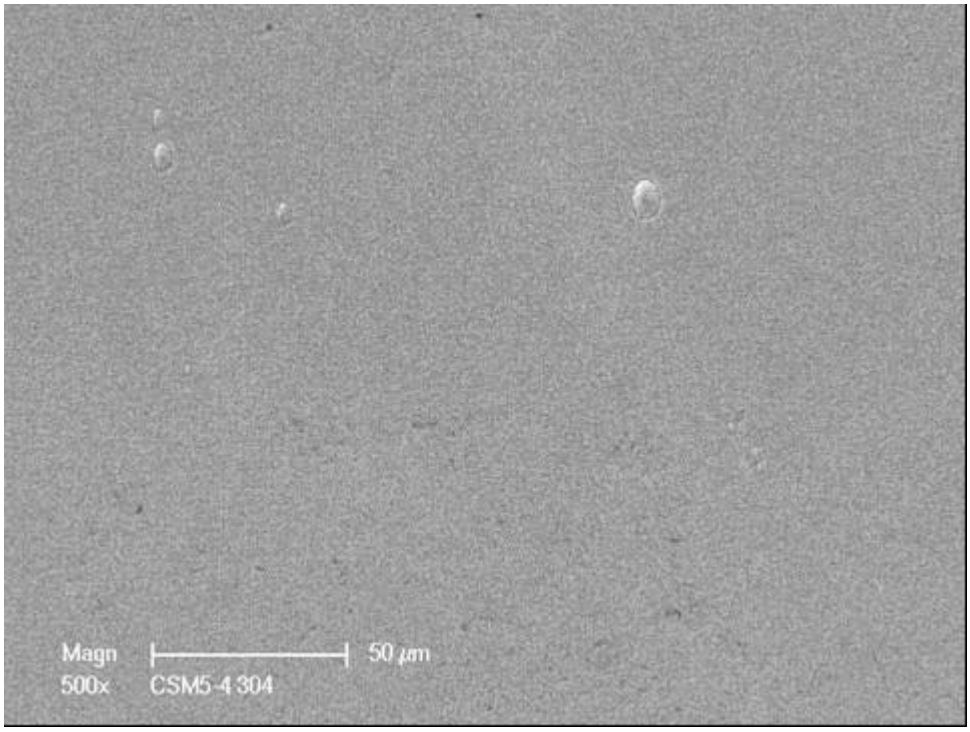

a)

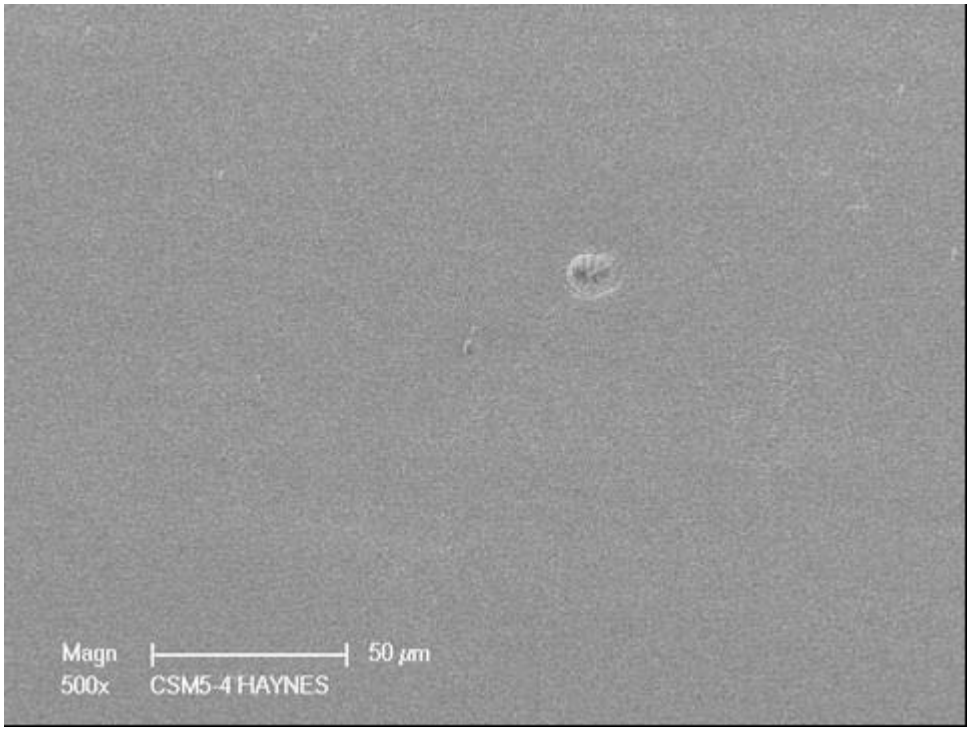

b)

Figure 4-28
Optical and SEM micrographs of transverse sections H160 + Al coating deposited using 1.5 kW power.

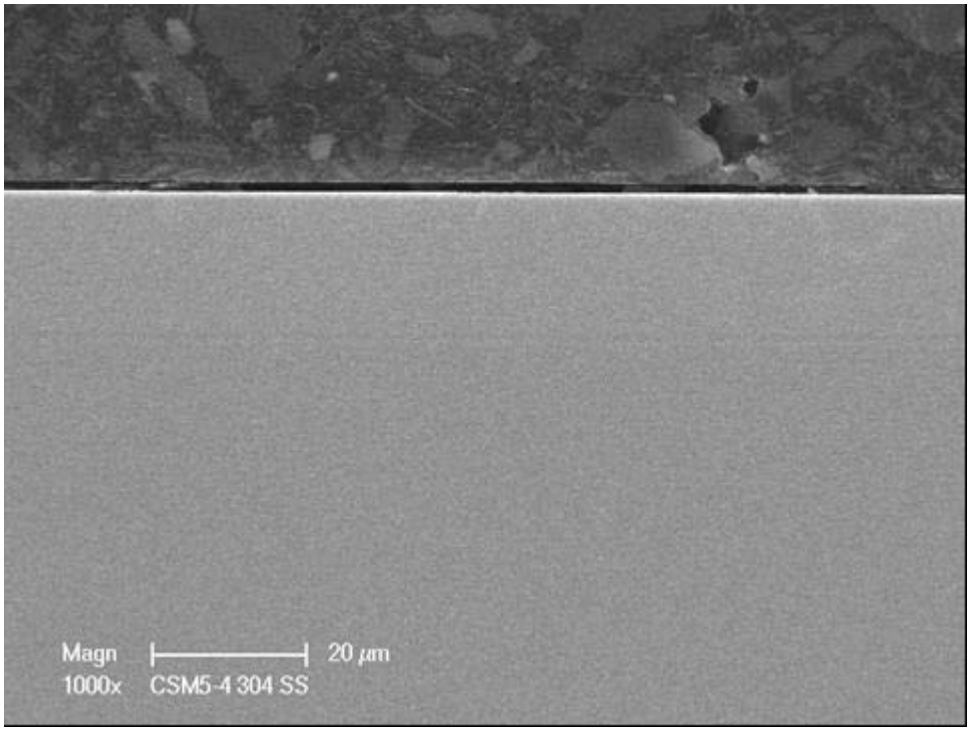

a)

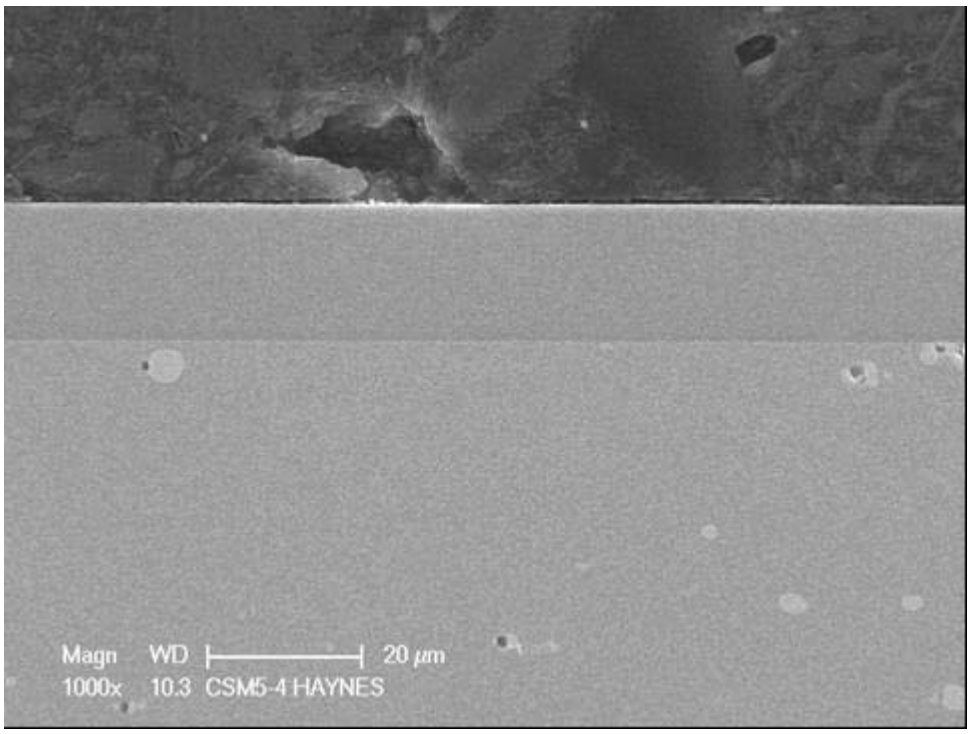

b)

Figure 4-29
SEM micrographs of the cross section of the CSM-5 coating without the TiN interlayer on a) 304 SS and b) Haynes 230 samples showing a dense coating.

4.4.4 Coating Quality Variability Assessment

For the quality variability assessment, four coating trials were conducted for deposition of a monolayer H160-Al coating (with out TiN interlayer) with intermittent Ar-sputter cleaning (plasma etching), two trials with a TiN interlayer between the monolayer H160-Al coating and the substrate, and four trials for deposition of a multilayer coating consisting of alternating MCrAl and Al layers. The coatings were deposited on the 304L SS and Haynes 230 samples at CSM.

All coating depositions were performed in a closed field unbalanced magnetron sputtering system at CSM. For the TiN/MCrAl coating deposition, two MCr targets were installed oppositely with a distance of 470 mm (the diameter of the chamber), while the Al and Ti targets were also installed at 180º apart in the system, as shown in Figure 4-30 (b).

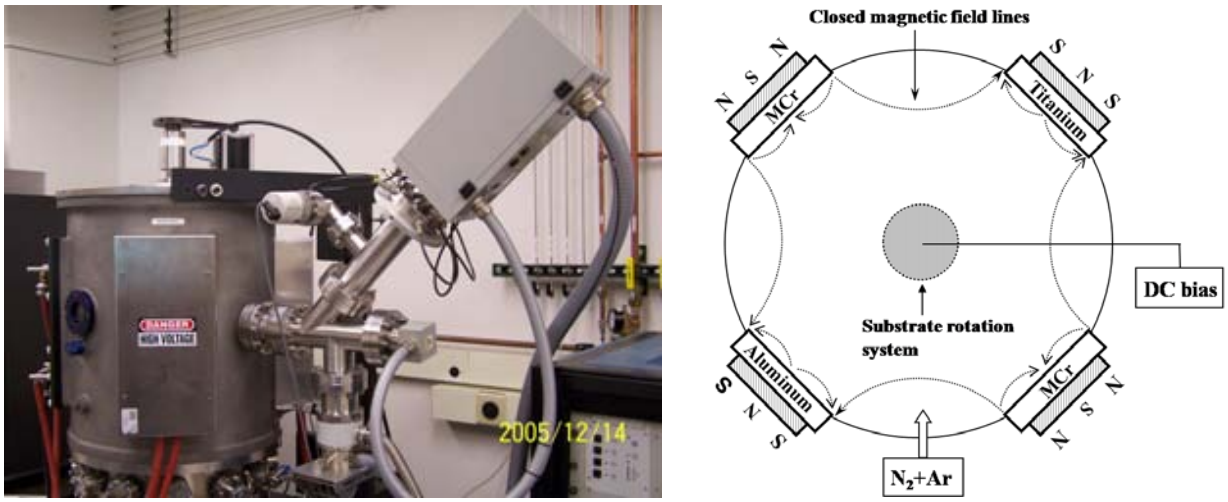

a) **b)**

Figure 4-30
a) Photo of the unbalanced magnetron sputtering system at CSM, and b) schematic drawing showing the target and substrate configurations in the system.

In each trial, the coating was applied on four to five 304L SS and Haynes 230 samples. One test run each was conducted for the deposition of the monolayer and multilayer coatings on the TiN-coated samples. The target thickness for the TiN interlayer was 1.2 µm. The coated samples were sectioned and metallurgical mounts were prepared using standard metallographic techniques for the coating quality variability assessment. These mounts were examined using optical and scanning electron microscopy (SEM).

Optical microscopic examination was performed on all the samples processed in 10 test runs to determine the coating quality variability from specimen-to-specimen. Two major sides were examined on each sample. The metallographic examination showed that the coating on all samples was dense and free from delamination and cracks. Although a few cauliflower-type defects were observed in the coating, the overall coating quality on all samples was excellent. The defects in the coating were quantified using image analysis software. The area fraction of defects in the coating among the different samples is summarized in Tables 4-6 through 4-8. The highlighted numbers in the tables denote either the lowest or the highest area fraction of defects observed in the coating for each deposition trial. The lowest or the highest area fraction area fraction of defects varied from 0.003 to 1.01 percent among all the samples, which is not considered abnormal. The largest area

fraction of defects observed in the single-layer coating with intermittent Ar cleaning (deposition Trials 1 through 4), multilayer with alternate MCrAl and Al layers (deposition Trials 6 through 9), and the coating with the TiN interlayer (deposition Trials 5 and 10) was 0.30, 0.63, and 1.10, respectively. The coating deposited in two trials (5 and 10) on the TiN-coated samples exhibited the highest defect density. Typical SEM micrographs of the coating (top view) are shown in Figures 4-31 through 4-35. One sample from each trial was independently evaluated by CSM. With respect to the surface defect density, the CSM results also showed that the coating deposited on TiN (Trials 5 and 10) showed the highest defect density (see Appendix C). Additional work is required to optimize the process parameters for improving the quality of the coating on the TiN coated samples.

Table 4-6
Variation of defects in the coating deposited with intermittent Ar cleaning.

Trial No.-Spec No.	Surface Defects, Area Fraction, %			
	304L SS Side 1	304L SS Side 2	Haynes 230 Side 1	Haynes 230 Side 2
1-1	0.13	0.14	0.09	0.12
1-2	0.18	0.03	0.06	0.1
1-3	0.02	0.2	0.23	0.18
1-4	0.04	0.12	0.25	0.28
2-1	0.06	0.04	0.11	0.23
2-2	0.30	0.11	0.08	0.14
2-3	0.18	0.09	0.16	0.15
2-4	0.12	0.08	0.14	0.09
2-5	0.08	0.07	0.04	0.06
3-1	0.02	0.03	0.4	0.04
3-2	0.03	0.03	0.12	0.08
3-3	0.04	0.05	0.06	0.05
3-4	0.04	0.03	0.04	0.06
3-5	0.05	0.04	0.05	0.03
4-1	0.03	0.02	**NM**	**NM**
4-2	0.003	0.02	**NM**	**NM**
4-3	0.02	0.003	**NM**	**NM**
4-4	0.03	0.006	**NM**	**NM**
4-5	0.02	0.006	**NM**	**NM**

Table 4-7
Variation of defects in the coating deposited on TiN-coated samples with intermittent Ar cleaning.

Trial No.	Surface Defects, Area Fraction, %			
	304L SS Side 1	304L SS Side 2	Haynes 230 Side 1	Haynes 230 Side 2
5-1*	0.41	0.56	**NM**	**NM**
5-2	0.58	0.65	**NM**	**NM**
5-3	1.10	1.01	**NM**	**NM**
5-4	0.91	1.01	**NM**	**NM**
10-1**	0.14	0.15	**0.59**	**0.37**
10-2	0.35	0.28	0.47	0.46
10-3	0.24	0.22	0.56	0.82
10-4	0.22	0.22	0.55	0.92

* Monolayer MCrAl
** Multilayer MCrAl/Al

Table 4-8
Variation of defects in the multilayer coating with alternate MCrAl and Al layers.

Trial No.-Spec No.	Surface Defects, Area Fraction, %			
	304L SS Side 1	304L SS Side 2	Haynes 230 Side 1	Haynes 230 Side 2
6-1	0.01	0.01	0.04	0.06
6-2	0.003	0.02	0.05	0.03
6-3	0.03	0.01	0.49	0.24
6-4	0.08	0.03	0.03	0.03
7-1	0.008	0.02	0.07	0.53
7-2	0.003	0.02	0.06	0.04
7-3	0.02	0.3	0.02	0.63
7-4	0.01	0.01	0.10	0.13
8-1	0.02	0.01	0.13	0.03
8-2	0.01	0.02	0.07	0.04
8-3	0.07	0.06	0.07	0.13
8-4	0.03	0.08	0.12	0.04
9-1	0.05	0.05	**0.08**	**0.02**
9-2	0.04	0.03	**0.03**	**0.12**
9-3	0.03	0.07	**0.07**	**0.15**
9-4	0.05	0.01	**0.02**	**0.03**

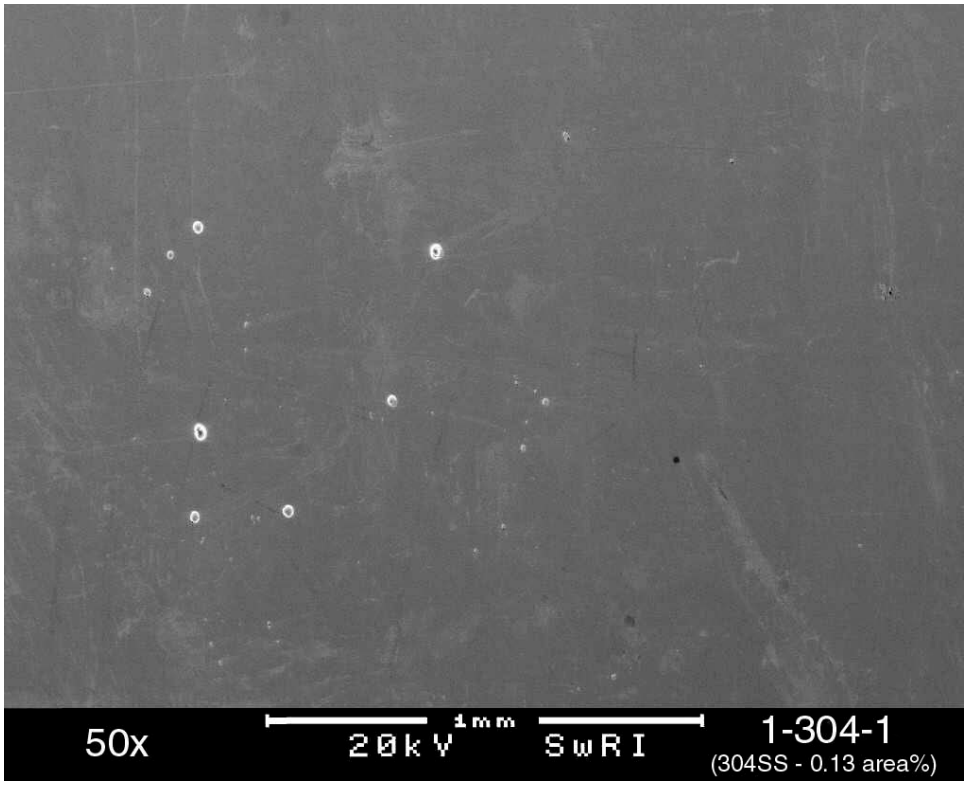

a)

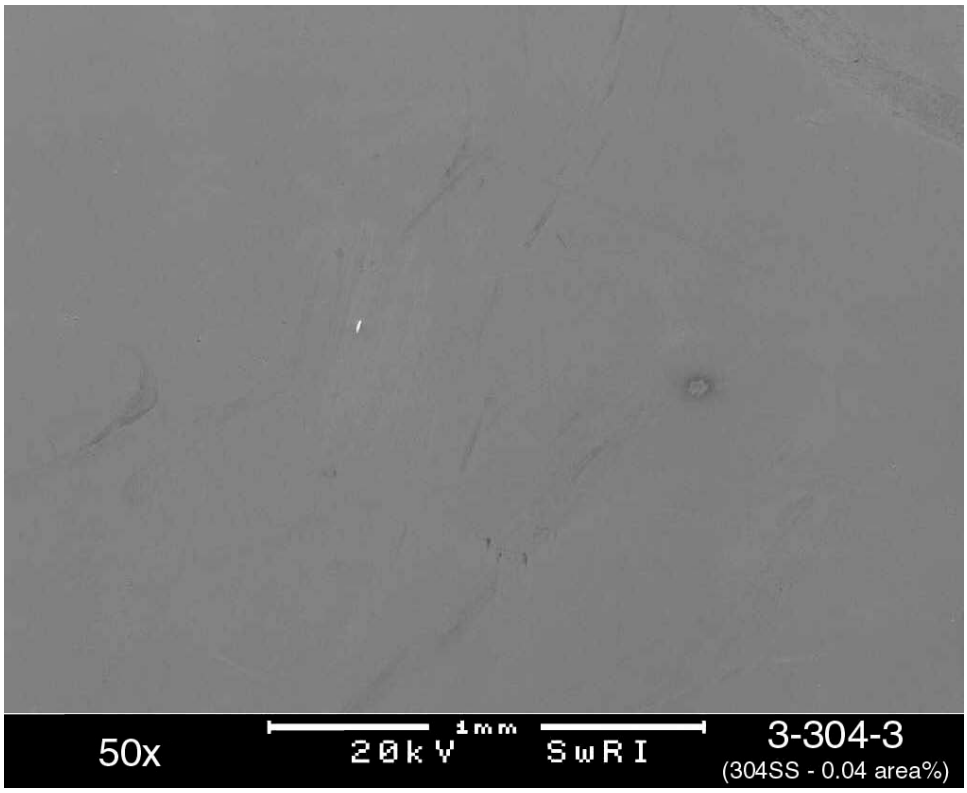

b)

Figure 4-31
SEM micrographs of the coatings on 304L SS (top view) showing the distribution of cauliflower-type defects in a) Sample 1 from Trial 1 and b) Sample 3 from Trial 3 with almost no defects (best sample).

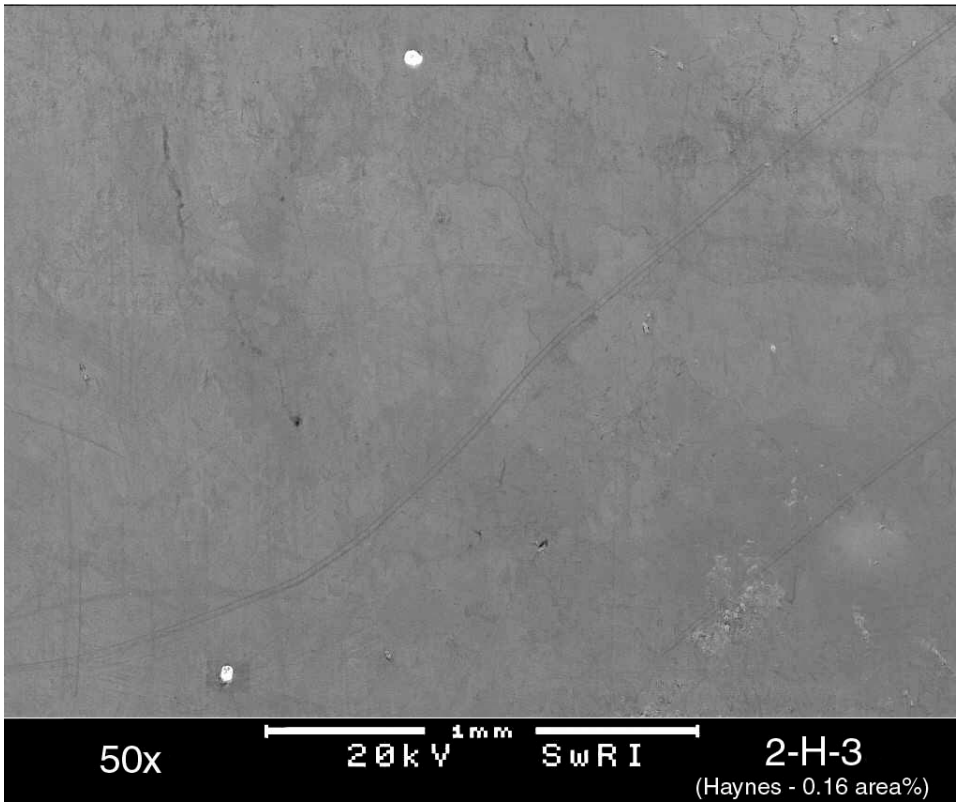

a)

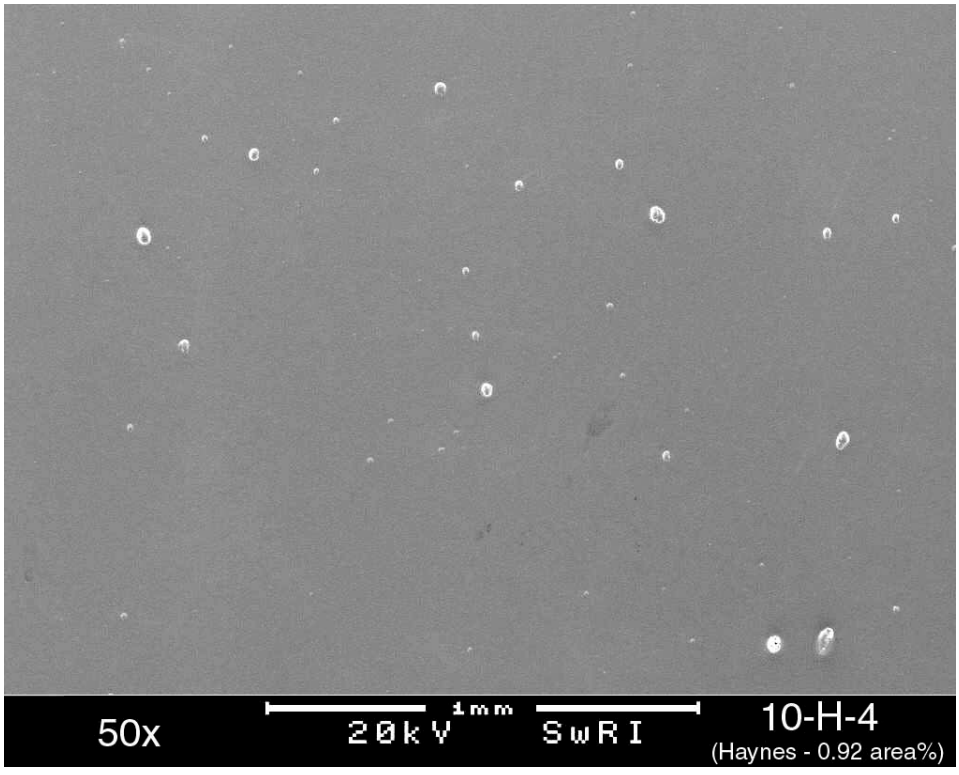

b)

Figure 4-32
SEM micrographs of the coatings on the Haynes 230 samples (top view) showing the distribution of cauliflower-type defects in a) Sample 3 from Trial 2 (best sample) and b) Sample 4 from Trial 10 (worst sample).

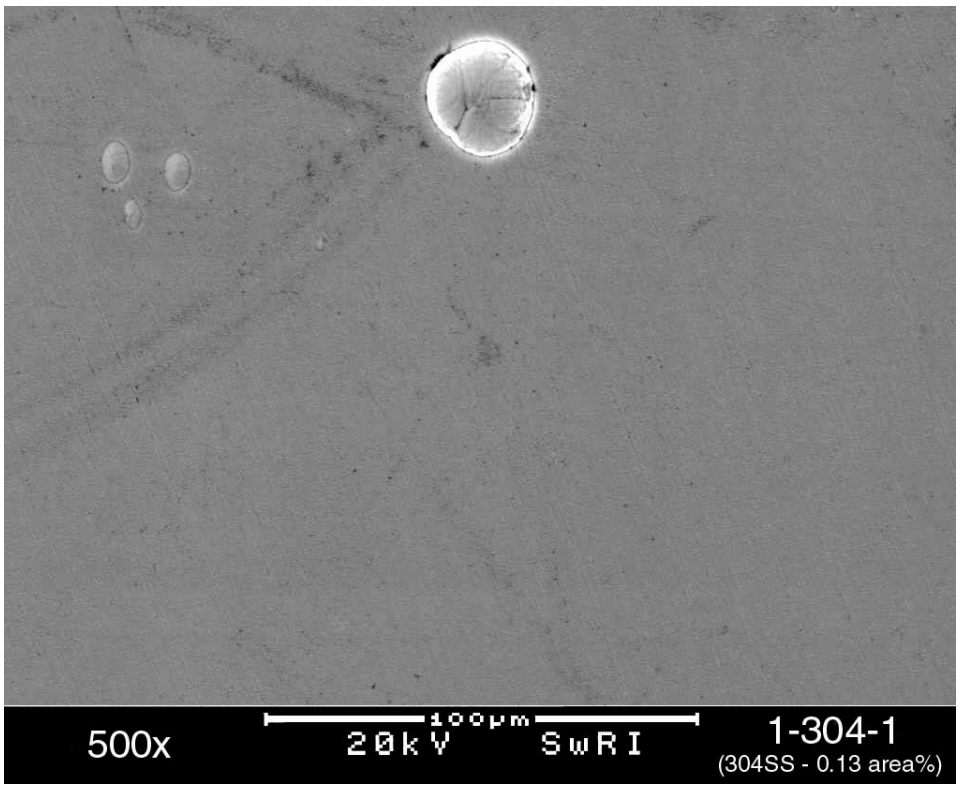

a)

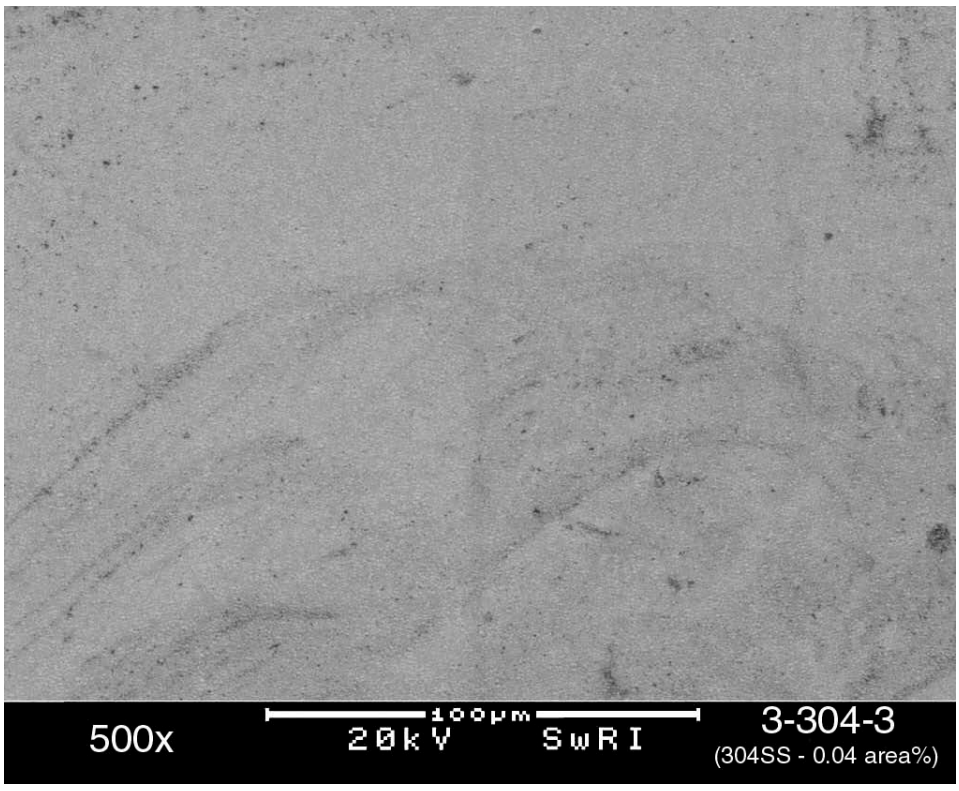

b)

Figure 4-33
SEM micrographs of coatings (top view) on the 304L SS samples showing typical morphology of cauliflower-type defects in a) deposition Trial 1 and b) deposition Trial 3. Note the absence of defects in image b).

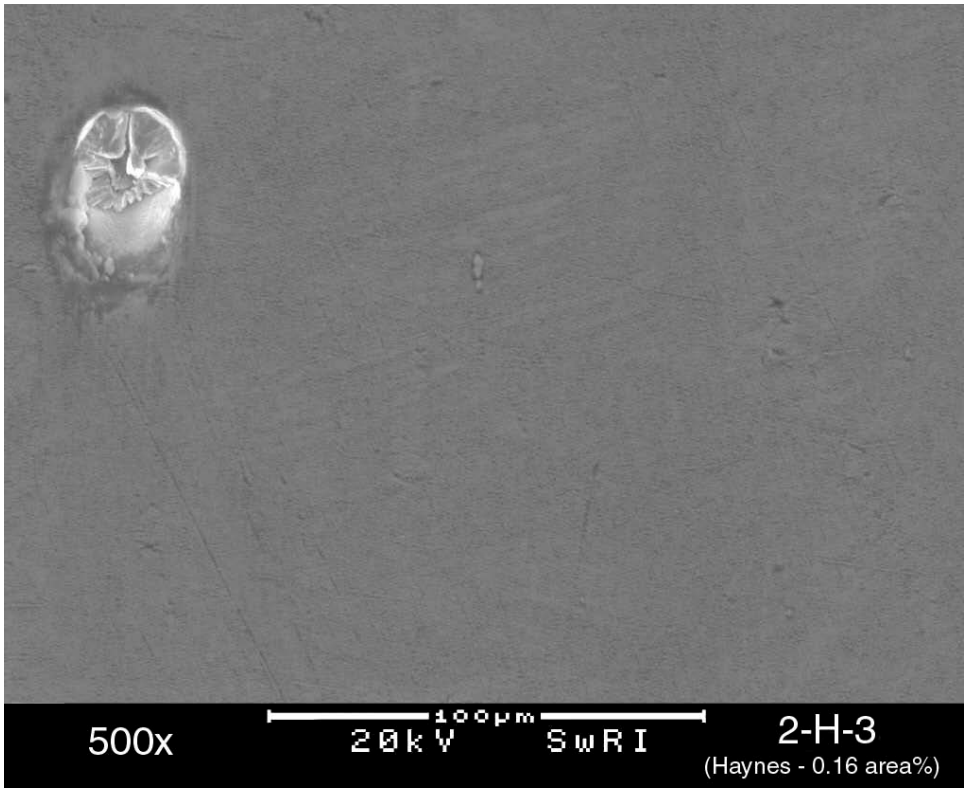

a)

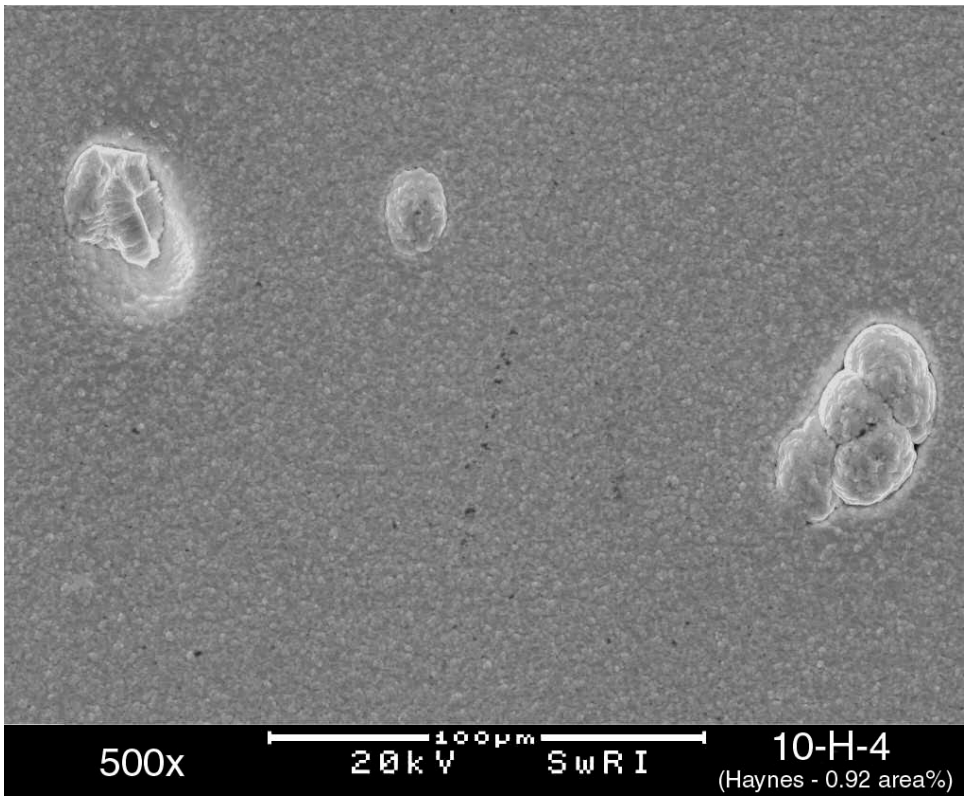

b)

Figure 4-34
SEM micrographs of coatings (top view) on the Haynes 230 samples showing the typical morphology of cauliflower-type defects in a) deposition Trial 2 and b) deposition Trial 10.

Chemical composition energy dispersive spectroscopy (EDS) analysis was performed on four samples from each coating deposition trial, two samples from each substrate. The variation of Al, Cr, and Si levels among the samples of each group is presented in Table 4-9. It is evident from the table that the Al content in the coating on the samples deposited in Trials 1, 3, and 5 varied significantly. The Al content varied over a factor of 2 in the samples coated in Trial 1. The Al content in the samples coated in Trials 2, 4 and 6 through 9 varied from 5.9 to 8.9 wt.%. This variation of Al in the coating is not considered to be significant because the EDS results are semi-quantitative and Al, being a lighter element, normally exhibits ± 1 to 1.5 wt.% scatter. As a result, the chemical composition of the coating deposited in these groups was considered comparable.

Table 4-9
Chemical composition variation of coating in the as-deposited condition, wt.%.

Trial No.	Coating	Al	Cr	Co	Si
1	Single layer coating with Ar cleaning	6.6 – 13.6	25.3 – 28.7	26.5 – 28.9	1.9 – 2.1
2		6.6 – 8.9	28.0 – 28.4	27.5 – 28.3	1.9 – 2.1
3		9.0 – 12.9	26.3 – 27.2	26.6 – 27.8	1.8 – 2.0
4		6.2 –7.4	27.7 – 27.9	28.2 – 28.9	2.0 – 2.1
5	Single layer coating with TiN interlayer	6.6 – 10.3	27.8 – 28.5	28.4 – 28.7	1.9 – 2.4
10		6.0 – 6.4	28.2 – 28.8	28.8 – 29.2	1.7 – 1.8
6	Multilayer with MCrAl and Al alternate layers	6.6 – 7.0	27.7 – 28.3	28.8 – 29.0	1.7 – 1.8
7		6.9 – 7.4	27.7 – 28.9	28.5 – 28.8	1.7 – 1.8
8		6.2 – 6.8	27.8 – 28.4	28.6 – 29.0	1.7 – 1.9
9		5.9 – 6.8	27.6 – 28.3	28.7 – 29.1	1.7 – 2.0

To understand the cause for variation of Al among the samples, a total of 14 samples, at least one from each deposition trial, were selected for the chemical analysis. A transverse section was removed from each sample and all sections were mounted and polished using standard metallographic techniques. The mounts were examined in optical microscope and SEM. The metallurgical examination showed that the coating on all samples was dense and free from cracks and showed no delamination at the MCrAl or TiN coating/ substrate interface. Typical SEM micrographs of the coating cross sections are presented in Figure 4-35 through Figure 4-39. The SEM micrographs reveal a few lighter and darker bands in the monolayer MCrAl. The Al content in lighter bands was lower than the targeted value of 10 wt.%. The darker bands contained significantly higher amounts of Al. The average Al content in the overall coating is comparable among the samples in some of the trials. Review of the coating processing revealed that the sample rotation was stopped due to malfunctioning of the rotation devise. It would take normally two to three minutes to reset the device. During this period the samples were ether closer MCr or Al targets, which results in formation of either MCr or Al-rich bands. This would result in a significant variation in Al content on the outer surface of the sample

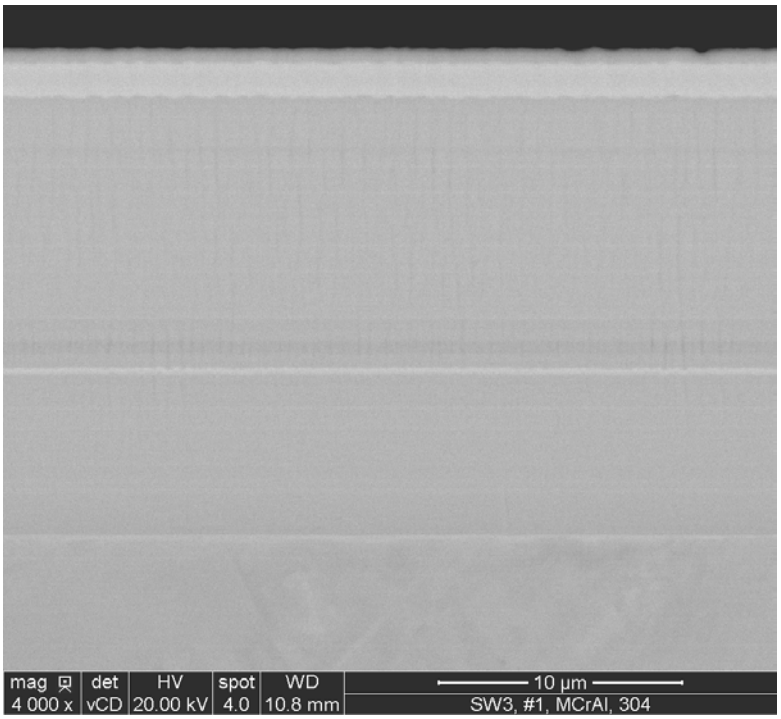

a)

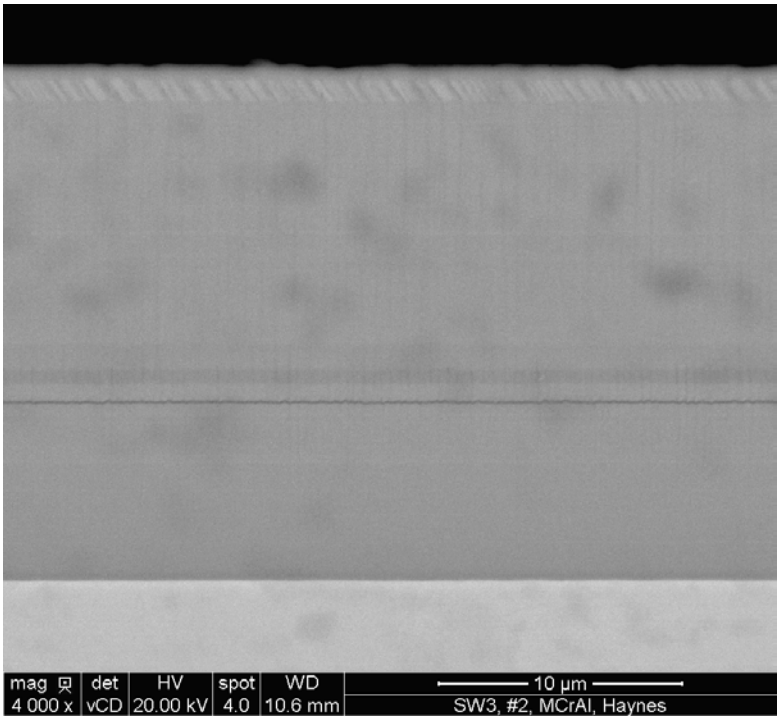

b)

Figure 4-35
Backscattered SEM images of the cross section of MCrAl coating on a) Trial 1 and b) Trail 2 samples.

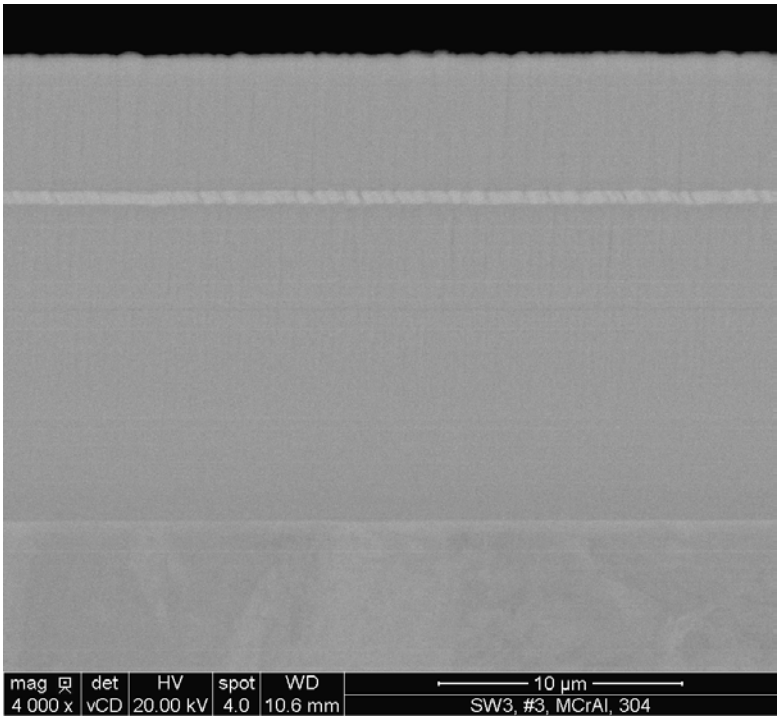

a)

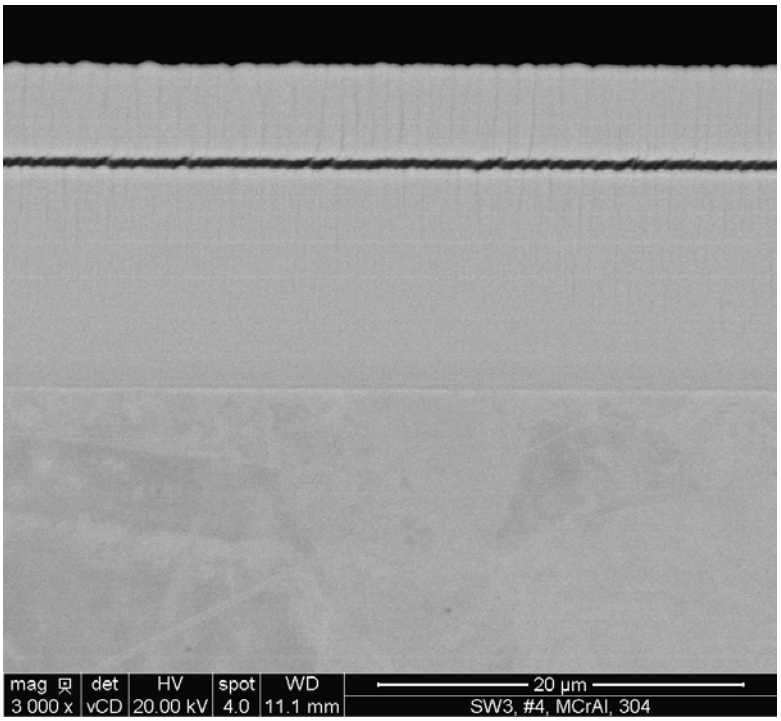

b)

Figure 4-36
Backscattered SEM images of the cross section of MCrAl coating on a) Trial 3 and b) Trial 4 samples.

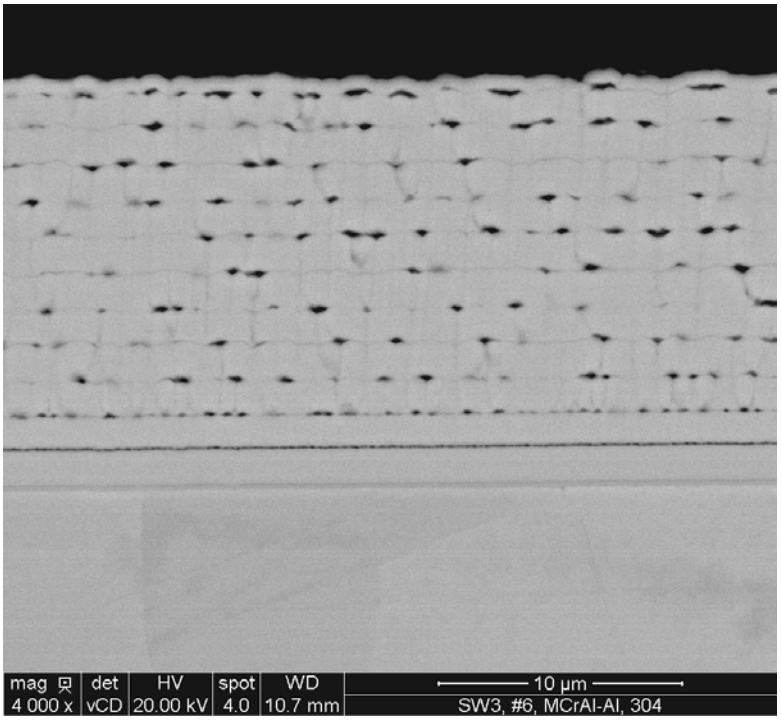

a)

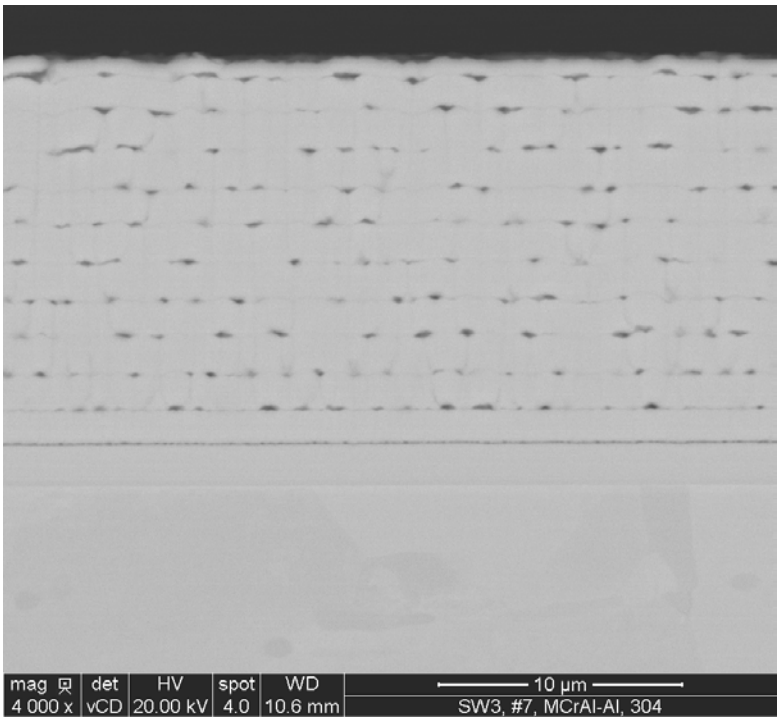

b)

Figure 4-37
Backscattered SEM images of the cross section of multilayer MCrAl/Al coating on a) Trial 6 and b) Trial 7 samples.

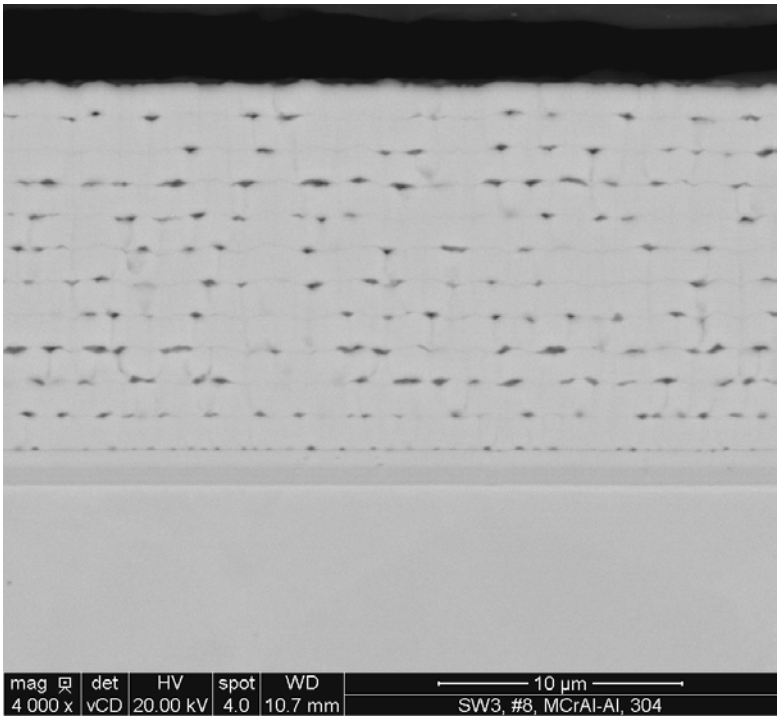

a)

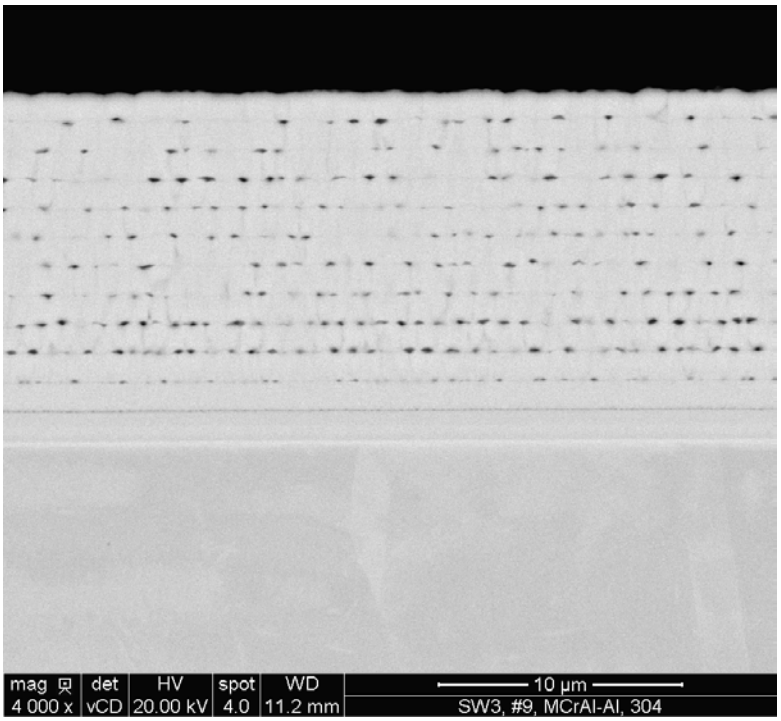

b)

Figure 4-38
Backscattered SEM images of the cross section of multilayer MCrAl/Al coating on a) Trial 8 and b) Trial 9 samples.

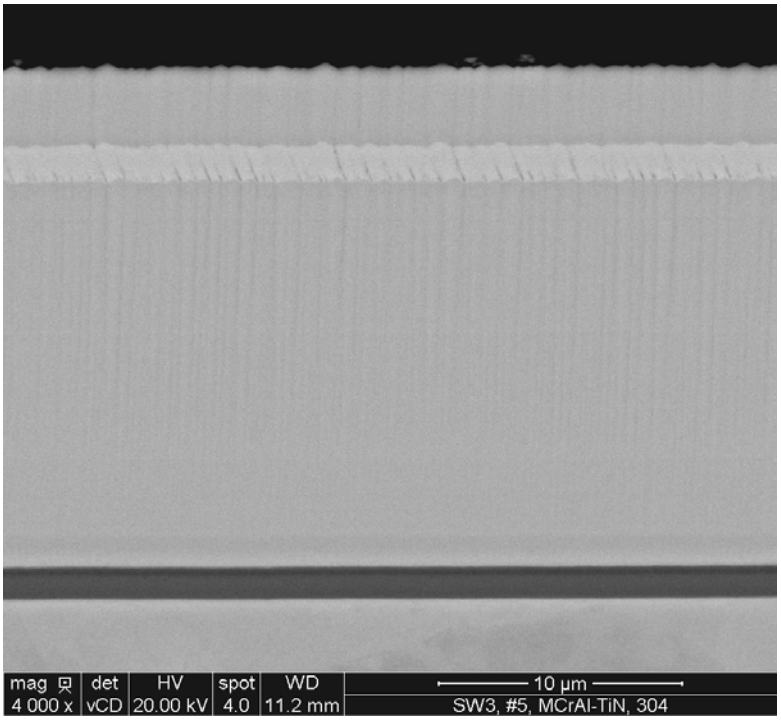

a) MCrAl

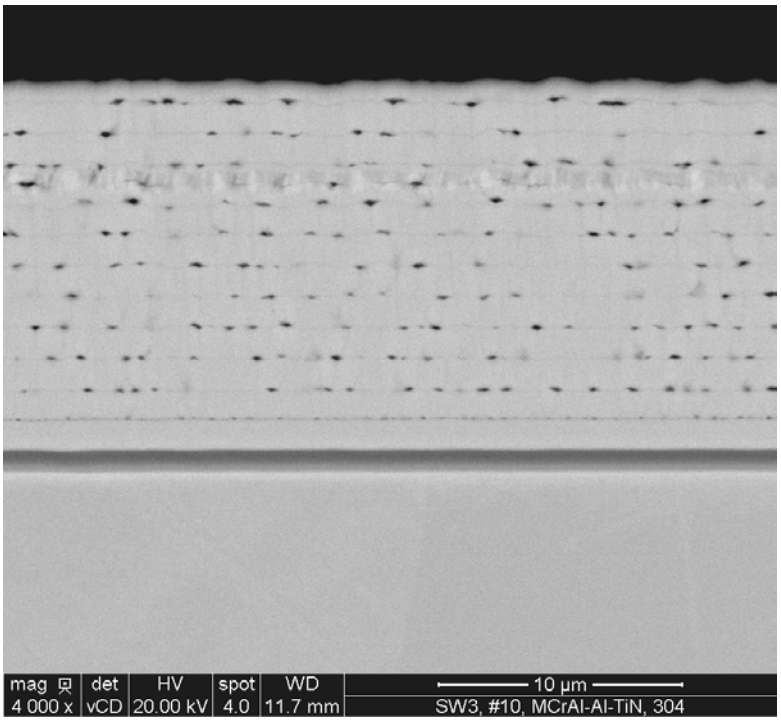

b) Multilayer MCrAl/Al

Figure 4-39
Backscattered SEM images of the cross section of multilayer MCrAl/Al coating on a) Trial 8 and b) Trial 9 sample.

The x-ray diffraction (XRD) technique was used to quantify the grain size of the coating on four samples from each trial, two from each substrate except the samples from the deposition Trail 4. XRD was performed only on two of the 304 SS samples from Trial 4. The grain size of the coating was determined using the width of the most intense Ni-rich phase peak of the XRD pattern, as shown in Figure 4-40. The grain size results are presented in Table 4-10. It is evident from these results that the grain size of the coating on all samples was comparable and varied from 4.0 to 8.0 nm, suggesting that the deposition process is repeatable.

In summary, the quality of the coatings deposited using Pulsed DC sputtering process is considered to be excellent and the process is repeatable. However, additional work is required to optimize the process parameters for reducing the number and size of defects in the MCrAl coating on the TiN interlayer.

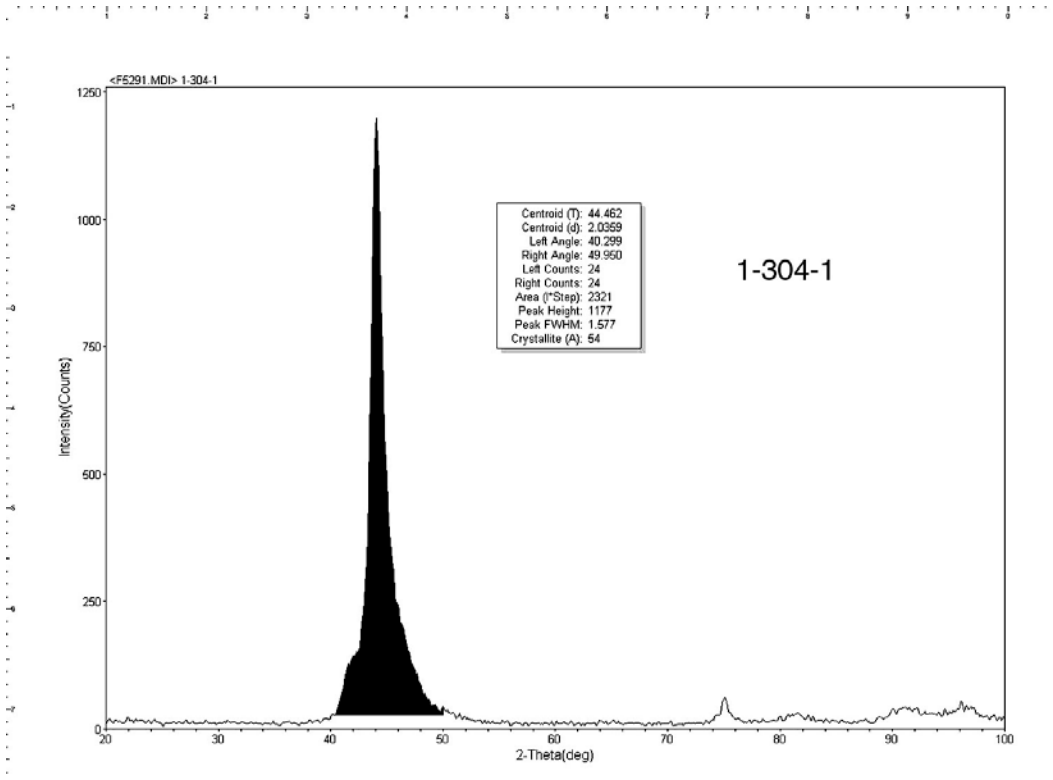

a)

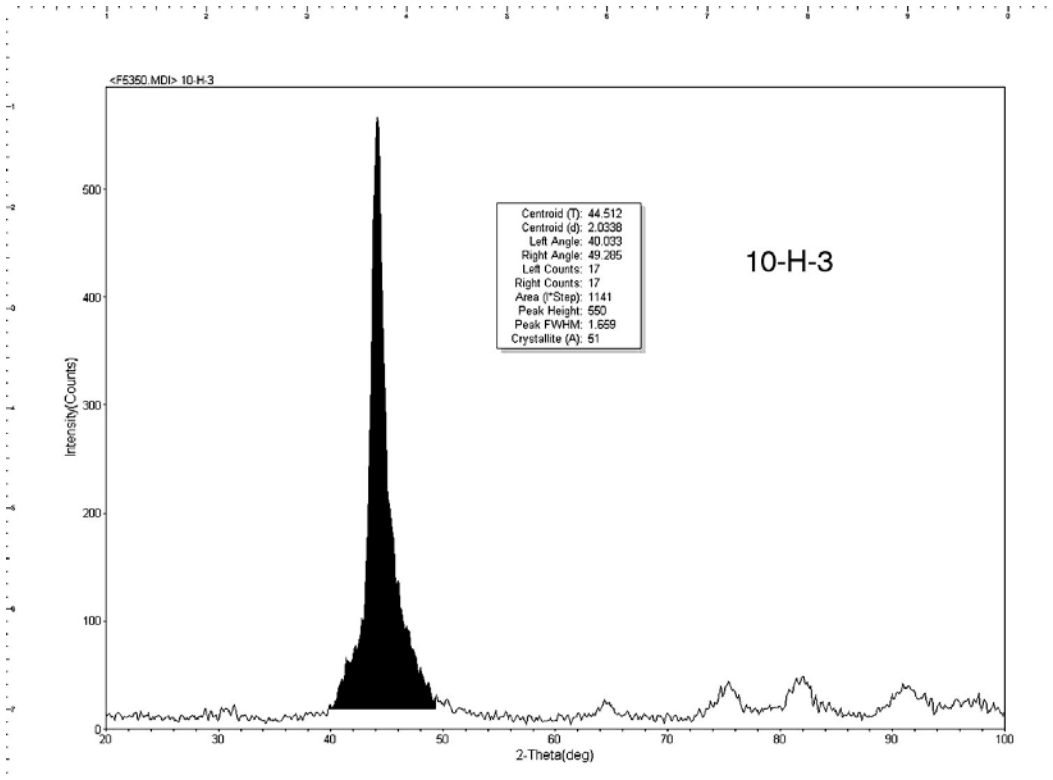

b)

Figure 4-40
XRD patterns of the as-deposited coatings for a) 304L SS Sample 1 of Trial 1 and b) Haynes 230 Sample 3 of Trial 10.

Table 4-10
Variation of coating grain size.

Trial No.	Grain Size, nm			
	304L SS Sample 1	304L SS Sample 3	Haynes 230 Side 1	Haynes 230 Side 3
1	5.4	4.5	**4.0**	**4.0**
2	8.0	7.6	**7.7**	**5.5**
3	4.4	4.4	**4.4**	**4.9**
4	4.3	4.4	**Not determined**	**Not determined**
5	5.1	4.8	**4.5**	**5.1**
6	4.5	5.0	4.7	5.2
7	4.7	4.9	4.4	5.1
8	4.6	4.8	4.5	5.2
9	4.3	4.8	4.4	5.1
10	5.6	5.0	4.3	5.1

4.5 Cyclic Oxidation Behavior of Advanced MCrAl (Ni-Co-Si-Al) Coating

Using these optimized parameters, 1.2.µm thick TiN-interlayer coating was deposited on the Haynes 230 coupons prior to deposition of NiCoCrSiAl (H160-10Al) coating. The coating was applied using the pulsed DC magnetron sputtering process at CSM. The coated samples were cycled between a peak temperature of 1010º C and room temperature. The samples were held at the peak temperature for 50 minutes and cooled for 10 minutes and exposed to 2100 cycles. The mass change results of the advanced nanocrystalline H160-10Al coating are compared with those of nanocrystalline Ni-20Cr-10Al coating and conventional plasma sprayed NiCoCrAlY coatings in Figure 4-41. The oxidation behavior of both nanocrystalline coatings is comparable. The mass of the nanocrystalline coatings was essentially unchanged following the initial gain through out the entire oxidation testing for over 2100 cycles. In other words, the absence of mass change indicates that the scale on the nanocrystalline coatings is extremely stable and the kinetics of scale spallation is almost negligible if not zero. The conventional plasma sprayed NiCoCrAlY coating, widely used on the hot section components of gas turbines exhibited weight loss after initial weight gain due to domination of scale spallation with increasing thermal cycles throughout the cyclic oxidation testing. These nanocrystalline coatings can be used to extend the service life of the hot section components of gas turbines.

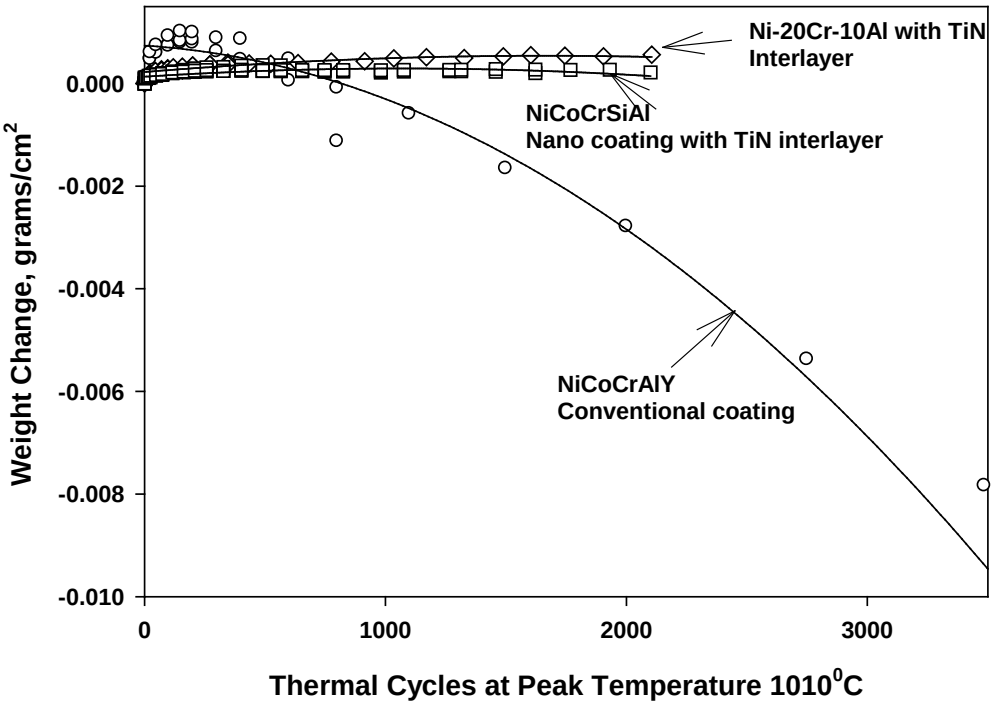

Figure 4-41
Comparison of weight change results of nanocrystalline NiCoCrSiAl and Ni-20Cr-10Al and conventional plasma sprayed NiCoCrAlY coatings at 1010º C.

5.
TASK 4: FIRE-SIDE CORROSION TESTING

5.0 Introduction

Accelerated tests were conducted on the commercial and nanocrystalline-coated samples produced in Tasks 2 and 3. The initial corrosion tests, at different temperatures with simulated ash/flue gas conditions, were conducted by Stanko *et. al* [1-16] at Foster Wheeler (FW) North America Corporation. The test conditions were chosen based on the previous experience in testing materials and coatings for USC waterwall (WW) and super-heater/re-heater (SH/RH) conditions. Extensive results and discussions on this work can be found in Reference 1-6. The 100 and 1000-hour results showed evidence of distress along the columnar grain boundaries and the defects in the coatings. The FW results are briefly summarized in the following sections.

To minimize the defects and improve the coating density, several processing techniques were investigated in Task 3 at SwRI and CSM was contacted for depositing the NiCoCrSiAl (Haynes 160-10Al) coating using a pulsed DC magnetron sputtering process. The results of these investigations showed that the use of a pulsed DC power supply coupled with intermittent Ar-sputter cleaning resulted in coatings with improved quality. The pulsed DC coatings were dense, free from cracks, and had a few cauliflower type defects. Additional fire-side corrosion testing was performed on the pulsed DC coated samples with and without simulated flue gas flow. The test temperatures, composition of synthetic ash deposits, and flue gases were selected to match the earlier FW test program. These results are also presented in this section.

5.1 Initial Fire-Side Corrosion Testing at Foster Wheeler

Several nanocrystalline coating composition applied on 304 SS, P 91 steel, and Haynes 230 substrate samples were tested at different temperatures. Four (4) Fe, three (3) Ni, and two (2) Co-based nanocrystalline coatings were evaluated along with two commercial coatings. The commercial coatings were applied to samples by the coating vendors and no process information was provided. The nanocoatings were deposited by SwRI using the original (non-optimized) PEMS process as described in Chapter 3. These coatings contained either 0% or 10% Al since the interdiffusion and oxidation research was being conducted concurrently to the corrosion testing, and the interdiffusion barrier layer had not been developed. The chemical compositions of these coatings are given in Table 5-1. Typical microstructures of the as-deposited coatings are shown in Figures 5-1 through 5-3. It is clear from the micrographs that nanocrystalline coatings (Figure 5-1) exhibited a high concentration of columnar grain boundaries and scattered defects. These defects could potentially act as pathways for the corrosive constituents to reach the coating/substrate interface. The commercial coatings, A1 and A2 (Figures 5-2 and 5-3), exhibited a number of macroscopic features including voids (pores) in the structure. This suggests these commercial coatings are more porous than the SwRI nanocoatings, but no attempt was made to quantify the actual density or number of pores in the coatings.

Table 5-1
Nominal composition and semi-quantitative EDS analysis of the as-received nanocoating materials [1-16].

Coating Designation	Nominal Composition	Layer	O	Mg	Al	Si	P	Ca	Ti	Cr	Mn	Fe	Co	Ni	Cu	Nb	Mo	W
A1	NA	Outer	42.0	3.8	1.9	0.7	13.0	0.3	18.2	13.9	—	0.3	—	—	5.9	—	—	—
		Inner	14.0	2.5	71.8	0.5	8.6	—	—	2.7	—	—	—	—	—	—	—	—
A2	NA	Bulk	13.1	2.1	75.2	—	7.0	—	—	2.0	—	0.5	—	—	—	—	—	—
A3	NA	Outer	44.7	—	43.7	—	10.1	0.2	—	0.3	—	0.7	—	—	—	—	—	—
		Inner	2.8	—	0.7	—	—	—	—	18.5	—	55.3	—	—	—	—	15.8	6.8
A4	Fe-18Cr-8Ni-10Al	Bulk	—	—	11.9	—	—	—	—	17.0	1.0	63.4	—	6.3	—	—	—	—
A5	Ni-20Cr-10Al	Bulk	—	—	8.9	0.2	—	—	—	19.3	—	0.4	—	71.3	—	—	—	—
B1	Fe-25Cr-20Ni-10Al	Bulk	—	—	12.8	0.7	—	—	—	23.9	0.7	47.6	—	14.4	—	—	—	—
B2	Fe-25Cr-37Ni-10Al	Bulk	—	—	11.2	0.5	—	—	—	23.6	0.3	32.9	—	31.0	—	0.6	—	—
B3	Fe-25Cr-37Ni	Bulk	—	—	0.2	0.6	—	—	—	26.4	0.2	37.0	—	34.9	—	0.8	—	—
B4	Ni-30Co-28Cr-3Si-10Al	Bulk	—	—	12.6	3.2	—	—	0.4	26.2	—	0.6	27.1	29.6	—	—	0.3	—
B5	Ni-30Co-28Cr-3Si	Bulk	—	—	0.3	3.3	—	—	0.5	29.4	0.2	0.8	30.4	34.9	—	—	0.4	—
B6	Co-23Ni-22-Cr-14W-10Al	Bulk	—	—	11.1	—	—	—	0.2	22.1	0.3	1.7	31.9	16.3	—	—	0.7	15.9
B7	C0-23Ni-22Cr-14W	Bulk	—	—	0.3	—	—	—	0.2	24.5	—	1.8	36.5	19.1	—	—	0.7	17.0

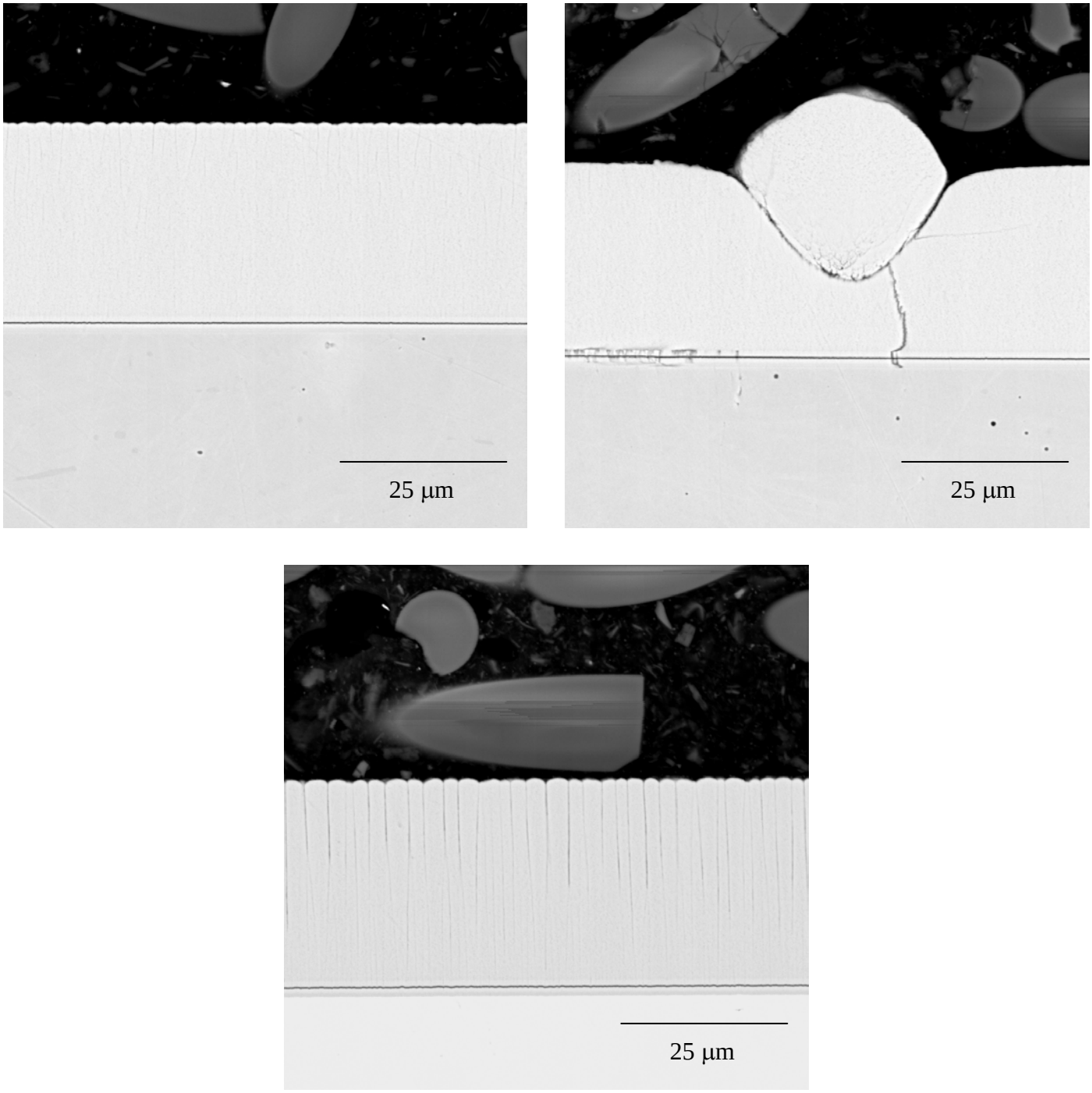

Figure 5-1
As-received nanocrystalline coating A5 (Ni-20Cr-10Al) on 304 SS (top) and Haynes 230 (bottom) [1-16].

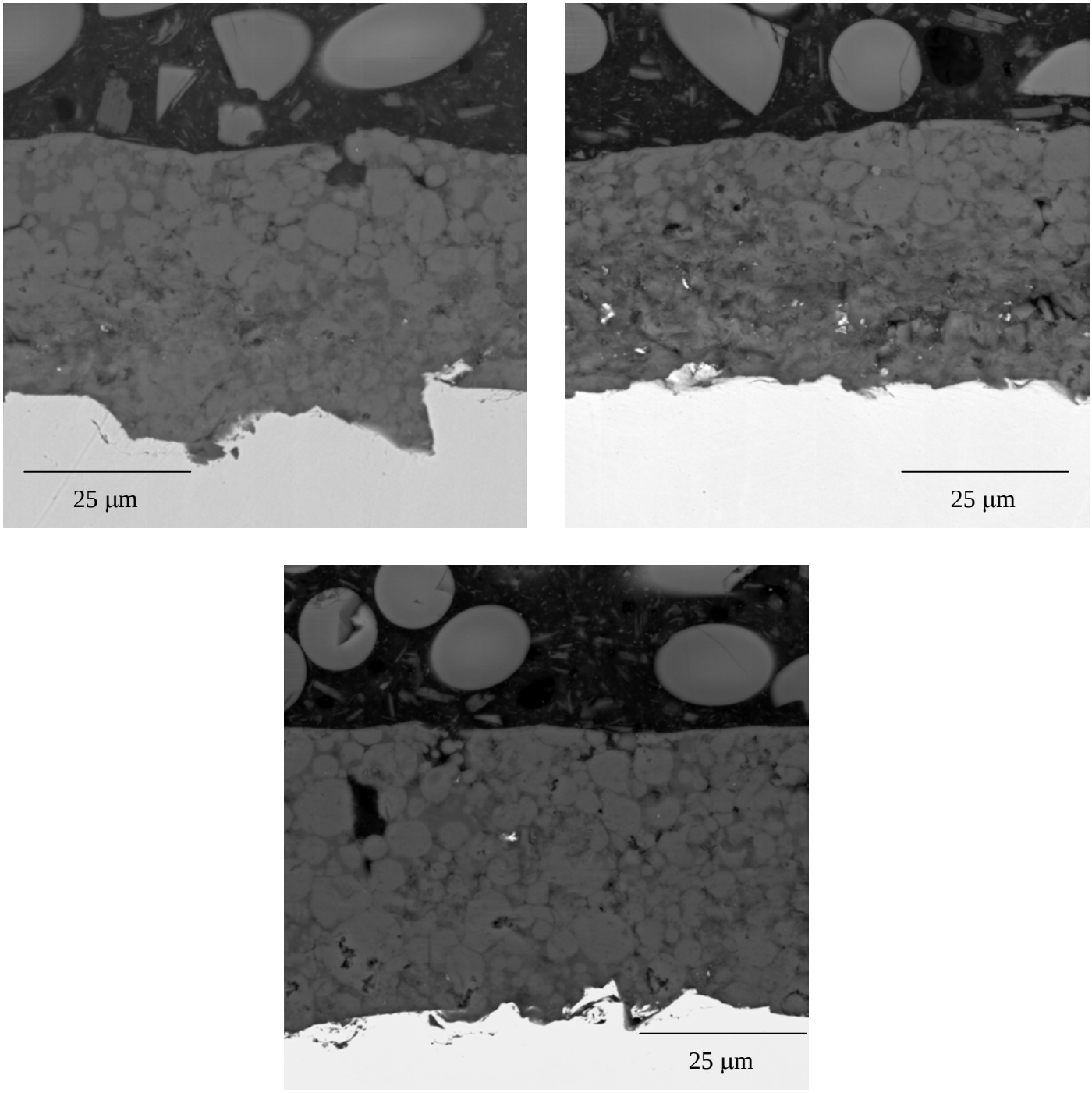

Figure 5-2
As-received commercial coating A2 on the 91 substrate material (top left), 304 SS (top right), and Haynes 230 (bottom) [1-16].

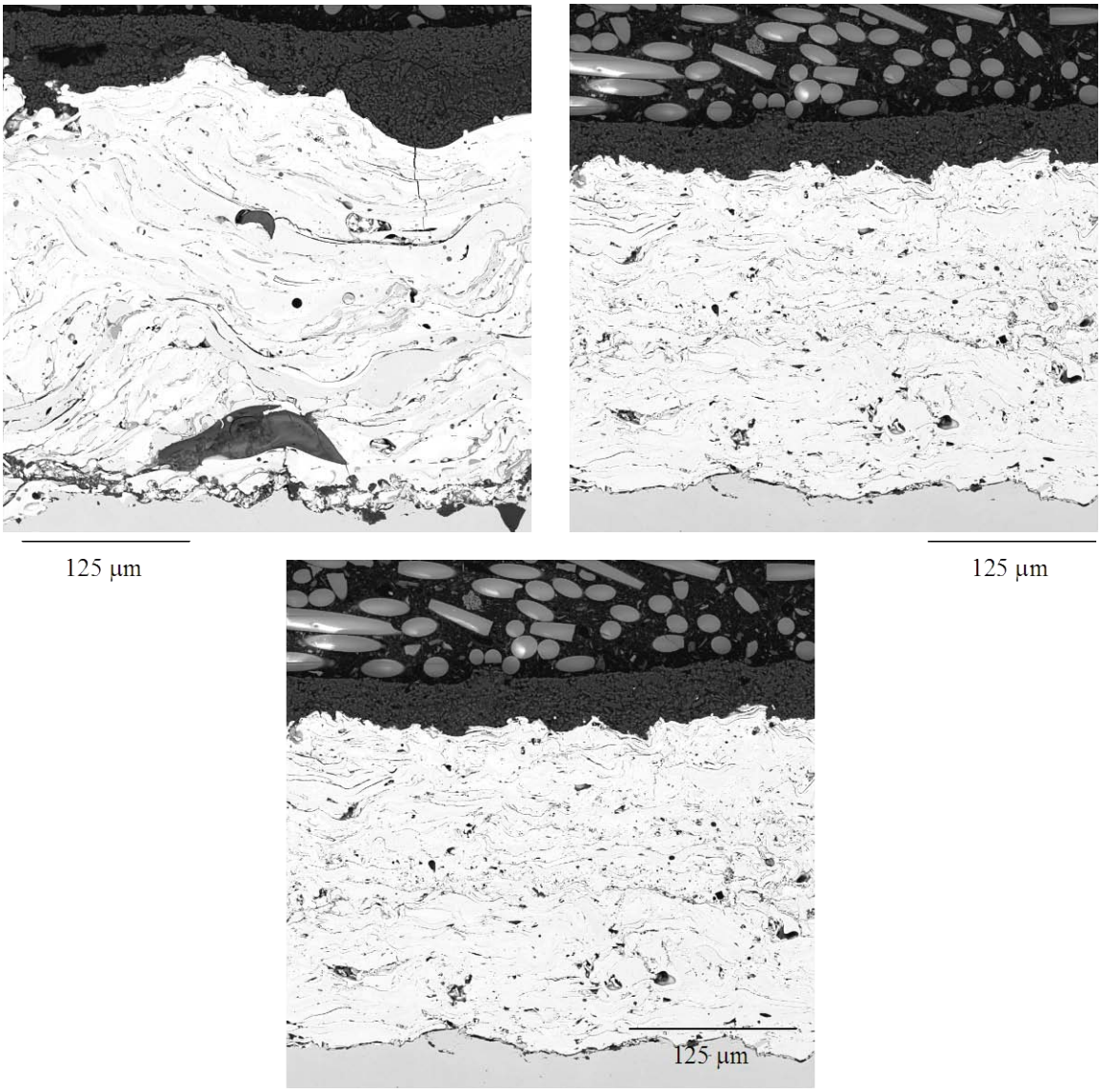

Figure 5-3
As-received nanocrystalline coating commercial coating on 91 substrate material (top left), 304 SS (top right), and Haynes 230 substrate material (bottom) [1-16].

5.1.1 Test Conditions

The samples were subjected to 100-hour screening tests at 649º C for SH/RH conditions and at 524º C for WW conditions. The compositions of synthetic flue gas and ash deposits for the 100-hour screening tests are presented in Tables 5-2 and 5-3. A very aggressive environment was selected for the initial screening tests. Based on the on the poor performance of the coatings in the screening test, the composition of the flue gas mixtures and the synthetic ash deposits for the WW and SH/RH conditions were changed from very aggressive to moderately aggressive as shown in Tables 5-4 and 5-5. This was accomplished by lowering the SO_2 in the synthetic gas from 0.37 and 0.50vol% to 0.12 and 0.25vol% for the WW and SH/RH conditions, respectively. Additionally, the FeS was reduced by 40wt%, and the NaCl, and KCl were reduced by 0.4wt% for the WW ash deposits, and the Na_2SO_4 and K_2SO_4 were reduced by 12.5wt% for the SH/RH. The same ash compositions were used in the earlier studies of the DOE-USC program.

Table 5-2
Composition of the synthetic flue gas used in the 100-hour screening tests [1-16].

Gas Species	Waterwall (vol. %)	Superheater (vol. %)
N_2	74.63	70.88
CO_2	17.00	15.00
H_2O	6.00	10.00
CO	2.00	0.00
SO_2	0.37	0.50
O_2	0.00	3.60
HCl	0.00	0.02
Total	**100.00**	**100.00**

Table 5-3
Synthetic ash composition for the 100-hour-corrosion tests [1-16].

Compound	Waterwall (wt. %)	Superheater (wt. %)
Fe_3O_4	10.00	0.00
FeS	75.00	0.00
Fe_2O_3	0.00	50.00
C	5.00	2.50
SiO_2	4.50	8.80
Al_2O_3	4.50	8.70
NaCl	0.50	0.00
KCl	0.50	0.00
Na_2SO_4	0.00	15.00
K_2SO_4	0.00	15.00
Total	**100.00**	**100.00**

Table 5-4
Synthetic flue gas composition for the 1000-hour corrosion tests [1-16].

Gas Species	Waterwall	Superheater
N_2	74.88	71.14
CO_2	17.00	15.00
H_2O	6.00	10.00
CO	2.00	0.00
SO_2	0.12	0.25
O_2	0.00	3.60
HCl	0.00	0.01
Total	**100.00**	**100.00**

Table 5-5
Composition of the synthetic ash deposits used in 1000-hour corrosion tests [1-16].

Compound	Waterwall (wt. %)	Superheater (wt. %)
Fe_3O_4	45.00	0.00
FeS	40.00	0.00
Fe_2O_3	0.00	30.60
C	5.00	2.50
SiO_2	4.90	31.30
Al_2O_3	4.90	30.60
NaCl	0.10	0.00
KCl	0.10	0.00
Na_2SO_4	0.00	2.50
K_2SO_4	0.00	2.50
Total	**100.00**	**100.00**

5.1.2 Corrosion Results

All nanocrystalline coatings experienced some degree of distress after 100-hour corrosion screening tests. The coatings subjected to the waterwall conditions generally fared much better than those tested under SH/RH conditions, as illustrated in Figures 5-4 and 5-5. The corrosion attack, in the samples exposed to the waterwall conditions, progressed along the coating morphological features such as the columnar grain boundaries and/or globular imperfections, as illustrated in Figures 5-4 and 5-5. The nanocrystalline coatings tested under SH/RH conditions, on the other hand, exhibited severe bulk corrosion resulting in partial or complete consumption of the coating materials in multiple locations and subsequent attack of the substrate material. Furthermore, the corrosion wastage of coatings, under the SH/RH test conditions, did not appear to be confined to imperfection sites, but rather were distributed across the entire sample surface.

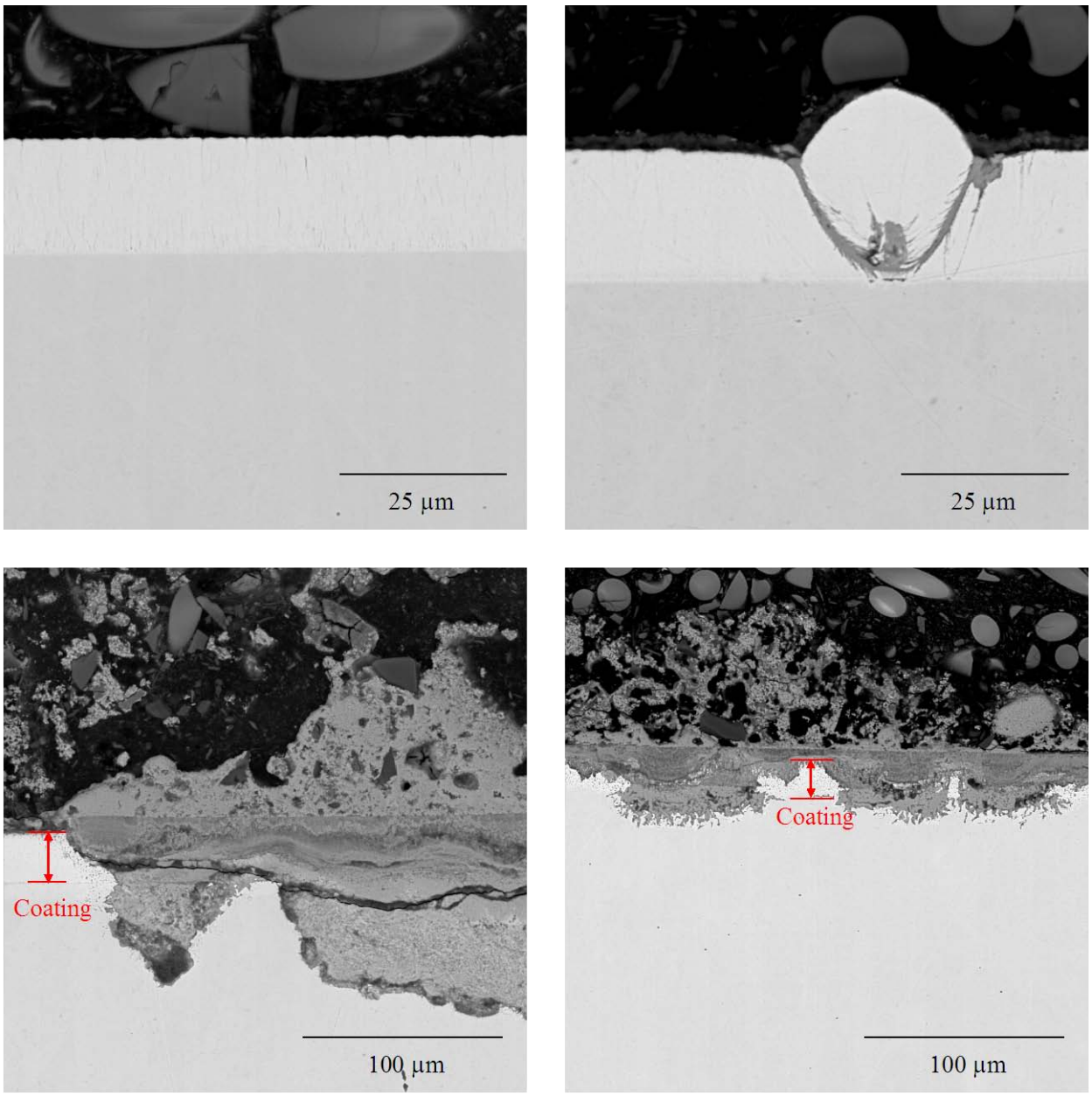

Figure 5-4
Representative backscatter SEM images of nanocrystalline coating B3 (Fe-37Ni-25Cr) in the as-received condition (top left); exposed for 100 hours to aggressive waterwall conditions on 91 substrate (top right); exposed for 100 hours to aggressive superheater conditions on 91 substrate (bottom left) and 304 substrate (bottom right) [1-16].

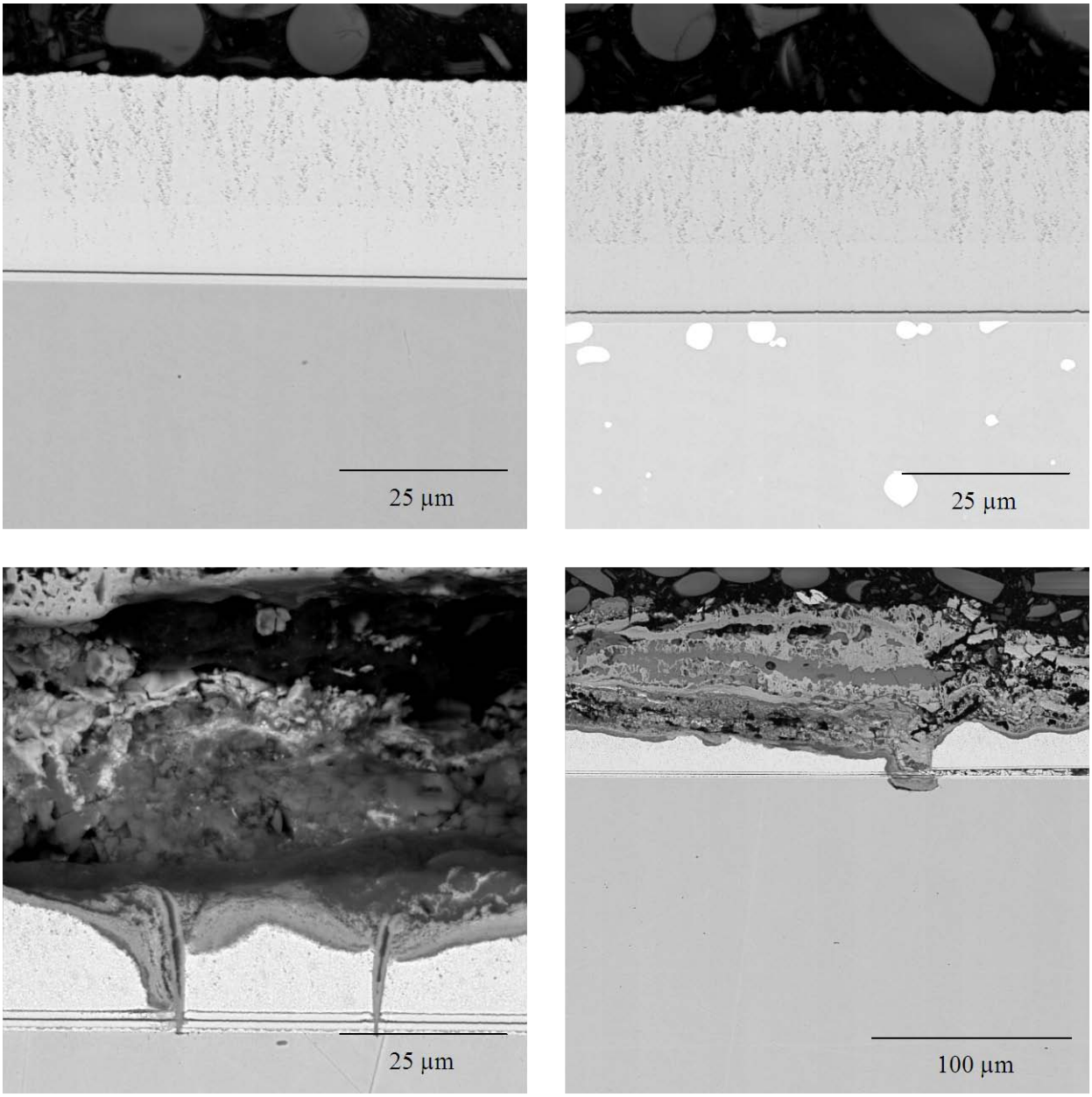

Figure 5-5
Representative backscatter SEM images of nanocrystalline coating B6 (Co-23Ni-22Cr-14W-10Al) in the as-received condition on 304 SS (top left) and Haynes 230 (top right); exposed for 100 hours to aggressive superheater conditions on 304 substrate (bottom) [1-16].

In light of the results from the screening tests, each long-term (1000 hour) test coupon was visually inspected for evidence of gross degradation following every 100-hour exposure period. Upon completion of 500 hours, and every subsequent 100-hour test period, a more detailed stereoscopic evaluation was also performed on every coupon to assess the coating integrity. After 600 hours of testing, coupons with coatings displaying significant evidence of distress, either in the form of cracking, fissuring, spallation and/or obvious wastage were removed from the test rig and placed in drying ovens to await further, in-depth evaluation.

The commercial coatings that appeared mottled (*i.e.*, not as a dense monolithic layer) and contained high concentrations of oxygen (like A1 and A2) provided seemingly little to no protection even at the lowest test temperatures exposed to WW conditions, as shown in Figure 5-6. The dense, more uniform coatings (A4, B1 – B6) on the other hand, especially those containing more than 20 wt.% Cr, tended to resist widespread corrosive attack, but exhibited penetration of oxide and sulfide species, especially along the columnar grain boundaries and gross defects, as illustrated in Figure 5-7. The micrographs shown in Figures 5-5 and 5-7 clearly show that the columnar grain boundaries provide pathways for corrosion species to reach the coating/substrate interface.

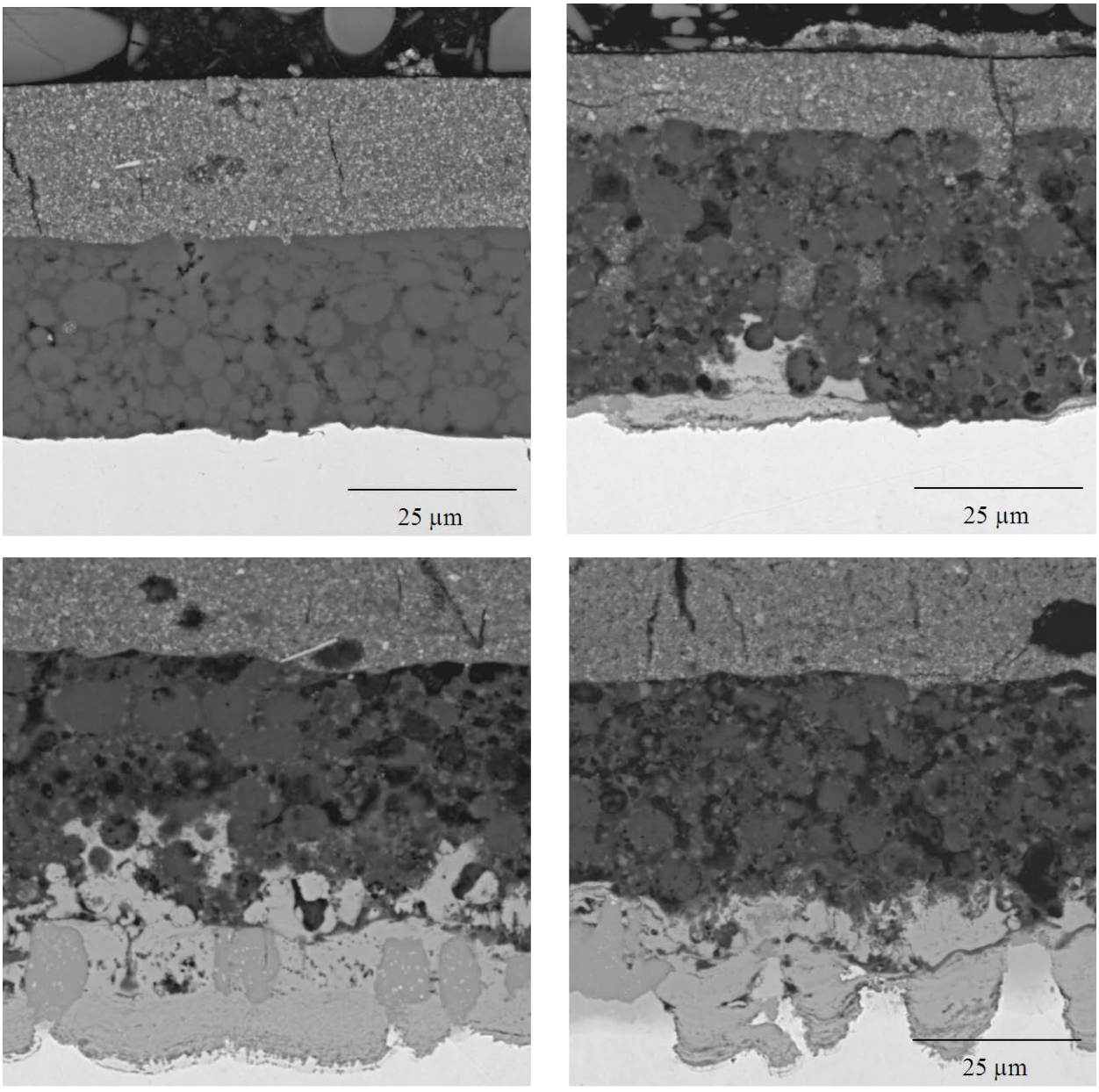

Figure 5-6
Representative backscatter SEM images of commercial coating A1 on 91 substrate material in the as-received condition (top left); after 1000 hours at 455º C (top right); after 1000 hours at 524º C) (bottom left); after 1000 hours at 593º C (bottom right) [1-16].

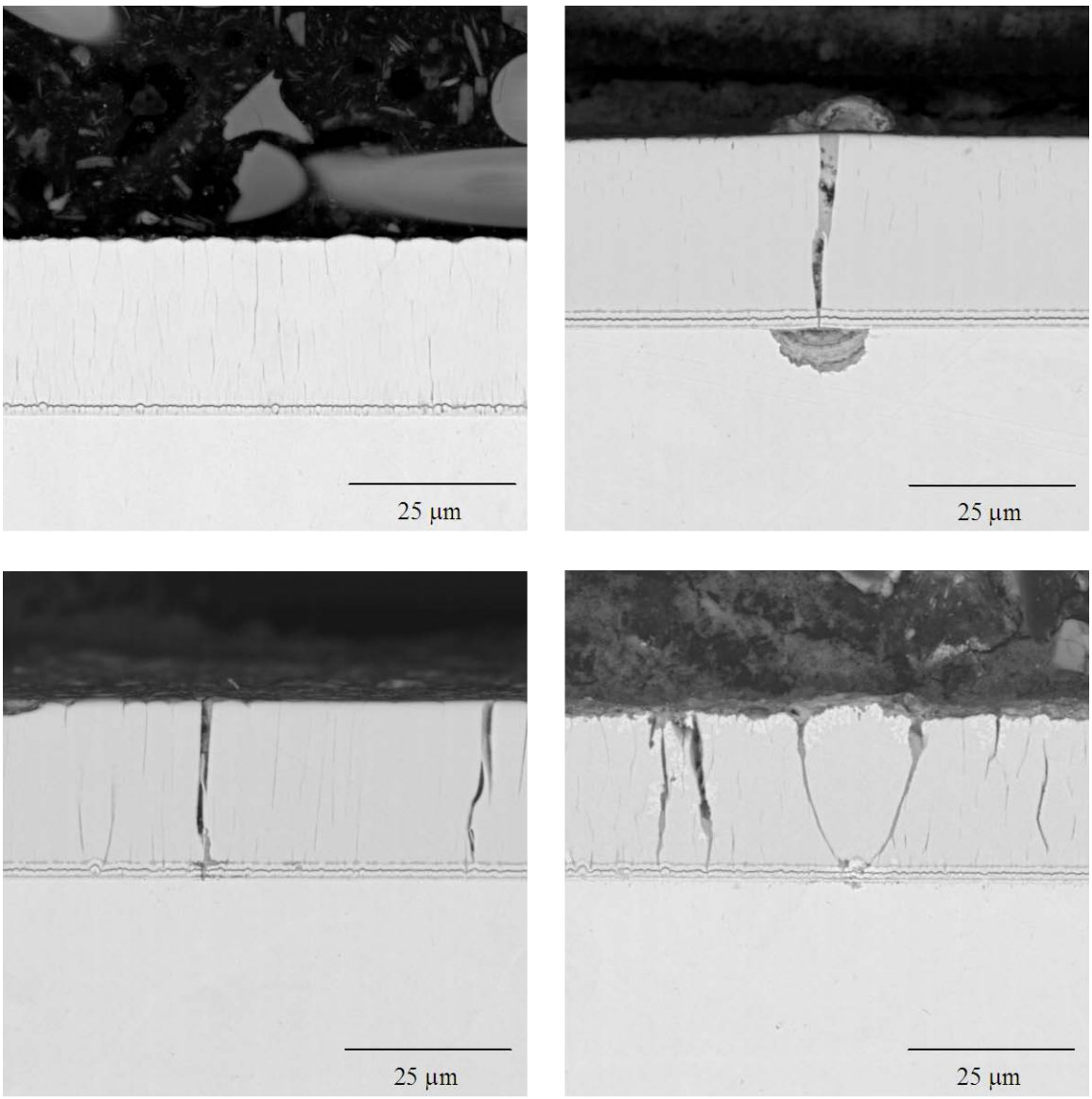

Figure 5-7
Representative backscatter SEM Images of nanocrystalline coating B1 (Fe-37Ni-25Cr) on 91 substrate material in the as-received condition (top left); after 600 hours at 455º C (top right); after 600 hours at 524º C (bottom left); after 1000 hours at 593º C (bottom right) [1-16].

Representative backscatter SEM images of as-received and post-exposure condition of various nanocrystalline coatings tested under synthetic SH/RH conditions are shown in Figures 5-8 through 5-10. It is evident from these SEM images, all nanocrystalline coatings tested sustained some degree of general corrosive attack. All of the nanocrystalline coatings, with the exception of nanocrystalline coating B5 (Ni-30Co-28Cr-3Si), were completely compromised in at least one location after 600 hours of exposure at 705º C and all of the samples (including B5) exhibited penetration of corrosive species into the substrate materials at 815º C. Furthermore, unlike the samples tested under WW conditions, in which the coating materials displayed little evidence of gross attack, majority of the coatings and substrate material systems tested under SH/RH conditions sustained widespread corrosion.

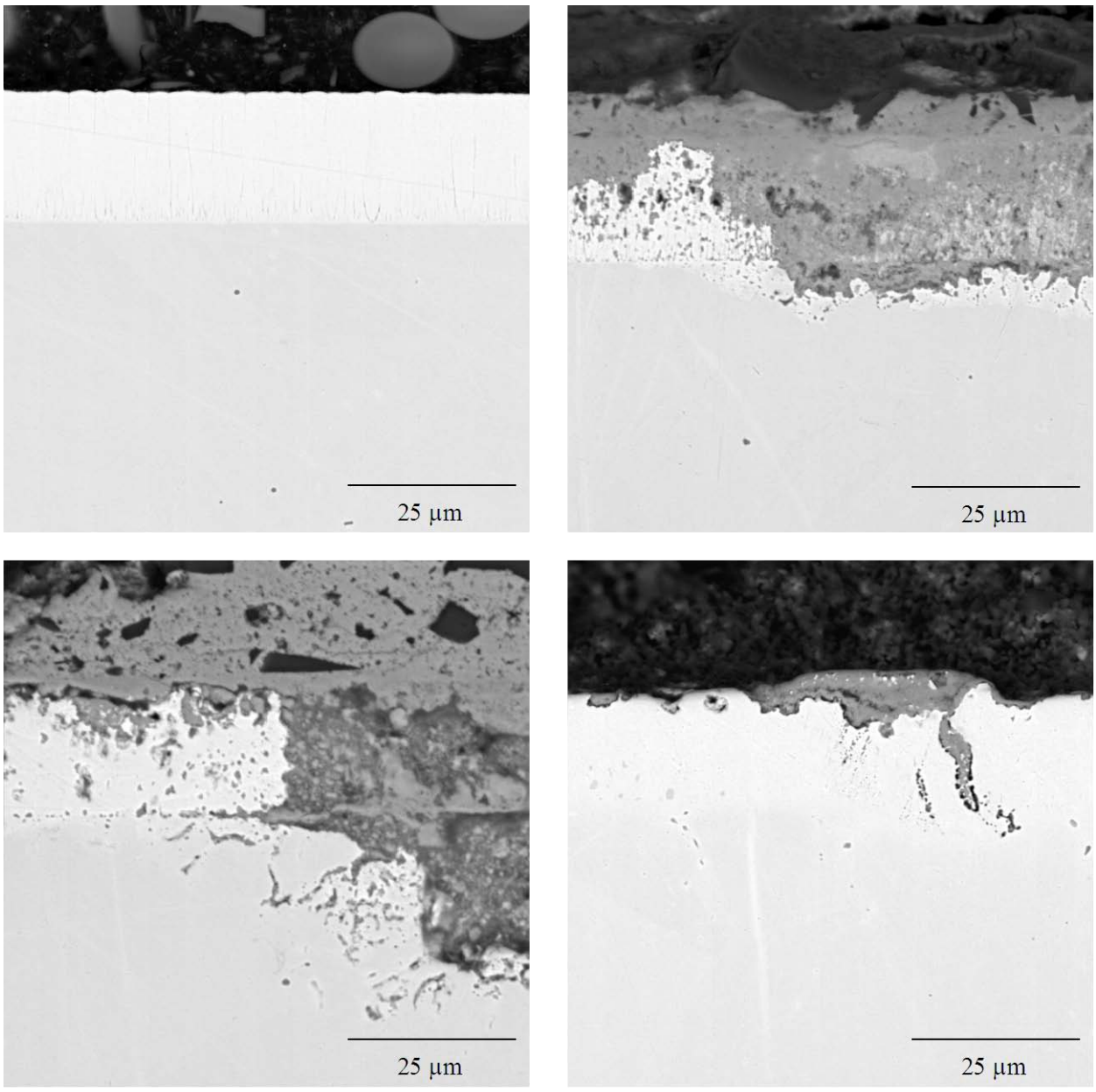

Figure 5-8
Backscatter SEM images of nanocoating B3 (Fe-37Ni-25Cr) on 304 SS in the as-received condition (top left); after 600 hours of exposure to SH/RH conditions at 593º C (top right); after 600 hrs of exposure to SH/RH conditions at 705º C (bottom left); after 600 hours of exposure to SH/RH conditions at 815º C (bottom right) [1-16].

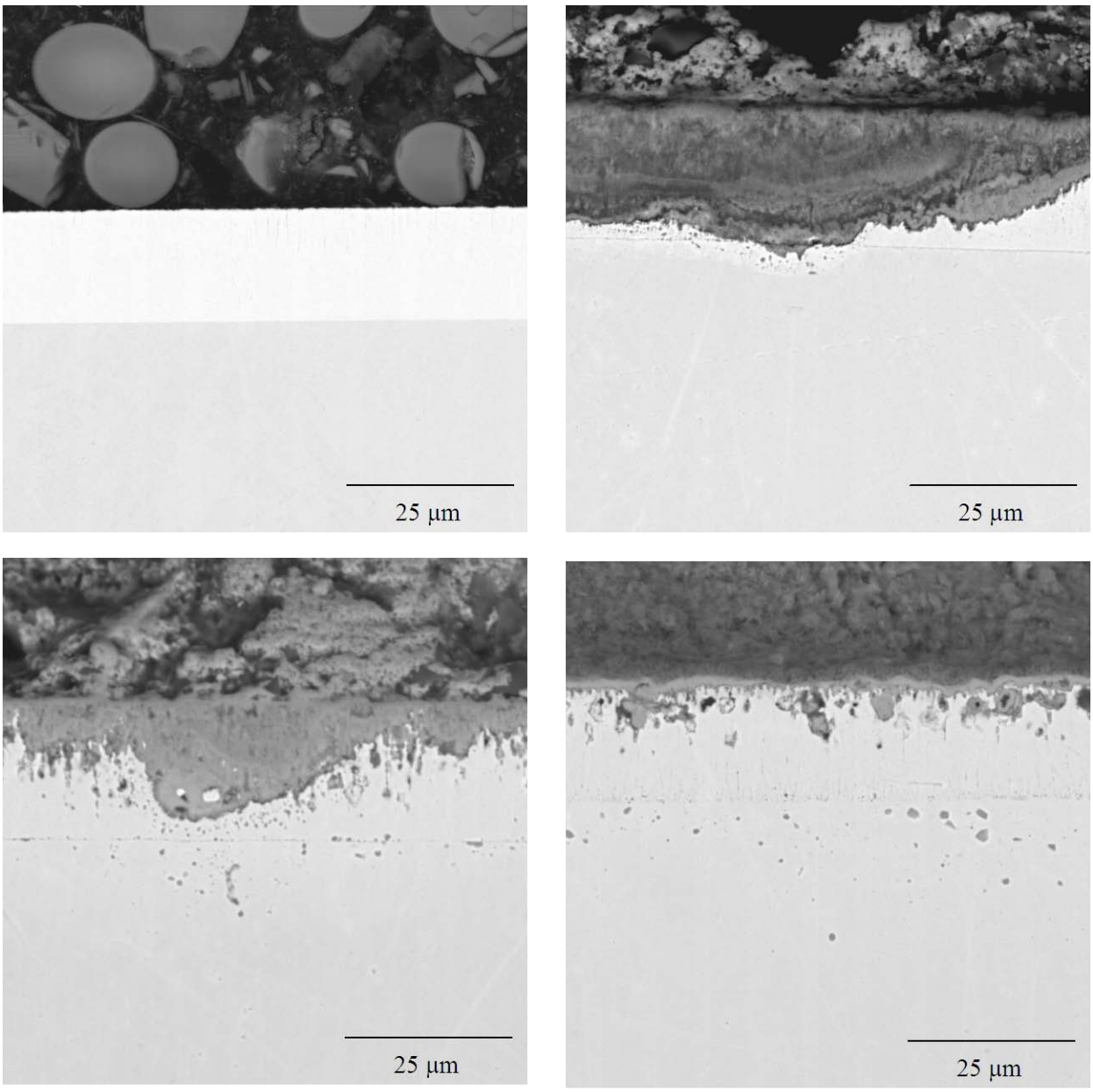

Figure 5-9
Representative backscatter SEM Images of nanocoating B5 (Ni-30Co-28Cr-3Si) on 304 SS in the as-received condition (top left); after 600 hours of exposure to SH/RH conditions at 593º C (1100º) (top right); after 600 hrs of exposure to SH/RH conditions at 705º C (bottom left); after 600 hours of exposure to SH/RH conditions at 815º C (bottom right) [1-16].

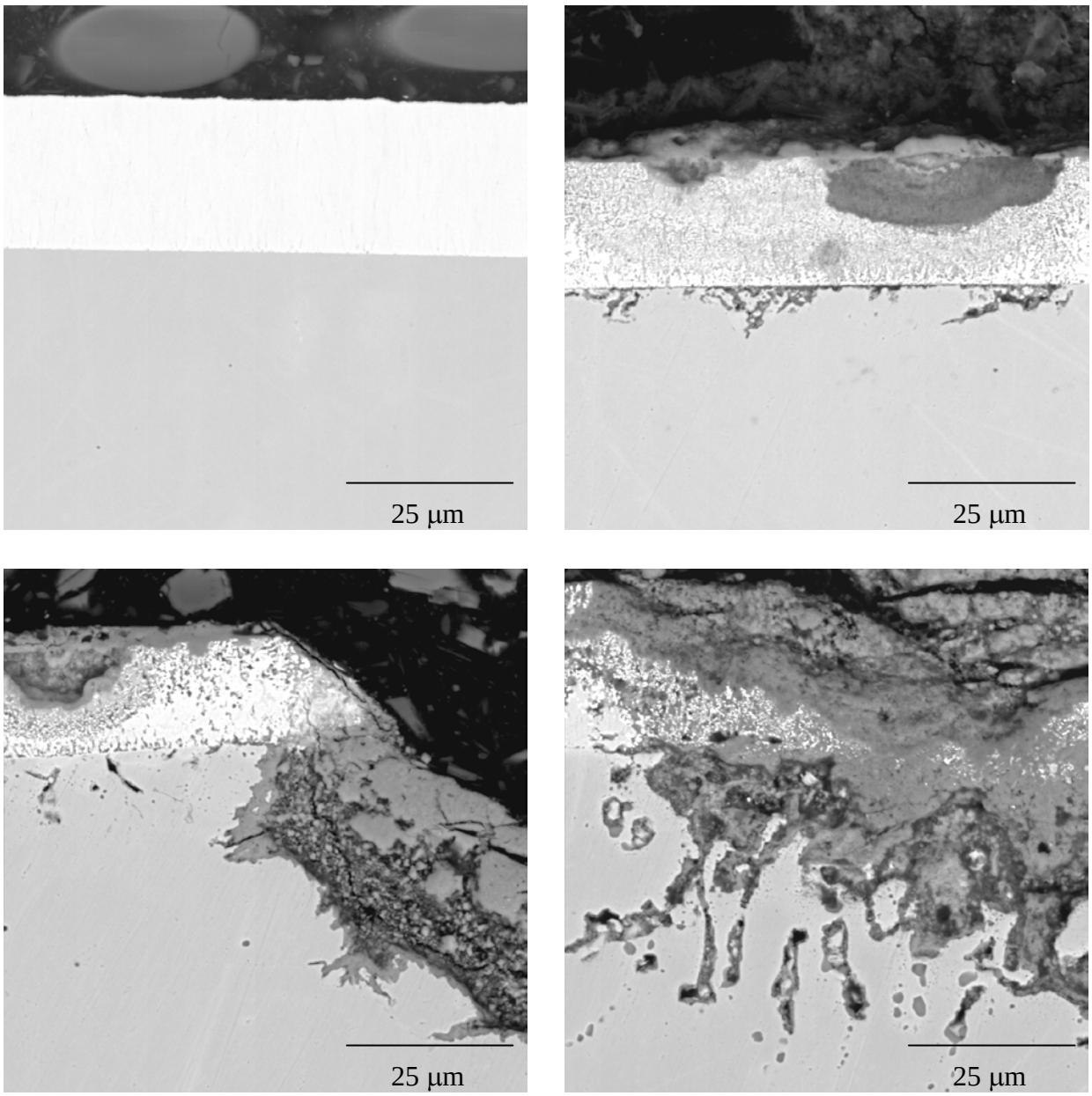

Figure 5-10
SEM images of nanocoating B7 (Co-23Ni-22Ce-14W) on 304 SS in the as-received condition (top left); after 600 hours of exposure to SH/RH conditions at 593º C (top right); after 600 hours of exposure to SH/RH conditions at 705º C (bottom left); after 600 hours of exposure to SH/RH conditions at 815º C (bottom right).

In summary, fire-side corrosion test results showed that the commercial coatings offer little or no corrosion protection. All nanocrystalline coatings performed better at low temperatures, when they are exposed to WW conditions and suffered some degree of corrosion attack at elevated temperatures, when they are exposed to SH/RH conditions. These corrosion test results also indicated that the quality of the coating needs to be improved to minimize the wide spread corrosion degradation.

5.2 Fire-Side Corrosion Testing at SwRI

Fire-side corrosion test were conducted at SwRI with out and with flowing synthetic flue gas. The coated samples were prepared at SwRI for the fire-side corrosion tests with out flowing synthetic flue gas using PEMS process. For the fire-side corrosion tests with flowing synthetic flue gas, the coated samples were prepared by CSM using a pulsed DC magnetron sputtering process.

5.2.1 Coating Application, Composition, and Microstructure

Nanocrystalline Ni-20Cr-Al, H160-Al, H120-Al, and 310 SS-Al coatings were applied using PEMS process in the SwRI's large chamber (36" × 36" × 36") with four targets. The coatings were applied on 304 SS and Haynes 230 rectangular coupons. The composition of the coatings in the as deposited condition is shown in Table 5-6. It is evident from the table that the Al content in the four coatings varied from 6.25 to 7.04 wt.%. The coating thickness of the Ni-20Cr-Al, H160-Al, H120-Al, and 310 SS-Al coatings was 25, 20, 22, and 18 μm, respectively. The Ni-20Cr-Al and H160-Al coatings exhibited a relatively dense structure with fine columnar grains, while the H120-Al and 310 SS-Al coatings revealed a relatively coarser columnar structure with voids betweens the grains as illustrated in Figures 5-11 through 5-14. The 310 SS-Al coating showed the least dense structure among the four coatings.

Table 5-6
Semi-quantitative chemical composition of the as-deposited coatings, wt%.

Element	Ni-20Cr-Al	H160-Al (NiCoCrSiAl)	H120-Al (FeNiCrSiAl)	310 SS-Al (FeCrNiSiAl)
Al	6.70	6.25	7.04	6.71
Cr	18.50	27.88	26.25	26.62
Ni	Balance	Balance	31.5	15.07
Si	0.58	2.45	0.53	0.55
Ti	Not detected	0.47	Not detected	Not detected
Fe	Not detected	0.29	Balance	Balance
Co	Not detected	29.5	Not detected	Not detected

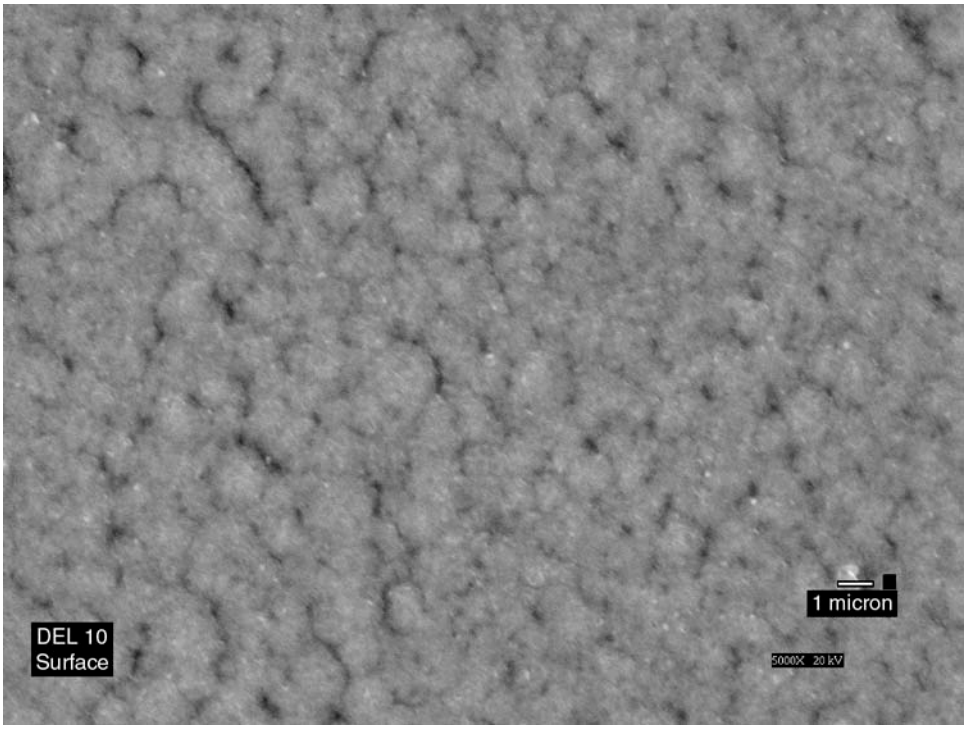

a)

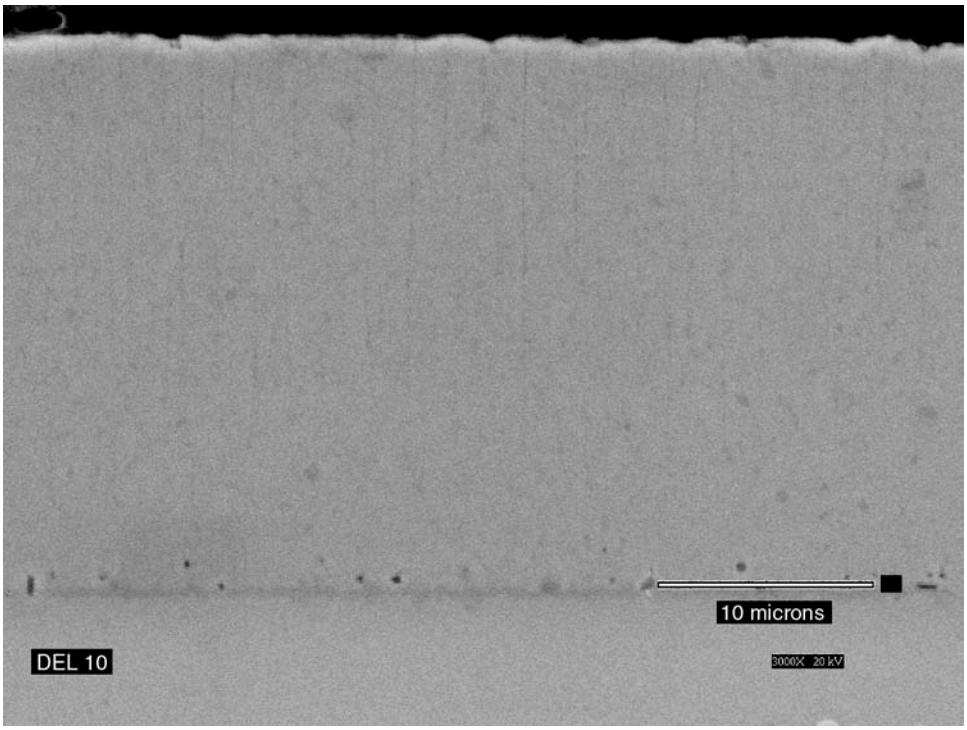

b)

Figure 5-11
SEM micrographs of the Ni-20Cr-Al coating: a) top view and b) cross-sectional view.

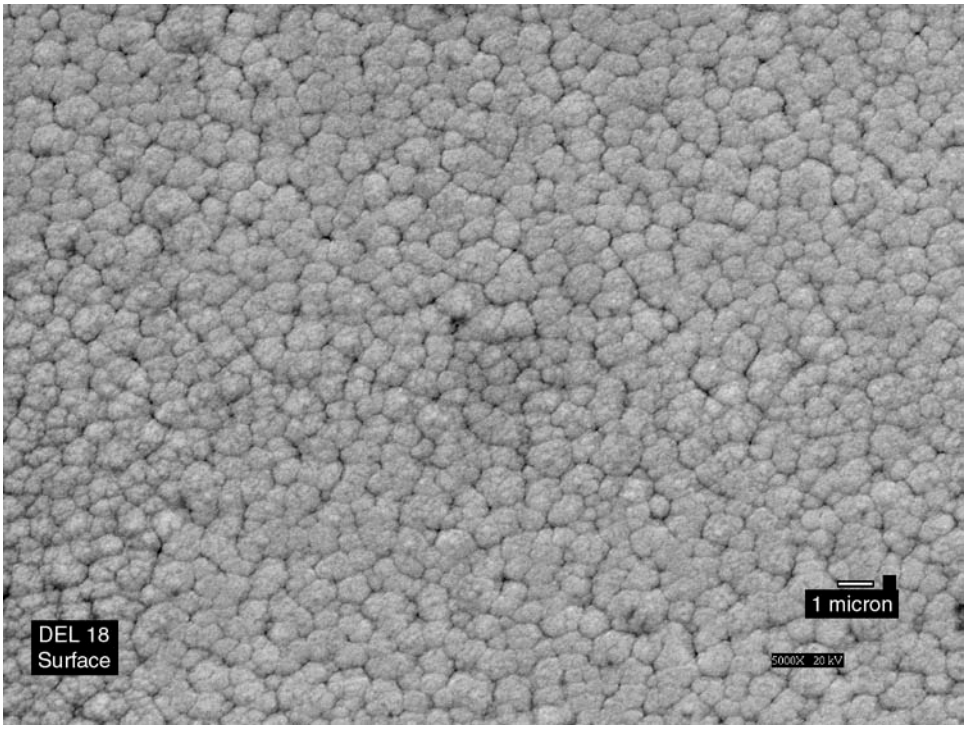

a)

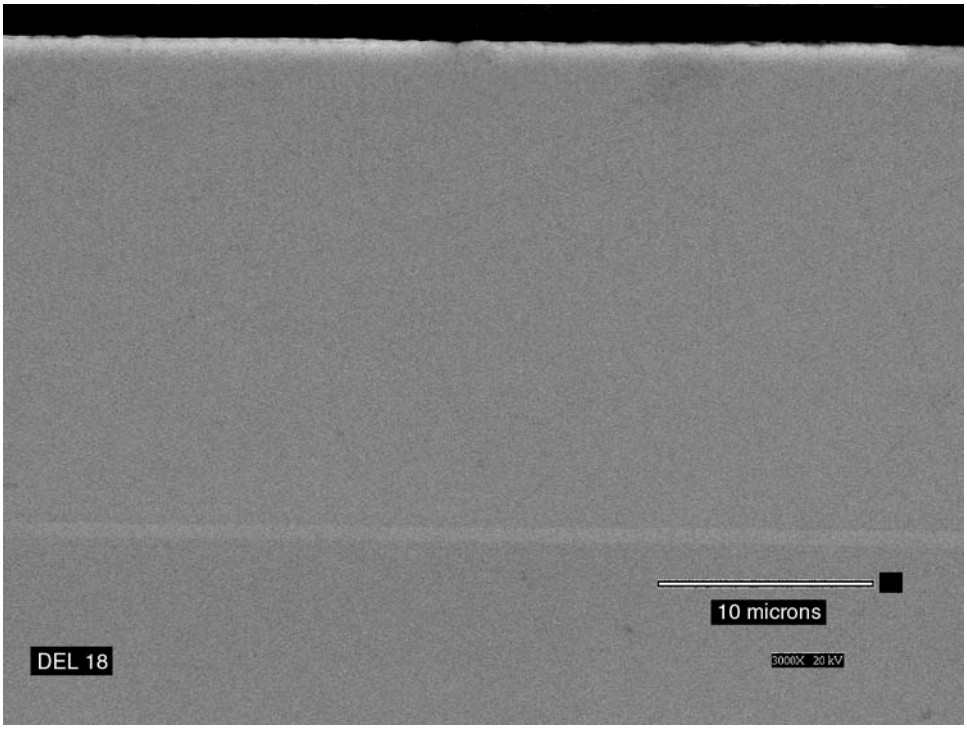

b)

Figure 5-12
SEM micrographs of the as-deposited H160-Al coating: a) top view and b) cross-sectional view.

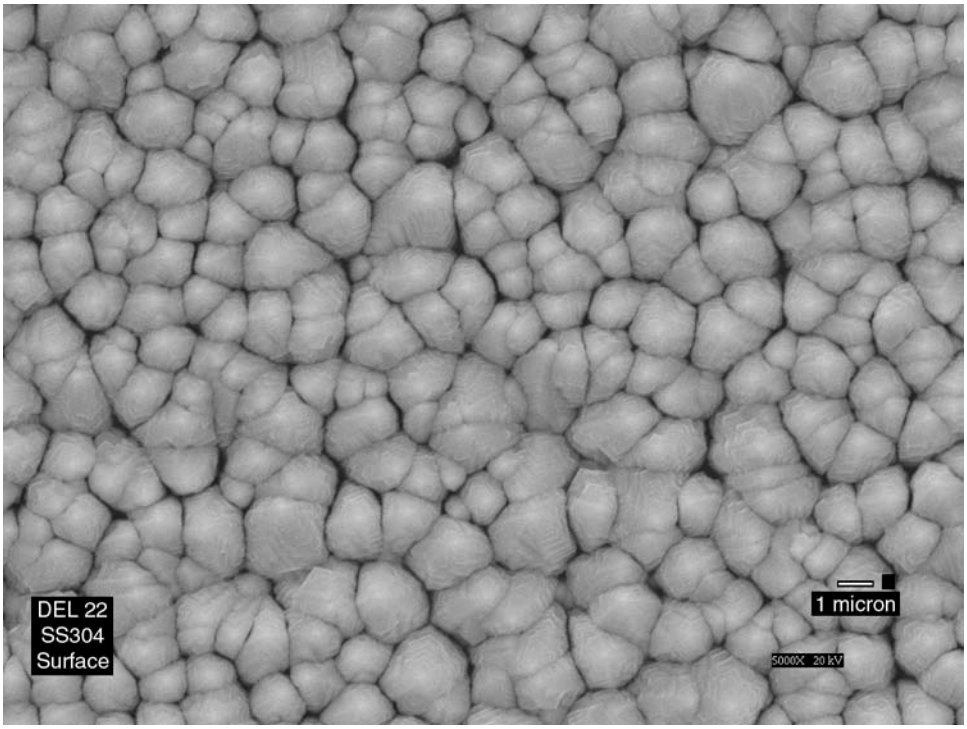

a)

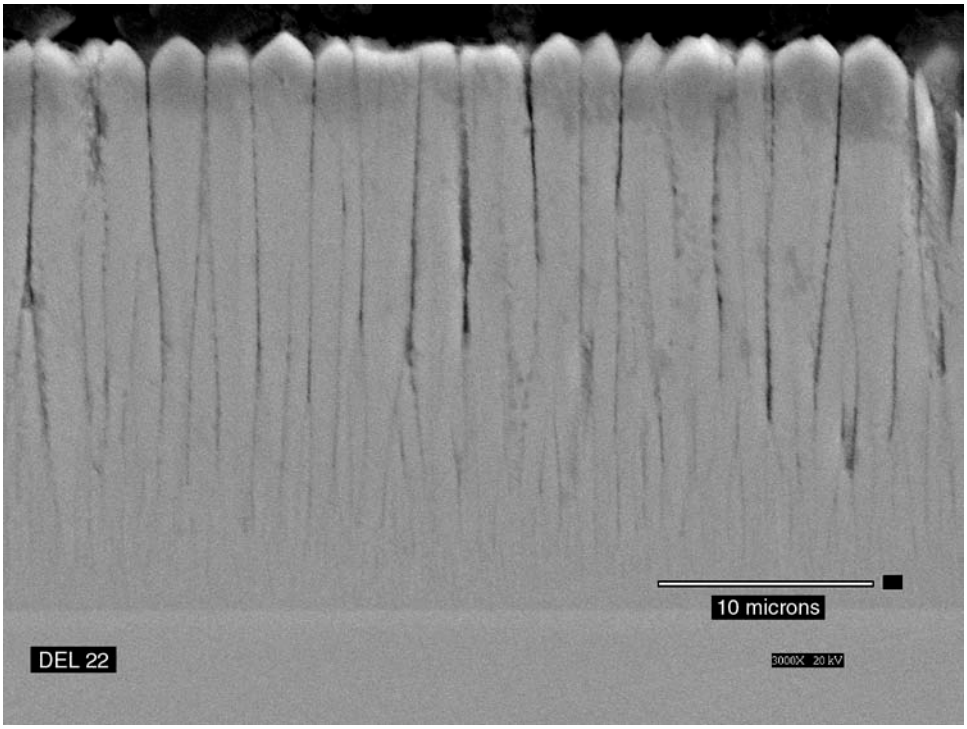

b)

Figure 5-13
SEM micrographs of the as-deposited H120-Al coating: a) top view and b) cross-sectional view.

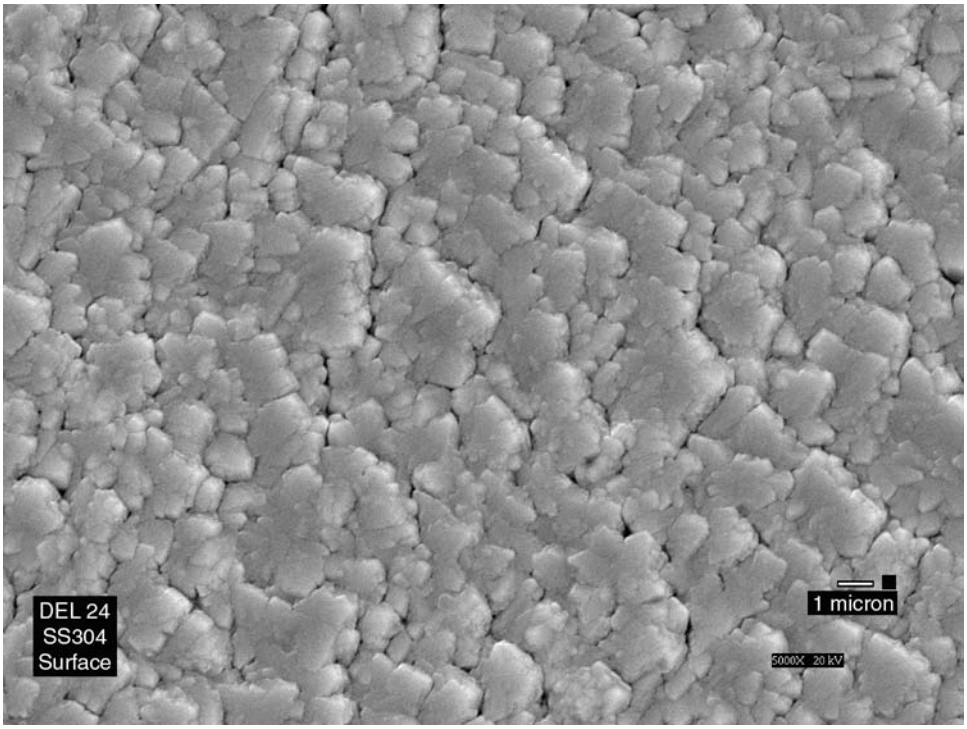

a)

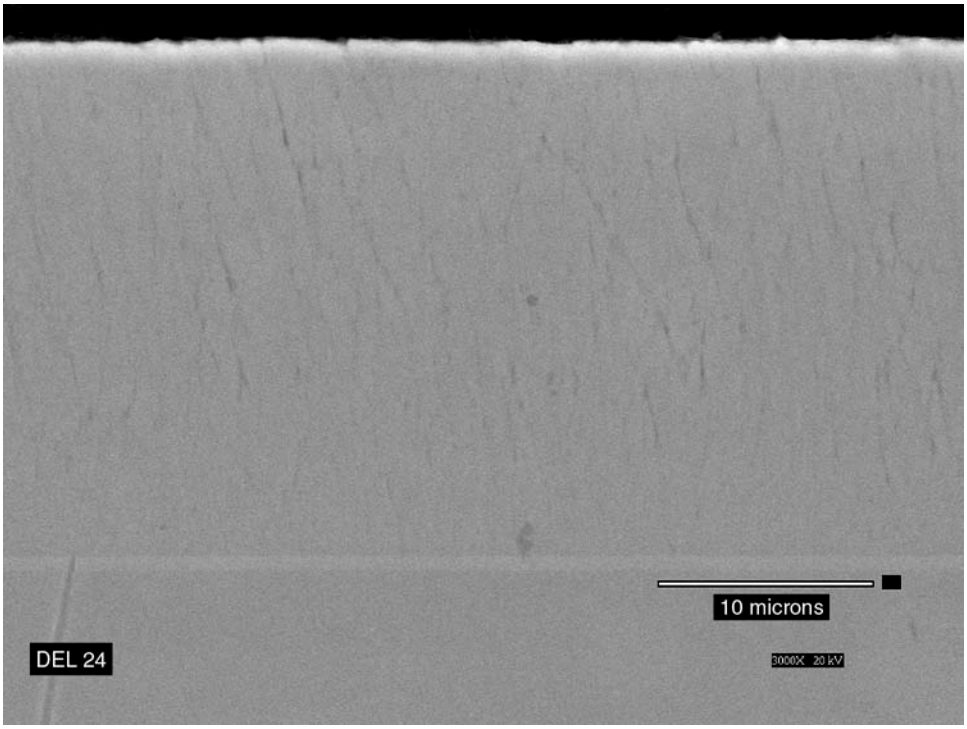

b)

Figure 5-14
SEM micrographs of the 310 SS-Al coating: a) top view and b) cross-sectional view.

5.3 Synthetic Fuel Ash

The composition of the ash deposit selected for the fire-side corrosion testing at 593º C for the WW condition is given in Table 5-7. The ash composition simulates the composition of the deposits that were found on the waterwall tube in the Eastern and Midwestern coal-fired boilers. The Midwestern ash is more aggressive when compared to the Eastern ash because it contains higher amounts of FeS, NaCl, and KCl than the Eastern ash. The test temperature of 593º C represents the maximum operating metal temperature of the waterwall tubes. The composition of the ash deposit selected for the fire-side corrosion testing at 705º C and 815º C is given in Table 5-7. These compositions represent the deposits found on the super-heater and re-heater tubes in the Eastern and Midwestern coal-fired boilers. The Midwestern ash deposit is more corrosive than the Eastern ash because it contains higher amounts of sulfates. The super-heater and re-heater tubes operated in the temperature range of 593º C to 815º C.

The ash was prepared by thoroughly mixing the powders of different compounds in desired proportions by weight. A camphor-ethanol solution was used to prepare the desired ash plate. Camphor was added to the ethanol for improving the adhesion of the deposit on the test sample. The paste was applied only on one side of the coated and uncoated test samples. The coated and uncoated Haynes 230 samples were tested at 815º C. The uncoated 304 SS samples were tested at 593º C and 705º C. Nanocrystalline Ni-20Cr-Al and H160-Al-coated samples were tested at three temperatures, 593º C, 704º C, and 815º C. The H120-Al and 310 SS-Al coated 304 SS samples were only tested at one temperature, 704º C.

Table 5-7
Synthetic ash composition for the WW conditions.

Compound	Eastern, wt.%	Midwestern, wt.%
Fe_2O_3	45.00	10.00
FeS	40.00	75.00
C	5.00	5.00
SiO_2	4.90	4.80
Al_2O_3	4.90	4.70
NaCl	0.10	0.25
KCl	0.10	0.25

Table 5-8
Synthetic ash composition for the SH/RH condition.

Compound	Eastern, wt.%	Midwestern, wt.%
SiO_2	31.30	29.30
Fe_2O_3	30.60	29.10
Al_2O_3	30.60	29.10
Na_2SO_4	2.50	5.00
K_2SO_4	2.50	5.00
C	2.50	2.50

5.4 Corrosion Testing

Following application of the ash, the samples were placed inside three furnaces which were heated to the target temperatures of 593º C, 704º C, and 815º C. After each 160 hours of exposure, the samples were furnace cooled to room temperature, the specimens were cleaned to remove the exposed ash deposit, re-coated with fresh ash paste, and the samples were re-inserted into the appropriate furnace for the next 160-hour cycle. The samples were exposed for 3040 hours at 593º C and 815º C and for 2040 hours at 704º C. For each condition, triplicate samples were tested at these temperatures.

5.5 Post-Exposure Evaluation

Following the thermal exposure, both uncoated and coated samples were cleaned to remove the ash deposit and examined using optical and SEM for evidence of corrosion attack. A transverse section was removed from a sample of each set of three samples and metallurgical mounts were prepared from these sections using standard metallographic techniques. The mounts were examined to determine the depth of penetration of corrosion attack and to characterize scale, and internal sulfidation.

5.6 Corrosion Results After Exposure at 593º C

The uncoated 304 SS specimen surfaces after 3040 hours exposure at 593 ºC with Eastern and Midwestern ash (simulated waterwall) deposits were covered with black scale. The cross sections of the uncoated samples showed approximately 12 and 20 µm thick corrosion/oxide scale under the Eastern and Midwestern ash deposited areas, respectively, as illustrated in Figure 5-15. Figure 5-16 shows the extent of corrosion attack and a few sulfide particles in the substrate under the scale. The side that was not covered with the ash deposit showed no oxide or corrosion scale, as illustrated in Figure 5-17. Comparison of the micrographs reveals that the extent of corrosion attack under the Midwestern ash deposit was more severe than those exposed to the Eastern ash deposit confirming that the Midwestern ash deposit was more corrosive than the Eastern ash. All coated samples were shiny and showed no evidence of corrosion and/or oxidation. The condition of the Ni-20Cr-Al and H160-Al coatings, after 3040 hours of exposure at 593º C, with Eastern and Midwestern ash deposits are illustrated in Figures 5-18 and 5-19. It is evident from the micrographs the coatings were free from sulfidation attack, suggesting that the coatings provided corrosion protection to the 304 SS substrate alloy.

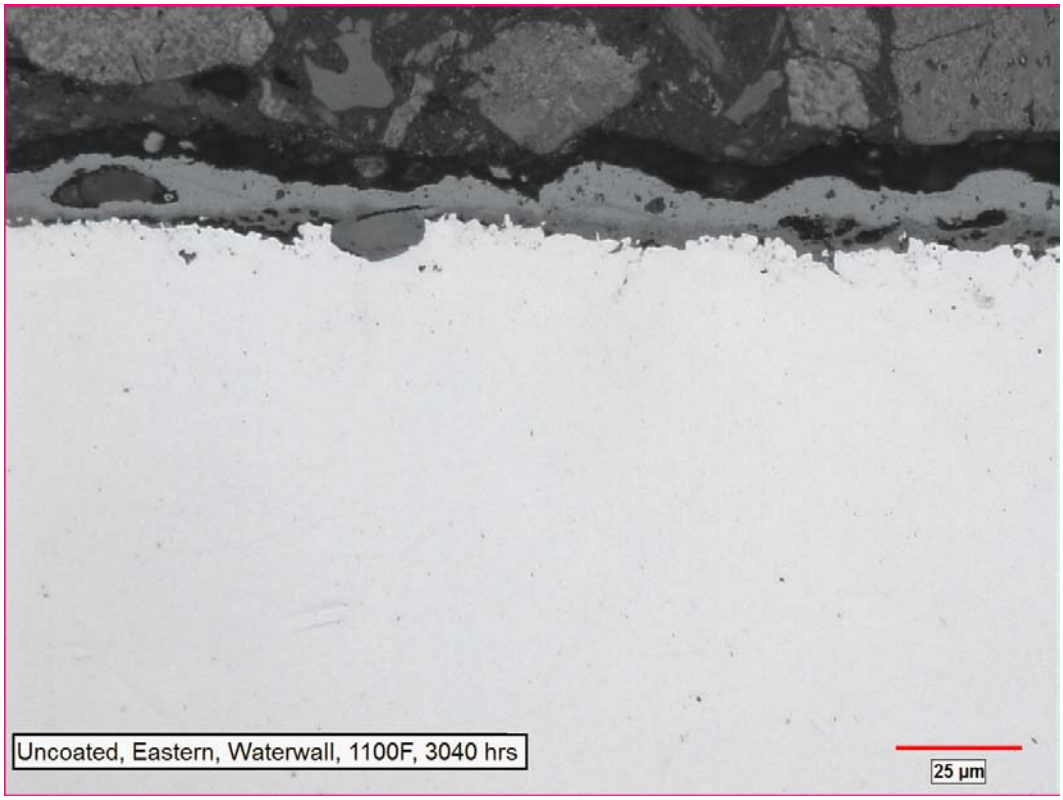

a)

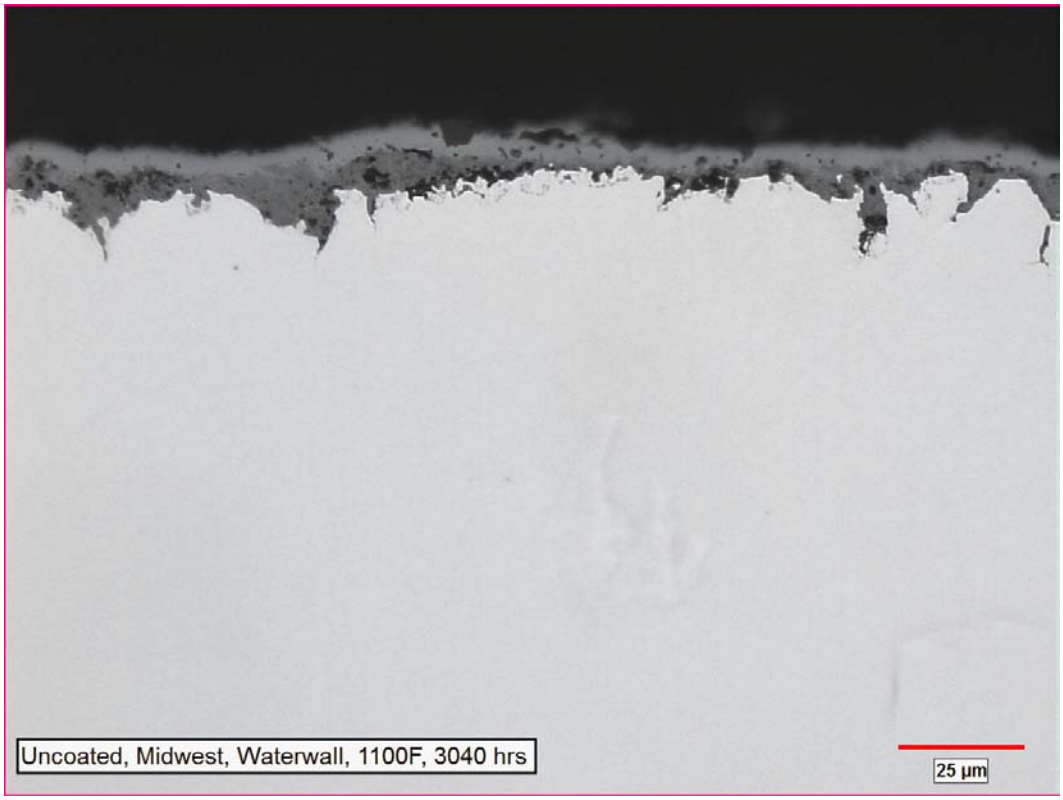

b)

Figure 5-15
Optical micrographs of the cross sections of uncoated 304 SS samples after exposure to 593º C for 3040 hours showing the corrosion attack under a) Eastern ash and b) Midwestern ash deposits.

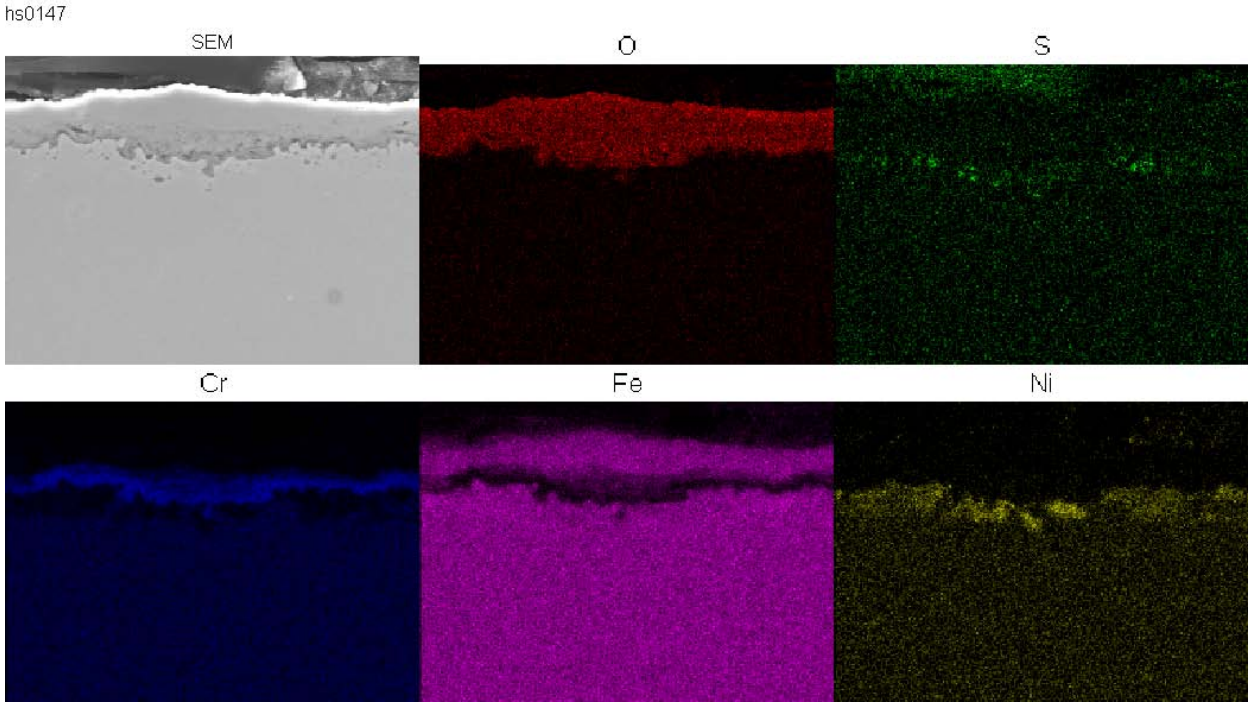

a) Eastern ash deposit

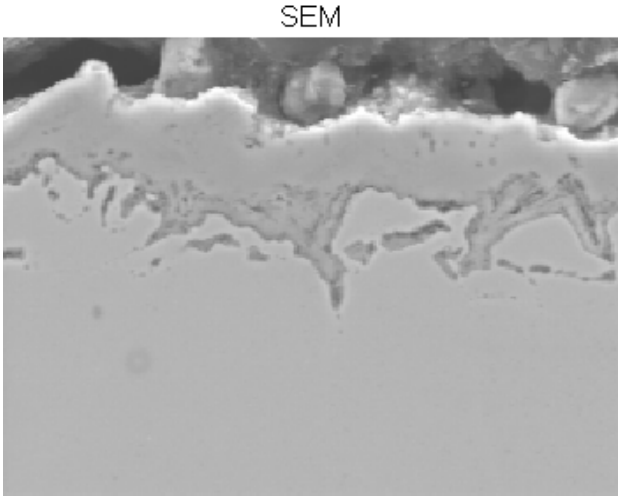

b) SEM

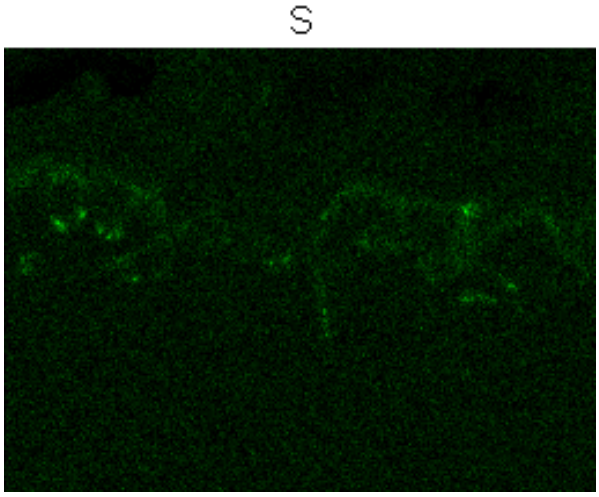

c) S map of micrograph b

Figure 5-16
SEM micrographs of the cross sections of the uncoated 304 SS samples after exposure to 593º C for 3040 hours along with the elemental maps showing sulfide particles in the corrosion attacked area under the a) Eastern ash and b) and c) Midwestern ash deposits.

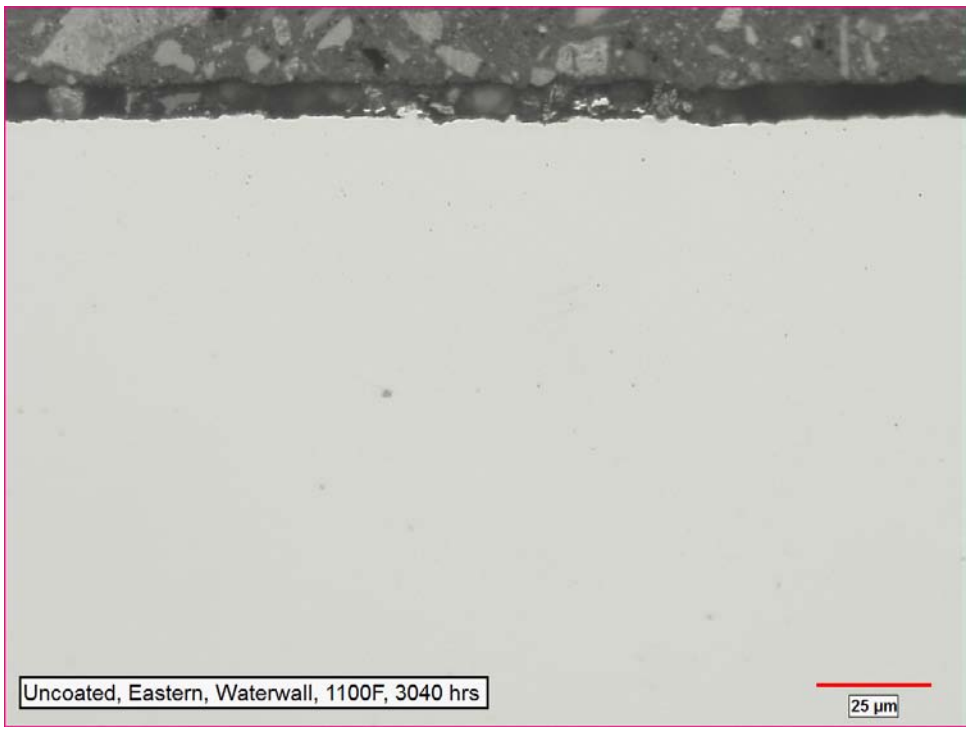

Figure 5-17
Optical micrograph of the cross section of the uncoated 304 SS sample after exposure at 593º C for 3040 hours showing the absence of oxidation attack on the side that was not covered with the ash deposit.

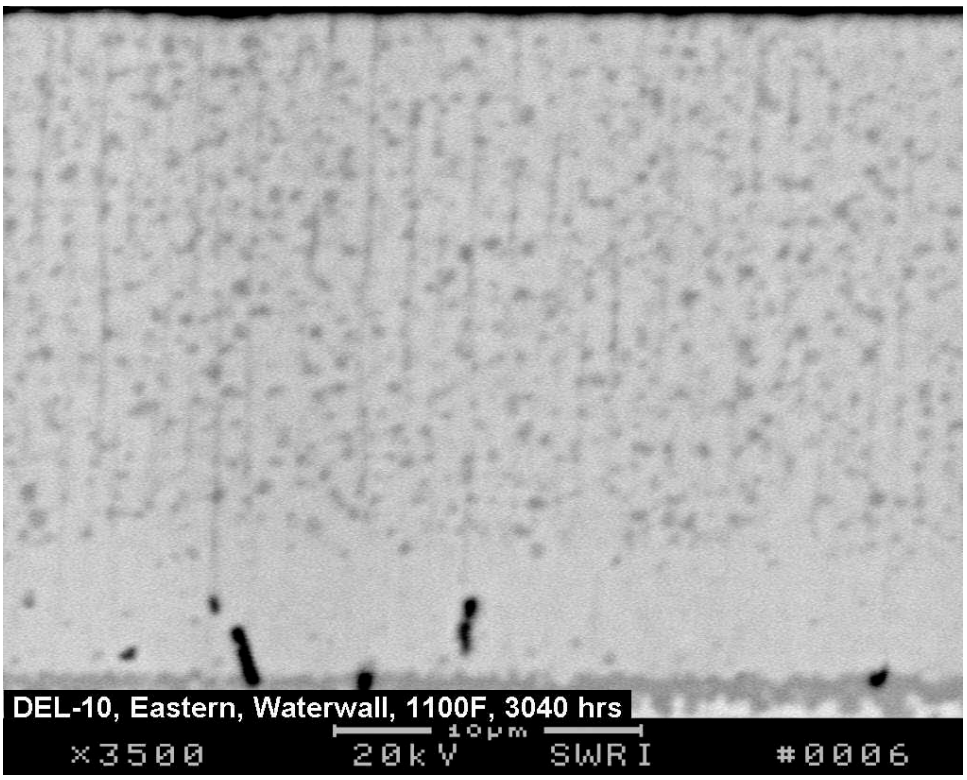

a) Ni-20Cr-Al

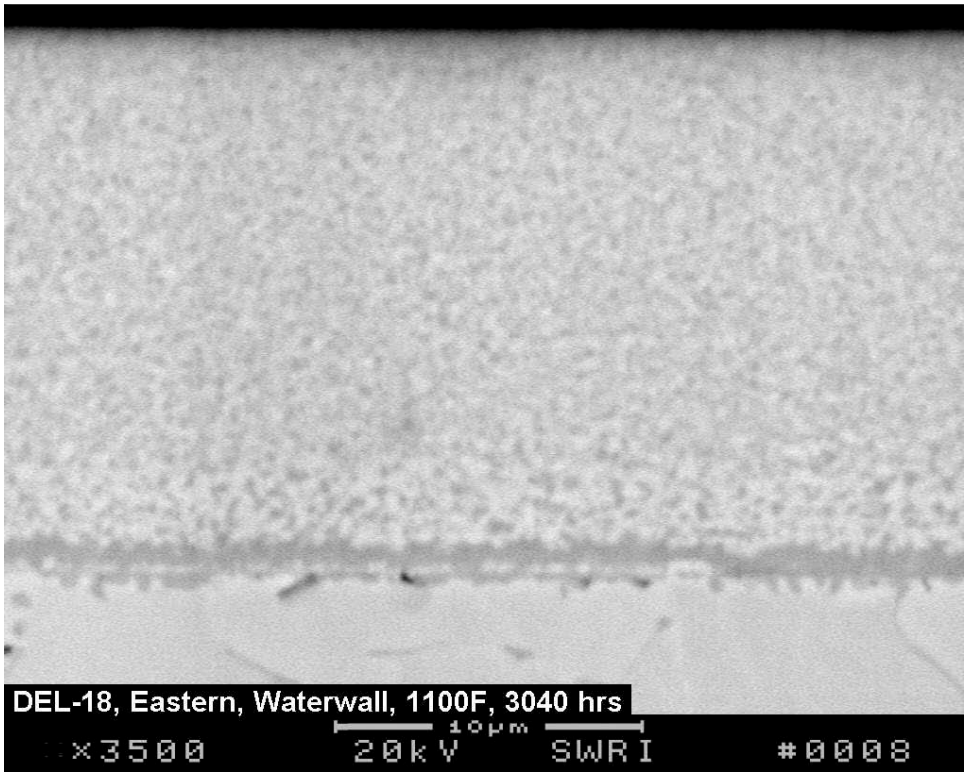

b) H160-Al

Figure 5-18
SEM micrographs of a) Ni-20Cr-Al and b) H160-Al cross sections showing the condition of the coating under the Eastern ash deposited area after 3040 hours exposure at 593° C.

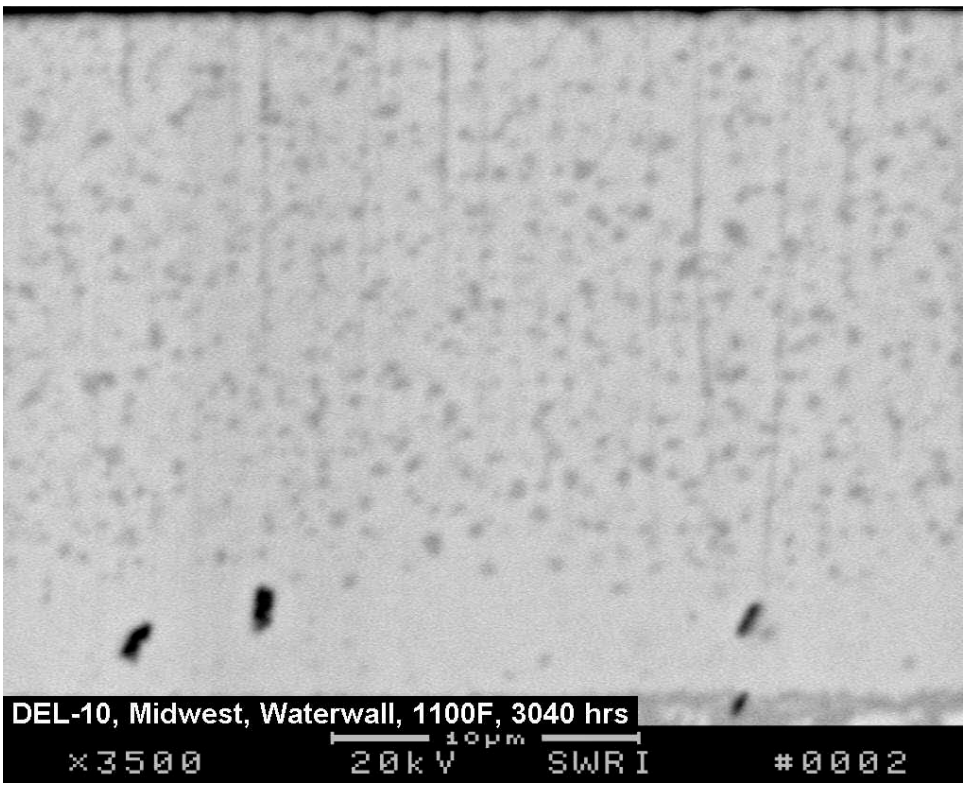

a)

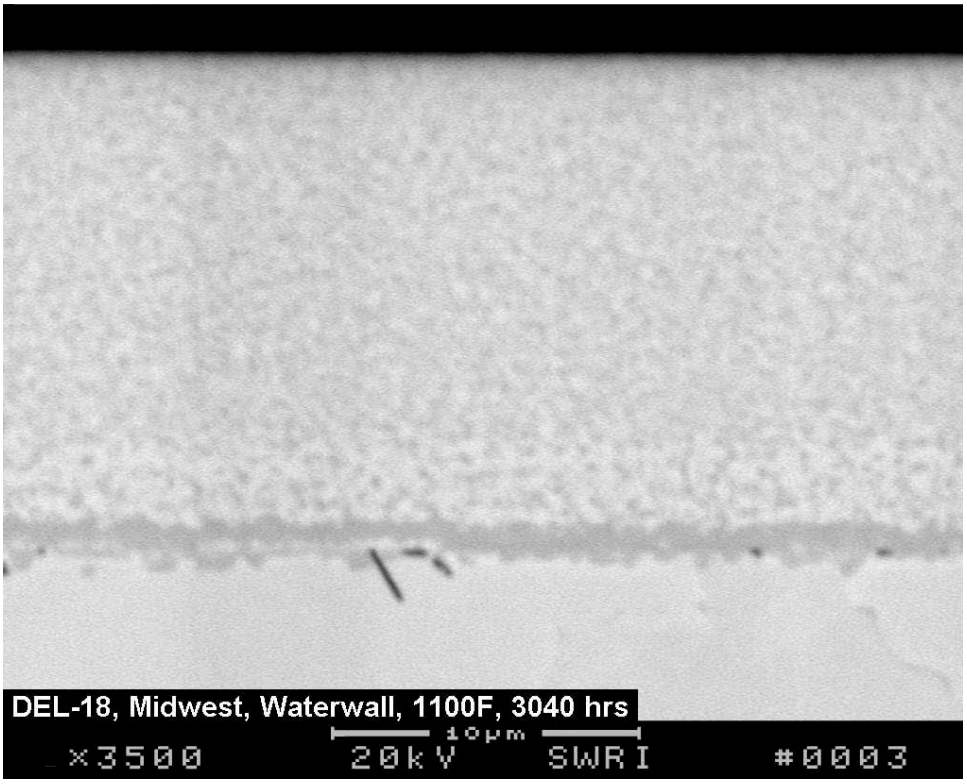

b)

Figure 5-19
SEM micrographs of a) Ni-20Cr-Al and b) H160-Al cross sections showing the condition of the coating under the Midwestern ash deposited area.

5.7 Corrosion Results After Exposure at 705º C

The uncoated sample surfaces after 2240 hours exposure at 705º **C** with Eastern and Midwestern ash (simulated super-heater) deposits were also covered with an approximately 25μm thick black scale. The extent of corrosion attack of the uncoated 304 SS samples under the Eastern and Midwestern ash deposits is shown in Figure 5-20. Comparison of the micrographs show that the extent of corrosion attack is more severe for the sample covered with Midwestern ash compared to the sample covered with the Eastern ash deposit. The presence of higher amounts of sodium and potassium sulfates in the Midwestern ash deposit presumably made it more corrosive compared to the Eastern deposit. SEM examination of the scale and elemental line scanning results indicated that the internal particles were chromium sulfide. Distribution of internal sulfide particles is shown in Figures 5-21 and 5-22. Comparison of these micrographs and those shown in Figure 5-16 reveal that the extent of sulfidation attack in the uncoated 304 SS sample increased with increasing exposure temperature from 593º C to 705º C However, the coated samples showed no evidence of corrosion and/or oxidation. Typical condition of the H120-Al and 310 SS-Al coatings after 2240 hours of exposure at 705º C with Eastern and Midwestern ash deposits are illustrated in Figures 5-23 and 5-24.

5.8 Corrosion Results After Exposure to 815º C

The extent of corrosion attack of uncoated Haynes 230 alloy samples, after 3040 hours exposure, under the Eastern and Midwestern ash deposits is shown in Figure 5-25. The thickness of the black scale was approximately 30 to 40μm not accounting for grain boundary penetration. The extent of oxidation attack on the side without ash deposit is shown in Figure 5-26. Comparisons of the micrographs show the presence of ash deposit resulted in severe corrosion attack. The extent of corrosion attack was more severe for the sample covered with Midwestern ash than those covered with the Eastern ash deposit. SEM examination of the scale and elemental line scanning results indicated that the internal particles were chromium and nickel sulfides. The morphology and distribution of sulfide particles are shown in Figure 5-27. The coated samples showed no evidence of corrosion and/or oxidation. Typical condition of the H120-Al and 310 SS-Al coatings after 3040 hours of exposure at 818ºC with Eastern and Midwestern ash deposits are illustrated in Figures 5-28 and 5-29.

In summary, fire-side corrosion test results in static air showed that the uncoated 304 SS and Haynes 230 alloys are susceptible to sulfidation in the presence of both ash deposits at elevated temperatures. The four nanocrystalline coatings (Ni-20Cr-10Al, H160-10Al, H120-10Al, and 310 SS-10Al) showed no sulfidation attack after long-term exposure, up to 3040 hours, at the three temperatures investigated, suggesting that these coatings have a great potential for providing long-term corrosion protection. The defects in the coatings did not provide pathways for corrosion species to diffuse to the coating/substrate interface. These results indicate that flowing flue gas is required for the columnar grain boundaries or defects in the coatings to act as pathways for corrosion species transportation.

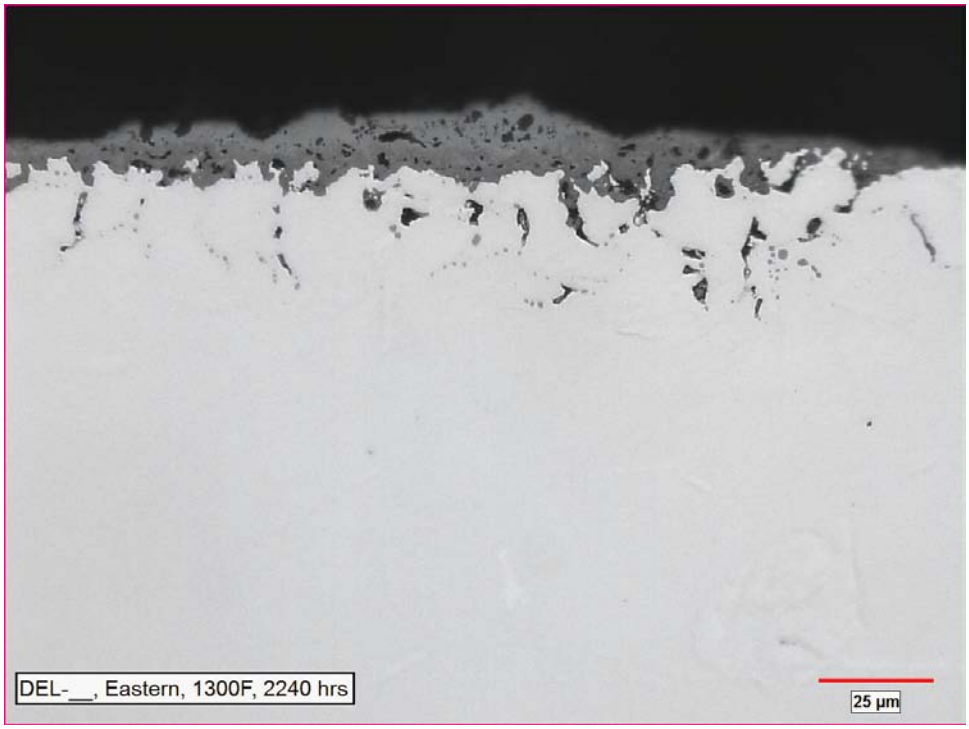

a)

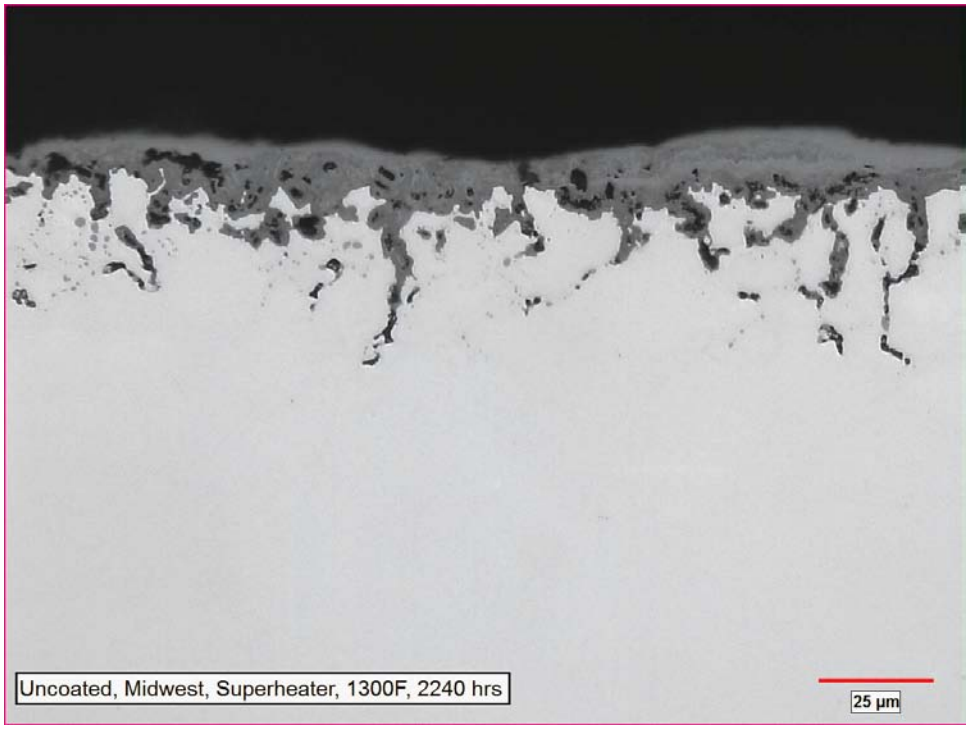

b)

Figure 5-20
Optical micrographs of the cross sections of uncoated 304 SS samples after exposure to 705º C for 2240 hours showing the corrosion attack under a) Eastern ash and b) Midwestern ash deposits.

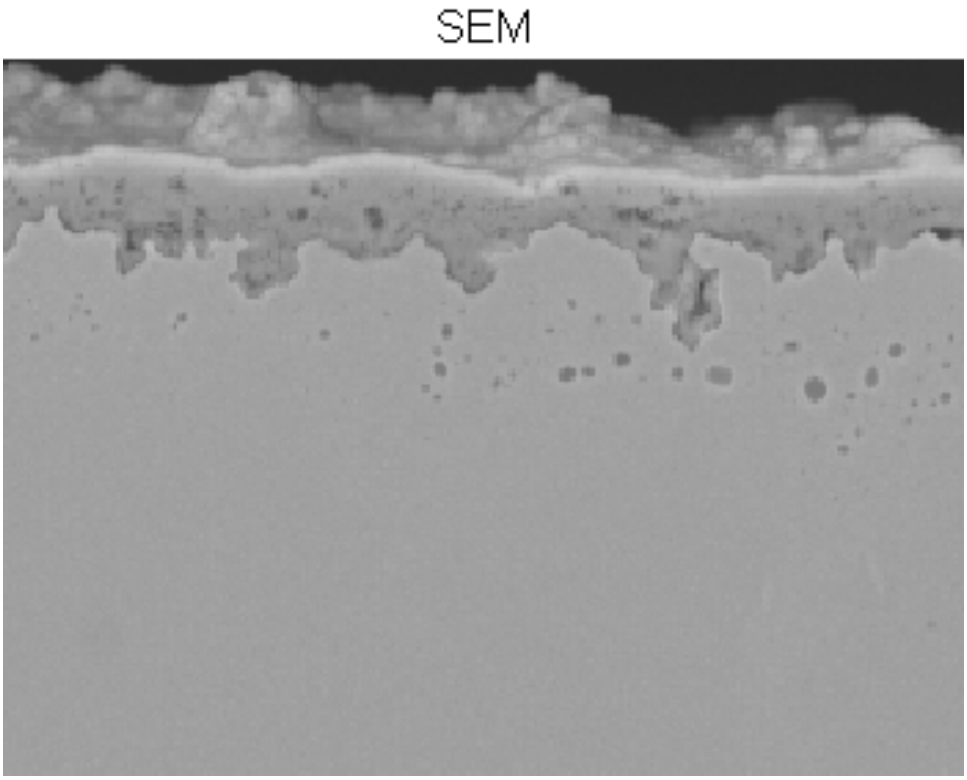

a)

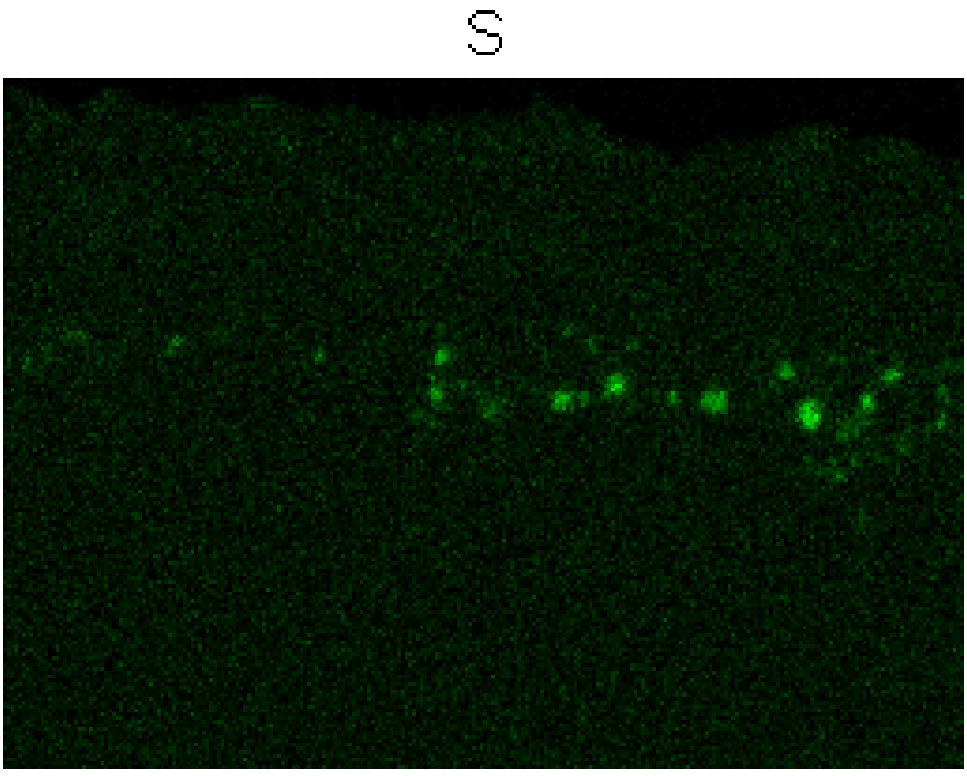

b)

Figure 5-21
a) SEM micrograph of the cross sections of the uncoated 304 SS sample after exposure to 704º C for 2240 hours along with b) the S map showing sulfide particles in the corrosion attacked area under the Eastern ash deposit.

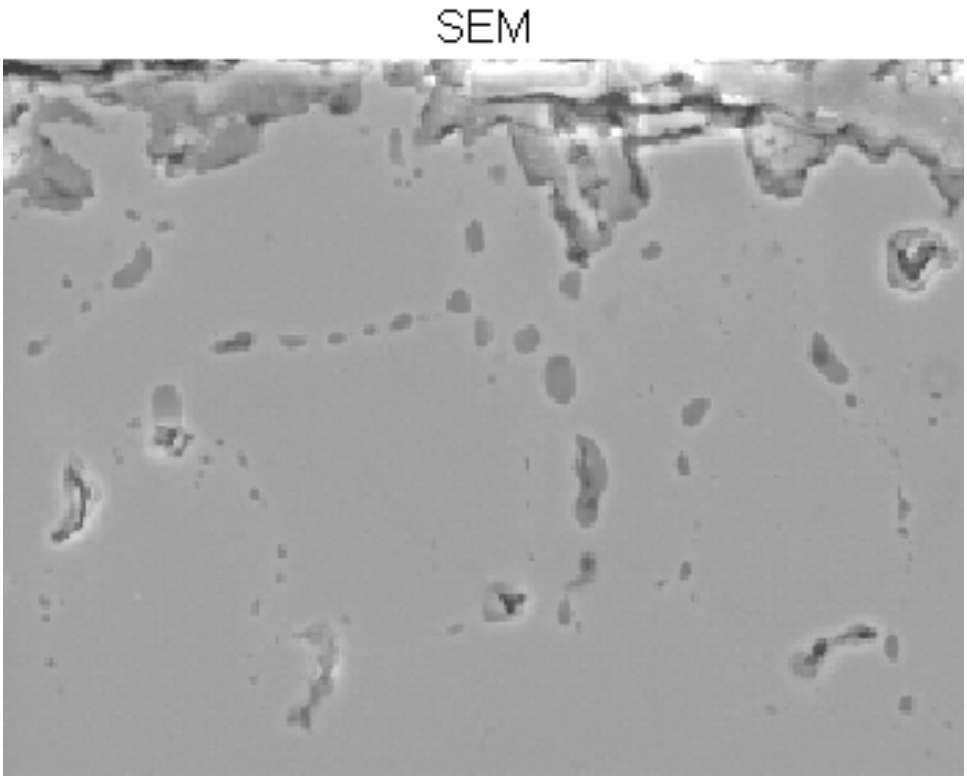

a)

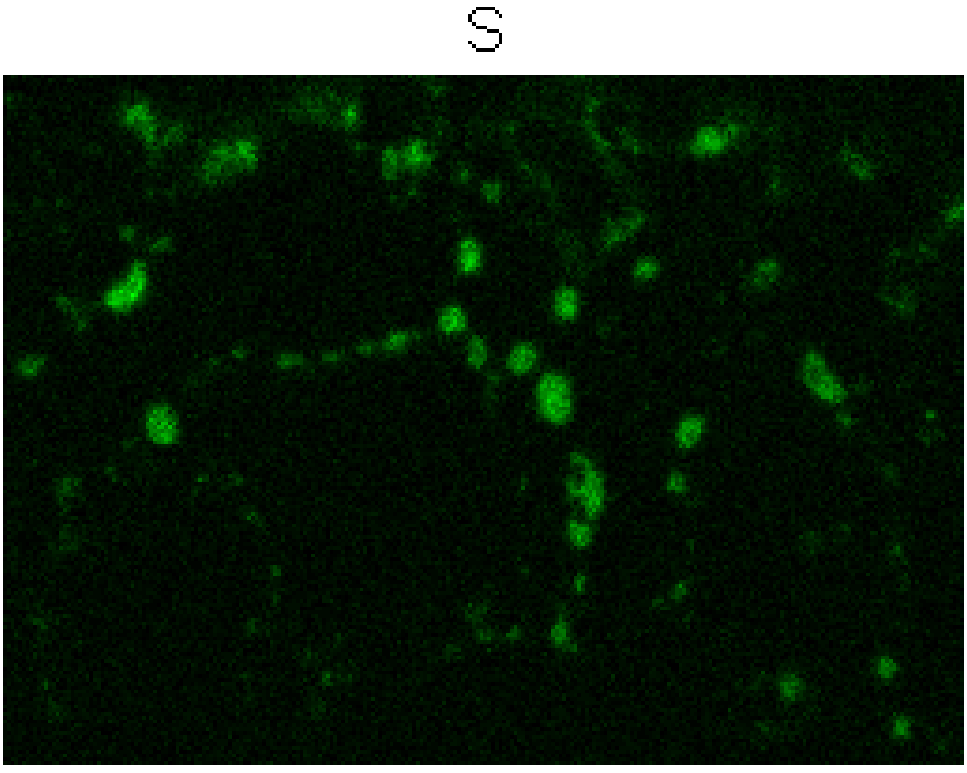

b)

Figure 5-22
a) SEM micrograph of the cross sections of the uncoated 304 SS samples after exposure to 704º C for 2240 hours along with b) the S map showing sulfide particles in the corrosion attacked area under the Midwestern ash deposit.

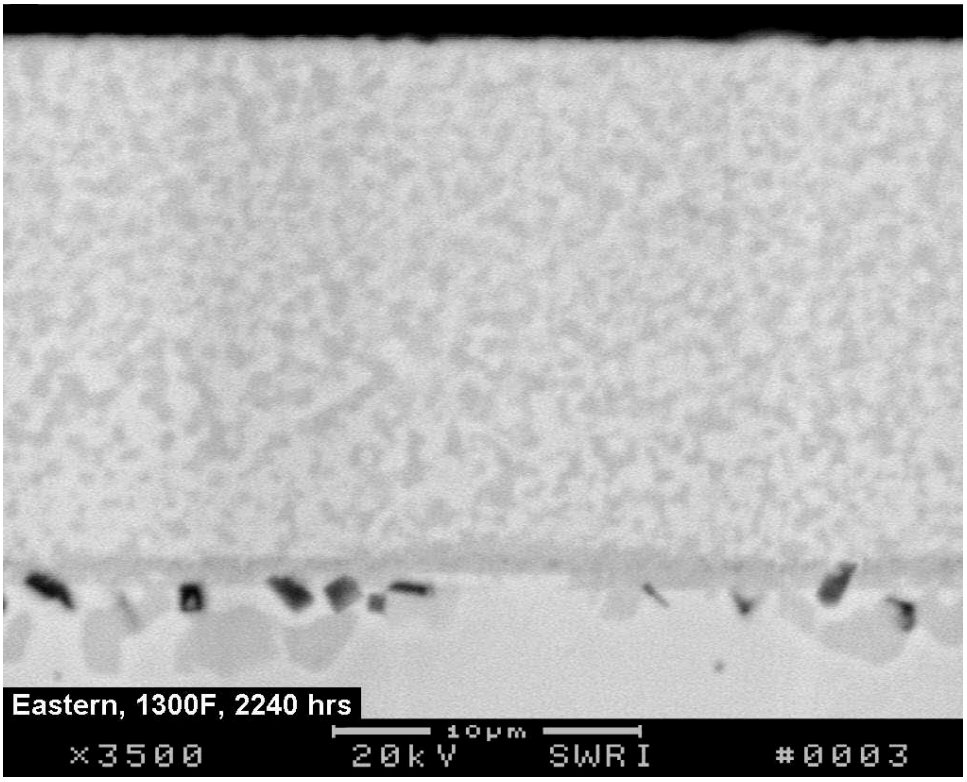

Figure 5-23
SEM micrograph of the cross section of the H160-Al coated 304 SS sample showing the absence of corrosion attack of the coating under the Eastern ash deposited area after exposure to 704° C for 2240 hours.

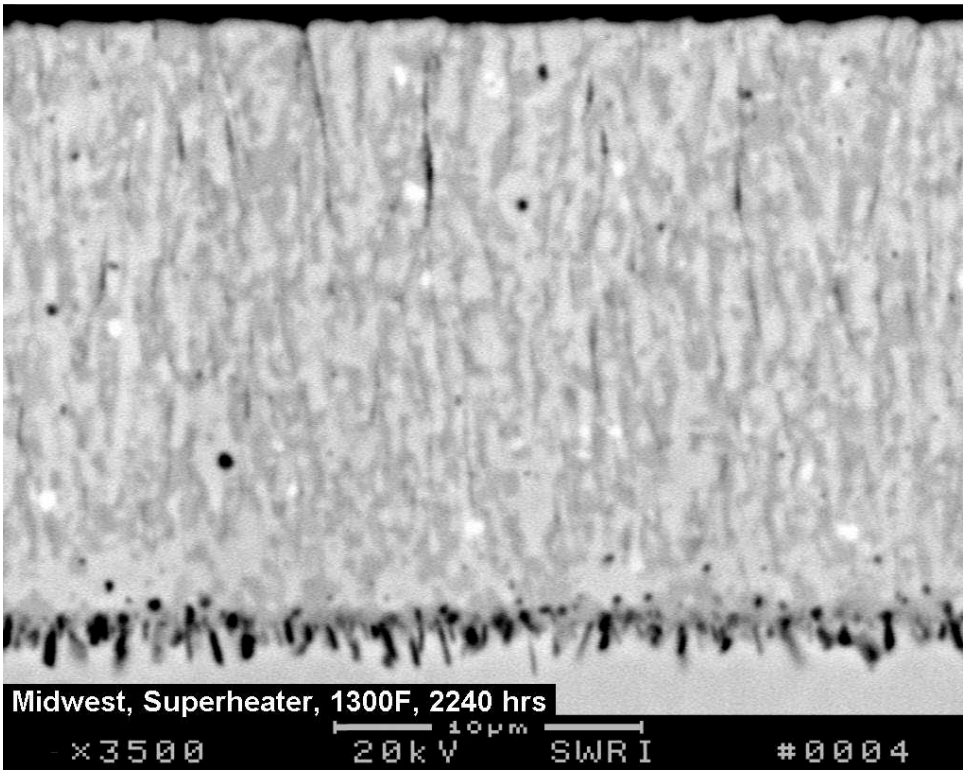

a)

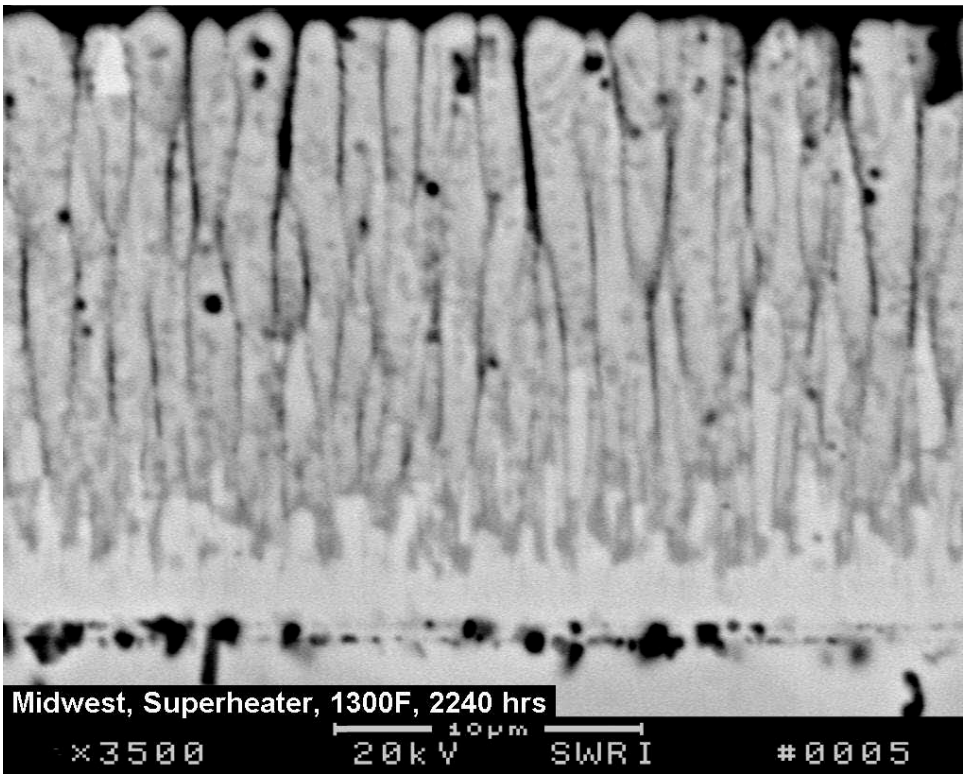

b)

Figure 5-24
SEM micrographs of the cross sections of: a) H120-Al and b) 310 SS-Al coated 304 SS samples showing the absence of corrosion attack of the coatings under the Eastern ash deposited area after exposure to 704° C for 224 hours.

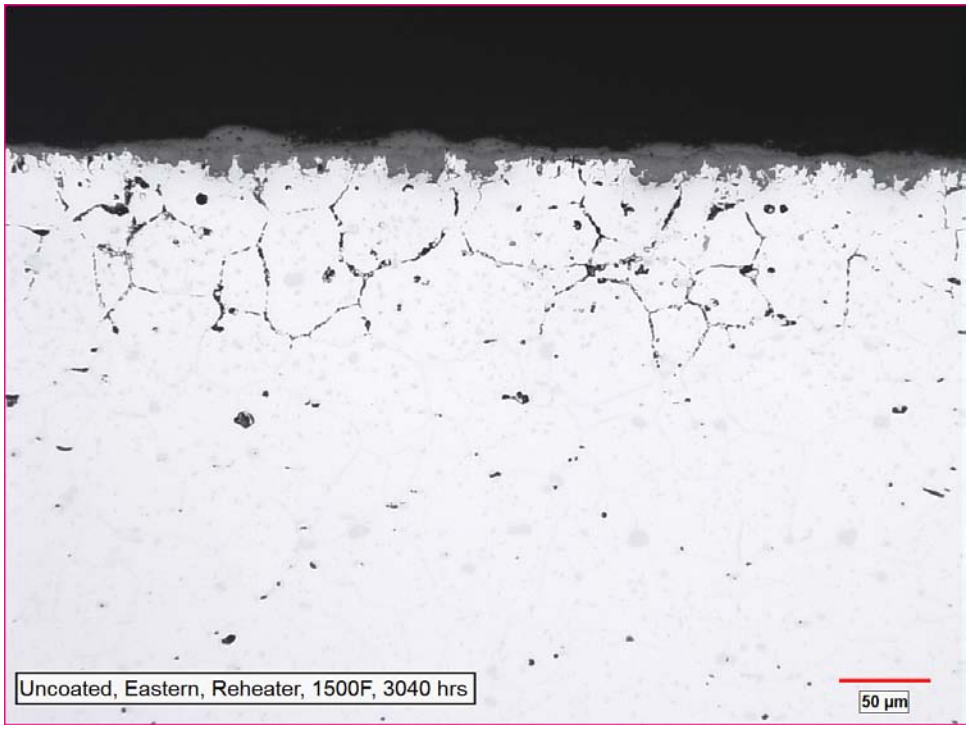

a)

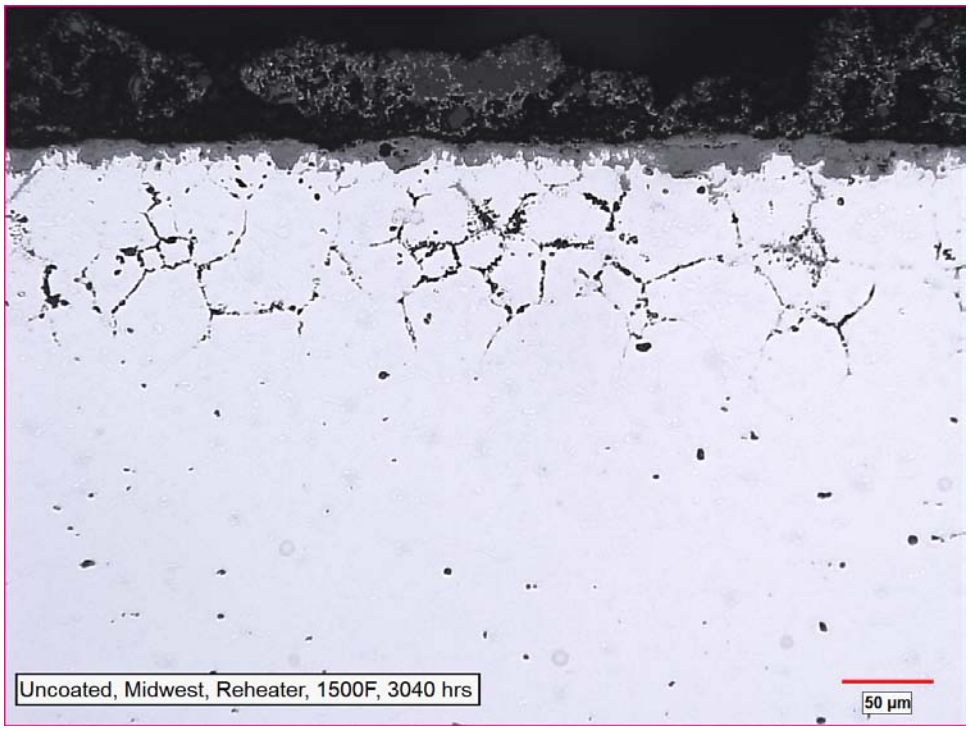

b)

Figure 5-25
Optical micrographs of the cross sections of the uncoated Haynes 230 samples after exposure to 815º C for 3040 hours showing the corrosion attack under a) Eastern ash and b) Midwestern ash deposits.

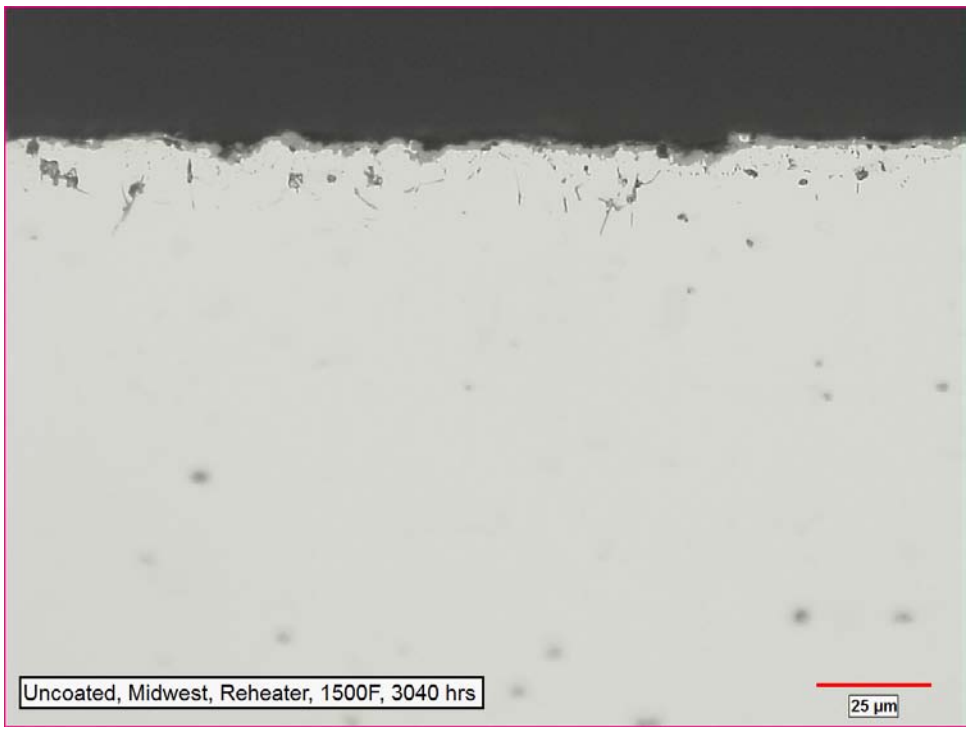

Figure 5-26
Optical micrograph of the cross section of the uncoated Haynes 230 sample after exposure to 815º C for 3040 hours showing the absence of oxidation attack on the side that was not covered with the ash deposit.

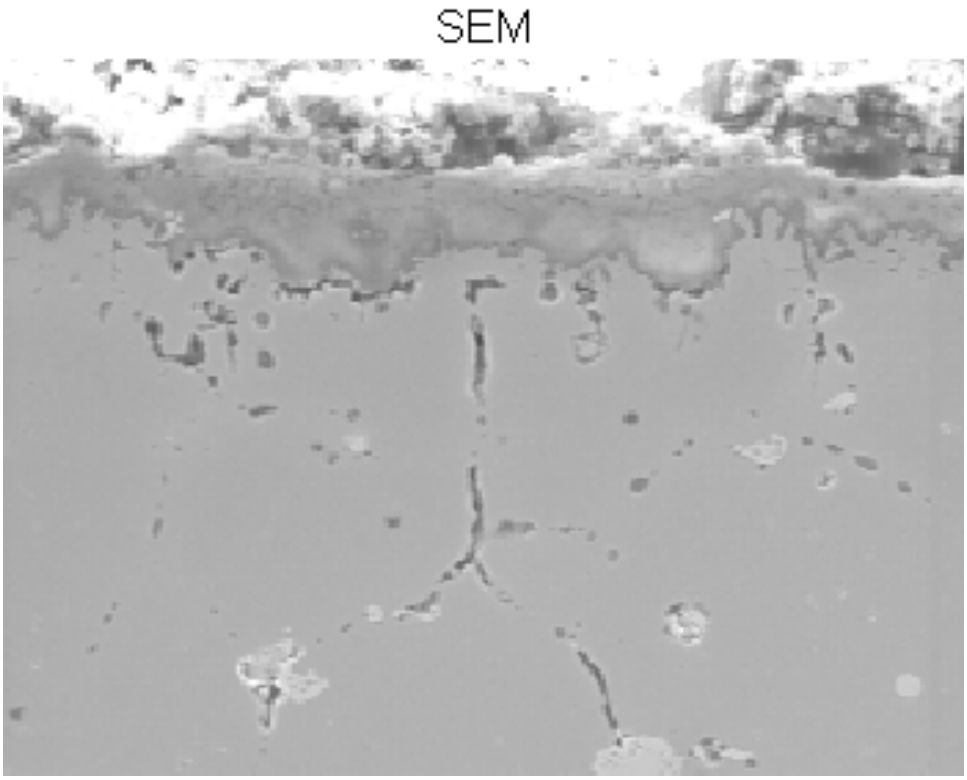

a)

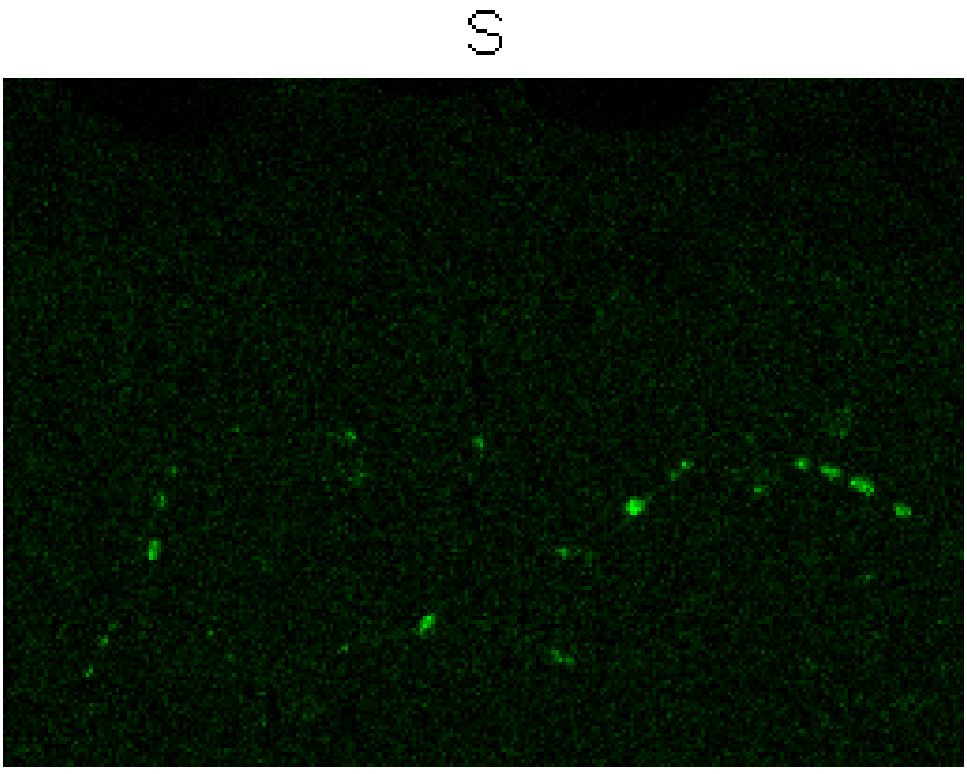

b)

Figure 5-27
a) SEM micrograph of the cross sections of the uncoated Haynes 230 samples after exposure to 815º C for 3040 hours along with b) the S map showing sulfide particles in the corrosion attacked area under the Midwestern ash deposit.

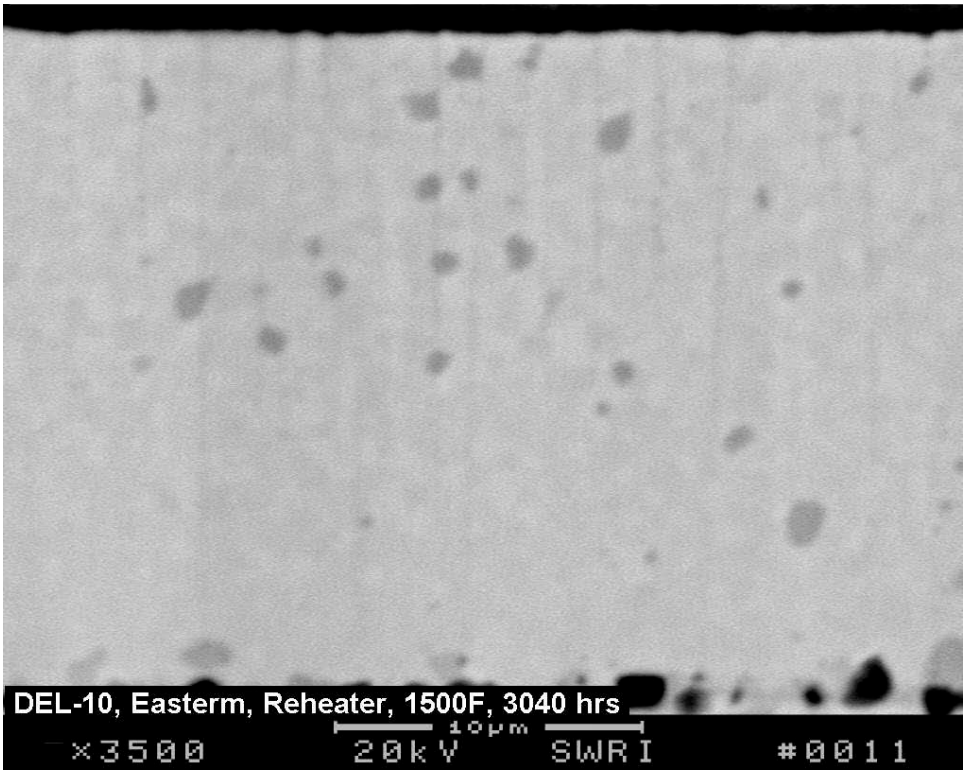

a)

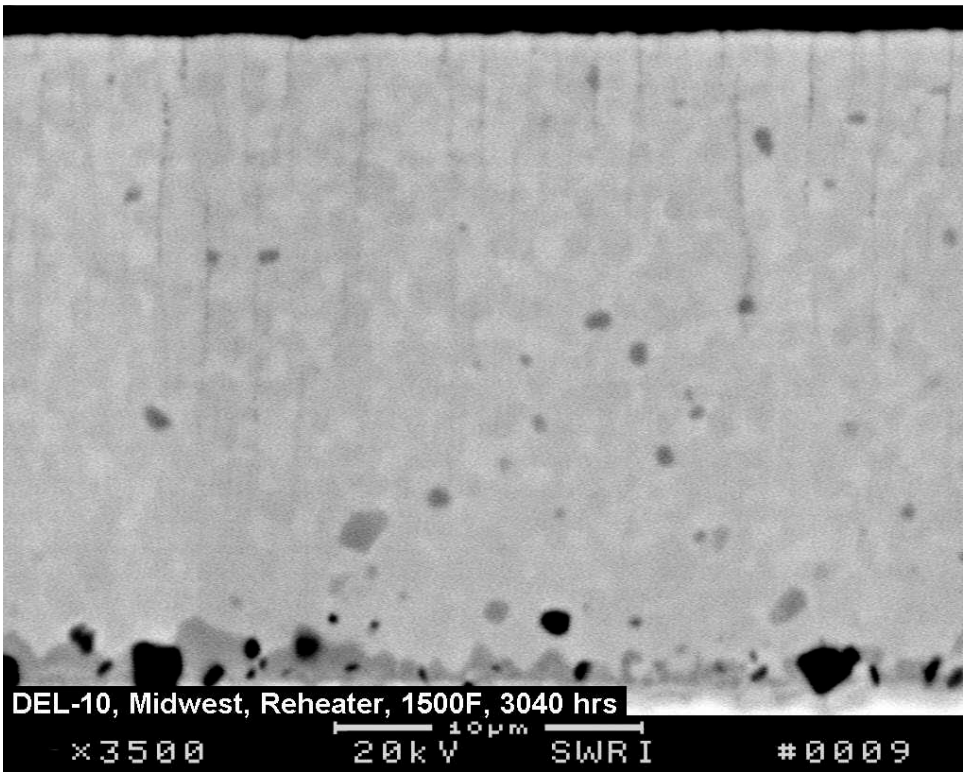

b)

Figure 5-28
SEM micrographs of the cross sections of a) H120-Al and b) 310 SS-Al coated Haynes 230 samples showing the absence of corrosion attack of the coatings under the Eastern ash deposited area after exposure to 815ºC for 3040 hours.

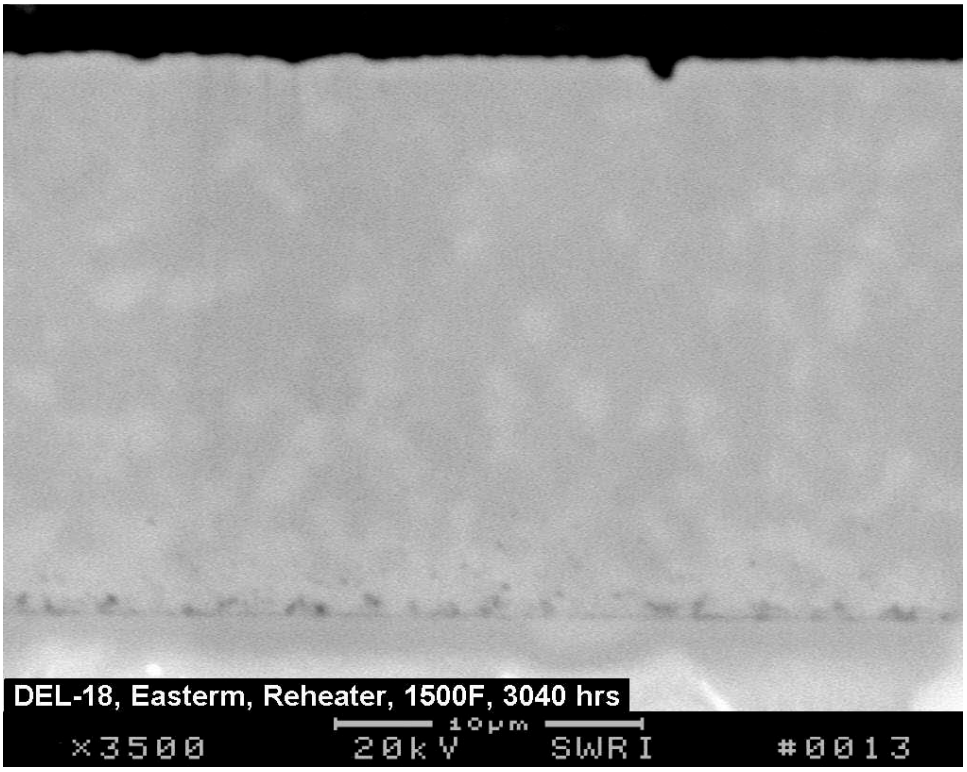

a)

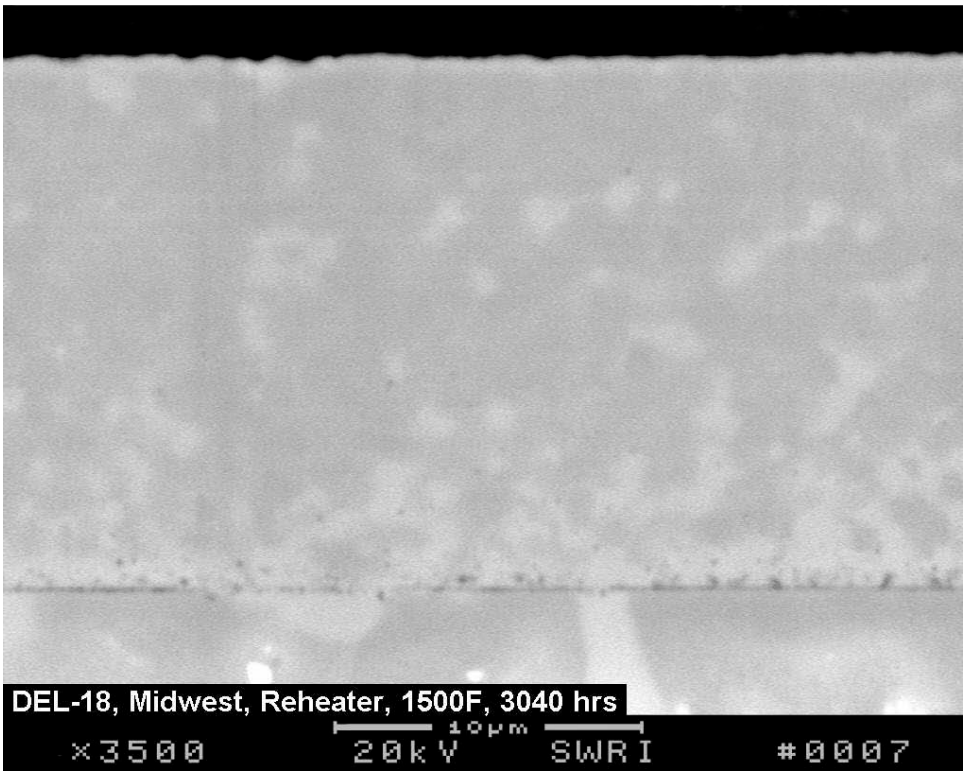

b)

Figure 5-29
SEM micrographs of the cross sections of a) H120-Al and b) 310 SS Al-coated Haynes 230 samples showing the absence of corrosion attack of the coatings under the Eastern ash deposited area after exposure to 815ºC for 3040 hours.

5.9 Fire-side Corrosion Testing with Simulated Flue Gas Flow

The nanocrystalline Haynes-10Al (NiCoCrAlSi) coating was applied on Haynes 230 samples utilizing a closed field unbalanced (pulsed DC) magnetron sputtering system at CSM (see Figure 4-30). The composition of the coating in the as-deposited condition is shown in Table 5-9 and the coating thickness was approximately 20 µm. Typical surface morphology of the coated sample is shown in Figure 5-30. The coating exhibited a dense structure with a few cauliflower-type defects in isolated areas. The coating substrate interface was clean, free from contamination and delamination.

Table 5-9
Semi-quantitative chemical composition of the as-deposited coatings, wt.%.

Coating	Al	Cr	Ni	Si	Ti	Co
	11.8	**27.9**	**balance**	**2.99**	**0.4**	**26.3**

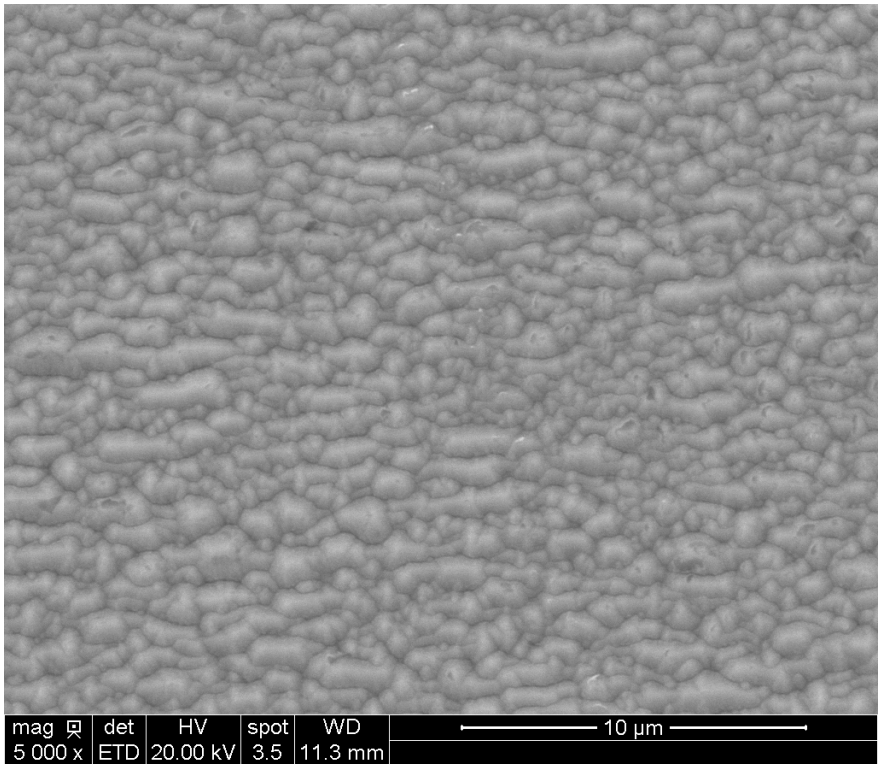

Figure 5-30
SEM micrograph showing the surface morphology of the coating on a Haynes 230-coated sample.

5.9.1 Synthetic Fuel Ash

The Eastern and Midwestern ash deposits were selected for the fire-side corrosion testing and the ash compositions are given in Table 5-8. The samples were subjected to simulated SH/RH conditions. The SH/RH tubes operate in the temperature range of 593º to 816º C. The highest operating temperature of 816º C was selected for 1000 hour corrosion testing.

The ash was prepared by thoroughly mixing the powders of different compounds in desired proportions by weight. A camphor-ethanol solution was used to prepare the desired ash paste. Camphor was added to the ethanol for improving the adhesion of the deposit on the test sample. The paste was applied only on one side of the coated samples.

5.9.2 Synthetic Flue Gas and Test Facility

For the SH/RH condition, the composition of the gas mixture selected for testing is presented in Table 5-10. The composition of the synthetic flue gas mixture is comparable to the gas used by FW for 1000 hours testing.

Table 5-10
Synthetic flue gas composition for 1000 hour corrosion test at 816º C.

Percentage	Gas Mixture Composition
70	N_2
15	CO_2
10	H_2O
0.25	SO_2

The tube furnace set up for corrosion testing is shown in Figure 5-31. The furnace contains a quartz tube and stainless steel end caps were fitted to the tube ends to allow the desired gas mixture to flow from one end to the other during testing. The gas inlet and outflow fittings, a vertical column flow indicator, and the tube pressure gauge *etc.* are also shown in Figure 5-31. Two separate gas lines were fitted into the tube furnace, one for the CO_2 and SO_2 mixture and the other for the humidified N_2. To add H_2O to the gas mixture, the N_2 gas passed through a temperature-controlled humidifying column prior to entering into the tube furnace. The humidity was monitored using an absolute humidity sensor at the N_2/H_2O flow outlet. The required levels of CO_2 and SO_2 gas mixture and N_2/H_2O were introduced through two separate lines into the tube furnace. The CO_2 and SO_2 gas mixture and humidified N_2 were blended in the tube furnace. The flow rates for the CO_2/SO_2 and humidified N_2 were maintained at 15 and 6.5 SCCM, respectively to achieve the desired gas composition.

a)

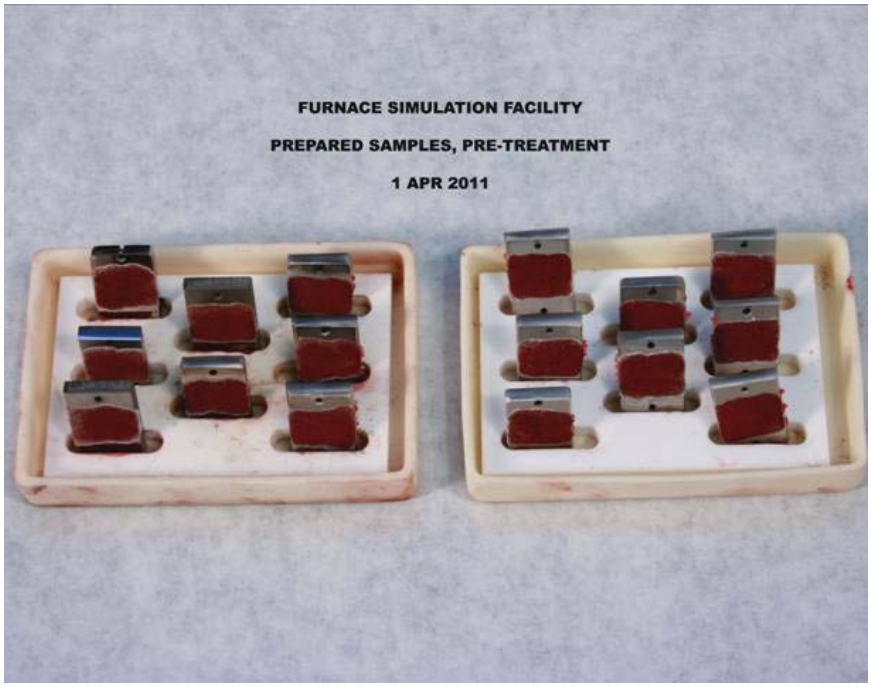

b)

Figure 5-31
Photographs of a) SwRI's Corrosion Test Facility and b) test samples with synthetic ash deposit.

5.9.3 Corrosion Testing

After application of synthetic ash paste, both uncoated and coated samples were placed vertically in an alumina racks as shown in Figure 5-31 (b) and then these racks were placed in the tube furnace. For each ash deposit condition, duplicate samples were tested. After each 100 hours of exposure, the samples were furnace cooled to room temperature, the specimens were cleaned to remove the exposed ash deposit, re-coated with fresh ash paste, and the samples were then re-inserted into the furnace for the next 100-hour cycle.

Two samples, one uncoated and one coated sample from each synthetic ash paste condition, were removed after 500 hours exposure for metallographic examination. The remaining samples were exposed to 1050 hours. Following exposure, the uncoated samples with Eastern and Midwestern ash deposits showed significant thickness loss due to metal wastage resulting from corrosion.

5.9.4 Post-Exposure Evaluation

Following thermal exposure, both uncoated and coated samples were cleaned to remove the ash deposit and examined using stereomicroscope for evidence of corrosion attack. After cleaning, the examination of the uncoated samples showed severe metal loss in the ash deposited area. The thickness measurements before and after exposure revealed that the samples with Eastern and Midwestern ash deposit lost 0.04 and 0.07 inches, respectively, after exposure. Corrosion attack was also noted around the holes of coated samples and the samples exposed to the Midwestern paste was more severely attacked as shown in Figure 5-32.

The coating on the sample under the Eastern ash deposit was in good condition and showed no evidence of localized coating spallation after 500 hours exposure. The sample after 1050 hours exposure, however, revealed coating spallation and evidence of corrosion attack of the substrate in isolated areas after 1050 hours of exposure. On the other hand, the sample with the Midwestern ash deposit showed evidence of coating loss and localized corrosion attack in isolated areas after 500 hours exposure. In contrast, no coating loss was observed on the sample that was exposed to 1050 hours and the coating showed no evidence of corrosion. These results indicate that the coating spallation is responsible for the localized corrosion attack. Minor variation in the coating quality among the samples is presumably resulted in localized coating spallation in two of four samples.

A transverse section was removed from all of the uncoated and coated samples and metallurgical mounts were prepared from these sections using standard metallographic techniques. The mounts were examined using optical microscope and SEM to determine the depth of penetration of corrosion attack, characterization of scale and internal sulfidation.

a)

b)

Figure 5-32
Photographs of coated samples after 500 hours exposure to synthetic flue gases at 816° C a) sample with Eastern ash deposit and b) sample with Midwestern ash deposit.

5.9.5 Corrosion Results

Figure 5-33 illustrates the cross section of the uncoated sample with the Eastern ash deposit after 500 and 1050 hours exposure to synthetic flue gas mixture at 816º C. The cross section of the sample showed approximately 2.0 to 3.0 µm thick corrosion/oxide scale in isolated areas on the sample after 500 hours exposure. A continuous scale, approximately 25 to 40 µm thick, was noted on the sample after 1050 hours exposure. The corrosion/oxidation attack had penetrated approximately 20 µm and 60 µm after 500 and 1050 hours exposure, respectively. The EDS analysis showed that corrosion scale on the samples was predominantly oxide. The particles below the oxide scale contained both oxygen and sulfur. A typical EDS spectra obtained from a particle below the oxide scale is presented in Figure 5-34. Figures 5-34 (a) and 5-35 show the distribution of sulfide particles.

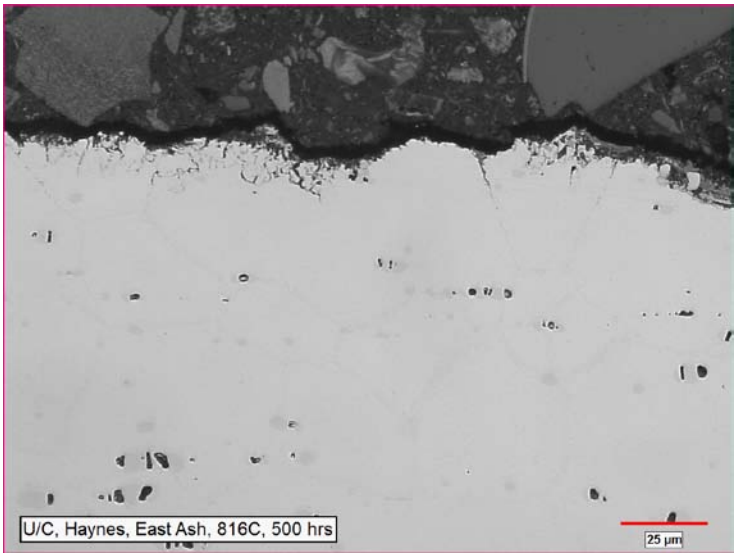

a)

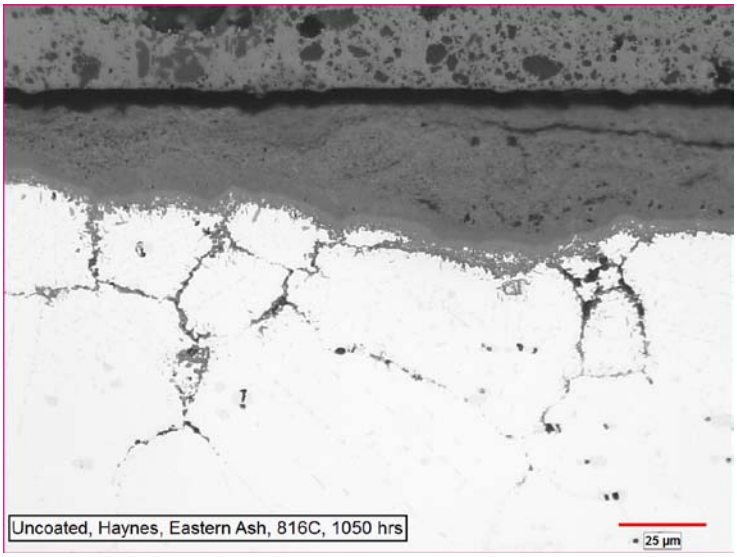

b)

Figure 5-33
Optical micrographs of the cross section of uncoated Haynes 230 sample after exposure to 816º C a) for 500 hours and b) 1050 hours showing the extent of corrosion attack under the Eastern ash deposited area.

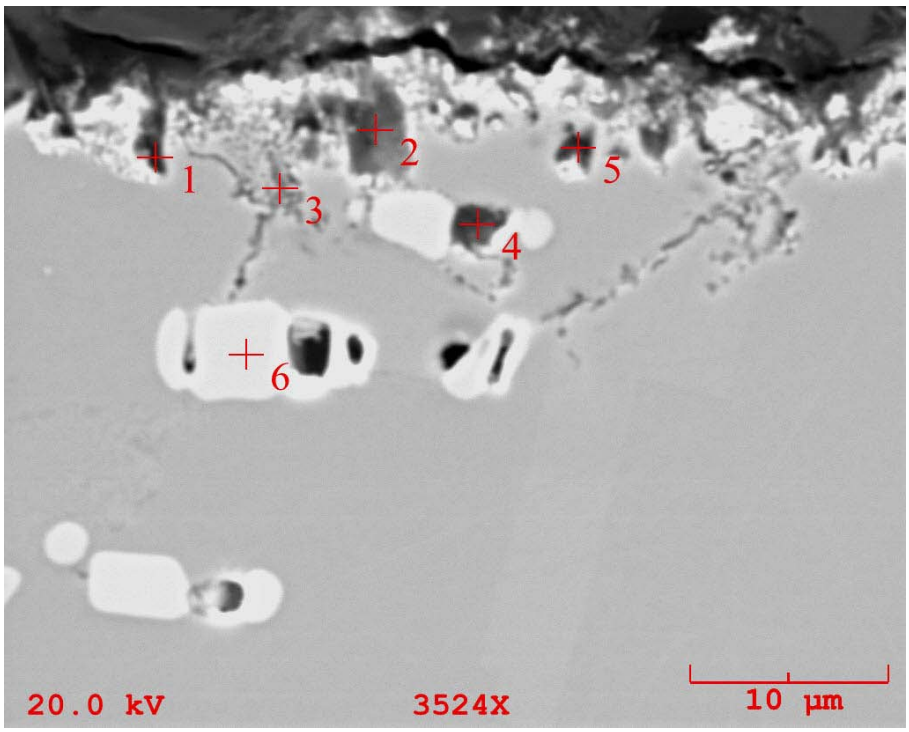

a)

Element	Concentration (wt.%)
O	5.39
Al	1.92
S	4.81
Cr	12.58
Fe	1.09
Ni	30.14
Mo	10.53
W	33.54
TOTAL	**100.00**

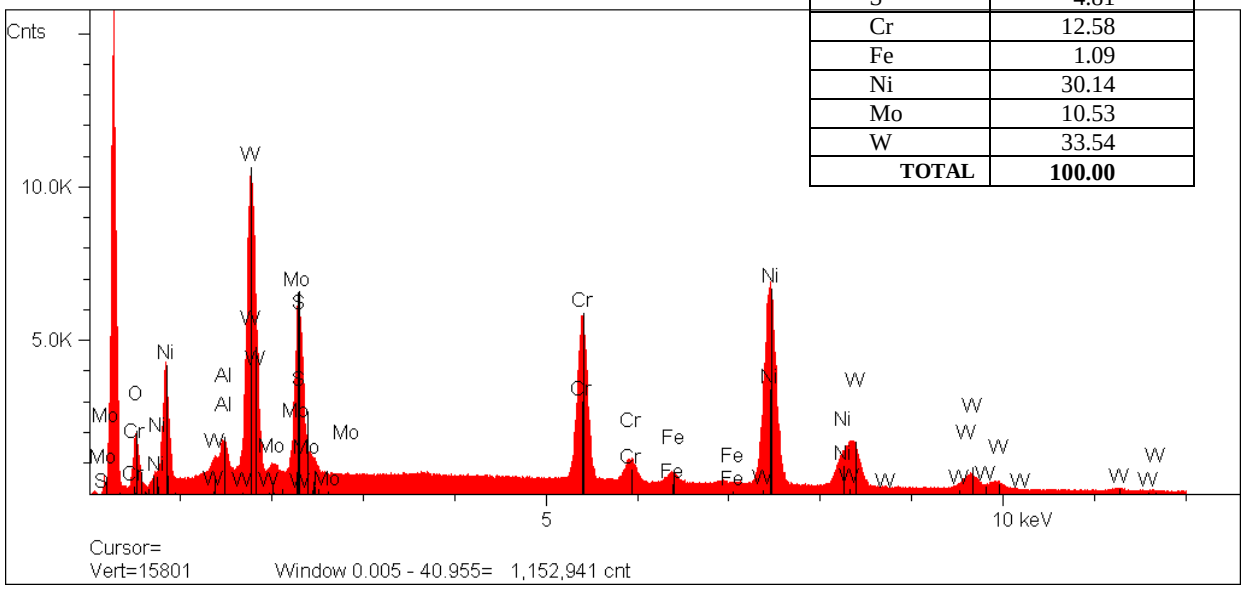

b)

Figure 5-34
SEM micrographs of the cross section of the uncoated Haynes 230 sample after exposure to 816º C for 500 hours showing the extent of corrosion attack penetration under the Eastern ash deposited area. The + on the SEM image a) denote oxide/sulfide particles analyzed by EDS, b) EDS spectrum obtained from Particle 2 shown on the SEM image (a).

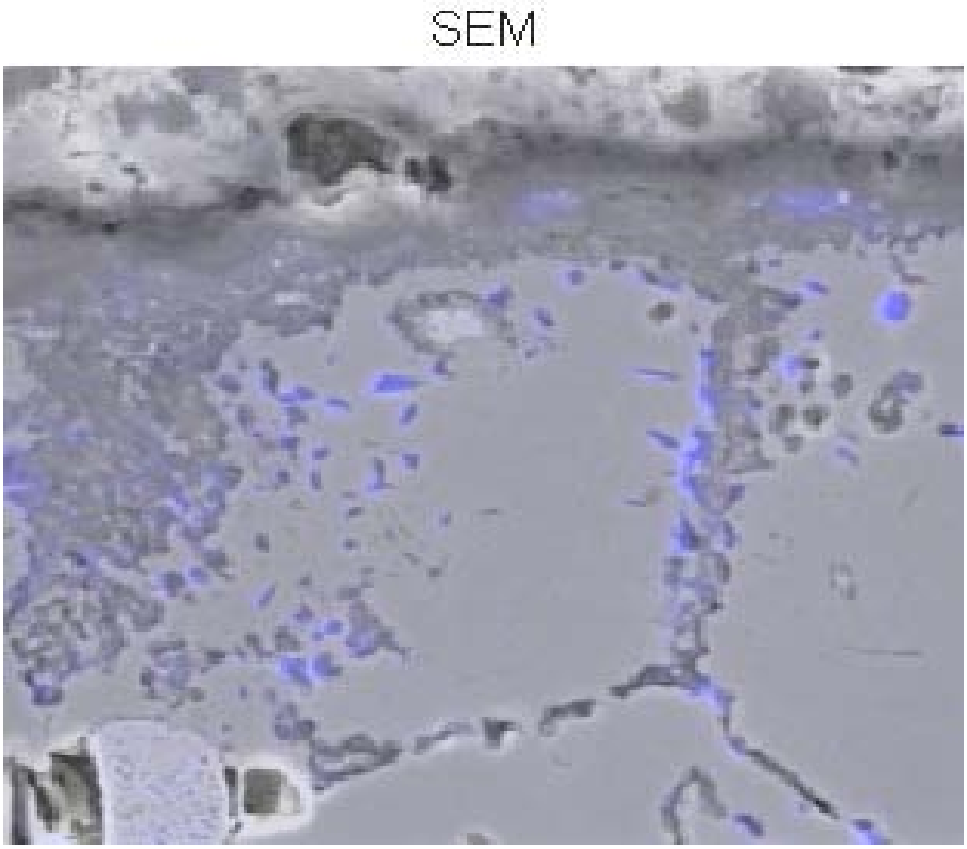

Figure 5-35
SEM micrograph of the cross section of the uncoated Haynes 230 sample after exposure to 816º C for 1050 hours showing the extent of corrosion attack penetration under the Eastern ash deposited area. The sulfur scan is superimposed to show the sulfide (blue) particles

Figures 5-36 and 5-37 show the morphology of corrosion attack of the uncoated samples under the Midwestern ash deposited area. The corrosion attack had penetrated about 100 µm after 1050 hours. Fine sulfide particles were seen within the grains and on the grain boundaries in the corrosion affected area as illustrated in 5-36 (b). The EDS analysis of the particles in the corrosion-affected area in Figure 5-36 (b) showed Cr, Ni, W, and S peaks, as shown in Figure 5-38 and the particles were confirmed to be sulfide particles, resulting from internal sulfidation.

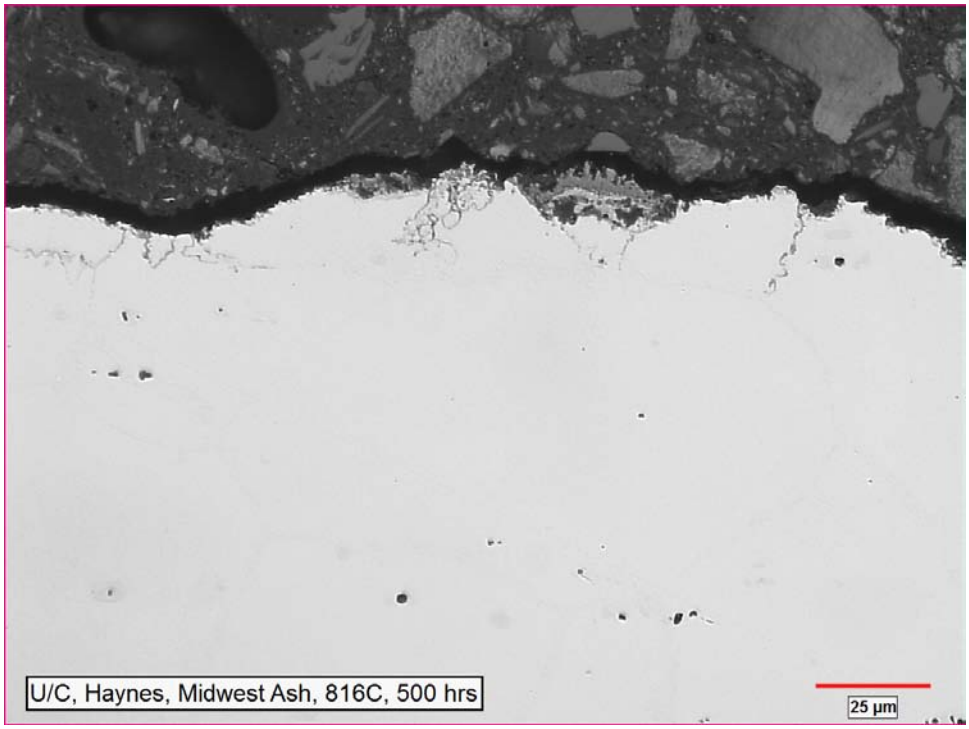

a)

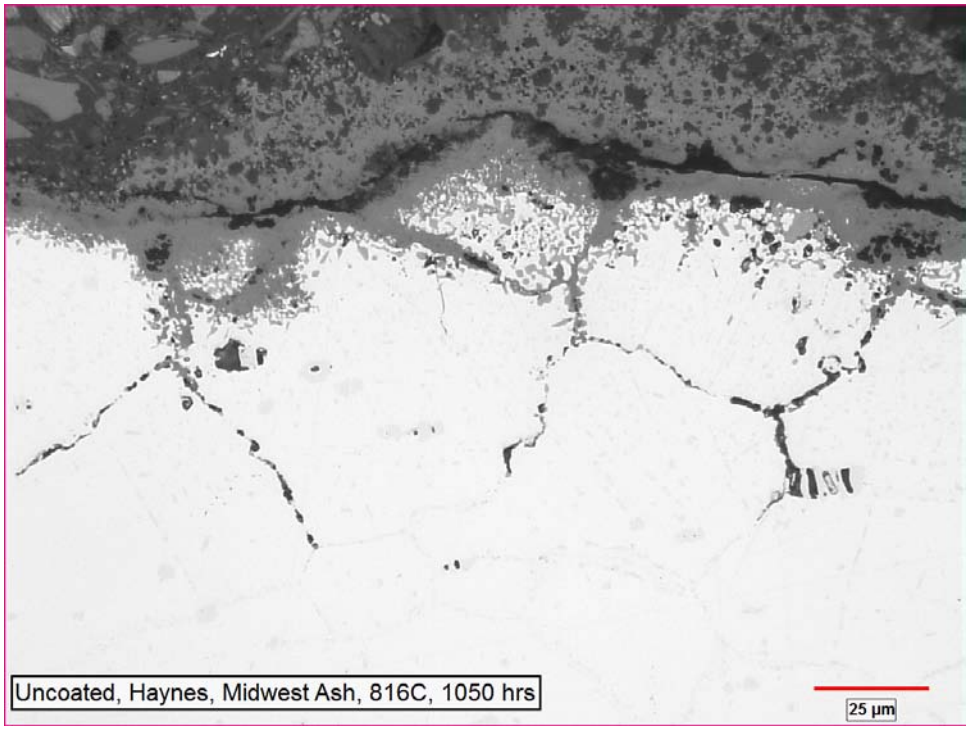

b)

Figure 5-36
Optical micrographs of the cross section of the uncoated Haynes 230 sample after exposure to 816º C for a) 500 hours and b) 1050 hours showing the corrosion attack under the Midwestern ash deposited area.

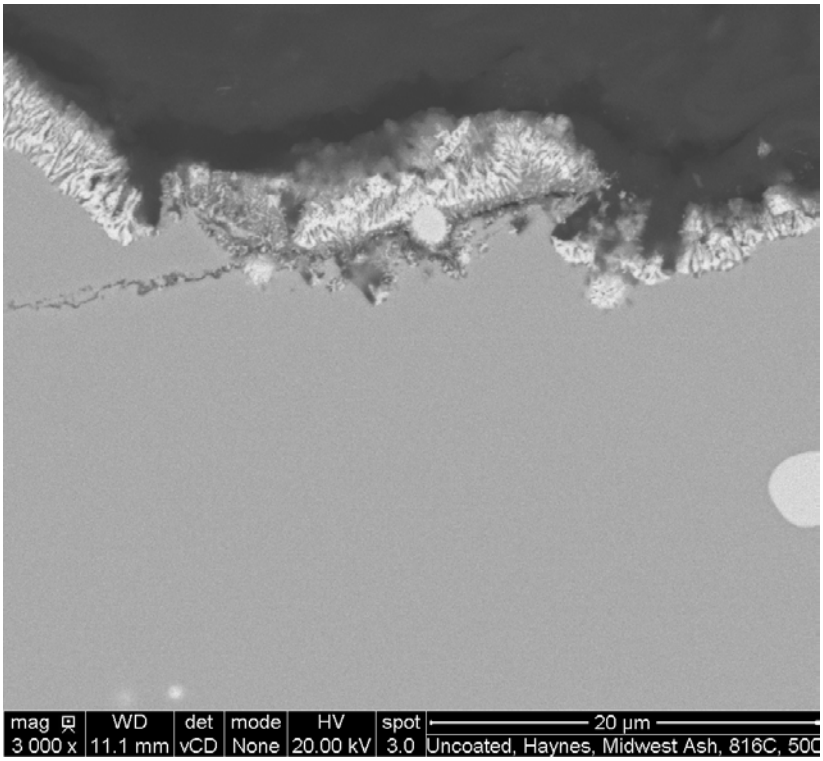

a)

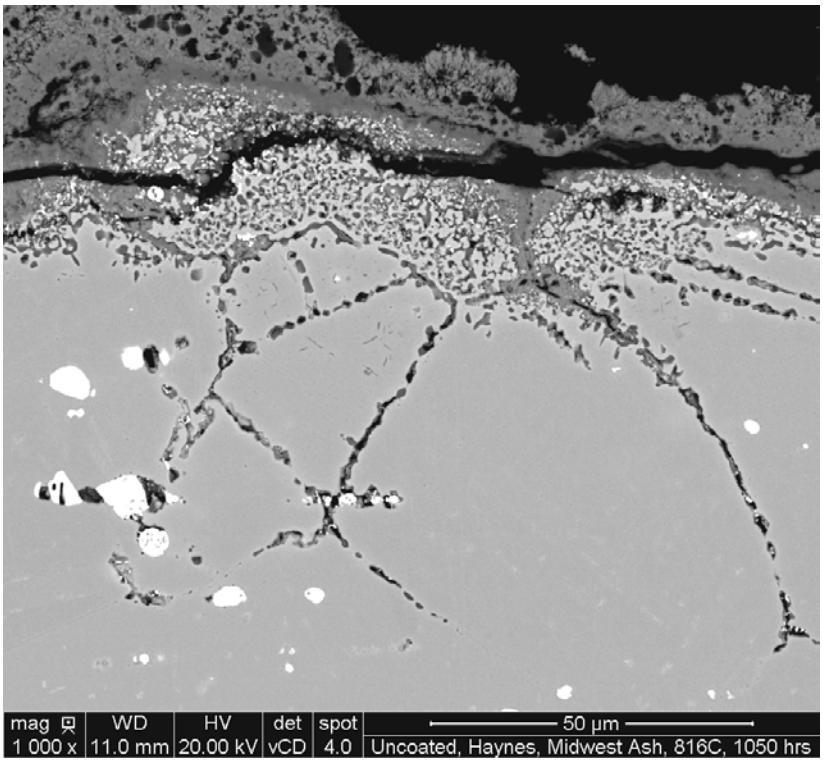

b)

Figure 5-37
SEM backscattered image of the cross section of the uncoated Haynes 230 sample with Midwestern ash deposit after exposure to synthetic flue gases at 816º C for a) 500 hours and b) 1050 hours showing the morphology of corrosion attack under the Midwestern ash deposited area. Note the extent of internal sulfidation.

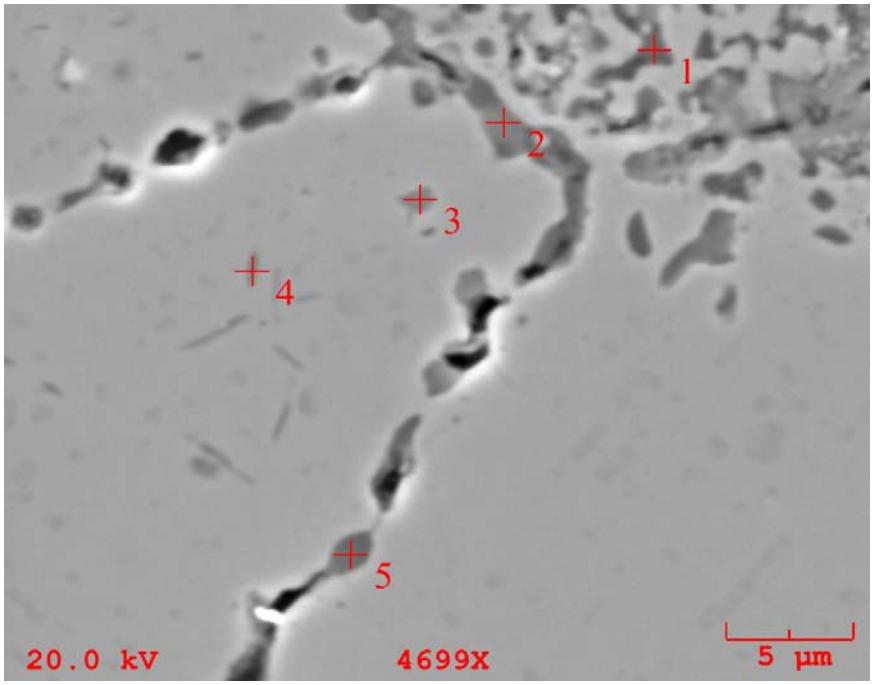

a)

Elt.	Line	Intensity (c/s)	Error 2-sig	Atomic %	Conc	Units	
O	Ka	99.94	1.912	12.14	4.32	wt.%	
Al	Ka	30.63	1.941	0.82	0.49	wt.%	
S	Ka	2,192.95	7.902	30.33	21.62	wt.%	
Cr	Ka	2,625.33	8.640	33.24	38.44	wt.%	
Fe	Ka	29.78	2.150	0.49	0.61	wt.%	
Ni	Ka	1,008.21	5.489	21.35	27.87	wt.%	
W	La	66.08	2.088	1.63	6.65	wt.%	
				100.00	**100.00**	**wt.%**	**Total**

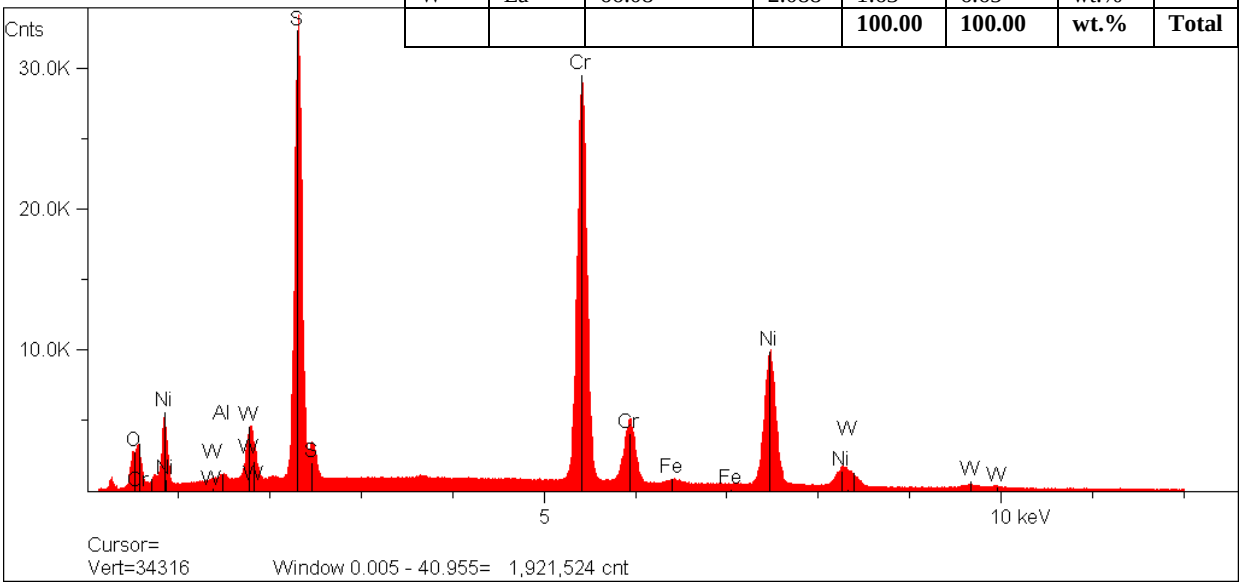

b)

Figure 5-38
SEM micrographs of the cross section of the uncoated Haynes 230 sample after exposure to 816º C for 1050 hours showing the extent of corrosion attack penetration under the Western ash deposited area. The + on the SEM image a) denote oxide/sulfide particles analyzed by EDS, b) EDS spectrum obtained from Particle 1 showing major peaks of Cr, Ni, S, *etc*.

The coated sample with the Eastern ash deposit after 500 hours exposure showed no evidence of corrosion and/or oxidation, as shown in Figure 5-39. After 1050 hours of exposure, the coating was also in excellent condition in most of the areas examined, as illustrated in Figure 5-40. However, in isolated areas where the coating was prematurely spalled, showed evidence of base metal sulfidation and oxidation. Typical corrosion and oxidation attack of the base metal in a coating spalled area is shown in Figure 5-41. Figure 4-42 shows distribution of sulfide particles. Comparison of Figures 5-33 (b), 5-35, 5-41, and 5-42 reveals that the morphology of the corrosion attack in the coating spalled area and in the uncoated sample is comparable.

The coating after 500 and 1000 hours exposure, (Figures 5-38 and 5-39 (b)), exhibited duplex structure consisting of a Cr-rich phase in a matrix of γ-phase (MCr solid solution). An analysis of the overall coating by EDS showed 9.94 wt.% Al in the coating, suggesting that the coating has not degraded as a result of 1050 hours exposure at 816º C.

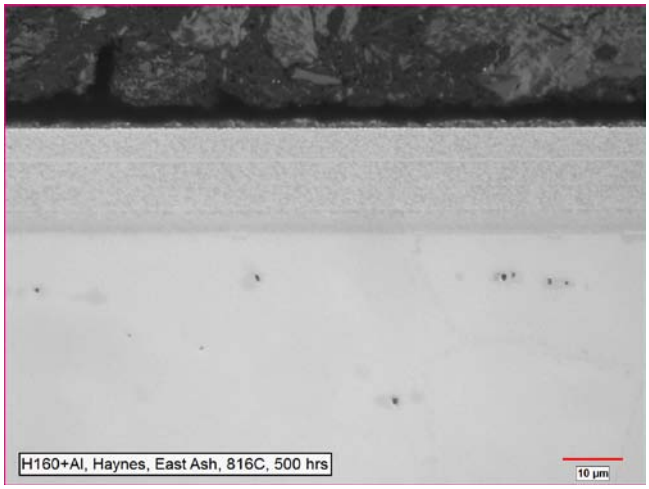

a)

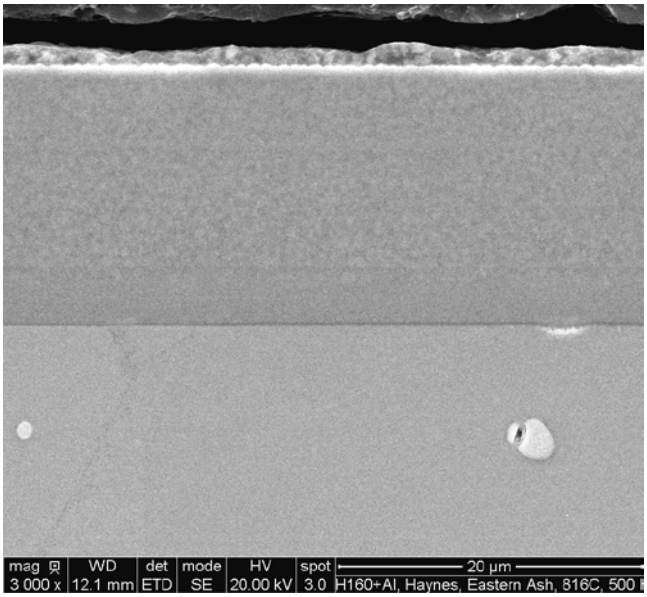

b)

Figure 5-39
The cross section of the coated sample after exposure to synthetic flue gas mixture at 816º C for 500 hours showing the condition of the coating under the Eastern ash deposited area a) optical micrograph and b) SEM micrograph.

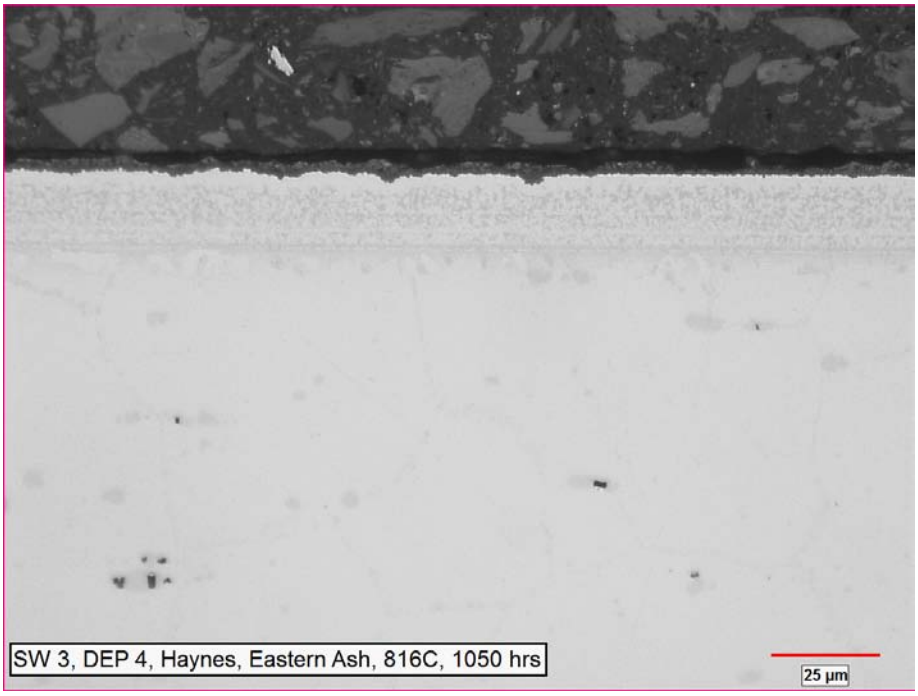

a)

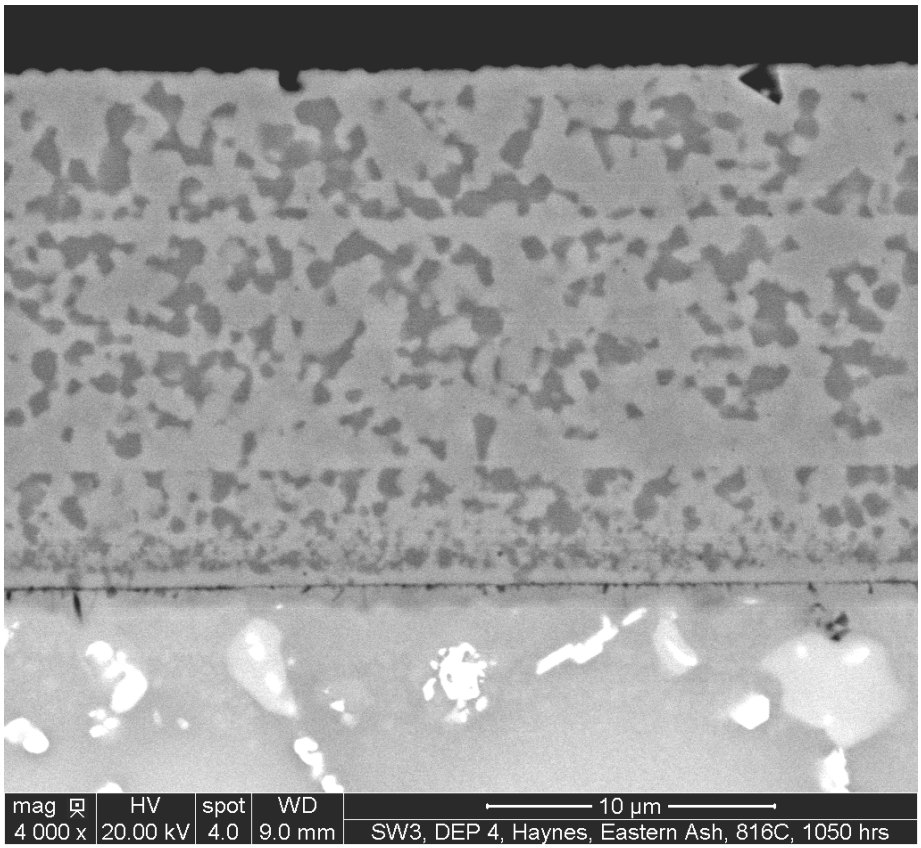

b)

Figure 5-40
The cross section of the coated sample after exposure to synthetic flue gas mixture at 816º C for 1050 hours showing the condition of the coating under the Eastern ash deposited area a) optical micrograph and b) SEM micrograph.

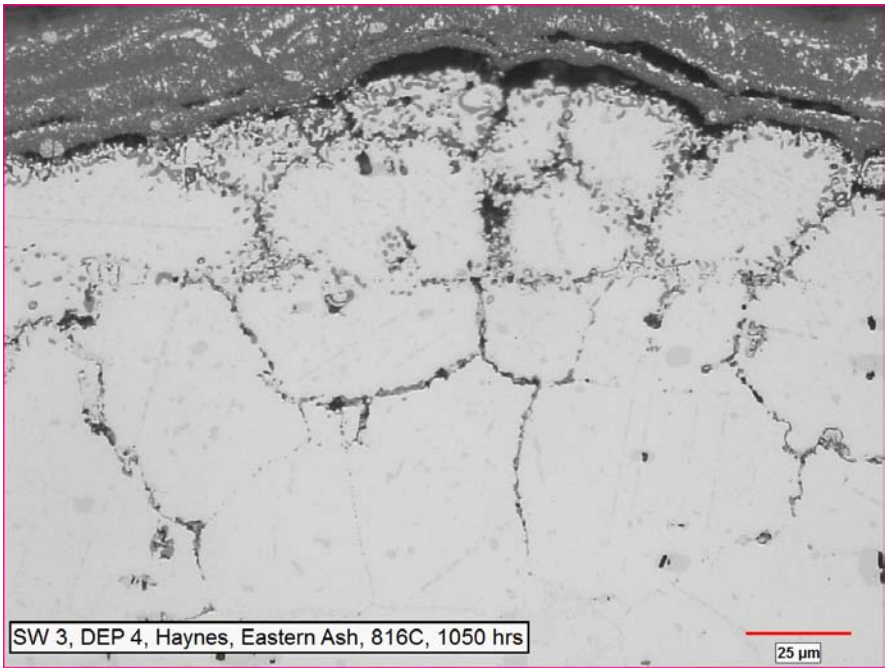

Figure 5-41
Optical micrograph of the cross section of the coated Haynes 230 sample with Eastern ash deposit after exposure to synthetic flue gases at 816º C for 1050 hours showing the morphology of corrosion attack of the substrate.

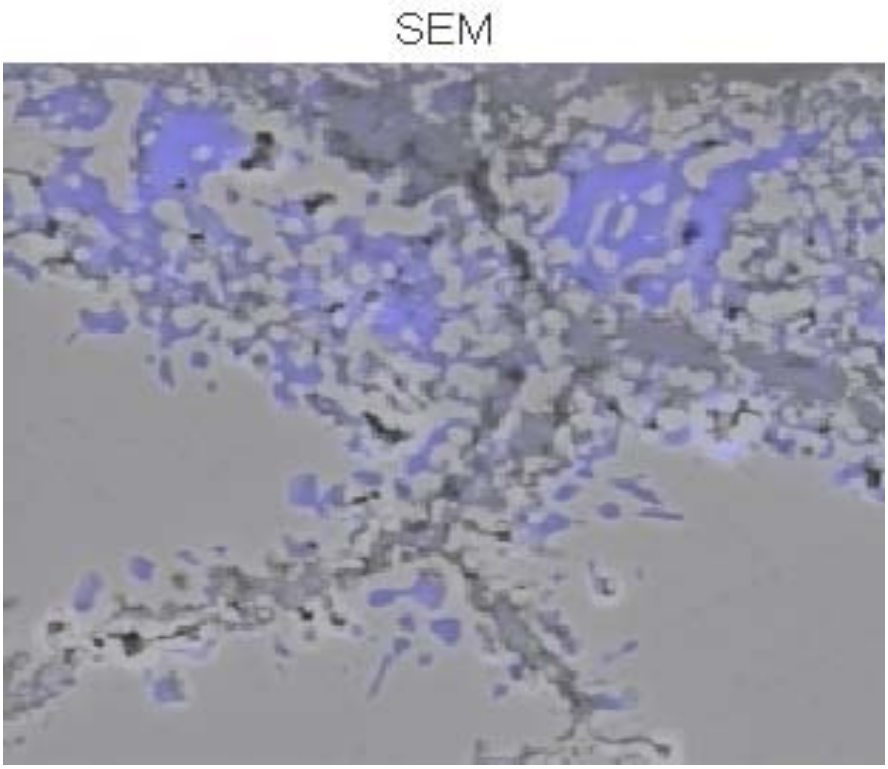

Figure 5-42
SEM micrograph of the cross section of the coated Haynes 230 sample after exposure to 816º C for 1050 hours showing the extent of corrosion attack penetration under the Eastern ash deposited area. Sulfur scan is superimposed to show the distribution of sulfide (blue) particles.

The coated sample with the Midwestern ash deposit after 500 hours exposure showed predominantly no evidence of corrosion, as illustrated in Figure 5-43. However, corrosion attack was observed only in an isolated area where the coating was prematurely spalled. Typical corrosion attack of the base metal in a coating spalled area is shown in Figure 5-44. It can be seen from the micrographs of Figures 5-36 (a) and 5-44 (b) that the morphology of corrosion attack in the coating spalled area and the uncoated sample is comparable. In contrast to these results, the coating after 1050 hours was in excellent condition and showed no evidence of localized spallation, degradation, and/or corrosion. Typical condition of the coating after 1050 hours exposure is provided in Figure 5-45. An analysis of the overall coating by EDS showed 10.48 wt.% Al in the coating, suggesting that the coating has not degraded as a result of 1050 hours exposure. The absence of corrosion attack under the most aggressive ash deposited area suggests that these nanocrystalline coatings have a great potential for corrosion protection of USC boiler tubes. These contrasting results after 500 and 1050 hours exposure suggest that the premature coating spallation in isolated areas may be related to the quality of the coating. It is suspected that the cauliflower-type defects in the coating were responsible for coating spallation in isolated areas. Thus, a defect free good quality coating is the key for the long- term durability of the nanocrystalline coatings in corrosive environment. Thus, additional process development work is required to produce defect free coatings prior to processing the production parts.

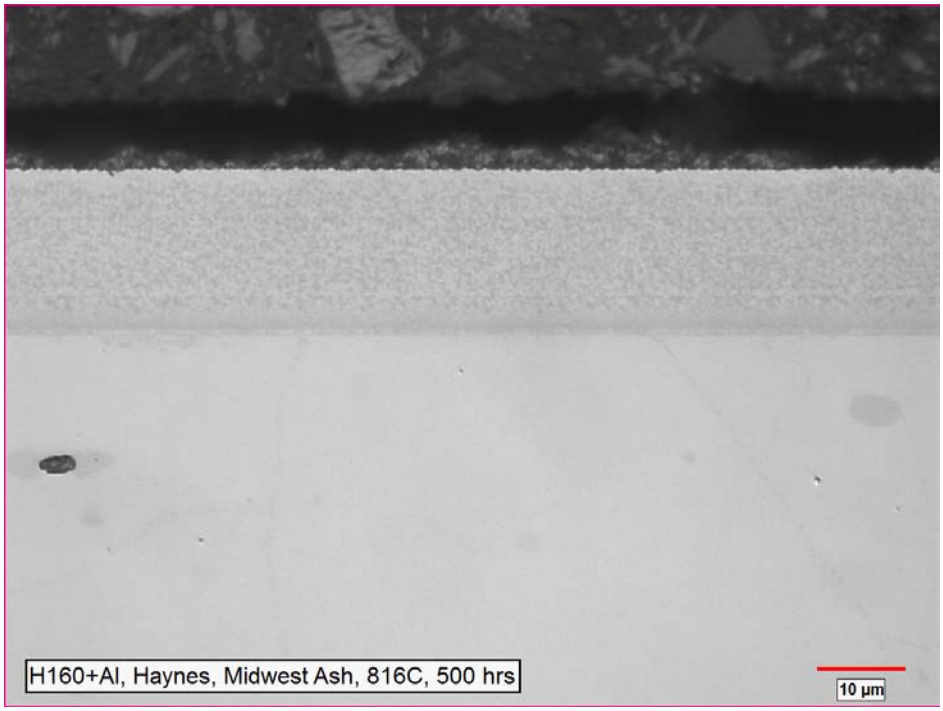

a)

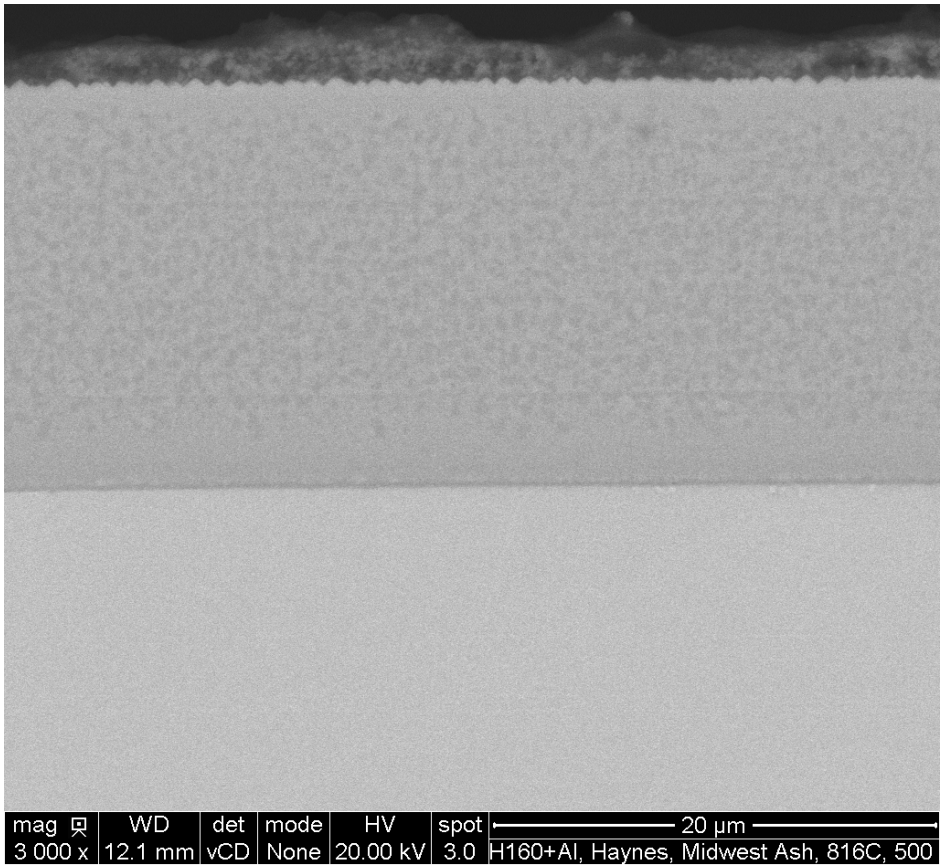

b)

Figure 5-43
The cross section of the coated sample after exposure to synthetic flue gas mixture at 816° C for 500 hours showing the condition of the coating under the Midwestern ash deposited area a) optical micrograph and b) SEM micrograph.

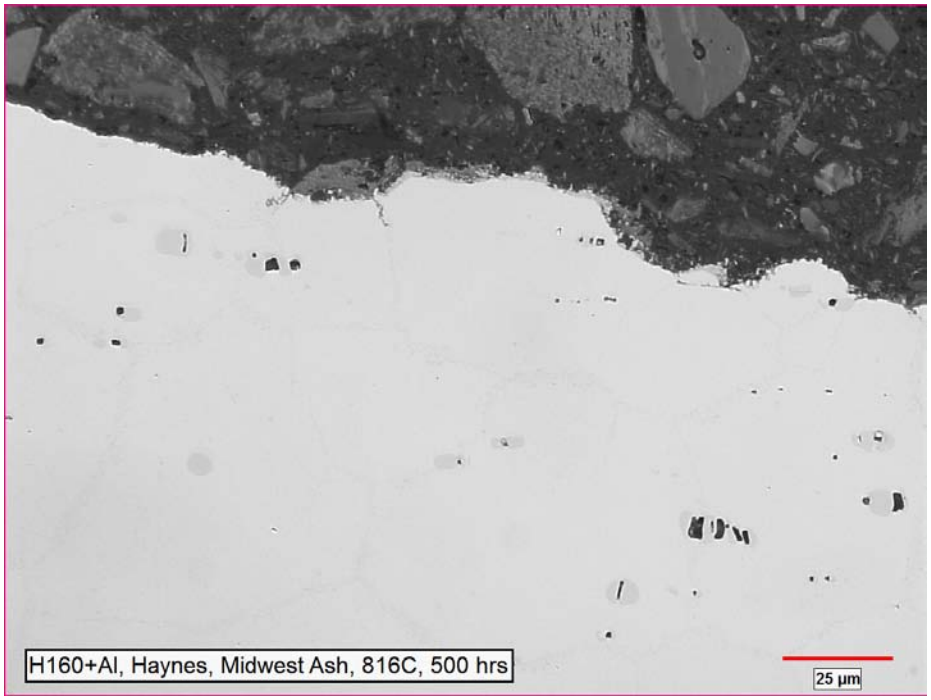

a)

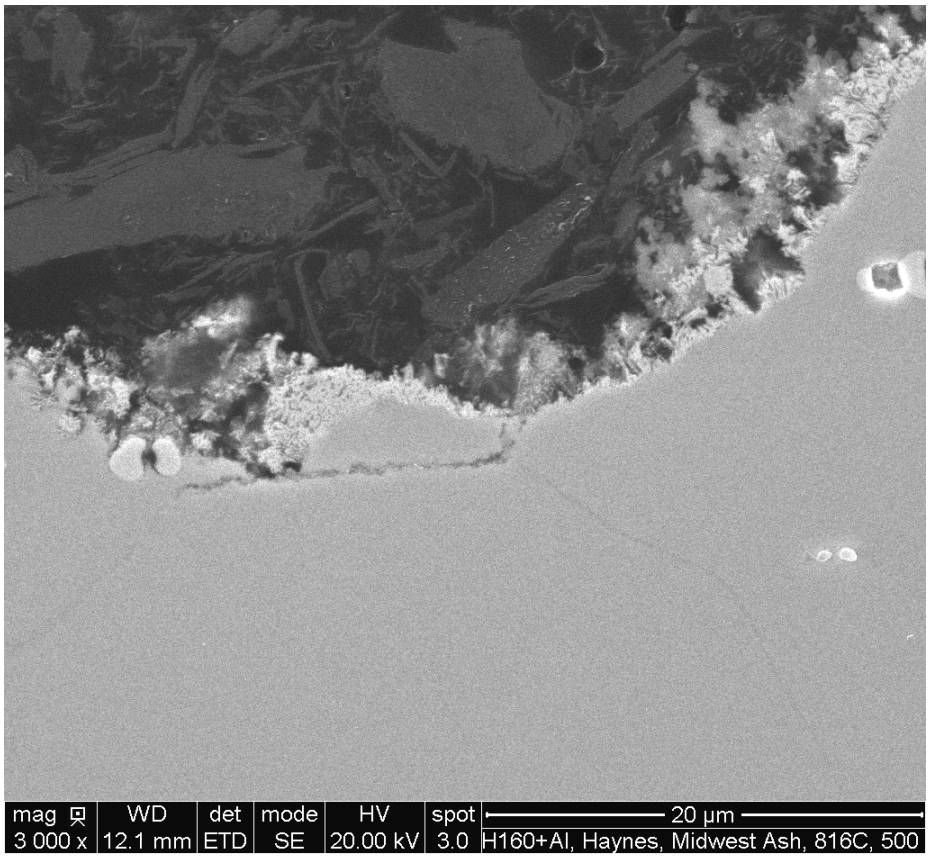

b)

Figure 5-44
The cross section of the coated sample after exposure to the synthetic flue gas mixture at 816º C for 500 hours showing the morphology of the substrate corrosion attack under the Midwestern ash deposited area where the coating was spalled a) optical micrograph and b) SEM micrograph.

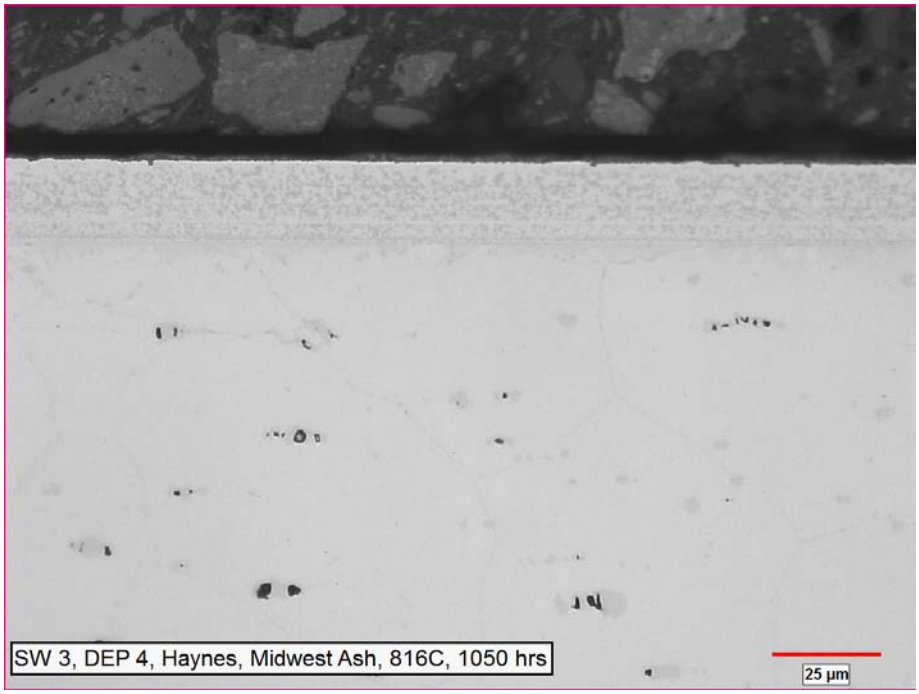

a)

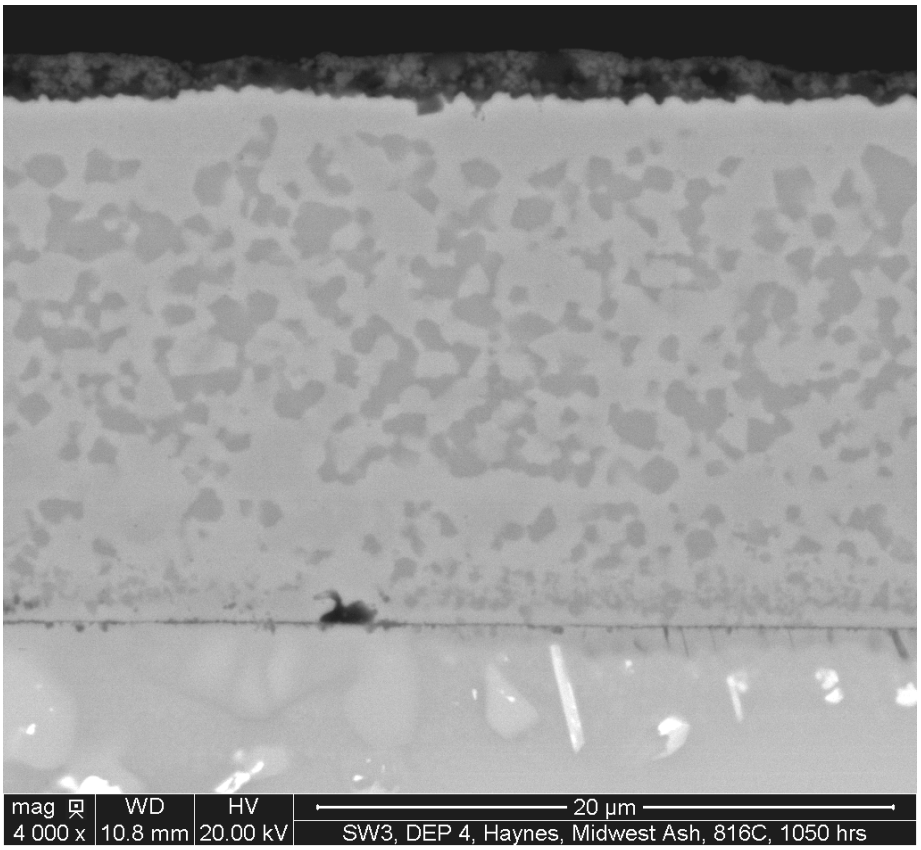

b)

Figure 5-45
The cross section of the coated sample after exposure to synthetic flue gas mixture at 816° C for 1050 hours showing the condition of the coating under the Western ash deposited area a) optical micrograph and b) SEM micrograph.

6.

TASK 5. COMPUTIONAL MODELING AND VALIDATION

6.0 Introduction

The alloy system selected for the computational modeling phase of the project was the Fe-Cr-Ni-Al system. Computational modeling of this system was targeted at producing a stable nanocrystalline coating that produces a protective, continuous scale of alumina or chromia [1-14]. For model validation, microstructure, continuous scale formation, grain growth and pore sintering in nanocrystalline-Fe-Ni-Cr-Al (304 SS + xAl) coatings were considered and the models were validated using the experimental results. Computational modeling for the nanocrystalline Ni-based (Ni-Cr-Al and Ni-Co-Cr-Si-Al) coating systems was beyond the scope of the project. The Ni-based systems were selected from those coatings that are widely used on the hot section components of land-based gas turbines for corrosion and oxidation protection. The grain growth model was utilized to deduce the activation energy for grain growth of these coatings. The experimental results are compared with the grain growth model predictions. These results are summarized in the following sections.

6.1 Fe-Ni-Cr-Al Coating's Microstructure Validation

The computational effort was intended to provide the guidance on the phase formations at different temperatures in Fe-Cr-Ni alloys with and without addition of Al. One of the goals of the phase diagram computation was to identify the minimum amounts of Al addition required to suppress σ-phase formation in Fe-Cr-Ni-Al alloys. The computational results indicated that a 4 wt.% Al addition or greater suppresses the formation of σ phase in the Fe-Cr-Ni-Al, as illustrated in Figure 6-1. The phase computational results [1-14] showed that the microstructure of Fe-Ni-Cr-Al contains ferrite (α-bcc), austenite (face centered cubic, fcc), or a combination of ferrite + austenite. However, rapid cooling promotes formation of metastable bcc in 304 and 310 steels, as shown in Figure 6-2. The XRD patterns of the targets used for the deposition of the coatings confirm that both 304 SS and 310 SS target samples are austenitic (γ-fcc). The XRD pattern of the as-deposited 304 SS coating revealed the presence of σ phase in a matrix of metastable bcc and 310SS coating exhibited a metastable bcc phase along with γ-fcc. The addition of Al to Fe-Cr-Ni alloys expands the bcc phase field because Al is a bcc stabilizer, but diminishes the σ phase and austenite (fcc) phase fields. Long-term exposure at 650° C led to complete dissolution of the σ phase in the matrix and partial transformation of α into γ [6-1] and the structure became predominantly austenite with small amounts of ferrite as the computational model predicted. The addition of 4 wt.% Al to the Fe-18Cr-8Ni (304 SS) suppressed the σ-phase formation in the coating, as illustrated in Figure 6-3. These experimental findings are in agreement with phase-diagram computations.

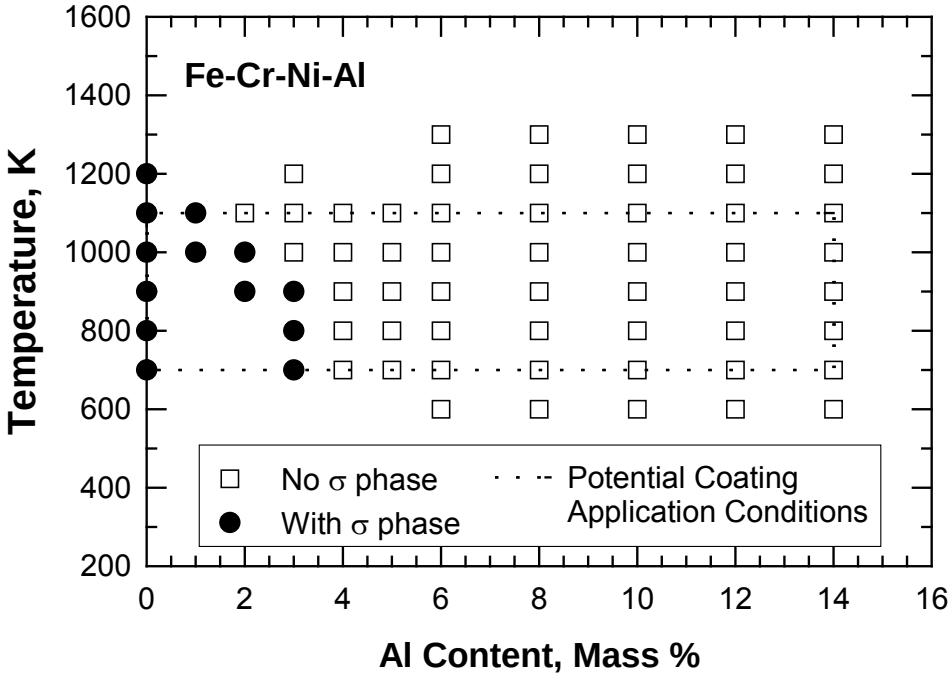

Figure 6-1
Computational results of Al contents required to suppress *σ*-phase formation in Fe-Cr-Ni-Al at a temperature in the range of 600-1300K [1-14].

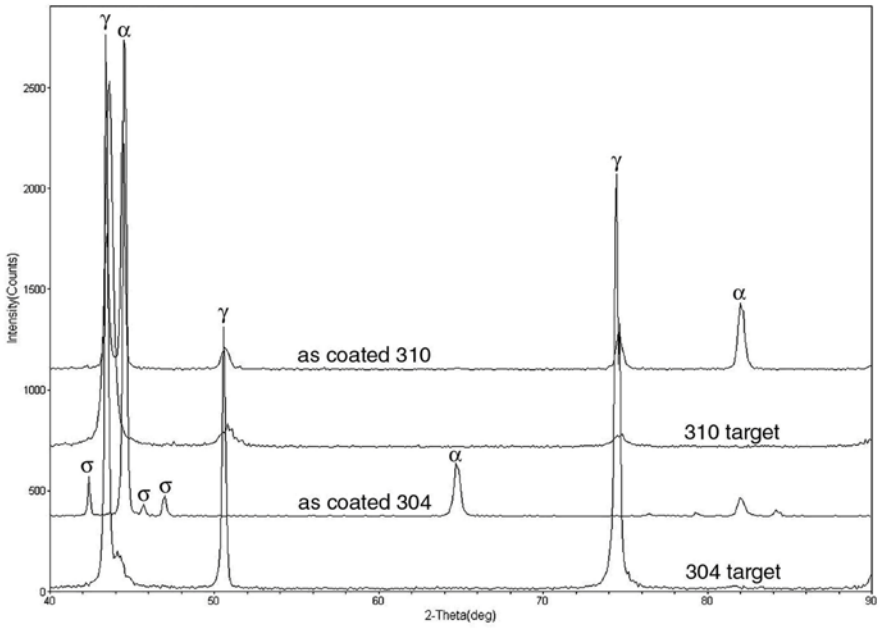

Figure 6-2
Comparison of the XRD patterns of as-deposited 304 and 310 SS coatings along with the target materials.

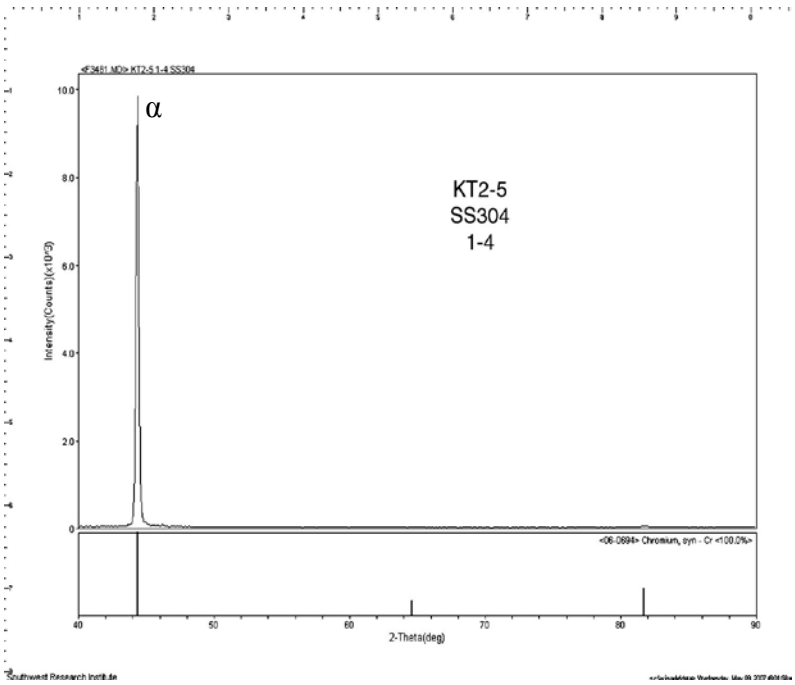

Figure 6-3
XRD pattern of the as-deposited Fe-Cr-Ni-Al (304 SS-4Al) coating showing absence of the σ phase.

6.2 Validation of Continuous Scale Formation

It has been reported that a minimum of 5 wt.% Al is required to form a continuous alumina (Al_2O_3) scale on coatings with a normal grain size (≈1-10 μm), as illustrated in Figure 6-4 [1-14]. The critical Al content was reduced from 5 wt.% to 3.5 wt.% Al for nanocrystalline coatings with a grain size of ≈60 nm because of greater Al-diffusion kinetics through grain boundaries [1-10]. Consistent with this, the experimental results showed formation of a continuous Al_2O_3 on 304 SS-4Al and Ni-20Cr-4Al coatings after exposure at 750° C [3-1 and 2,1-10, 2-9,6-1]. Figure 6-5 shows the cross section of a 304 SS-4Al coating after exposure to 990 cycles at 750º C. It is evident from the figure that addition of 4 wt.% Al resulted in formation of a continuous oxide scale and precipitation of FeAl particles in the substrate below the coating. Analysis of the continuous oxide scale by energy dispersive x-ray spectroscopy (EDS) showed a very high Al peak indicating that the scale was Al_2O_3.. Inward diffusion of Al from the coating into the substrate resulted in precipitation of FeAl particles in the substrate.

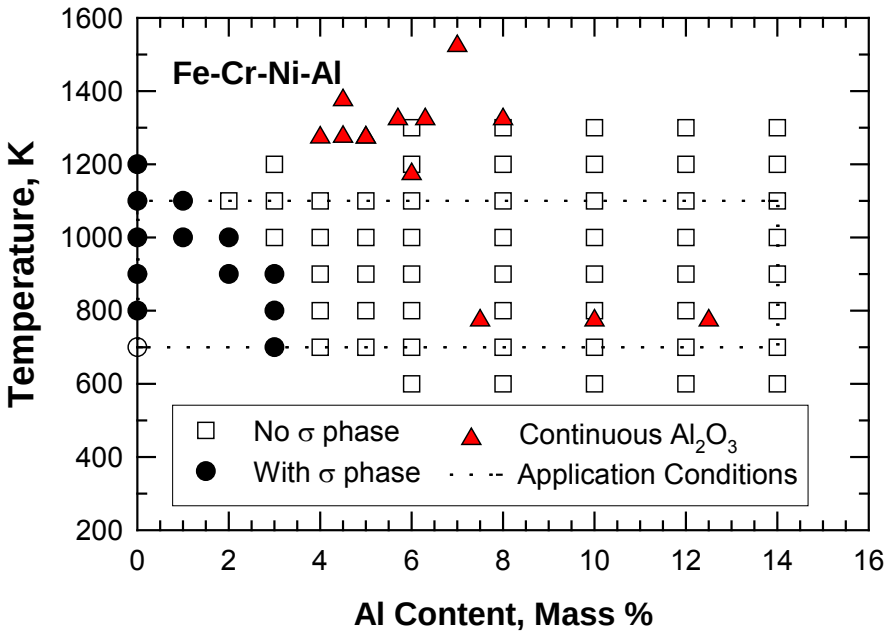

Figure 6-4
Minimum Al contents for the formation of a continuous Al_2O_3 scale on Fe-Cr-Ni-Al alloys at various temperatures. Experimental data (triangles) are from the literature [1-14].

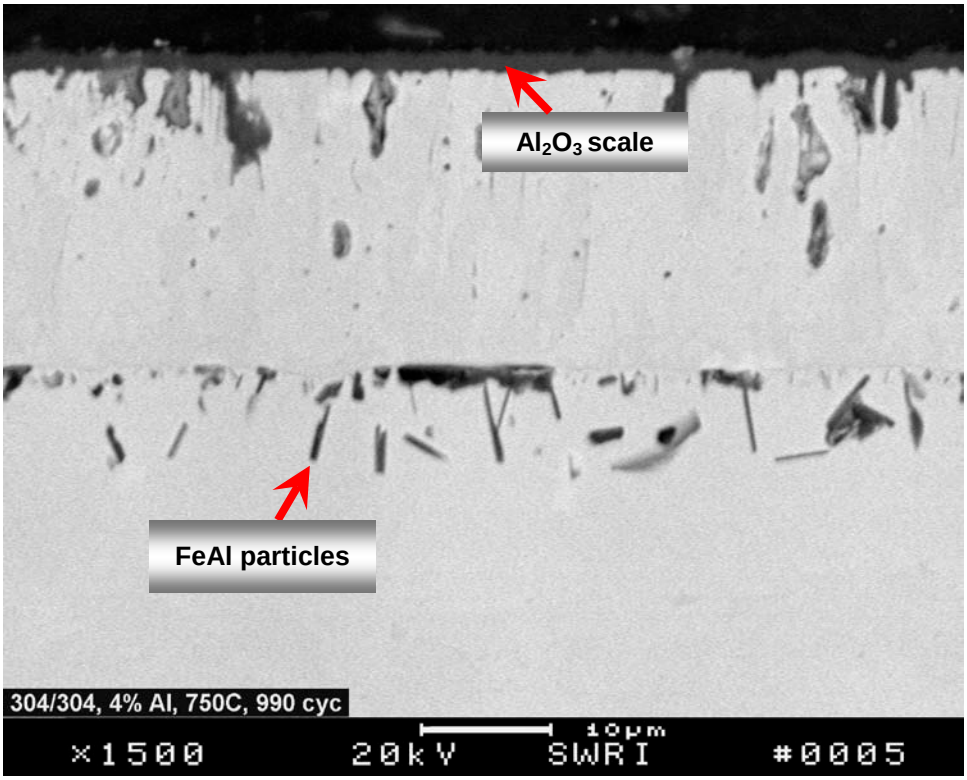

a)

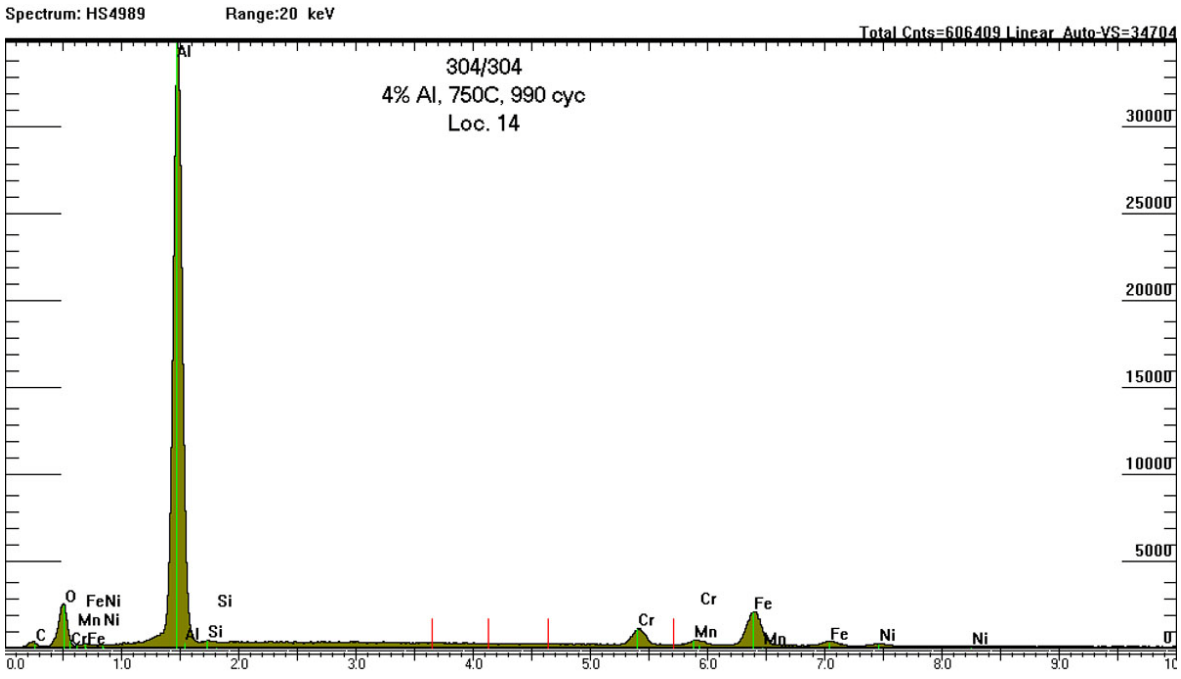

b)

Figure 6-5
SEM micrograph of the cross section of the 304 SS-4Al-coated sample and b) EDS spectrum obtained from the continuous oxide scale on the outer surface of the coating.

6.3 Validation of Inward Diffusion

Results of the interdiffusion of Al, Cr, and Ni were computed for Fe-18Cr-8Ni-10Al coating on 304 SS substrate at 750° C for exposure times of 625, 825, 1250, 2500, and 8760 hours [1-14]. The results showed that inward diffusion of Al occurred fairly rapidly and the Al concentration deceased from 10 wt.% in the as-deposited condition to about 4.1 wt.% after 625 hours and to 2 wt.% after 8760 hrs (1 yr), suggesting that these coatings have limited service life and a diffusion barrier interlayer coating is required to shutoff inward diffusion of Al. The experimental results showed that the inward diffusion of Al resulted in formation of FeAl precipitation in the interdiffusion zone as shown in Figure 6-5.

The computed concentration profiles of Al, Cr, and Ni-based on inward diffusion are compared against experimental data from cyclic oxidation specimens of Fe-18Cr-8Ni-10Al on Fe-18Cr-8Ni (304 SS) substrate tested at a maximum temperature of 750° C. All chemical compositions were determined by EDS. Figure 6-6 (a) shows a comparison of the predicted and measured Al profiles in the coating and in the substrate after 825 hrs of thermal exposure. In general, the predicted Al profile was in good agreement with the observed profile. The Al content in the coating was predicted to decrease from 10 wt.% to 3.7 wt.% in the coating. The depth of the interdiffusion zone is predicted to be about 70 μm. Both predictions are in excellent agreement with the experimental data as shown in Figure 2-6 (a). Consistent with these results, the Al content in the Ni-20Cr-10Al nanocrystalline coating decreased from 10 wt.% in the as-deposited condition to 1.7 wt.% after 347 thermal cycles at 1010° C [3-2]. The corresponding concentration profiles for Cr and Ni are compared against experimental data in Figures 2-6 (b) and (c), respectively. For both Cr and Ni, the complex profiles detailed by the computations could not be verified by the experimental data. On the other, the model predictions of minimal Cr and Ni loss to the substrate by inward diffusion are confirmed in general.

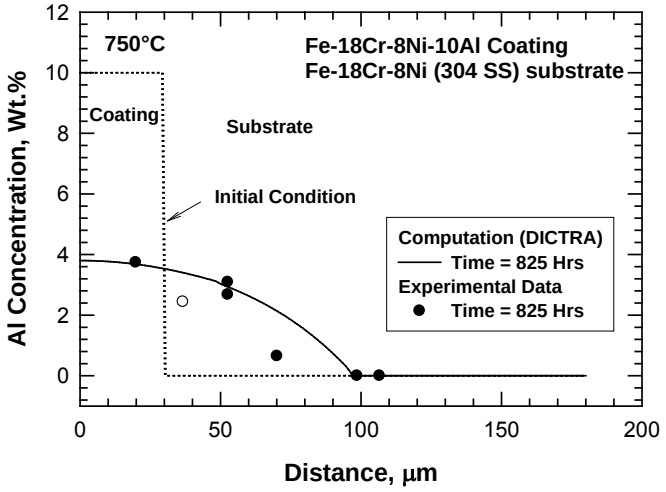

a)

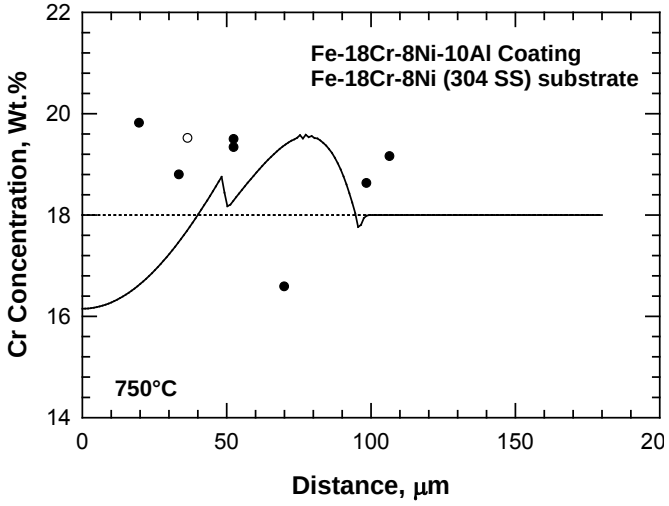

b)

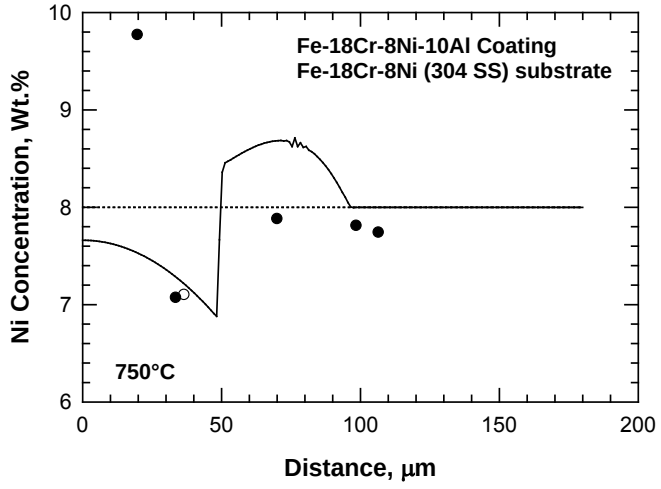

c)

Figure 6-6
Calculated concentration profiles compared against experimental data for Fe-18Cr-8Ni-10Al coating on Fe-18Cr-8Ni substrate after 825 hours at 750º C: a) Al content, b) Cr content, and c) Ni content [1-14].

6.4 Grain Growth Modeling and Validation for Fe-Ni-Cr-Al Coatings

The expression for grain growth kinetics is generally given by [6-2]

$$d^2 - d_o^2 = k_g t \tag{6-1}$$

where d and d_o are current and initial grain diameter, respectively, t is time, and k_g is a microstructure parameter given by

$$k_g = \frac{4}{3} M_{gb} \gamma_{gb} (n-6) \tag{6-2}$$

where M_{gb} and γ_{gb} are the mobility and energy of the grain boundaries, respectively, and n is the number of the grain neighbor. The grain boundary mobility is related to the diffusion coefficient (D) as given by

$$M_{gb} = \frac{\Omega D_o}{\delta_b RT} exp\left(-\frac{Q}{RT}\right) \tag{6-3}$$

where Ω is the molar volume, δ_b is the grain boundary thickness, D_o is the pre-exponent coefficient for diffusion, Q is the activation energy for diffusion, R is the universal gas constant, and T is absolute temperature.

The activation energy for grain growth is closely related to the activation energy for the controlling diffusive mechanisms. In Fe-based alloys, the activation energy for grain growth can vary from 91 kJ/mol to 404 kJ/mol [6-3]. The high value is associated with grain growth in a columnar–grained structure, as shown in Table 6-1 [6-3].

Table 6-1
Activation energy values for grain growth in Fe-based alloys [6-3].

Grain Growth Process	Q, kJ/mol
Self-diffusion of Fe in ferrite	245
Grain-boundary diffusion of Fe in ferrite	178
Grain-boundary mobility of Fe in ferrite	145
Columnar grain growth (Rolling Direction)	240
Columnar grain growth (Normal Direction)	404
Unspecified mechanism	91

Eqs. (6-1) – (6-3) were utilized to compute the grain diameter as a function of anneal times for equiaxed and columnar microstructures at 750° C. The calculated results are compared against experimental data for the columnar grained nanocrystalline coating in Figure 6-7. The grain sizes

of the columnar grain structure in the nanocrystalline coatings were measured on a plane normal to the columnar growth direction via Orientation Image Microscopy (OIM). The distribution of the grain diameter for the as-deposited Fe-18Cr-8Ni-10Al nanocrystalline coating is presented in Figure 6-8. The grain mean diameter was measured to be 1.23 μm with a standard deviation of 0.43 μm.

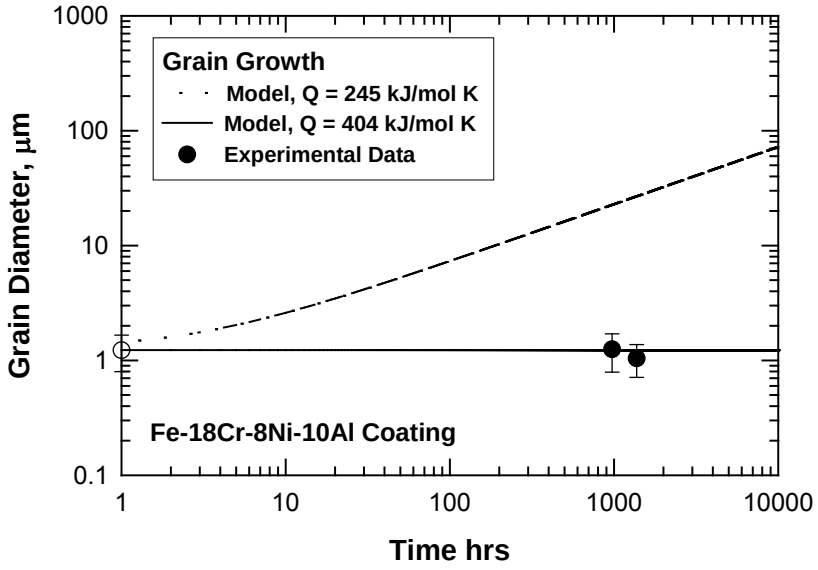

Figure 6-7
Predicted grain growth kinetics using the activated energy values for equiaxed and columnar grain structures compared to experimental data for Fe-18Cr-8Ni-10Al nanocrystalline coatings with a columnar grain structure.

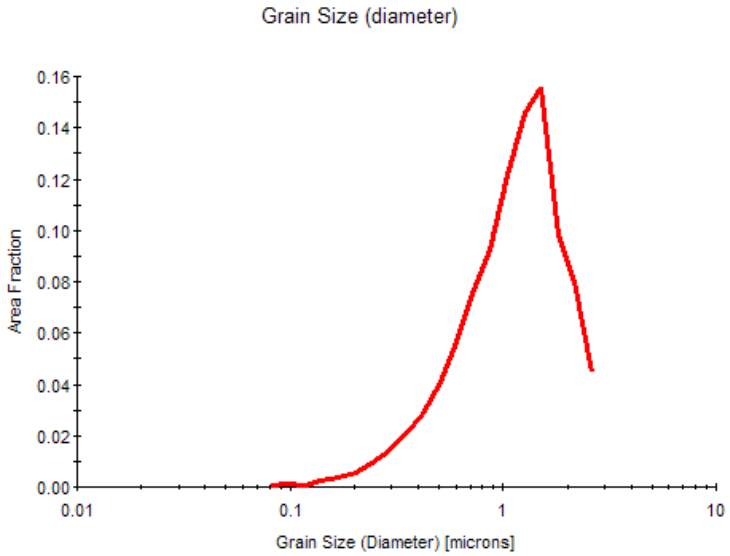

Figure 6-8
Grain diameter distribution for Fe-18Cr-8Ni-10Al nanocoating in the as-coated condition.

The theoretical calculation, utilizing an activation energy of 404 kJ/mol K, indicated that very little grain growth occurred in the columnar microstructure after exposure at 750° C for 1,000 hours, which is in agreement with the experimental data. The average grain size of the two samples after thermal exposure at 750° C was measured to be 1.05 and 1.25 μm. In contrast, the model predicts a substantial grain growth for the equiaxed, conventional microstructure. The different grain growth kinetics between the equiaxed and columnar grain structures is due to the large difference in the activation energy for grain growth, which is 404 kJ/mol for columnar grain structure and 245 kJ/mol for the equiaxed grain microstructure [6-3].

To understand the high activation energy for the columnar grain structure, OIM was also utilized to characterize the grain orientation, and the grain boundary characters in the Fe-Cr-Ni-Al nanocrystalline coatings. The grain boundaries in the columnar structure are mostly low angle boundaries with 49% of the grain boundaries having less than a 15° misorientation angle. Figure 6-9 shows that approximately 39% of the grain boundaries are misoriented by 4° or less. The distribution at higher misorientation is fairly uniform at misorientation angles higher than 4°. The grain boundaries of the nanocrystalline coating after thermal exposure remained mostly as low angle boundaries. The grain size distribution before and after thermal exposure was comparable. The higher activation energy for grain growth in the columnar structure appears to be the result of the presence of a large fraction (about 50%) of low angle boundaries (<15% misorientation) in the microstructure. Hence, the key to maintain a fine grained structure that resists grain growth is to have a high population of stable low angle grain boundaries in the nanocrystalline coatings.

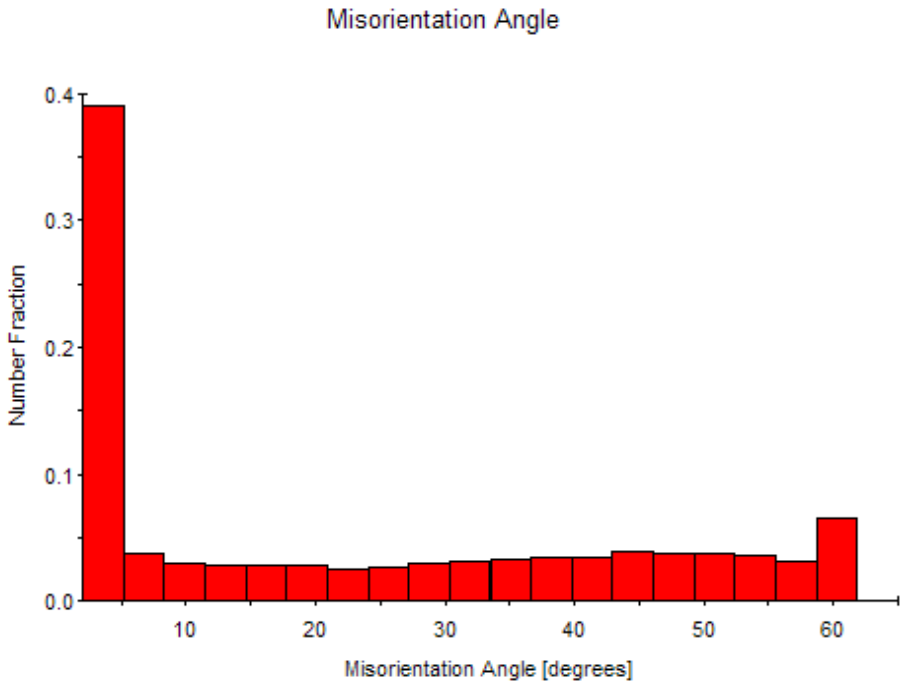

Figure 6-9
Grain boundary misorientation distribution for as-deposited Fe-18Cr-8Ni-10Al nanocrystalline coating on 304 SS substrate.

6.5 Grain Growth Validation for Ni-Based Coatings

The experimental results showed that the columnar grain structures in the nanocrystalline Ni-Cr-Al (4, 7 and 10 wt.%) are not stable at 750º C and 1010º C. In contrast, the columnar grain structure in the nanocrystalline Ni-Co-Cr-Si-Al coating is stable. The experimental results can be found in Reference 1-17. The grain growth model was utilized to deduce the activation energy for grain growth in nanocrystalline Ni-20Cr-xAl coatings. For Ni-20Cr-xAl nanocrystalline coatings thermally cycled at 750° C under one-hour cycle, the deduced activation energy was 290 KJ/mol K, as shown in Figure 6-10. This value of the activation energy is in excellent agreement with the experimental value of 285 ± 30 KJ/mol K reported for lattice diffusion of Ni-20Cr [6-4]. On the other hand, the deduced value for the activation energy was for Ni-20Cr-xAl nanocrystalline coatings thermally cycled at 1010° C was 340 KJ/mole K, as shown in Figure 6-11. This value is higher than the reported value of 285 KJ/mol K for lattice diffusion.

For Ni-Co-Cr-Al-Si nanocrystalline coatings, the columnar grain size was essentially unchanged at 800 nm before and after thermal cycling at 1010° C for 1007 one-hour cycles (Appendix C). As shown in Figure 6-12, the activation energy must be clearly higher than the 340KJ/moleK determined for the Ni-20Cr-xAl coatings. A best fit to the limited data resulted in an activation energy of 404KJ/mol K. This particular activation energy value is consistent with the observation made in Fe-18Cr-8Ni-10Al, which exhibited little or no grain growth in a columnar grained nanoscaled microstructure during thermal cycling at 750° C, as presented in Figure 6-13. The deduced value of 404 KJ/mol K is also in agreement with the activation energy for lattice diffusion in a columnar grained microstructure in steels [6-3]. This suggests the mechanism which is significantly impeding high-temperature grain growth is not only related to composition but to the structure obtained from the PEMS process. Additional data coupled with more fundamental research to understand this phenomenon would be a useful scientific endeavor.

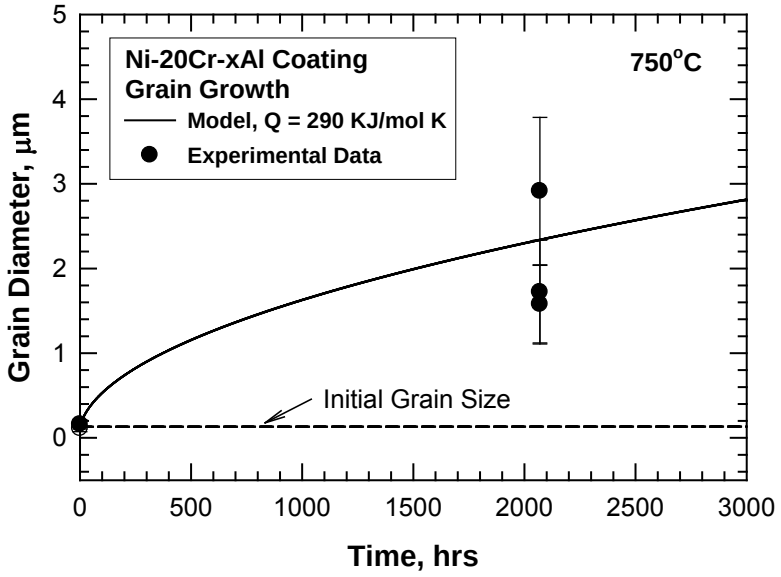

Figure 6-10
Computed and measured grain sizes in Ni-20Cr-xAl nanocrystalline coatings as a function of exposure time at 750° C. The activation energy was deduced by fitting the grain growth model to the measured grain size.

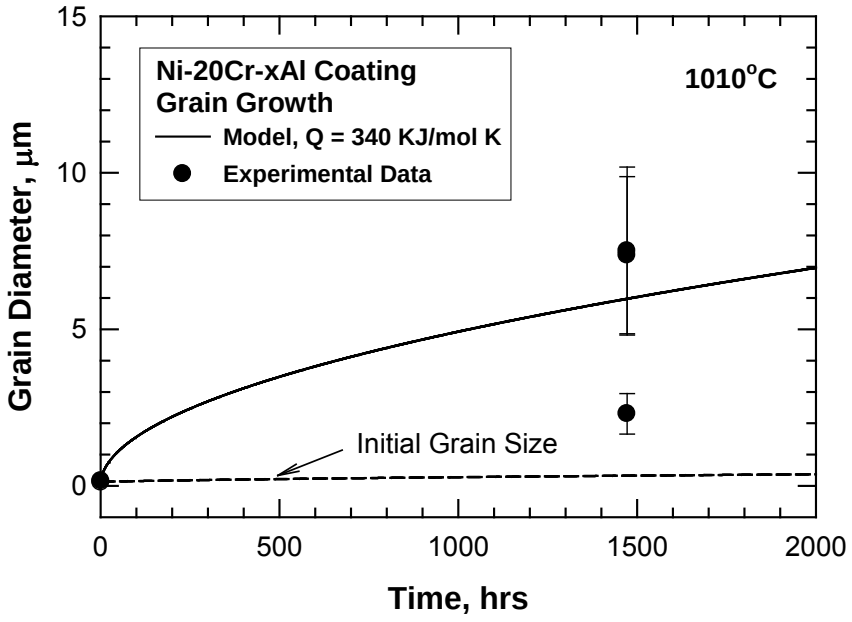

Figure 6-11
Computed and measured grain sizes in Ni-20Cr-xAl nanocrystalline coatings as a function of exposure time at 1010° C. The activation energy was deduced by fitting the grain growth model to the measured grain size.

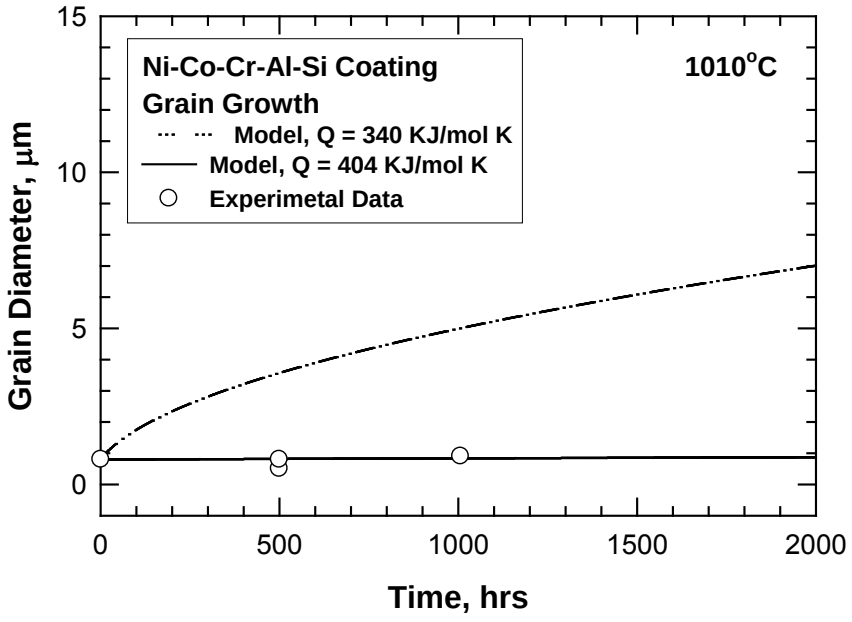

Figure 6-12
Computed and measured grain sizes in Ni-Co-Cr-Al-Si nanocrystalline coatings as a function of exposure time at 1010° C. The activation energy was deduced by fitting the grain growth model to the measured grain size.

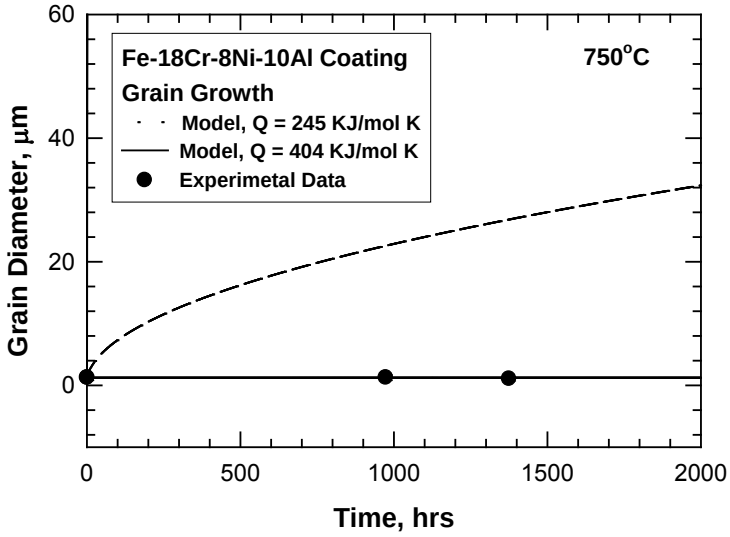

Figure 6-13
Computed and measured grain sizes in Fe-18Cr-8Ni-10 nanocrystalline coatings as a function of exposure time at 750° C. The activation energy used is an experimental value for the activation energy of diffusion in a columnar grained structure in steel from Reference 6-3.

The modeling results indicate that the apparent activation energy for grain growth in Ni-Cr-xAl nanocrystalline coatings varies with coating chemistry. Hence, a systematic research effort is required to understand the factors affecting the grain growth kinetics and formation stable low angle boundaries in the Ni-based nanocrystalline coatings

6.6 Sintering Modeling and Validation for Fe-Ni-Cr-Al Coatings

Connected grain boundary pores are undesirable in coatings because they promote internal oxidation by providing access of oxygen and corrosive elements to interior grains. Experimental data showed the presence of voids and gaps between columnar grains in the nanocrystalline coatings. The volume fractions of voids ranged from 10% in the as-processed condition to about 2% after thermal cycling exposure at 750° C for 1500 one-hour cycles. The decrease in void density was the result of sintering after high-temperature exposure.

An existing sintering model was utilized to compute the linear shrinkage rate ($\Delta L/L$) according to [6-5]

$$\frac{\Delta L}{L} = \left(\frac{15a^4}{r^4} \frac{D\gamma}{kT} \right)^{1/3} t^{1/3} \qquad (6\text{-}4)$$

where D is self-diffusion coefficient, γ is surface energy, r is grain radius, a is lattice parameter, t is time and k is Boltzmann's constant. The relative density is given in terms of the linear shrinkage rate as [6-5]

$$\rho = \rho_i \left[1 - \frac{\Delta L}{L} \right]^{-3} \qquad (6\text{-}5)$$

where ρ_i is the initial density.

Using Eqs. (6-4) and (6-5), the relative density was computed as a function of time for Fe-Cr-Ni-Al nanocrystallines and the results are compared against experimental data in Figure 6-14. The as-coated Fe-18Cr-8Ni-10Al coating was about 90% dense, but the relative density increased with increasing times cyclic oxidation to almost 98% dense after about 1373 hours of thermal exposure at 750° C. The model prediction was in good agreement with the experimental data. The presence of pores in the coating allows oxygen penetrations and internal oxidation deep inside the nanocrystallines. To eliminate oxygen penetration through connected pores, the grain boundaries pores must be eliminated or sealed off from the interior grains. The sintering model was utilized to estimate the times required to eliminate the pores. The results indicate that the initial density of the as-fabricated coating must be greater than 98% dense (*i.e.*, less than 2% porosity) in order to eliminate all pores in less than 45 hours at 750° C. The sintering time increases to 320 hours at an initial relative density of 95%.

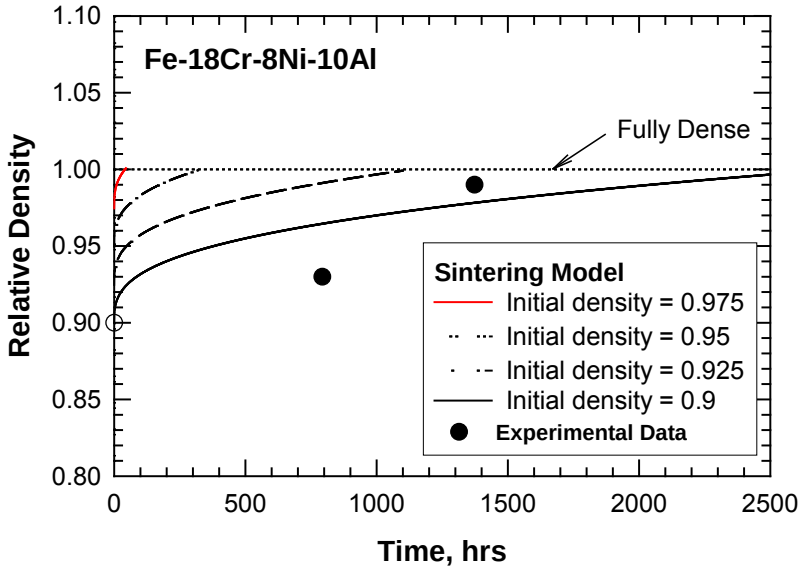

Figure 6-14
Theoretical relative density based on the sintering model compared to experimental data. The initial relative density of the as-processed coating must be greater than 98% in order to achieve the full density in less than 45 hours of exposure at 750° C.

6.7 Coating Oxidation Life

Both Fe and Ni based nanocrystalline coatings exhibited superior oxidation resistance. The coatings showed almost no mass change after initial weigh gain throughout the entire cyclic oxidation testing. The cyclic oxidation test results further showed that the nanocrystalline Ni-based coatings exhibit superior oxidation resistance at 1010° C compared to the conventional plasma sprayed MCrAlY coatings. The Ni-Cr-Al and Ni-Co-Cr-Si-Al nanocrystalline coatings, after the initial weight gain, exhibited little mass change throughout the entire cyclic oxidation testing for over 2000 one-hour thermal cycles at 1010°C, suggesting that the oxide scale was highly resistant to spallation . Hence, long-term testing is necessary to generate constants for these coatings to assess the oxidation life using the coat life model. Considering oxidation is not a concern for these coatings at the USC boiler operating temperatures, no attempt was made to perform long-term testing for the coat life assessment. The detailed experimental results can be found in Reference 1-17.

6.8 Heat Transfer Performance Analysis

Finite element and one-dimensional calculations show that the effect of a very thin (20-30 µm) corrosion/oxidation resistant nanocrystalline coating has little effect on the thermal properties of a boiler tube. While a full boiler analysis would include temperature changes in the internal fluid as well at the bending of the boiler tube within the firebox, this model gives a clear indication that the total impact of the coating on heat transfer is negligible. The heat transfer performance analysis results in detail can be found in Reference 1-17.

6.9 REFERENCES

6-1. N.S. Cheruvu, R. Wei, M.R. Govindaraju, and D.W. Gandy, "Cyclic Oxidation Behavior and Microstructure of Nanocrystalline Ni-20Cr-4Al Coating," *Oxidation of Metals*. Vol. 73, Nos. 5-6, p. 493 (2010).

6-2. M. Hillert, "On Theory of Normal and Abnormal Grain Growth," *Acta Metallurgica*. Vol. 13, No. 3, p. 227 (1965).

6-3. Y. Sidor, F. Kovac, and V. Petrychka, "Secondary Recrystallization in Non-Oriented Electric Steels," *Metalurgija*. Vol. 44, No. 3, p. 169 (2005).

6-4. N.R. Dudova, R.O. Kaibyshev, and V.A. Valitov, "Deformation Mechanisms in Cr20Ni80 Alloy at Elevated Temperatures," *The Physics of Metals and Metallography*. Vol. 107, No. 4, p. 409 (2009).

6-5. D.L. Johnson and I.B Cutler, "Diffusion Sintering I: Initial Stage Sintering Models and Their Application to Shrinkage of Powder Compats," *Journal of the American Ceramic Society*. Vol. 46, No. 11, p. 541 (1963).

7.
CONCLUSIONS

A summary of findings reached as the result of this study are as follows:

Task 1: Computational Modeling of MCrAl Systems

- Pseudo-ternary phase diagrams computed via Thermo-Calc software provided detailed information on the constituent phases in Fe-Cr-Ni-Al alloys at various temperatures.
- The formation of σ phase in Fe-Cr-Ni-Al alloys is suppressed for Al contents in excess of 4 wt.% for temperatures in the range of 600 to 1200K.
- The compositions of Fe-Cr-Ni-Al alloys required for the formation of continuous Al_2O_3 or continuous Cr_2O_3 without the formation of σ phase have been identified from the Thermo-Calc computations.
- Interdiffusion modeling using the DICTRA software package indicated that the inward diffusion results in substantial to moderate Al and Cr losses from the nanocrystalline coating to the substrate during thermal exposure at 750° C.
- Interdiffusion computation indicated certain Fe-Cr-Ni-Al nanocrystalline coatings form a diffusion barrier layer at the coating/substrate interface that reduces the inward diffusion of Al or Cr into the substrate.
- Interdiffusion computations identified a new series of Fe-Cr-Ni-Al coating compositions that form a diffusion barrier at the coating/substrate interface.
- Computational modeling identified two coating compositions (Fe-25Cr-40Ni and Fe-25Cr-40Ni-10Al) as potential candidate coatings on the basis of their abilities to maintain a high Cr or Al content during high-temperature exposure. Fe-25Cr-40Ni forms a σ-phase diffusion barrier layer and Fe-25Cr-40Ni-10Al forms a γ-phase layer at the coating/substrate interface that significantly reduces inward diffusion.

Task 2: Establishment of Baseline Coating Data

- The as-coated microstructure of the Fe-18Cr-8Ni coating without Al showed the presence of a small amount of sigma phase (σ) in a body centered cubic (bcc), αFe matrix. The addition of Al suppressed the formation of σ and stabilized αFe.
- Nanocrystalline coatings exhibited excellent oxidation resistance. The coatings containing Al in excess of 4 wt.% showed no evidence of weight loss during the entire cyclic oxidation testing following the initial weight gain.

- The nanocrystalline Ni-20Cr-10Al coating showed better oxidation resistance compared to the conventional plasma-sprayed NiCoCrAlY and PWA 286 coatings which are widely used on the hot section components of gas turbines.
- The nanocrystalline grain structure promoted selective oxidation of either Cr in the coatings without Al and/or Al. The protective oxide scale on the nanocrystalline coating is highly resistant to spallation.
- Evidence of internal oxidation was observed along the columnar grains in both Fe-18Cr-8Ni-4wt.% Al and Ni-20Cr-4Al coatings after thermal exposure. On the other hand, the coatings containing 7 or 10 wt.% Al were free from internal oxidation after thermal exposure at 750º and 1010º C, suggesting that the coatings should contain at least 7 wt.% Al for their long-term durability.
- Thermal exposure led to rapid loss of Al content in both Fe-18Cr-8Ni-4Al and the Fe-18Cr-8Ni-10Al coatings due to inward diffusion. For long-term durability, these coatings require a diffusion barrier interlayer coating.

Task 3: Process Advanced MCrAl Nanocoating Systems

- The advanced coatings deposited on 304 SS, P91, and Haynes 230 samples using the PEMS with two magnetrons exhibited cracks and surface defects. Additional research work is required to produce defect-free coatings.
- Successfully developed a diffusion barrier TiN coating and demonstrated that the interlayer is effective in preventing the inward diffusion of Al from the coating into the substrate alloys
- Three new deposition methods were investigated to improve the quality of the coating:
  a) High Power Impulse Magnetrons Sputtering (HIPIMS) produced dense and crack-free coatings; however, the coatings were found to be extremely brittle.
  b) Coatings deposited using the four magnetrons also showed cauliflower-type defects and cracks. The process was not reproducible.
  c) Pulsed DC magnetron sputtering process produced crack free coatings with a few cauliflower defects. Overall the quality of these coatings was excellent and it was demonstrated that the process was reproducible. Additional research work is required to understand the effects of process parameters on the coating quality.
- The nanocrystalline coatings with a diffusion barrier interlayer can be used to extend the service life of nanocoatings.

Task 4: Fire-Side Corrosion Testing

Fire-side corrosion tests in still air:

- The four nanocrystalline coatings at three temperatures, 593º, 704º, and 815º C for up to 3040 hours, showed no evidence of corrosion under the simulated ash deposited areas.

- The corrosive constituents in the simulated ash deposits did not migrate through the columnar grain boundaries to the coating/substrate interface during thermal exposure, suggesting that flowing flue gas is required for these boundaries to act as pathways for corrosion species transportation.
- The defects in the nanocrystalline coatings did not adversely affect corrosion performance.

Fire-side corrosion tests in flowing simulated flue gases:

- Commercially available 'nano-coatings' performed poorly in all fireside corrosion testing
- Initial tests on nanocoatings showed the need to eliminate through-thickness defects which served as a pathway for hot-corrosion 'short-circuiting' potentially good behavior.
- Premature coating spallation in isolated areas of optimized nanocoatings led to corrosion attack of the base metal after exposure to 815º C in two of four samples tested.
- Variation of defects in the samples was considered to be responsible for the premature coating spallation in isolated areas.
- Though the corrosion attack was noted in two samples, the coated sample exposed 1050 hours showed no evidence of corrosion under the most aggressive ash deposited area suggesting that the nanocrystalline coatings have a great potential in providing corrosion protection of boiler tubes.
- The Al content in the coating before and after thermal exposure was comparable suggesting that the coating had not degraded as a result of thermal exposure.
- A defect free (no through-thickness defects) good quality coating is the key for the long-term durability of nanocrystalline coatings in corrosive environments.
- Additional process development work is required to produce defect free coatings prior to development processing method for large scale production parts.

Task 5: Computational Modeling and Validation

- Grain growth modeling indicated that the columnar grain structure in the nanocrystalline Fe-18Cr-8Ni-10Al and Ni-Co-Cr-Si-Al coatings was stable and resistant to growth because of high activation energy for grain growth. The grain growth model prediction is in agreement with the experimental results
- In contrast to the iron-based (Fe-Cr-Ni-Al) coatings, the experimental results showed that the columnar grain structures in the nanocrystalline Ni-Cr-xAl (x = 4, 7, and 10 wt.%) Al coatings were not stable. The grain growth model indicated that the lower activation energy for grain growth is responsible for the grain coarsening of the Ni-20Cr-xAl coatings.
- A systematic research effort is required to understand the factors that effect the formation of stable low/high angle boundaries and grain growth kinetics of Ni-based coatings.
- Sintering modeling indicated that the initial relative density of the as-processed coatings must be greater than 98% in order to achieve full density in less than two days of thermal exposure at 750º C. The sintering model was validated with the experimental results.

- Both Fe and Ni based nanocrystalline coatings exhibited superior oxidation resistance. The coatings showed almost no mass change after initial weight gain throughout the entire cyclic oxidation testing. Hence, long-term testing is necessary to generate constants for these coatings to assess the coat life using oxidation model
- Considering oxidation is not a concern for these coatings at the USC boiler operating temperatures, no attempt was made to perform long-term testing for the coat life assessment.
- Finite element and one-dimensional calculations agree that the effect of a very thin (20-30 μm) coating has very little effect on the thermal properties of a boiler tube.

Overall Conclusions & Recommendations

Based on this research and the finding summarized in this chapter, a number of conclusions can be made. The research clearly shows that nanocrystalline coatings reduce the mininimum required Cr or Al content needed to produce oxidation and corrosion resistant scales compared to traditional coatings (microscopic grain size). However, at A-USC temperatures, interdiffusion of Al into the base metal substrate will occur. To alleviate this concern for long-term coating durability, this work produced a significant scientific finding that a thin nanostructured interdiffusion barrier made of TiN can effectively shut-off diffusion of Al into the substrate. A significant amount of experimental evidence including cyclic oxidation testing and fireside corrosion testing was used to confirm this behavior for long-term performance. In addition to USC boiler applications, the use of this interlayer could be applied to other traditional coating systems which are life-limited by interdiffusion of Al.

The computational modeling and validation results showed generally good agreement between modeling results and experimental findings. However, the PEMS process produced non-equilibrium structures which were not predicted by thermodynamics. Furthermore, the activation energies for some of the Ternary Ni-Cr-Al systems were much lower (and hence grain growth was observed) compared to the other multicomponent coating systems produced by the same process. Although extensive microscopy was conducted, the reason for this behavior was unclear. Therefore, a more basic study to understand non-equilibrium structures produced via the PEMS process and the role chemical composition and structure play in grain growth would be of scientific interest.

The research suggested the Fe-40Ni-25Cr-10Al system (Haynes 120+Al) and the Ni-30Cr-3Si-10Al (Haynes 160+10Al) systems would be the best performing nanocoatings for fireside corrosion resistance on ferritic and nickel-based alloys, respectively. Fireside corrosion tests showed both of these coatings, if made with minimal defects, performed well in simulated waterwall testing. Fireside corrosion testing showed the Haynes 160+10Al coating could perform with little to no attack in aggressive testing at superheater/reheater conditions and thus had great potential as a candidate coating.

However, the research also showed that even the best coatings were subject to localized corrosion attack at coating defects. The research eliminated a number of coating methodologies based on the PEMS process. Repeatability is clearly a concern with this type of coating application with pulsed DC giving the lowest area fraction of defects. A defect free (no through-thickness defects) good quality coating is the key for the long-term durability of nanocrystalline coatings in

corrosive environments, and additional process development work is required to produce defect free coatings prior to development processing method for large scale production parts.

Assuming through-thickness defects could be eliminated, the possibility of coating a waterwall panel remains a possibility utilizing production equipment. Nanocoatings using the PEMS process have been successfully applied to the inner and outer diameter of tubing for erosion resistant applications, so the industrial applicability of coating superheater/reheater tubing would also be a future option.

Overall, thin nanocoatings are a promising technology for reducing fireside corrosion damage in today's and tomorrow's boilers. This research advanced the technology by developing a first-of-a-kind nanocoating interdiffusion barrier. It also identified key areas where more scientific understanding is required. Finally, coating quality was greatly improved, but more research is still needed before this technology can take the next step to large scale application and field testing.

Publications as a result of this research

- "Computational Design of Corrosion Resistant Fe-Cr-Ni-Al Nanocoatings for Power Generation" by K. S. Chan, et. al, Journal of Eng. for Gas Turbines and Power, Vol 132, May 2010 052101.
- "Evaluation of Nanocrystalline Coatings for Coal Fired Ultra-supercritical Boiler Tubes" by N. S. Cheruvu et. al. Journal of Pressure vessel Technology, Vol. 132, Dec 2010, 061403
- "Oxidation Behavior of Sputter Deposited Nanocrystalline and Conventional Plasma Sprayed MCrAl(Y) coatings" Proc. of the ASME Turbo Expo 2010, ASME Gas Turbine Tech Congress& Exposition, Paper # GT2010-22645, June 2010, Glasgow, UK
- "Cyclic Oxidation behavior and Microstructure of Nanocrystalline Ni-20Cr-4Al Coating" by N. S. Cheruvu et. al. Oxidation of Metals, vol. 73, 2010, 493
- "Influence of Thermal Exposure on the Stability of Metastable microstructure of Sputter deposited Nanocrystalline 304 and 310 Stainless steel coatings" by by N. S. Cheruvu et. al. Surface & coatings Technology, Vol. 205, 2010, 1211
- "Microstructure oxidation resistance of Nanocrystalline 304SS-Al coatings" by N. S. Cheruvu et. al. Surface & coatings Technology, Vol. 204, 2009, 751

Patent applications as a result of this research

- U.S. Patent Application entitled "Corrosion Resistant Coatings Suitable for Elevated Temperature", filed on December 1, 2008, SwRI Invention Disclosure Docket No. 3351
- U.S. Patent Application entitled "Method for Applying a Diffusion Barrier Interlayer for High Temperature Components", filed on November 11, 2009, SwRI Invention Disclosure Docket No. 3402
- U.S. Patent Application entitled "Oxidation Resistant Nanocrystalline MCrAl(Y) Coatings and Methods of Forming Such Coatings", filed on April 15, 2010, SwRI Invention Disclosure Docket No. 3468

MICROSTRUCTURAL CHARACTERIZATION OF Fe-18Cr-8Ni-xAl AND Ni-20Cr-yAl COATINGS

A Report

Submitted to

Dr. N.S. Cheruvu
Southwest Research Institute
San Antonio, TX
Tel: 210-522-2492
e-mail: scheruvu@swri.org

By

Professor C. Suryanarayana
Department of Mechanical, Materials and Aerospace Engineering
University of Central Florida
Orlando, FL. 32816-2450
Tel: 407-823-6662; FAX: 407-823-0208
e-mail: csuryana@mail.ucf.edu

EXECUTIVE SUMMARY

Vapor deposited samples of SS 304 containing 0, 3, 7, and 10 wt.% Al deposited on SS 304 substrates and Ni-20Cr containing 3, 7, and 10 wt.% Al deposited on Ni-20 Cr substrates were received from the Southwest Research Institute. All these seven samples were characterized for their structural features using X-ray diffraction (XRD) and transmission electron microscopy (TEM) techniques.

The predominant phase in all the SS 304-based coatings was the α (BCC) phase, instead of the expected g (FCC) phase, a result of the "rapid quenching" process that occurs during vapor deposition. Further, the coating without any Al in it, additionally showed the presence of a σ phase and this was absent in the Al-containing coatings. A lath structure was observed in all the samples and the lath width increased with increasing Al content, reaching a large value of 1200 nm in the coating that contained 10 wt.% Al. Another phase with a BCC structure, in small quantities, was also detected in all the samples. In samples containing large quantities of Al (say 7 and 10 wt.%), an ordered FeAl (B2) phase was also detected, confirmed both by XRD and TEM techniques.

The structural and microstructural features were significantly different in the Ni-20Cr-based alloy coatings. The matrix phase was the expected γ (FCC) phase in all the coatings. Free Al was also found to be present, confirmed from XRD patterns and elemental mapping methods in the TEM. These two phases formed alternate layers with about 12 nm-wide Ni-Cr layers and 3 nm-wide Al layers. The presence of these two independent phases in the diffraction patterns and observation of a multilayered structure in the electron micrographs suggests that alloying did not occur in these coatings. Since alloying did not take place, formation of the ordered NiAl (B2) phase did not occur in this case. It is possible that this heterogeneous microstructure will lead to poor oxidation resistance during cyclic oxidation behavior of these coated samples.

1. OBJECTIVE OF THE PROJECT

The primary goal of this project was to characterize the alloy coatings for their crystal structure and microstructure. This involved crystallographic study using X-ray diffraction (XRD) and microstructural characterization using optical microscopy (OM), scanning electron microscopy (SEM) and transmission electron microscopy (TEM) techniques, and then to establish a correlation between the two groups of characterization techniques.

2. SAMPLES RECEIVED

The following samples were received from the Southwest Research Institute (SwRI), San Antonio, TX through Dr. N.S. Cheruvu. Surface coatings of about 25 μm thick were deposited by the plasma-enhanced magnetron sputtering method on two commercially known alloy substrates, viz., Stainless Steel 304 (SS 304, Fe-18Cr-8Ni) and a Haynes Alloy 230, i.e., Ni-20 wt.% Cr (referred to as Ni-20Cr from now on) alloy. The coatings on stainless steel consisted of SS 304 to which different amounts of Al were added. Similarly, for the Ni-20Cr alloy also, the coating consisted of Ni-20Cr to which different amounts of Al was added. Table I summarizes the different samples received.

Table I. Summary of Samples received from the Southwest Research Institute, San Antonio, TX.

Substrate	**Coating**
SS 304	SS 304 + 0 wt.% Al
	SS 304 + 3 wt.% Al
	SS 304 + 7 wt.% Al
	SS 304 + 10 wt.% Al
Ni-20Cr (Haynes Alloy 230)	Ni-20Cr + 3 wt.% Al
	Ni-20Cr + 7 wt.% Al
	Ni-20Cr + 10 wt.% Al

3. CHARACTERIZATION

All the coatings were characterized using different metallographic techniques. Characterization involved the use of OM, SEM, XRD, TEM (Philips Tecnai F30, operated at 300 kV) techniques. Samples for TEM study were prepared by the Focused Ion Beam (FIB) technique. XRD was used primarily for phase identification and following this detailed TEM investigations were done to study the number of phases, their microstructural features and composition.

4. RESULTS OF SS 304 + xAl COATINGS (x = 0, 3, 7, and 10 wt.%)

4.1. Optical Microscopy

All the coatings have been shown to have a columnar or lath structure with preferred orientation (texture) in them. Fig. 1(a) shows an optical micrograph of the coating of SS 304 + 3 wt.% Al on an SS 304 substrate. It may be noted that the coating is uniform with a thickness of about 30 μm. A typical secondary electron image from FIB is shown in Fig.1 (b). Similar microstructural features were shown by all the other samples.

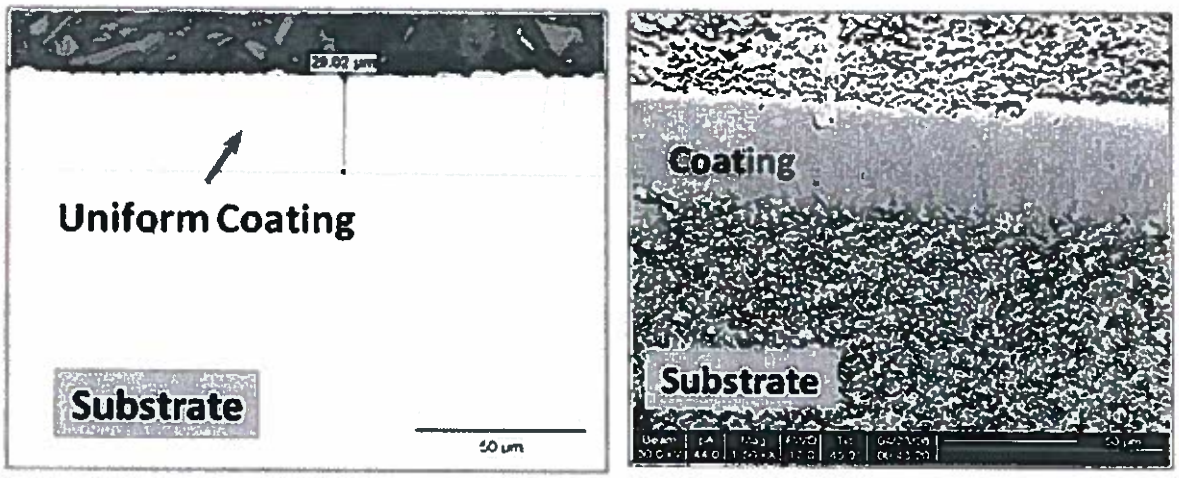

Fig. 1 (a) (left) Optical micrograph of the SS 304+3 wt.% Al coating on an SS 304 substrate. (b) (right) Secondary electron micrograph obtained from the FIB of the SS 304+3 wt.% Al coating (tilt 45°).

4.2. X-ray Diffraction (XRD) Studies

XRD patterns provide vital information related to the number and types of phases present in the samples. This technique is very useful in identifying the phases, their grain sizes, and any texture, if present in them. All the alloy coatings were characterized using XRD in the as-deposited condition. The XRD patterns of the SS 304 + xAl coatings along with their indexing are shown in Fig. 2. Details of the phases present and their crystal structures and lattice parameters are presented in Table II.

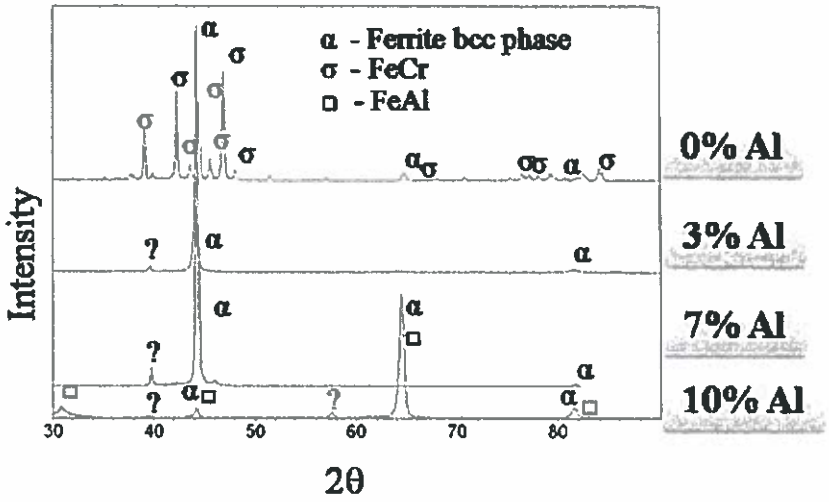

Fig. 2 XRD patterns of the SS 304 + xAl coatings (x = 0, 3, 7, and 10 wt.%)

Table II. Summary of results of crystal structures and lattice parameters of the different SS 304 based coatings as identified from the X-ray diffraction patterns.

Sample	Designation	Wt.% Al	Phase	Crystal Structure	Lattice parameters	
					a (nm)	*c* (nm)
1	Uncoated SS 304	0	γ	FCC	0.3590	-
2	SS 304 + 0Al	0	α	BCC	0.2876	-
			Sigma (σ)	Tetragonal	0.882	0.458
3	SS 304 + 3Al	3	α	BCC	0.2882	-
4	SS 304 + 7Al	7	α	BCC	0.2882	-
5	SS 304 + 10Al	10	α	BCC	0.2880	-
			FeAl	B2	0.2880	-

It may be noted that the SS 304 substrate material is austenitic and therefore has an FCC structure. The XRD pattern from the substrate material (not shown here) confirms that the structure is FCC with the expected lattice parameter of 0.359 nm (Table I). But, an FCC phase was not observed in any of the coatings, even without any Al present. Instead, a BCC phase (designated as the α phase here) with a lattice parameter of about 0.288 nm was observed in all the coatings. While this was the predominant phase in all the coatings, other minor phases were also noted to be present in some of the coatings.

The additional reflections in the coating without any Al in it could be satisfactorily indexed on the basis of a phase with a tetragonal structure and with the lattice parameters a = 0.882 nm and c = 0.458 nm. By comparing the structure and lattice parameters of this phase with those reported in the literature, this precipitate phase was designated as the σ (sigma) phase with the Pearson symbol tP30. It is also important to remember that this σ phase is present only in the coating without any Al in it. This phase did not form in the presence of Al in the coating. Accordingly, the σ phase was not present in the coatings that contained Al in them.

Ignoring the peak at the 2θ value of approximately 40°, marked "?" in the XRD patterns shown in Fig. 2, no other secondary phase was present in the XRD patterns of the coatings with different Al contents (3, 7, and 10 wt.%). By careful analysis of the XRD patterns containing this "?" phase (Fig. 3), it has been indexed to have a BCC structure with the lattice parameter a = 0.319 nm, or close to 0.32 nm. According to the structure factor calculations, the (110) peak in the BCC structure is expected to be more intense than the (200) peak. But, the point of interest in the coatings with 3 and 7 wt.% Al is that the (110) peak of this BCC phase is quite intense, but the (200) peak is almost absent, suggesting that this could be due to textural effects. However, the (200) peak is more intense than the (110) peak in the coating with 10 wt.% Al.

The XRD pattern of the coating containing 10 wt.% Al needs a special mention. Even though peaks are present at the angular positions expected of the α (BCC) phase, there is an additional low-intensity peak at a 2θ value of about 31°. Interestingly, this peak corresponds to the (100) peak of the α phase. Based on the observation that the (100) peak is present, and also coupled with the electron diffraction evidence, to be presented later, this phase has been identified to be the ordered BCC phase and hence will be designated as the B2 (FeAl) phase, rather the α phase. The other superlattice peaks are not present, possibly due to their low

intensities. Another reason for their absence could be that the ordered phase was not present throughout the sample; it was present only in some areas of the sample, as confirmed by the presence of superlattice reflections. Therefore, it may be assumed that this coating with 10 wt.% Al added to SS 304 contains both the α and B2 phases.

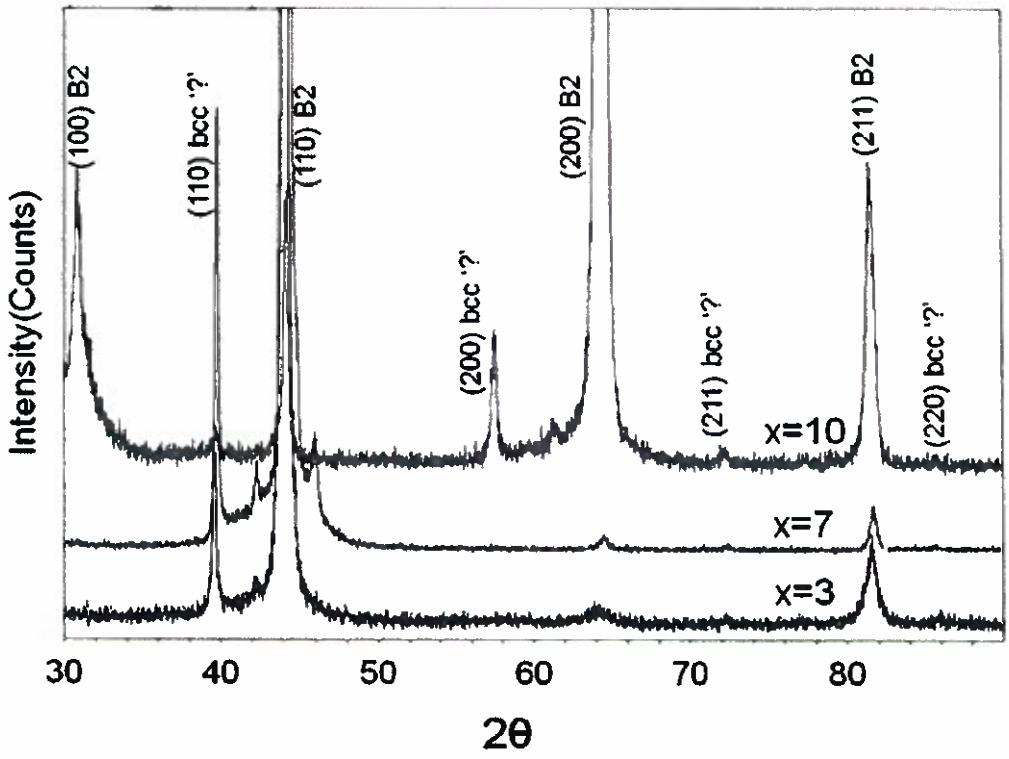

Fig. 3 XRD patterns of SS 304+xAl coatings (x = 3, 7, and 10 wt.% Al)

4.3. Transmission Electron Microscopy Studies

Transmission electron microscopy (TEM) studies helped in unraveling several important and novel structural features of the coatings. Thin foil samples of about 20 μm in length, 7 μm in width and 100 nm in thickness were prepared using the Focused Ion Beam (FIB) technique. The samples were then examined in a Philips Tecnai F30 TEM operating at 300 kV. In all the coatings, grains in the form of laths were observed. The lath size was measured using the linear intercept method and the lath width was used as a measure to characterize the alloy coatings. The average lath width was found to increase with increasing Al content in the SS 304 + xAl

coatings. In addition to the lath width measurements, TEM was also used to identify the type of phases and their distribution. Electron diffraction experiments were also conducted to understand the crystal structure features and relate them to the microstructural features. The following paragraphs briefly focus on each alloy coating from 0% Al to 10% Al.

4.3.1. SS 304 + 0%Al Coating

Fig. 4(a) shows a general view of the microstructure of the SS 304 coating containing 0% Al. The lath width varied from 40 to 230 nm, with an average lath width of about 130 nm, calculated using the linear intercept method across the laths. A typical diffraction pattern taken from this coating is shown in Fig. 4(b). Indexing of the ring pattern confirmed that the matrix is the α-Fe solid solution. Some precipitates of nanometer dimensions were found to be embedded in the α-Fe solid solution matrix. The size of these precipitates varied from about 5 to100 nm (Fig. 5). Many of them looked like larvae of butterfly with aspect ratios up to 20. They were also aligned parallel with the laths of the BCC matrix and most of them were present at the intersections of the lath boundaries. However, these precipitates were not seen to be present all over the matrix; they are limited to few areas.

As mentioned above, the average lath width was about 130 nm. The smallest selected area diffraction (SAD) aperture in our TEM was about 250 nm and therefore, diffraction patterns contained information from at least 2 or 3 laths. Consequently, the resultant SAD patterns contain information from multiple laths and so the diffraction pattern would be a superimposition of diffraction spots from many laths. A typical diffraction pattern is shown in Fig. 6(a). Obtaining a "single crystal" diffraction pattern from the precipitate region containing only the precipitate spots is very difficult as the size of the precipitate is <100 nm. Indexing of the diffraction pattern presented in Fig. 6(a) is shown in Fig. 6(b). It clearly confirms that the matrix phase has a BCC structure, and that the precipitate phase (σ, tP30) has a tetragonal structure. Preliminary information about the σ phase from the XRD patterns made the TEM indexing easy.

In this coating, the results of both XRD and TEM were similar and complemented each other to the maximum extent.

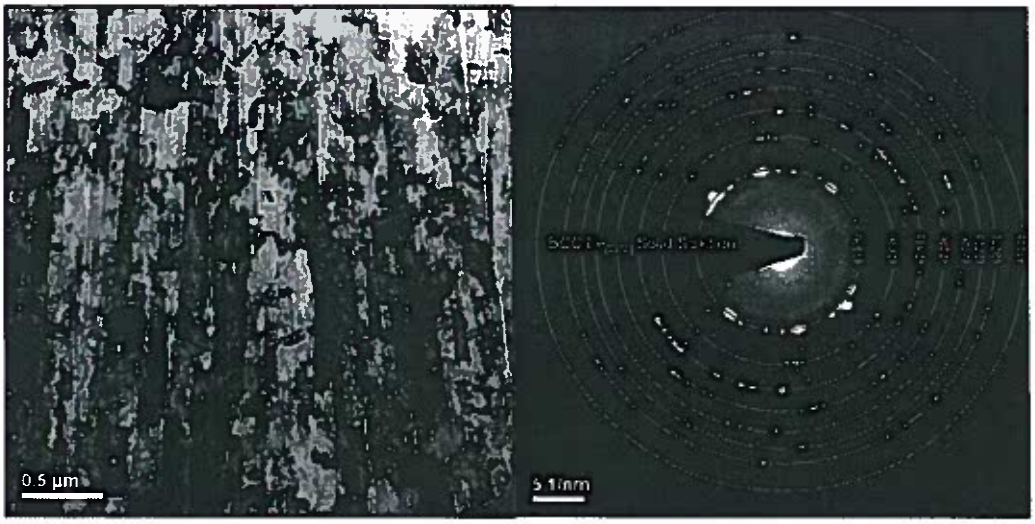

Fig. 4(a) (left) TEM bright-field image of the SS 304 coating containing 0 wt.% Al and (b) (right) shows the corresponding diffraction pattern. The diffraction rings have been indexed to belong to the α phase with a BCC structure and a = 0.28 nm.

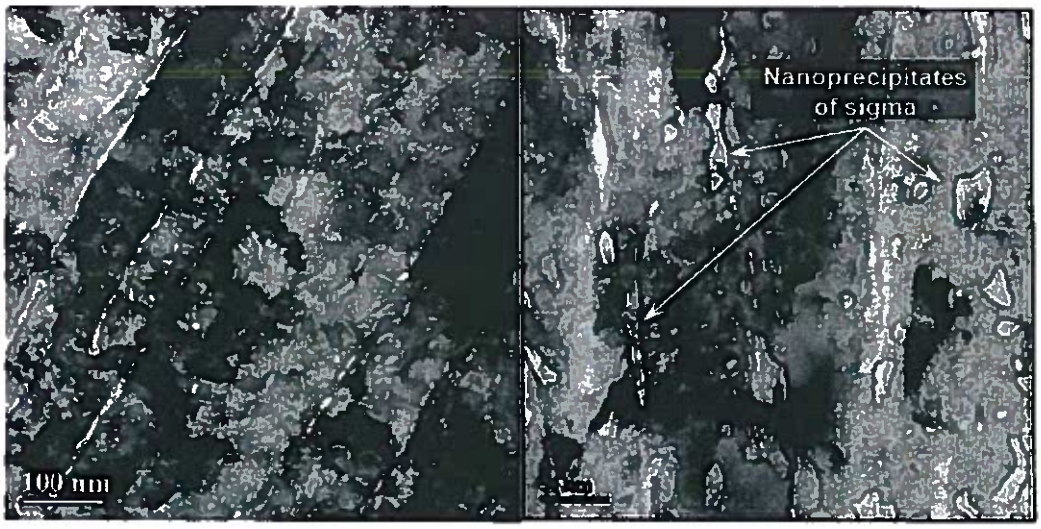

Fig. 5 TEM bright-field images of the SS 304 coating containing 0 wt.% Al showing the presence of some precipitates. Based on the diffraction evidence, shown in Fig. 6, these precipitates have been identified to belong to the sigma (σ) phase.

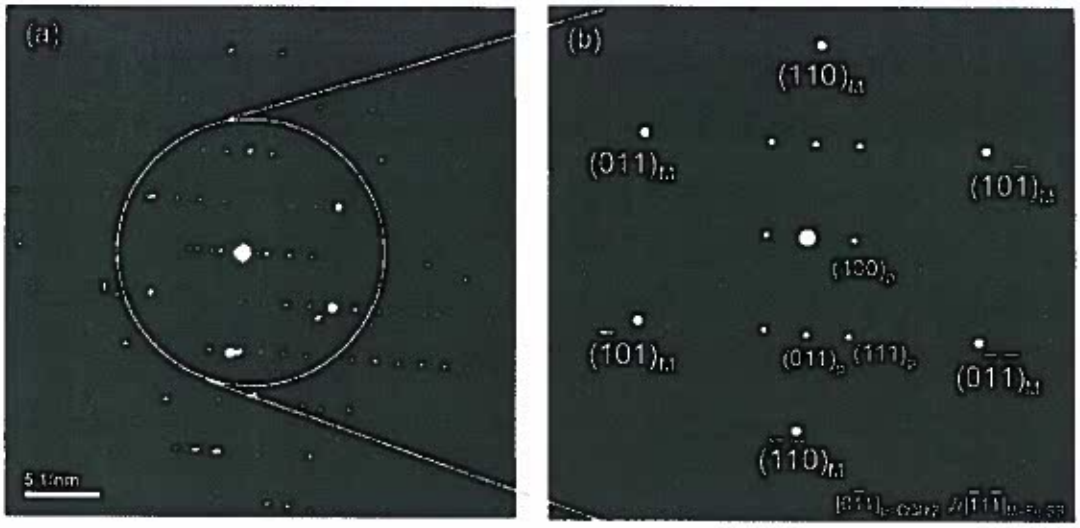

Fig. 6 (a) Selected Area Diffraction Pattern from a precipitate region of the coating with 0% Al. The indexing of the pattern in (b) shows that the low intensity spots near the transmitted beam belong to the σ phase.

4.3.2. SS 304 + 3 wt.% Al Coating

Fig. 7 shows a typical bright-field transmission electron micrograph from the coating of SS 304 containing 3 wt.% Al. In agreement with the XRD pattern from this coating, the TEM results show that the matrix (laths) has a BCC structure, which is the α-Fe solid solution. However, from the contrast in the laths it appears that they contain some defect structure. The coating has laths with an average lath width of about 600 nm. In addition to the above microstructural features, a multilayer lamellar structure was observed in the coating (Fig. 8) with an approximate lamellar thickness of 10 to15 nm. Similar structures were also noted to be present in Ni-20Cr+Al coatings on the Ni-20Cr substrates. Since these coatings have been well characterized in the Ni-20Cr system, the structural details will be described in the section on N-20Cr alloy coatings and will not be repeated here.

Fig.7 Bright-field electron micrograph from the SS 304 + 3 wt.% Al coatings showing the presence of laths and some internal "defect" structure inside them,.

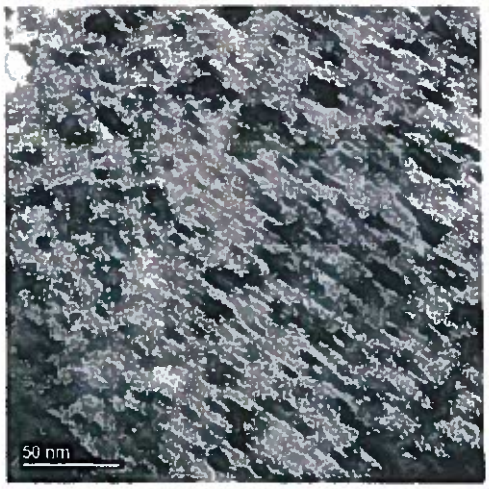

Fig. 8 Transmission electron micrograph the SS 304 + 3 wt.% Al coatings showing the presence of a layered structure.

4.3.3. SS 304 + 7 wt.% Al Coating

The structural details of the coating could be examined in detail using the TEM technique, which helped in revealing features that could not be identified on the basis of the

XRD technique alone. From the XRD pattern shown in Fig. 2, it appears that this alloy contained mostly the α-Fe solid solution (BCC) phase. A small peak corresponding to the "?" phase, which also has a BCC structure with the lattice parameter a = 0.32 nm, was also noticed to be present.

Fig. 9(a) shows a typical bright-field electron micrograph from this coating. Presence of lath structure, with a typical lath width of about 1000 nm, can be clearly seen. Even though there appears to be some internal structure inside the laths, it could not be clearly identified. By observing the electron diffraction pattern from this area, shown in Fig. 9(b), it becomes clear that superlattice spots are present. This suggests that, in addition to the α-Fe solid solution phase, the coating contains precipitates of an ordered phase, identified as the B2 (FeAl) phase.

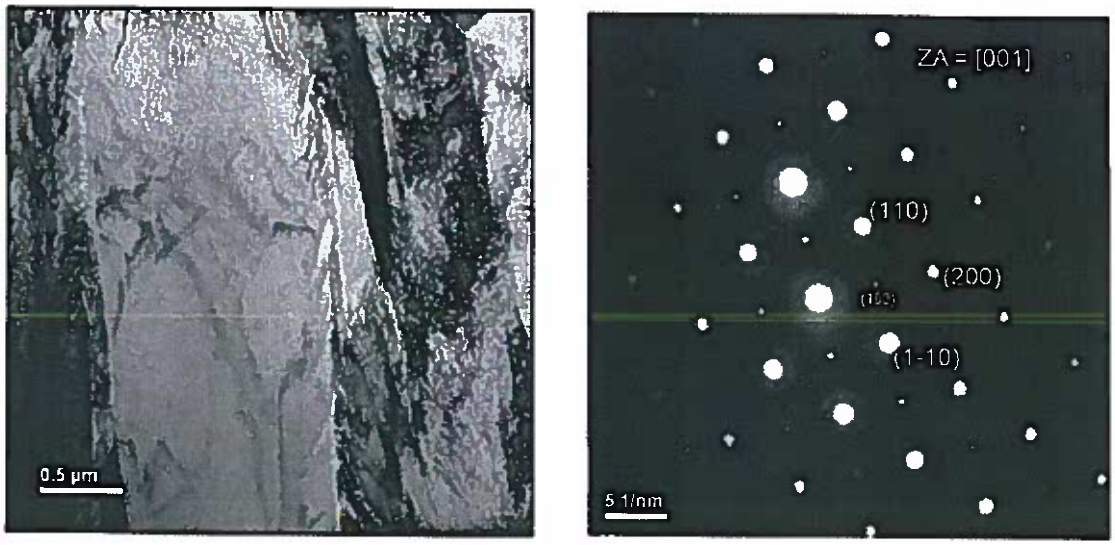

Fig. 9 (a) (left) Bright-field electron micrograph from the SS 304 + 7 wt.% Al coating. (b) (right) shows the corresponding diffraction pattern, clearly revealing superlattice spots suggesting that, in addition to the matrix phase, possibly precipitates with an ordered structure are present. Thee precipitates have been identified as FeAl with a B2 structure.

In addition to the α-Fe laths and the B2 (FeAl) phase inside the laths, which are clearly identified, and the "?" phase identified as another BCC phase, additional multilayer structure is also observed in this alloy coating. Preliminary observations suggest that this multilayer structure could consist of two layers, viz., an Fe-Cr-Ni solid solution layer and an Al layer, which could be either the pure metal or the solid solution. This inference is made based on the results from the

Ni-based alloy coatings which will be discussed in detail under the section on Ni-20Cr coatings. It is important to remember, however, that the multilayer structure is limited to only a few grains.

This particular coating with 7 wt.% Al added to SS 304 clearly brings out the importance and necessity of using the TEM technique in conjunction with the XRD technique in determining the number of phases and their identification. For example, from the XRD patterns, it was not possible to observe ordering since superlattice peaks were not present, nor any indication of the presence of a secondary phase could be obtained. But using the TEM technique, it was possible to detect the presence of ordering. One possible reason why the XRD patterns were not able to show the presence of ordering could be due to localization of ordering and/or the fact that the amount of the ordered phase is small in quantity.

4.3.4. SS 304 + 10 wt.% Al Coating

As mentioned earlier, XRD patterns from this coating show the presence of three phases, viz., the α-Fe solid solution phase, the FeAl (B2) ordered phase, and a partially identified BCC phase. Additionally, texture in the [200] direction was also noted.

Fig. 10 shows a typical bright-field electron micrograph and the corresponding diffraction pattern from this coating. Laths with an average width of approximately 1200 nm, representing the primary α-Fe solid solution phase, confirmed by selected area electron diffraction patterns, were present throughout the coating. The diffraction patterns also clearly show the presence of superlattice spots, indicating the presence of an ordered phase. Thus, these observations are consistent with the XRD observations. However, surprisingly, we did not observe any anti-phase boundaries (APBs), which are typically expected to be present in the electron micrographs from ordered alloys. Possible reasons for not observing the APBs are mentioned in the discussion section 4.4.6.

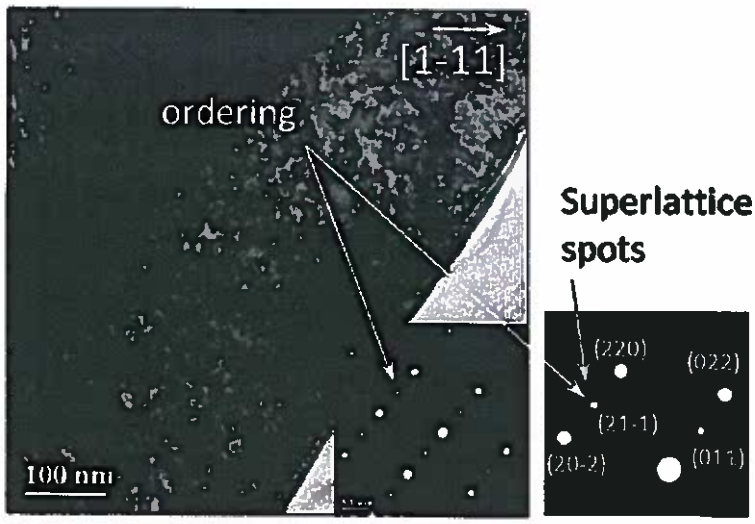

Fig. 10 Typical bright-field electron micrograph and the corresponding diffraction pattern from the SS 304 +10 wt.% Al coating. Observation of superlattice spots in the diffraction pattern clearly confirms the presence of an ordered phase in the coating.

4.4. Discussion

The following points become obvious from the above XRD and TEM observations made on the SS 304 + Al coatings:

1. Laths were present in all the samples, but the lath width was different in the samples with different Al contents.
2. The matrix phase in all the coatings was identified as the α-Fe solid solution with a BCC structure.
3. A sigma (σ) phase was found to be present in the form of precipitates in the Al-free coating (i.e., SS 304 + 0 wt.% Al coating), but not in the coatings that contained Al.
4. A multilayered structure was observed in majority of the samples.
5. A BCC phase, with a lattice parameter of 0.32 nm, was also detected in all the coatings that contained Al.
6. Clear presence of ordering was noticed in the coatings that contained Al; clearly identified in coatings that contained 7 and 10 wt.% Al.

4.4.1 Variation of Lath Width with Al Content

There was significant variation in the measured lath width in each sample, from region to region. For example, in the coating with 0 wt.% Al, the minimum and maximum measured values were 40 nm and 230 nm, respectively; the average value was approximately 130±100 nm. In spite of this variation, the observed trend was that the average lath width in the coatings increased with increasing Al content in the SS 304 + Al coatings. The average lath widths were 130 nm, 600 nm, 1000 nm, and 1200 nm for the coatings with the Al contents of 0, 3, 7 and 10 wt.% Al, respectively. Fig. 11 shows the variation of the lath width as a function of the Al content, and it may be noted that the lath width increased more or less linearly with Al content, although it appears that the value may reach an asymptotic value at very high Al contents.

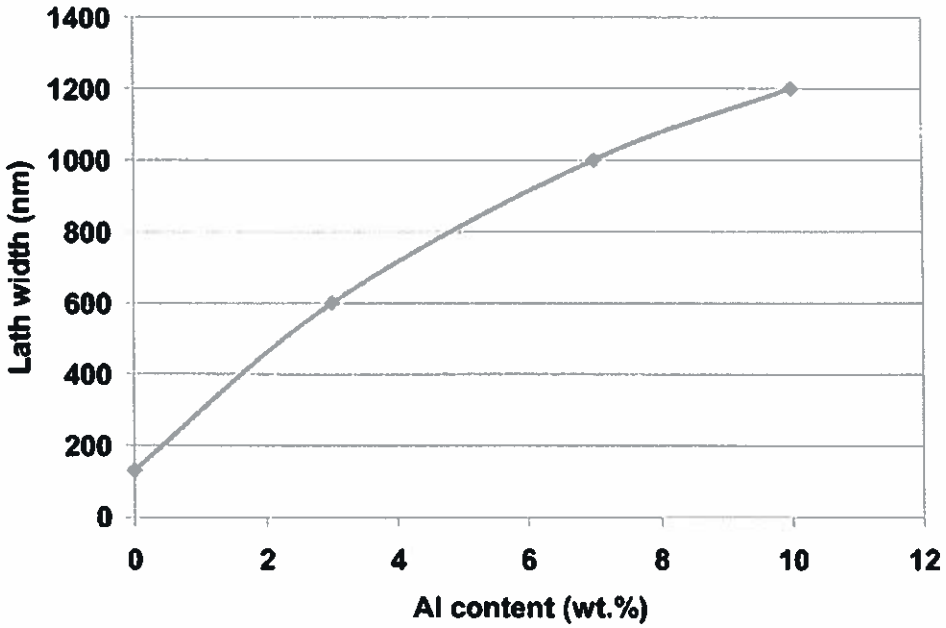

Fig. 11 Effect of Al content on the lath width in SS 304 + xAl coatings (x = 0, 3, 7, and 10 wt.%).

It may be appreciated that the lath width will have an important effect on the mechanical properties of the coating. As per expectation, the mechanical properties should be better with a decrease in the lath width. Therefore, controlling the lath width will provide a means of controlling the mechanical properties of the coating and consequently, it becomes important to

determine what factors determine the lath width in the coating. But, there could be many factors that determine the size of the laths that form which include the nucleation behavior of the laths, the influence of nature and amount of alloying additions added (Al, in the present case), the sputtering conditions, and the cooling behavior from the deposited state down to room temperature. Such a detailed study is beyond the scope of this project and therefore it has not been undertaken.

4.4.2. Formation of the α (BCC) Phase Matrix in all the Coatings

The starting alloy for the Fe-based coatings is 304 austenitic stainless steel, which has an FCC crystal structure (γ phase). Upon sputtering, the FCC phase has changed to a BCC phase in all the coatings, irrespective of whether they contained Al or not. But, the second phase present in the coatings has been found to be different depending upon whether Al was present or not. When the coating did not contain any Al in it, a σ phase was present, and this was absent when the coatings contained Al.

Al is a known to be a strong α (BCC) stabilizer, and therefore it is not surprising that the α phase has formed in the coatings that contained 3, 7 or 10 wt.% Al in them. If this were the reason for the formation of the BCC phase, then the BCC phase should not have been observed in the coating that did not contain any Al in it. But, both XRD and electron diffraction patterns confirm that the BCC phase was present in these coatings as well. Thus, it appears that the presence of Al is not the reason for the formation of the BCC phase in these coatings. There have been some studies earlier on the microstructure and properties of austenitic stainless steels solidified rapidly from the liquid state. In all the cases, it was reported that due to the non-equilibrium conditions of solidification, the ferrite (BCC) phase was stabilized instead of the expected austenite (FCC) phase. Retention of metastable phases as a result of non-equilibrium processing has been quite well known. Thus, we believe that in the present case also, sputter deposition of the coatings (a non-equilibrium "rapid solidification" process) is responsible for the formation of the α (BCC) phase in all the coatings.

4.4.3. Formation of the σ Phase in the Coating with 0 wt.% Al

As mentioned above, precipitates of a σ phase were found to be present in the α (BCC) matrix in the coating with 0 wt.% Al in it. The σ phase has a tetragonal (tP30) structure and this type of phase is observed in more than 40 binary systems. It is also present in many Fe-based alloys such as Fe-Cr, Fe-Mo, Fe-V, etc. The σ phase is brittle and so its presence is considered deleterious to the steel as the brittle precipitate phase consumes corrosive-resistant elements such as Cr and Mo during its formation and depletes the matrix of the same, especially near the grain boundaries. This makes the alloys very brittle and poor in corrosion resistance. Hence, formation of the σ phase is not desirable.

Addition of Al to SS 304 has been shown to suppress the formation of the σ phase. Consequently, there will not be any depletion of Cr from the matrix and therefore loss of corrosion resistance. Thus, Al addition seems to help improve not only the oxidation resistance of the alloy by forming a protective Al_2O_3 scale, but also the corrosion resistance in an indirect way.

4.4.4. Formation of Lamellar or Multilayer Structure in Coatings with 3 and 7 wt.% Al

Multilayer structures were observed extensively in all the Ni-based alloy coatings with different Al contents. On revisiting the transmission electron micrographs from the coatings on SS 304 samples, it was noted that the multilayered microstructures were present even in SS 304 + xAl coatings. The multi-layered structures were clearly seen in the coatings that contained 3 and 7 wt.% Al. But, the layers were limited to few grains. Each layer in the multilayered structure has a band width of about 12 nm, which is somewhat similar to that observed in the Ni-based alloy coatings. An explanation for the possible occurrence of multilayered structures is provided in the Section on Ni-based alloy coatings.

4.4.5. New BCC Phase in the SS 304 + xAl Coatings

In addition to the primary α (BCC) phase, presence of another BCC phase with a lattice parameter a = 0.32 nm was identified in almost all the SS 304 coatings that contained Al. Fig. 3

showed a series of XRD patterns which showed the evolution of this new BCC phase with the Al content.

Comparison with standard XRD patterns suggested that the metal Mo has a BCC structure with a lattice parameter a = 0.3146 nm, close to the observed value of 0.32 nm. No other equilibrium intermetallics in the Fe-Cr-Ni-Al system matched with the lattice parameter of the new BCC phase. But, there was no indication of the presence of Mo in the EDS spectra recorded during either SEM or TEM observations. Further, if it were to be present in small amounts, it would be dissolved in the Fe lattice to form a solid solution phase and will not be present as a separate phase. Therefore, it can be concluded that this new BCC phase does not correspond to the pure metal Mo.

If Al were to transform from the FCC to a BCC structure, then the expected lattice parameter for the new BCC Al would be a = 0.33 nm, and the observed lattice parameter for the new BCC phase is close to this value. Thus, a possible and tentative explanation for the occurrence of a BCC phase with a = 0.32 nm is that FCC Al has transformed to BCC Al.

Formation of metastable phases in thin films has been known for a long time. It has been reported that when a thin film is deposited, it will assume the crystal structure of the substrate on which it is deposited, if its thickness is below a critical value. In the present case, the SS 304 + Al coating has been deposited from two different sources, viz., SS 304 and Al. It has also been reported above that the deposited SS 304 layer assumed an α (BCC) structure. Since Al is now deposited on this BCC layer, the thin Al layer is likely to deposit into a BCC structure.

4.4.6. Presence of Ordering

Al can easily alloy with Fe to form the intermetallic FeAl, which has the ordered B2 or cP2 type structure. Such an ordered phase has been observed to form in the SS 304 + Al coatings containing 7 and 10 wt.% Al. Strong diffraction evidence for the presence of ordering is obtained from the selected area electron diffraction patterns shown in Figures 9 and 10. However, such ordering was not seen clearly in the coating with 3 wt.% Al in it. It is possible that since the amount of Al is less in this coating, the volume fraction of the FeAl phase formed is less and consequently we were not able to obtain clear diffraction evidence for its presence.

As was briefly alluded to earlier, anti-phase boundaries (APB's), typical of ordered structures, were not seen in the electron micrographs, even though diffraction evidence seems to strongly suggest the presence of ordering. Some possible reasons why the APB's are not seen in the electron micrographs are:

1. Ordered domains are larger than the laths. This is highly unlikely as the lath dimensions are very large. Their width is about 1 μm and their length is of several micrometers. A part of the domain boundary should have been seen under these conditions.
2. Ordered domains are very small. Observation of very small domains is not a big problem with advanced microscopes such as Tecnai TEM, which is being used by us.
3. Very localized ordering. As we have multilayers of Fe-rich and Al-rich layers in the coating, ordering might be taking place only at the interface between the Fe rich layer and Al layer. This can be easily detected by diffraction patterns but not in micrographs. This could be the most probable reason why the APB's are not detected. Special attention will be paid to this aspect in the future work.

5. RESULTS OF Ni-20Cr+yAl COATINGS (y = 3, 7, and 10 wt.%)

There were several structural features that were common between the Fe-based and Ni-based alloy coatings. These include the laths and multilayer structures. But, there were also significant differences between the two. For example, while ordering was observed in the Fe-based coatings, no evidence for ordering was present in the Ni-based coatings.

Since all the three Ni-based coatings exhibited very similar phase and microstructural features, all the three Ni-based alloy coatings will be discussed together to avoid repetition of the explanations.

5.1. X-ray Diffraction (XRD) Studies

XRD patterns of the Ni-based coatings i.e., Ni-20Cr + yAl, where y = 3, 7 and 10 wt.% are shown in Fig. 12. In all the three coatings, there are two phases, viz., the Ni-based solid solution (γ phase) with an FCC structure (a = 0.3586 nm) as the primary phase, and Al with an FCC structure as the secondary phase. All the coatings exhibited a texture with the (111) peak

being much more intense than the expected value and the (200) peak being virtually non-existent. Additionally, the γ(111) peak is very broad, i.e., the full width at half maximum (FWHM) is about 2°, with the 2θ value ranging from 43° to 45°. This peak broadening could be due to the following reasons: (i) extremely small crystallite size of γ phase, (ii) strain in the as-deposited coatings, or (iii) continuous extension of Ni lattice parameter due to the formation of solid solution of Ni with Al dissolved at the interfaces of Ni/Al multilayers.

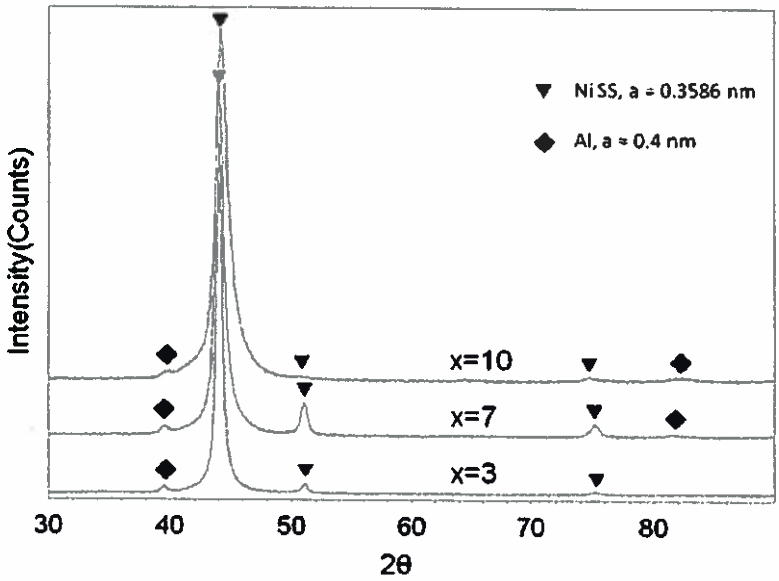

Fig. 12 X-ray diffraction patterns of the Ni-20Cr + yAl coatings (y = 3, 7, and 10 wt.%). All the XRD patterns show the presence of two phases. The Ni-based solid solution with an FCC structure is the major phase. Al with an FCC structure is also seen as a minor phase.

5.2. Transmission Electron Microscopy (TEM) Studies

Lath structures were observed in the Ni-based alloy coatings also that contained 3 and 10 wt.% Al. The average lath width in the coating with 3 wt.% Al was 440 nm, while that in the coating with 10 wt.% Al was 510 nm. From these values, it appears that the typical average lath widths were smaller in the Ni-based alloy coatings in comparison to those in the SS304 + Al coatings. The corresponding values in the SS 304 + 3 and 10 wt.% Al coatings were 600 and 1200 nm, respectively. Most surprisingly, no laths were observed in the coating that contained 7

wt.% Al either in the bright-field micrographs or in STEM micrographs. Typical bright-field electron micrographs of the coatings with 3, 7, and 10 wt.% Al are shown in Fig. 13.

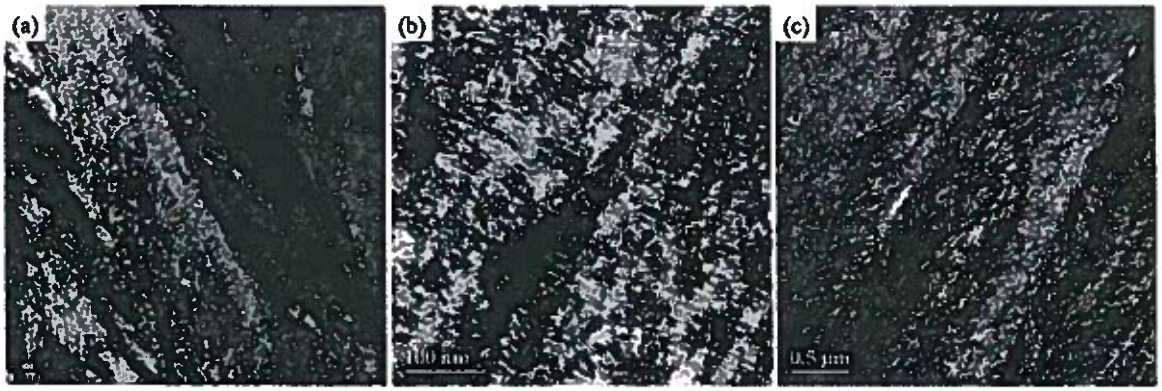

Fig. 13 Bright-field transmission electron micrographs of Ni-20Cr + yAl coatings with (a) y = 3 (b) y = 7, and (c) y = 10 wt.% Al. Laths could be clearly observed in the coatings with 3 and 10 wt.% Al. A multi-layered structure is clearly observed in the coating with 7 wt.% Al.

5.2.1 Multilayered Structure

In the microstructure of the Ni-based coatings, wavy and modulated structures of approximately 13 nm in thickness were observed. They were mostly oriented normal to the direction of deposition, i.e., across the laths. A thorough analysis was done using the different modes in the TEM, viz., bright field (BF), selected area diffraction (SAD), scanning transmission electron microscopy (STEM), energy dispersive spectroscopy (EDS), and Elemental Mapping in electron energy loss spectroscopy (EELS), to characterize the modulated/lamellar structure. These analyses were then correlated with the XRD results.

5.2.2. Bright Field Micrographs and SAD Patterns

Fig. 14 shows the bright-field transmission electron micrographs from the Ni-based alloy coatings containing 3, 7, and 10 wt.% Al. All three coatings show similar microstructures with two types of alternate bands in them. One type of the bands has a grey contrast with a width of about 13 nm, and the other band has a white contrast and a width of about 2 nm. The lamellar structure is prominent in all the coatings, but appears to be particularly prominent in the coating with 10 wt.% Al.

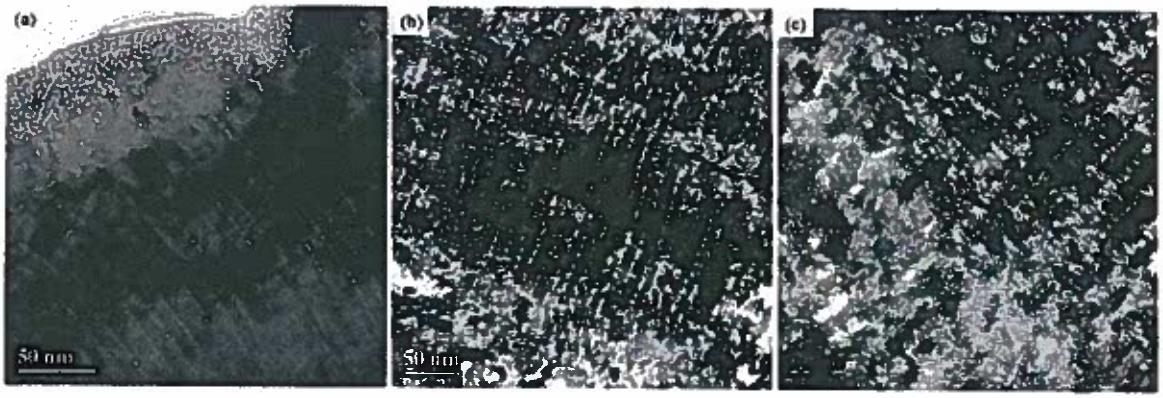

Fig. 14 Bright-field transmission electron micrographs showing the multilayered structure in the Ni-20Cr + yAl coatings with (a) y = 3, (b) y = 7, and (c) y = 10 wt.% Al.

Electron diffraction patterns from the thin samples of Ni-20Cr-yAl coatings are shown in Fig. 15. All the diffraction patterns show ring patterns characteristic of fine-grained polycrystalline material. The sequence of diffraction rings is characteristic of an FCC structure, from which the lattice parameter was calculated to be a = 0.356 nm. This value should be compared with the lattice parameter of Ni, which is a = 0.357 nm. These two lattice parameters are very close to each other suggesting that what we are dealing with here is the Ni solid solution in the coatings. Some differences also are noted in the diffraction patterns. While a combination of both rings and spots is seen in the coatings containing 3 and 7 wt.% Al, only a ring pattern is observed in the coating containing 10 wt.% Al. All the diffraction patterns were indexed to be having two phases - FCC γ phase and another FCC Al phase.

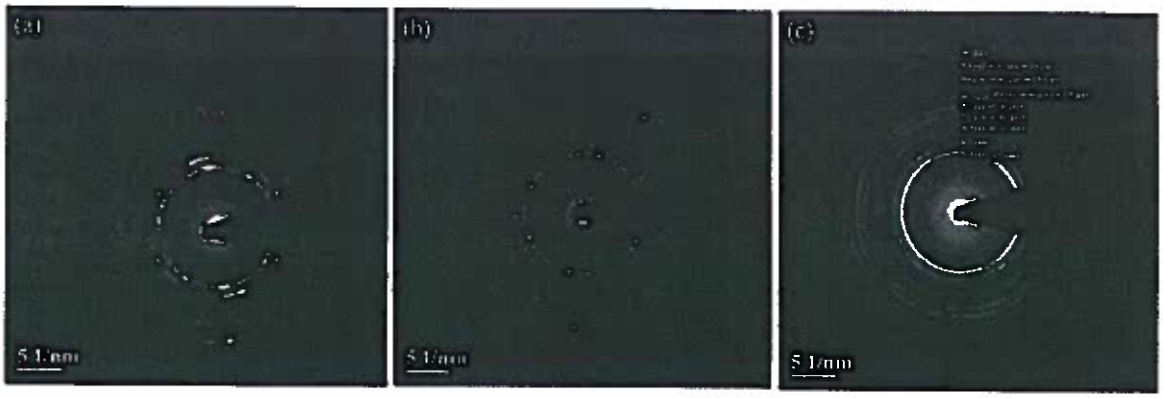

Fig. 15 Diffraction patterns from the Ni-20Cr + yAl coatings with (a) y = 3, (b) y = 7, and (c) y = 10 wt.% Al. The diffraction patterns were indexed on the basis of FCC γ and FCC Al phases.

5.2.3 STEM and EDS

The layers (bands) are much more clearly revealed in the STEM mode than in the bright-field micrographs. Fig. 16 shows a high-magnification STEM micrograph of the band structure from a Ni-20Cr-3Al coating and the corresponding line profile analysis using Ni Kα, Cr Kα and Al Kα. It can be clearly seen from the micrograph that there are two different types of bands in the wavelength span of about 15 nm. These are (i) Ni-rich Ni-Cr layer of about 12 nm width and (ii) Al layer of about 3 nm width. The Ni-rich layer further exhibits 3 different thicknesses, typically ~14, 12 and 10 nm, while the Al layer has a fixed thickness of about 3 nm. Since the band structure contains two types of layers with different compositions, this structure will be referred to as a multilayer structure. Very similar microstructures were observed in the coatings with 7 and 10 wt. % Al, shown in Fig. 17 and Fig. 18, respectively.

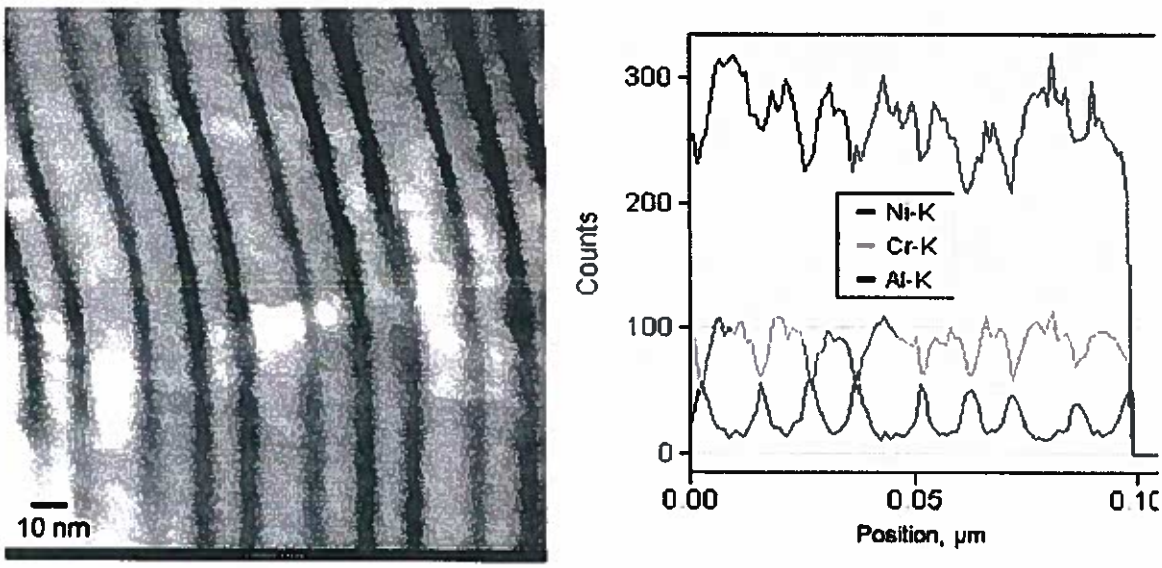

Fig. 16 Typical STEM micrograph of the Ni-20Cr + 3 wt.% Al coating and the corresponding line profile across the bands

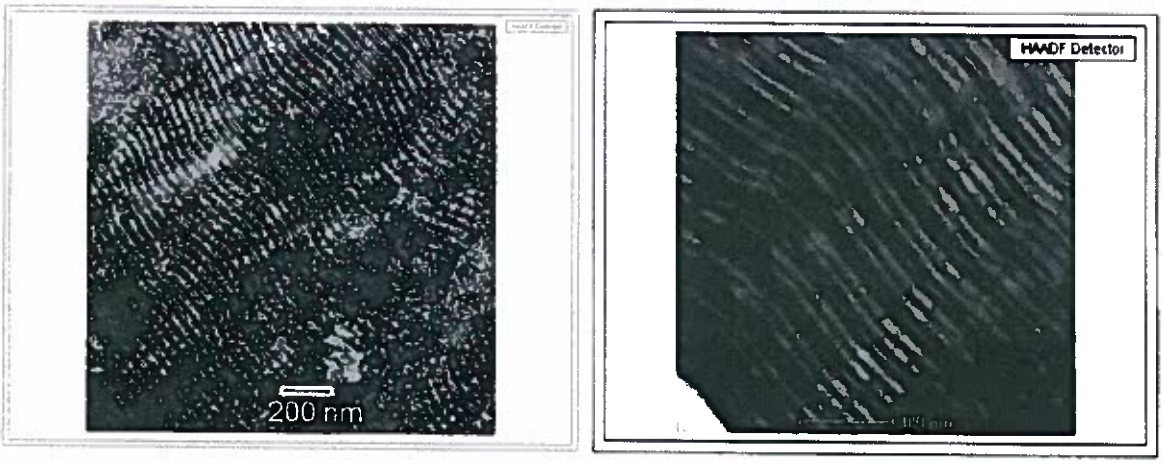

Fig. 17 Typical STEM micrograph of the Ni-20 Cr coating with 7 wt.% Al at low and high magnifications

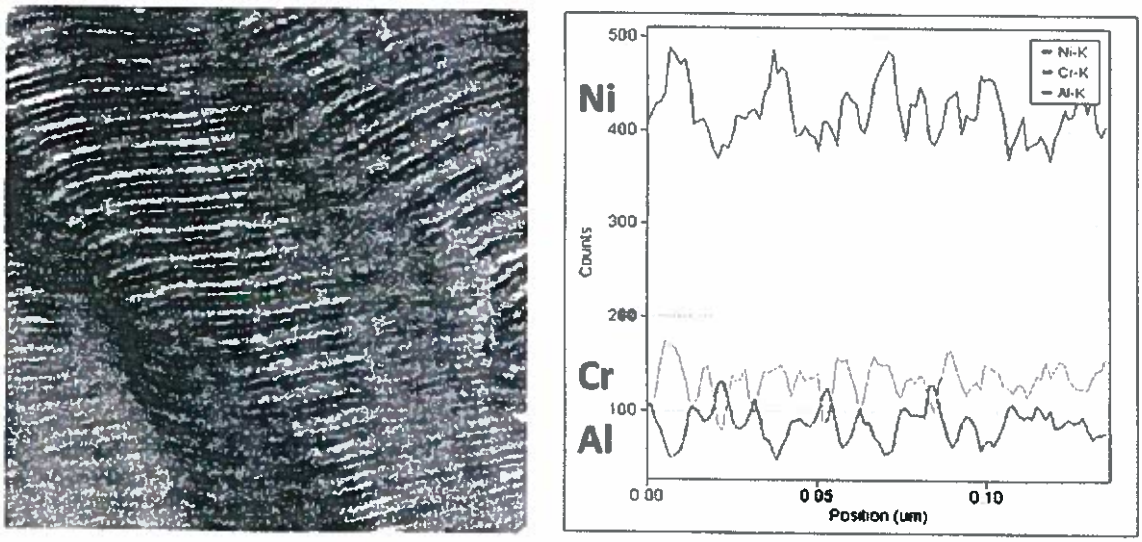

Fig. 18 A typical STEM micrograph of the Ni-20 Cr coating with 10 wt.% Al and the corresponding line profile across the bands.

5.2.4 Energy-Filtered TEM (EFTEM)

Energy filtering is a valuable tool for materials characterization and can be used to solve different problems. (i) **Zero-loss filtering** - By using only the zero-loss beam, all inelastically scattered electrons are omitted (reduction of noise). This leads to increased contrast in the TEM

images (especially important for specimens with low contrast, e.g., biological specimens) or in diffraction patterns. (ii) **Electron spectroscopic imaging** - By using electrons with a well-defined energy loss (ionization edge), elemental distribution maps can be generated. In the present case, since the coating contained three elements, viz., Ni, Cr, and Al, mapping for these three metals was done. The selected edges were Ni Kα, Cr Kα and Al Lα. Fig. 19 shows the elemental mapping of the multilayer structure in the Ni-20Cr-3Al coating. From these three maps, it can be unambiguously concluded that the wide bands (about 14, 12, 10 nm in width) belong to Ni-Cr solid solution (γ phase) and the narrow bands (2-4 nm) belong to Al. The band structure repeats at about 14 nm on average. That is like, 14, 3, 12, 3, 10, 3, 14, 3, 12....etc.

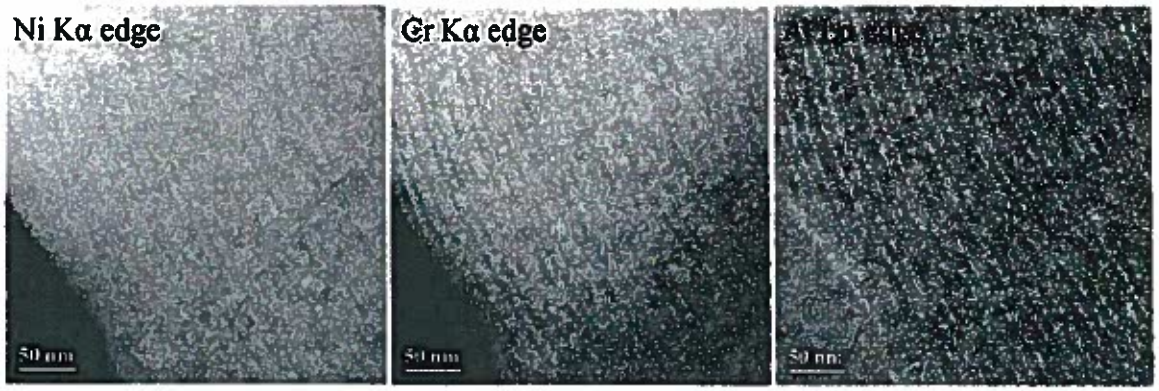

Fig. 19 Elemental mapping of the Ni-20Cr-3Al coating using Ni, Cr and Al ionization edges. It becomes clear from these images that the thin bands are Al-rich and that the thick bands are Ni-Cr-rich.

From the above observations, it become clear that the Ni-20Cr-yAl coatings (y = 3, 7, and 10 wt.% Al) contain primarily two types of bands. One is the γ phase, and the other is Al. The γ phase further has three different widths which are about 14, 12, and 10 nm, while the Al layer has a fixed width of 2-4 nm.

5.3. Discussion

Briefly summarizing the above results, we note that the Ni-20Cr-Al coatings showed the presence of laths in the coatings that contained 3 and 10 wt.% Al, but, surprisingly, not in the coating that contained 7 wt.% Al. But, more significantly, the microstructure showed a layered structure with 12-nm-thick layers of Ni-Cr and 3-nm-thick layers of Al stacked

alternately. It was also noted that the XRD patterns clearly showed the presence of the Al phase in all the coatings. These two observations put together suggests that alloying did not occur between these two components during the deposition process. That this is the possible reason for the formation of a layered structure gains support from the observation that the multilayer structure is more prominent at higher Al contents, e.g., 10 wt.% Al. However, there is not much change in the layer width either in γ phase layers of Al layers.

The formation of a layered structure during the deposition process will be easy to understand when we realize that two different targets were used to deposit Ni-20Cr and Al separately. But, the layered structure is likely to have an important influence on the oxidation resistance of the coatings.

6. CONCLUDING REMARKS

Vapor deposition, of either SS 304 (austenitic stainless steel) or Ni-20Cr alloy (Haynes alloy 230) to which different amounts of Al was added, on to SS 304 and Ni-20Cr alloy substrates, respectively, showed a variety of structural changes. The number of phases present, their crystal structures, and the microstructural features were different depending upon the Al content added. A lath structure was observed in all the coatings based on SS 304, while it was not so in the Ni-20 CR coatings. Addition of Al increased the lath width in both the SS 304 + Al and Ni-20Cr + Al coatings; but, the effect was much more significant in the SS 304 + Al coatings. Multilayered structures were observed very clearly in the Ni-20Cr coatings, but they were much less prominent in the SS 304 coatings. An ordered B2 phase (FeAl) was observed in the SS 304 + Al coatings, and such a phase was absent in the Ni-20Cr coatings.

Microstructure of SS304+x Al (x = 0, 3, 7, and 10 wt.%) and Ni-20Cr-10 wt.%Al Coatings

A report submitted by

By

Professor C. Suryanarayana

Department of Mechanical, Materials, and Aerospace Engineering

University of Central Florida

Orlando, FL. 32816-2450

1. INTRODUCTION

A significant amount of research has been carried out on the synthesis and characterization of nanocrystalline materials for the past two decades. One of the promising areas has been identified as nanocrystalline coatings, since they exhibit enhanced properties. For example, they show higher spallation resistance and wear resistance than their coarse-grained counterparts. The present work has been undertaken to study the effect of Al on the microstructure and oxidation resistance of coatings synthesized by magnetron sputtering. The specific coatings studied included 304-type austenitic stainless steel (SS304) coatings with different amounts of Al (0, 3, 7, and 10 wt.%) on SS304 and Ni-20Cr alloy coatings with different amounts of Al (0, 3, 7, and 10 wt.%) on Ni-20Cr alloy substrates.

The major objective of the current project is to characterize the alloy coatings for their grain size. This primarily involved metallographic study using transmission electron microscopy (TEM) to determine the grain size. Since the grain size of the coating affects oxidation resistance, we can estimate the potential of the alloy coatings, if they can resist oxidation and provide competitive life cycles similar to that in superalloys. Thus, the study reports the effect of Al on the grain size of SS304+xAl (x =0. 3, 7, and 10 wt.% Al) and Ni-20Cr+yAl (y =10 wt.%) alloy coatings before and after cyclic oxidation.

Plasma-enhanced magnetron sputtering technique was used to deposit the coatings of (i) 304-type austenitic steel (SS304) containing different amounts of Al on top of the SS304substrate, and (ii) Ni-20Cr with 10 wt.% Al on top of the Haynes 230 (Ni-20Cr) alloy substrate. X-ray diffraction (XRD) and transmission electron microscopy (TEM) were carried out to study the structure of the coatings. Samples for TEM were prepared either by Focused Ion Beam (FIB) or Ion Milling (IM) methods. In TEM, bright-field, dark-field, selected area diffraction, and energy dispersive spectroscopy (EDS) coupled with scanning transmission electron microscopy (STEM) were carried out to obtain useful information on the microstructure of the coatings. Phases present in the coatings were identified from the selected area electron diffraction patterns and the grain sizes were estimated from the bright-field and/or dark-field micrographs.

II. RESULTS - SS304-xAl

II.1. Phase Identification

X-ray diffraction patterns from all the coatings (both with and without Al in them) showed that ferrite (body-centered cubic (BCC) structure with a = 0.2882 nm) was the primary phase. In addition, when x = 0 (i.e., when the coating did not contain any Al) the coating contained the sigma intermetallic phase (tetragonal structure with a = 0.882 nm and c = 0.458 nm). An additional phase, B2 (an ordered phase based on the BCC structure) was also noticed in the coatings with x = 3, 7, and 10 wt.% Al coatings, and its amount increased with Al content. It was just barely noticeable in the coating with 3 wt.% Al and it was maximum in the coating with 10 wt.% Al.

II.2. Grain Size Measurements

II.2.1. SS304+10 wt.% Al Coating

Fig. II. 1(a) and (b) show bright-field electron micrographs of the SS304+10 wt.% Al coating. While (a) shows the cross-section micrograph, (b) shows the in-plane micrograph. The microstructure of the cross section clearly shows columnar grains which have grown in a direction perpendicular to the substrate, i.e., parallel to the direction of deposition. On the other hand, the in-plane micrograph shows an equi-axed microstructure. From Fig. II. 1(b), the grain size in the coating was estimated to be 1.4 μm; it should be noted, however, that the grain size varies somewhat and it is only the average value that has been reported here. Even though such micrographs represent the true grain size, one of the limitations is that only a few grains are noted. On the other hand, a very large number of columnar grains can be observed in the cross-sectional micrograph. Therefore, in this study, the width of the columnar grains was taken as a measure of the grain size.

The grain size was measured for a large number if grains shown in Fig. II. 1(a). Only those columnar grains were taken into account which had their length at least 4 times the width. The grain size was found to vary from as low as 130 nm to as high as 2.75 μm and the average grain size for this composition, from the columnar grains, was estimated to be 980 nm (Fig. II. 2).

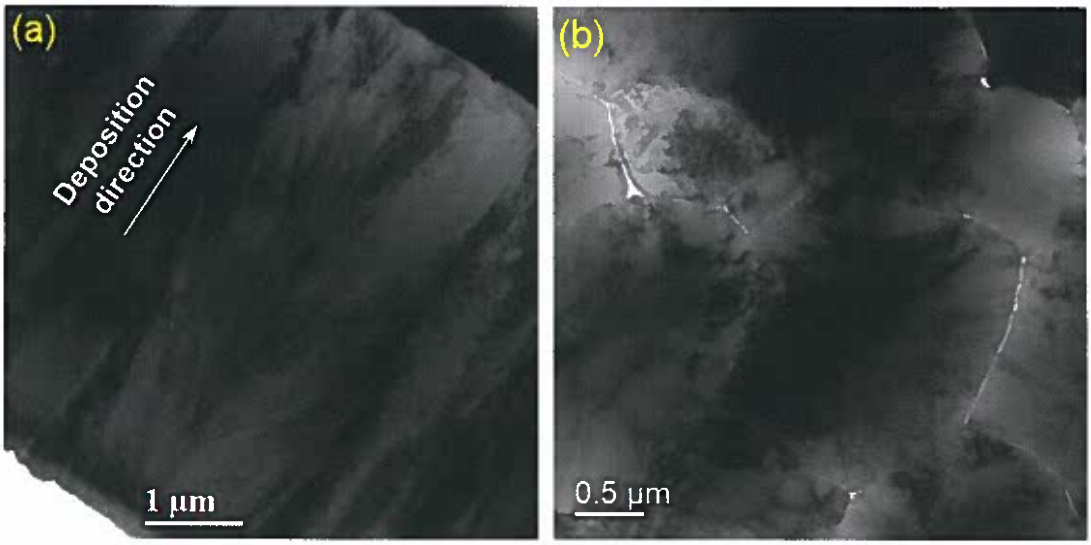

Fig.II.1(a) Microstructures of the SS304+10 wt.% Al coatings in the as-deposited condition. (a) Cross-section showing uniformly distributed columnar grains, and (b) in-plane sample showing equi-axed microstructure.

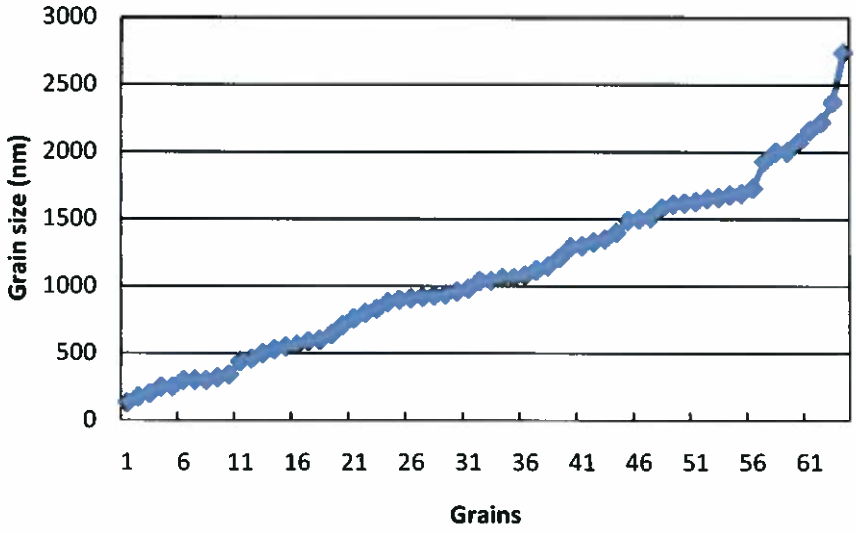

Fig.II.2. Variation of grain size in the SS304+10 wt.% Al coating. The grain size varied from about 130 nm to 2750 nm and the average grain size was estimated as 980 nm.

Grain sizes for the coatings in other compositions were also estimated in a similar way and the results of these estimates are presented in the following sections with increasing Al content.

II.2.2. SS304+0 wt.% Al Coating

Fig. II.3 shows a bright-field electron micrograph of the overall microstructure of the as-deposited SS304 coating. The microstructure contains columnar grains perpendicular to the substrate, with their longitudinal direction parallel to the deposition direction. The grain sizes of 101 grains were counted and their sizes are plotted in Fig. II.4. The grain sizes varied from 20 to 270 nm, and the average grain size was nearly 100 nm; the corresponding histogram of the distribution is shown in Fig. II.5. It may be noted that more than 60% of the grains were below 100 nm in size.

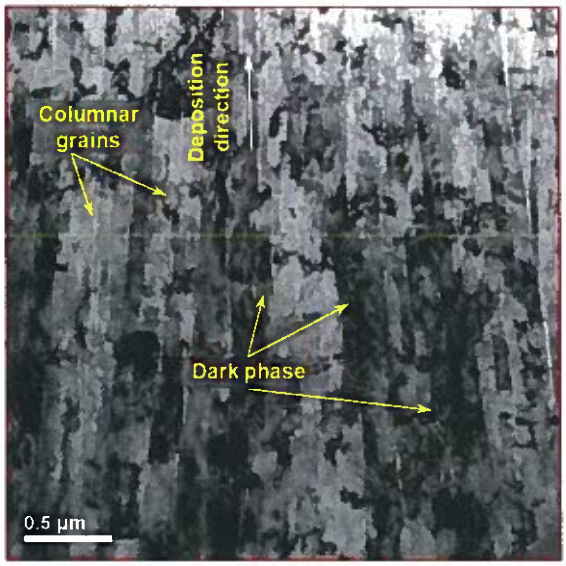

Fig. II.3. Typical bright-field electron micrograph showing the presence of columnar grains in the SS304+0 wt.% Al coating. These columnar grains are oriented in a direction parallel to the direction of deposition.

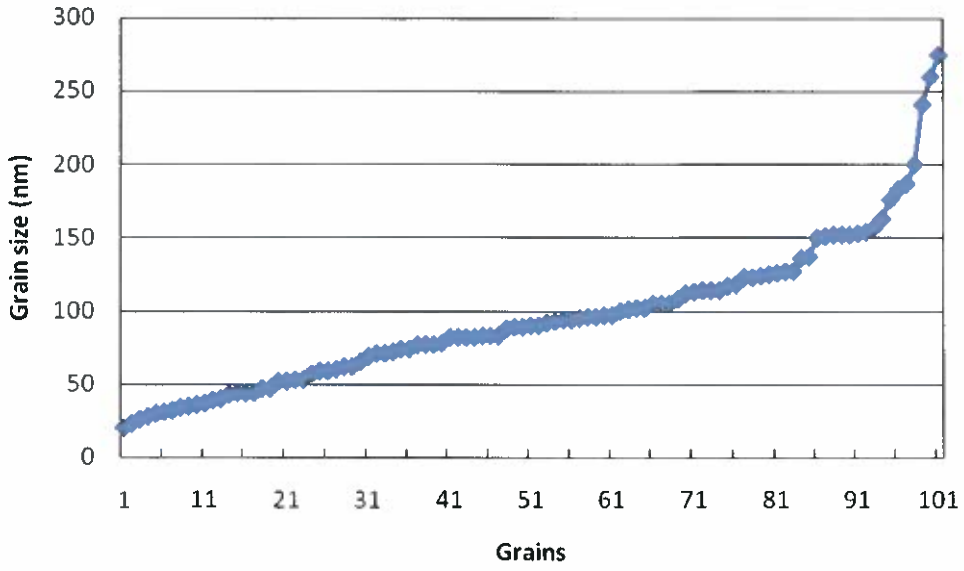

Fig. II.4. Variation of grain size in the SS304+0 wt.% Al coating. The grain size varied from about 20 nm to 270 nm, and the average grain size was nearly 100 nm.

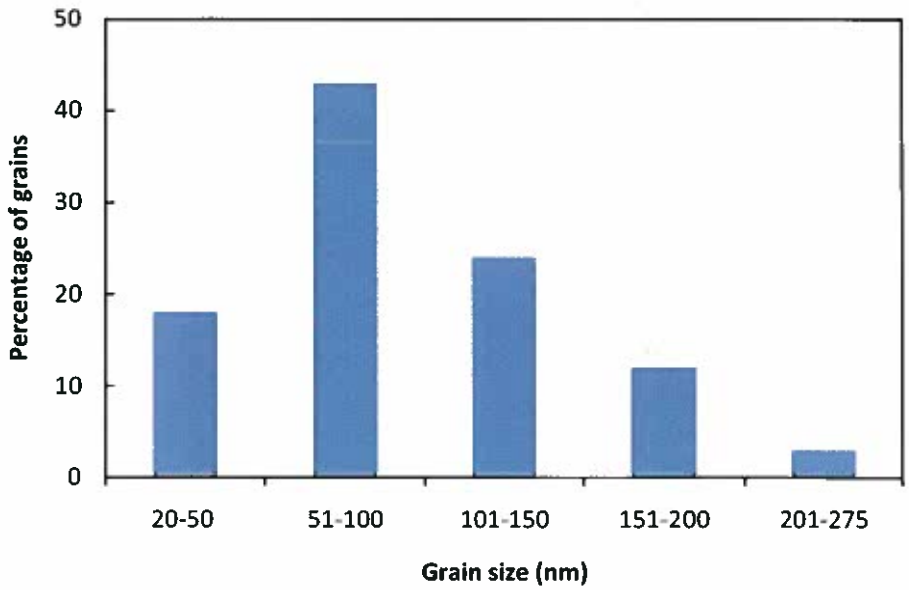

Fig. II.5. Histogram showing the grain size distribution in the SS304+0 wt.% Al coating.

II.2.3. SS304+3 wt.% Al Coating

Typical bright-field electron micrographs from the SS304+3% Al coating are shown in Fig. II.6. X-ray diffraction patterns from the coating indicated that the coating contained the ferrite phase with a BCC structure. The selected area diffraction pattern, shown as inset in Fig. II.6, also confirmed that the phase present is ferrite with the BCC structure. The grain size was measured in 2 samples of different thicknesses and their values varied from 30 nm to 1.2 μm. The average grain size was 190 nm for the thinner sample and 420 nm for the thicker sample. The average grain size of both the samples was estimated as 290 nm. Fig. II.7 shows the variation of grain size for all the grains in these coatings.

Fig. II.6. Bright-field transmission electron micrographs from the SS304+3% Al coating. A selected area diffraction (SAD) pattern is shown as an inset. From the indexing of SAD pattern, it is clear that the phase present is ferrite.

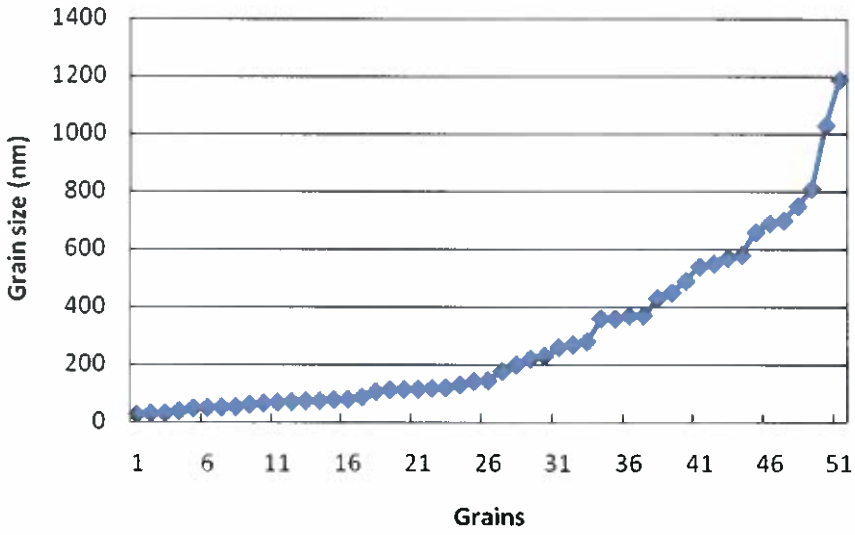

Fig.II.7. Variation of grain size in the SS304+3% Al coating. The grain size varied from about 30 nm to 1200 nm, with an average value of 290 nm.

II.2.4. SS304+7 wt.% Al Coating

The microstructure of the SS304+7 wt.% Al coating is shown in Fig. II.8. An important difference of the microstructure from the others is that the columnar grains in this coating were more randomly oriented. The grain size for this coating was shown to vary from 20nm to 1.6 μm, and the average grain size was estimated to be about 320 nm. The grain size distribution is shown in Fig. II.9.

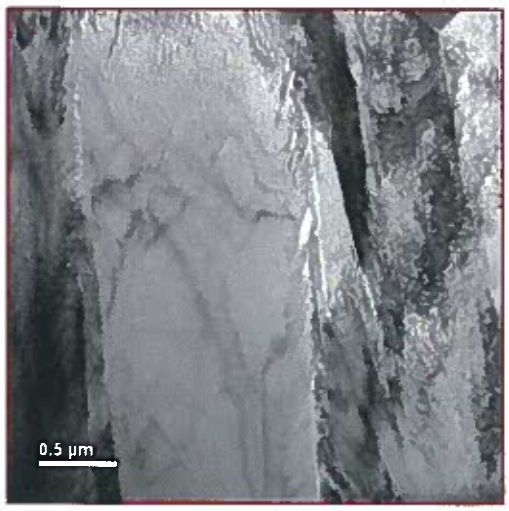

Fig. II.8. Bright-field electron micrograph of the SS304+7 wt.% Al coating. This microstructure appears to be different from the others described so far. For example, one can observe here one very wide grain and next to it several narrow grains.

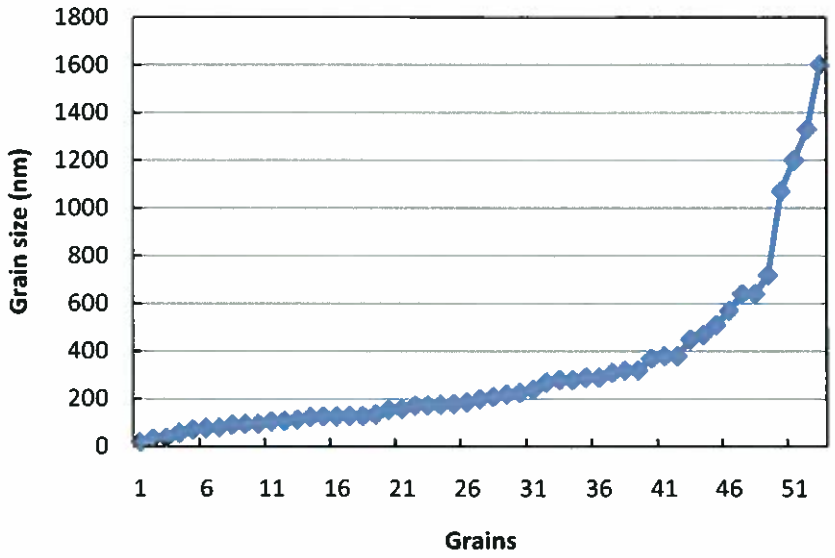

Fig.II.9. Variation of grain size in the SS304+7 wt.% Al coating. The grain size varied from about 20 nm to 1.6 μm, and the average grain size is about 320 nm.

The variation of grain size in all the four coatings of SS304+x Al (where x = 0, 5, 7, and 10 wt.% Al) is shown in Fig. II.10. The average grain sizes in the coatings were 100 nm, 290 nm, 320 nm, and 980 nm for the coatings with 0, 3, 7, and 10 wt.% Al, respectively. The largest grain size in these coatings increased with increasing Al content (Fig. II.11).

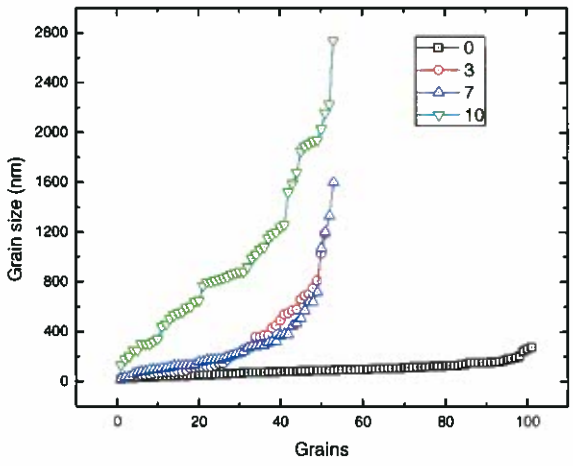

Fig. II.10. The variation of grain size in the SS304+x Al (where x = 0, 5, 7, and 10 wt.% Al) coatings.

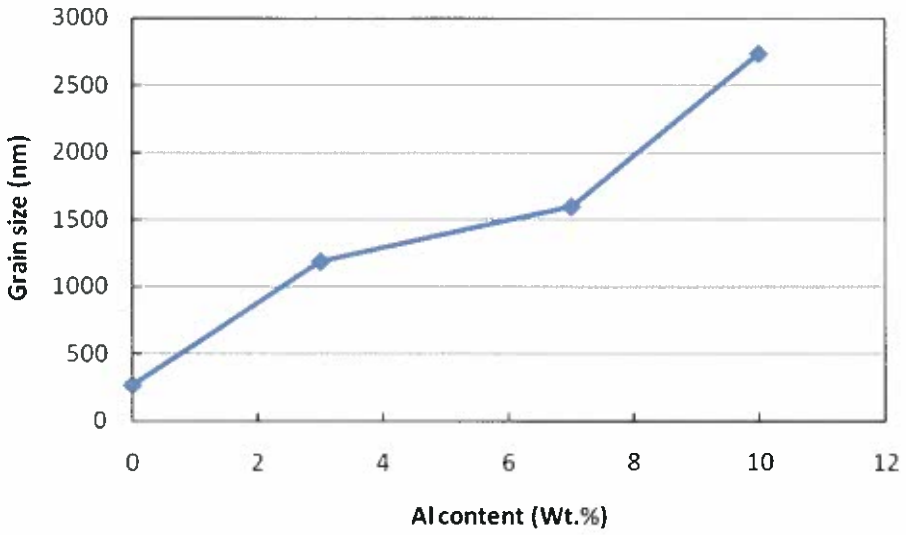

Fig. II.11 Effect of Al on the largest grain size in the SS304+x Al (where x = 0, 5, 7, and 10 wt.% Al) coatings.

III. MICROSTRUCTURE OF CYCLICALLY OXIDIZED SS304 COATINGS

Microstructural characterization was also conducted on cyclically oxidized SS304+0 wt.% Al coatings. Cyclic oxidation was carried out at 750 °C for 610 h (732 cycles, 50 min each). The samples were characterized using scanning electron microscopy (SEM), XRD and TEM techniques. Fig.III.1 shows an SEM micrograph containing a 2-3 μm oxide scale on top of coating. EDS analysis in the TEM showed that the oxide scale predominantly contained Cr_2O_3.

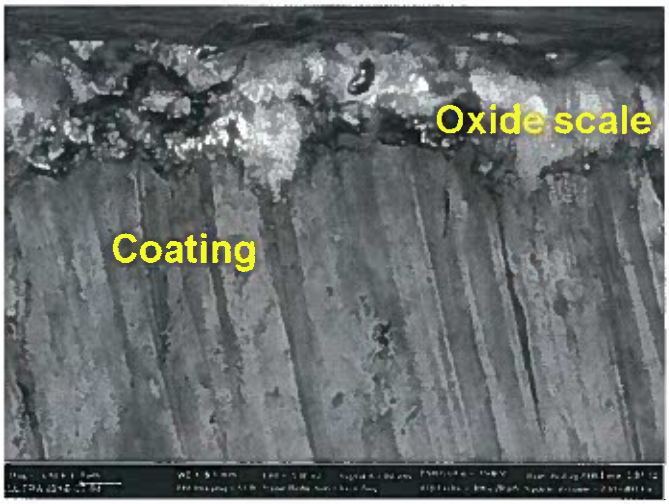

Fig. III. 1 SEM micrograph of cyclically oxidized SS304+0 wt.% Al coating. (scale marker corresponds to 1 μm). The oxide scale was mostly made up of Cr_2O_3., as determined by EDS in the TEM.

The main focus of the present work was on the measurement of grain size. Bright-field electron micrographs, similar to those presented in Fig. III.2, were used for this purpose. The grain size distribution is shown in Fig. III. 3. The grain size in the coating, after cyclic oxidation, varied from about 100 to 470 nm, with the average size of about 330 nm. Spallation occurred at the interfaces of these columnar grains as shown in Fig. III. 4.

In addition to the ferrite phase, the cyclically oxidized coating contained another secondary phase. This phase is in the form of small particles of about 100 nm in size and they appear near-circular in cross section (Fig. III.5). STEM micrographs with EDS analysis showed that theee particles contained predominantly Si.

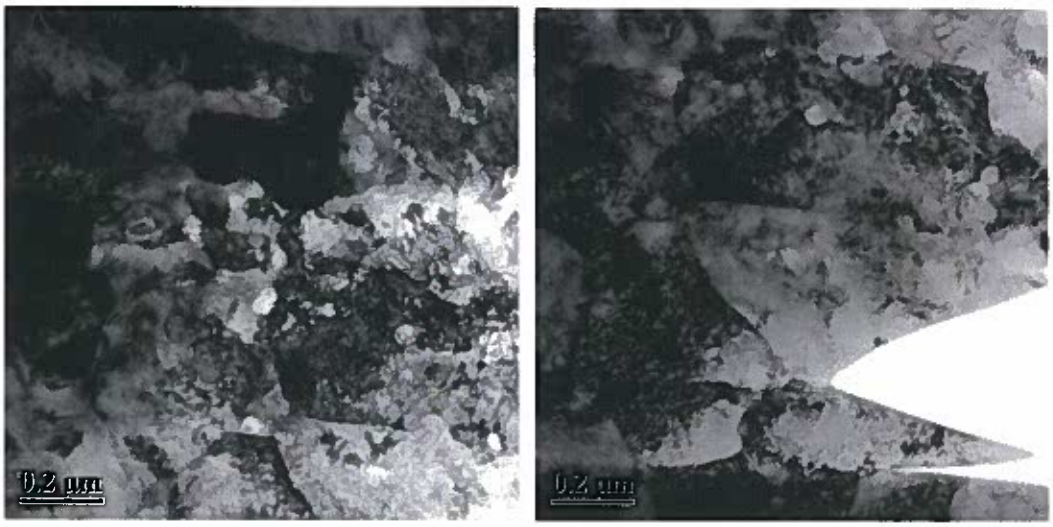

Fig. III. 2 Bright-field electron micrographs of the cyclically oxidized SS304+0 wt.% Al coating. Near-equiaxed grains are present with a typical average grain size of about 330 nm.

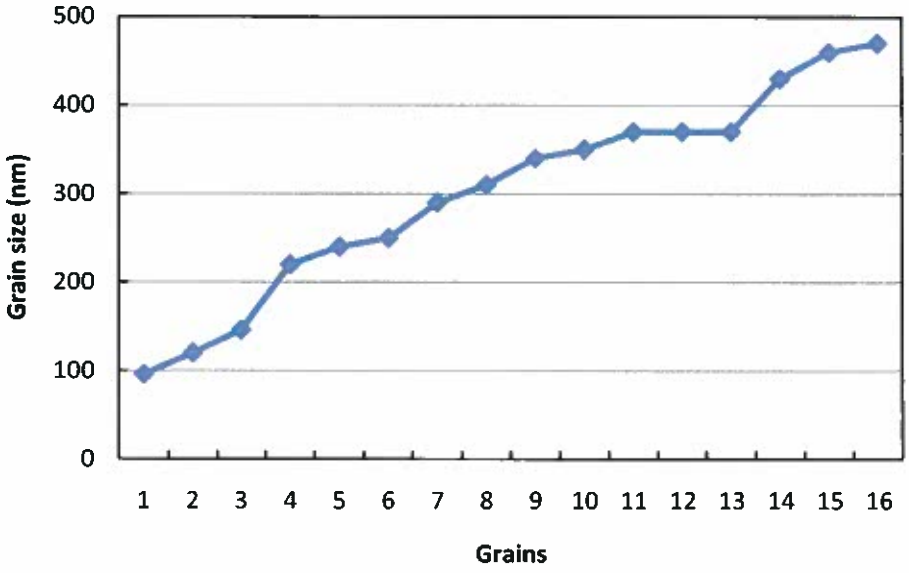

Fig. III. 3 Variation in the grain size of SS304+0 wt.% Al coating. The grain size varied from about 100 nm to 470 nm with an average size of 330 nm.

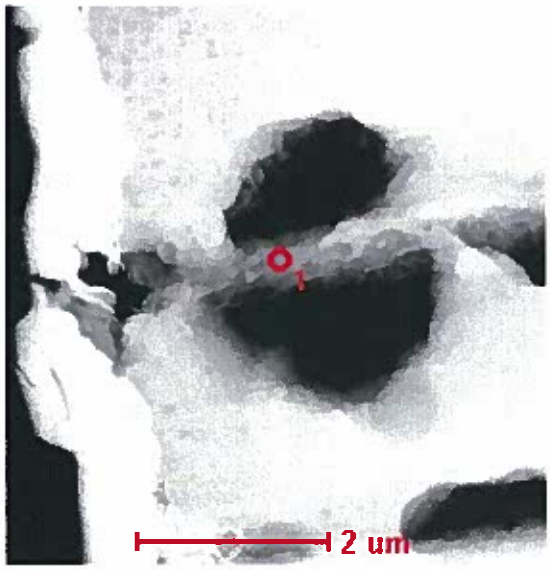

Fig. III. 4 Holes at the intersection of columnar grains in the SS304+0 wt.% Al coating indicating that spallation had occurred in the oxidized coating.

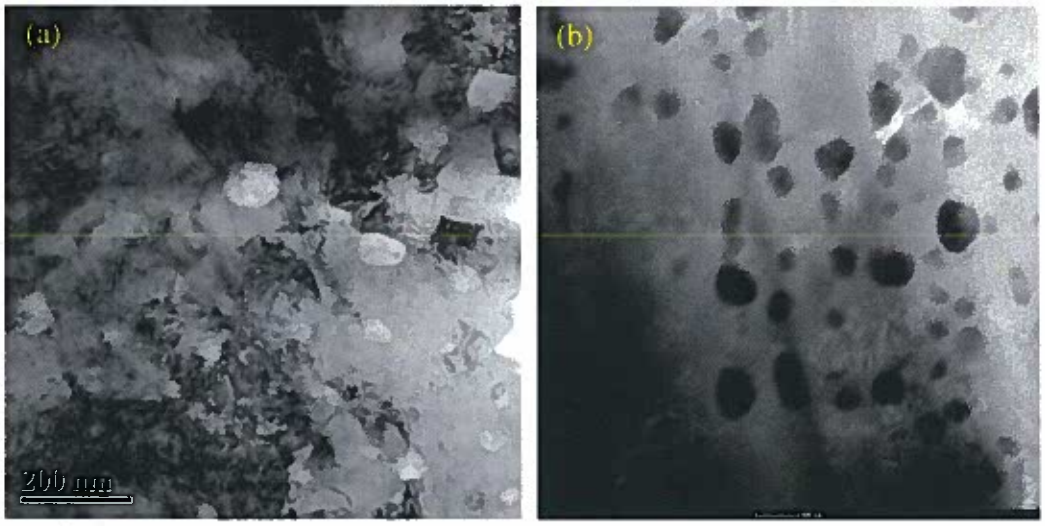

Fig. III. 5 (a) Bright-field electron micrograph showing the presence of embedded particles of up to 100 nm size. (b) STEM micrograph of the particles (scale marker 100 nm).

Energy-filtered transmission electron microscopy (EFTEM) was used to identify the elemental distribution. Fig. III. 6 shows the energy-filtered micrographs for Fe, Cr, Si, and O. These micrographs clearly indicate that these particles are SiO_2. However, no major Fe/Cr/Ni depletion was observed around the particles. From this it is clear that Si got oxidized at high

temperatures during cyclic oxidation experiments, even though Si was present only in a small quantity.

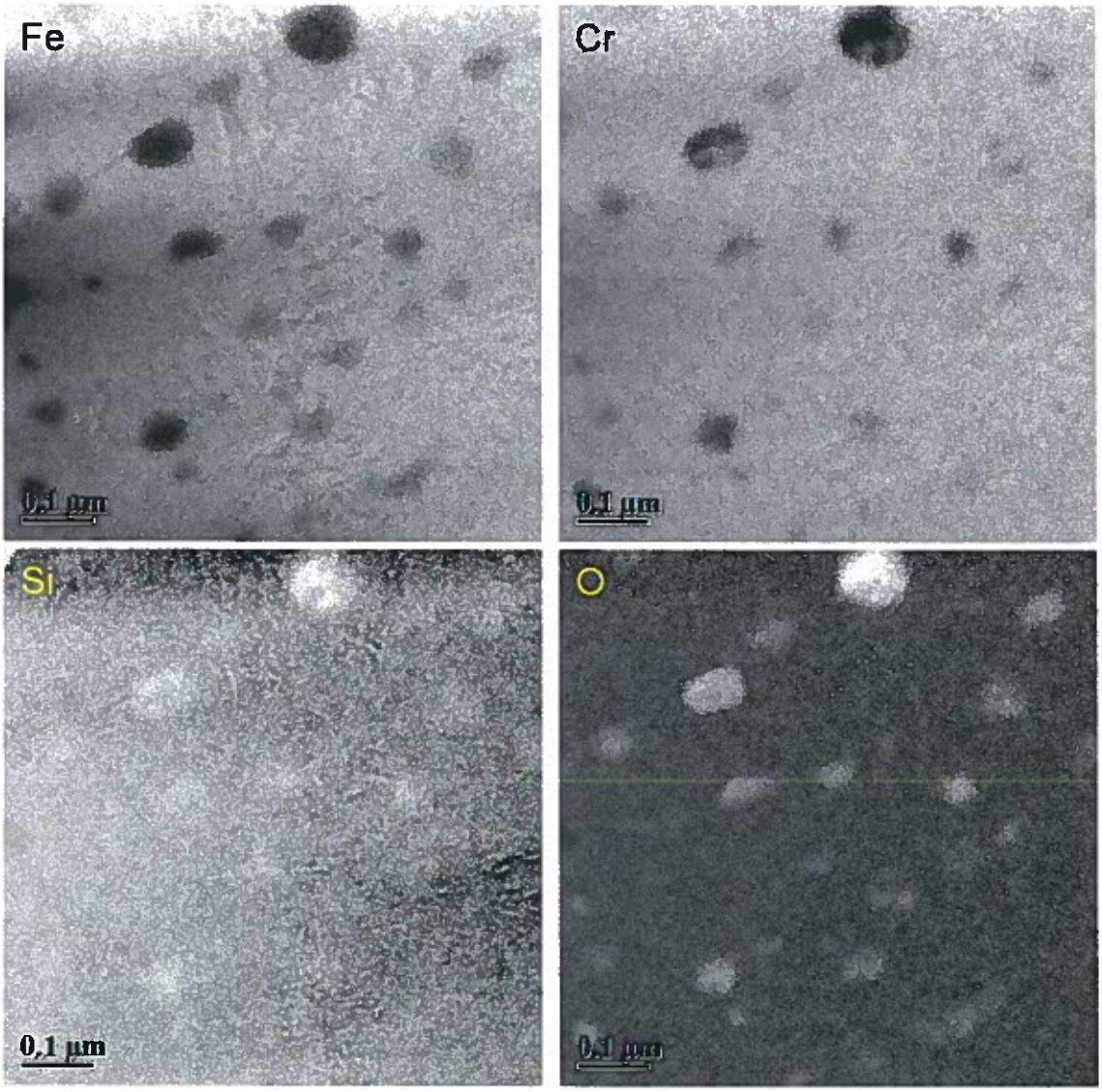

Fig. III. 6. Energy-filtered transmission electron micrographs for the elements Fe, Cr, Si, and O. The oxide particles contain Si and O indicating that they are SiO_2.

IV. MICROSTRUCTURE OF OXIDE ON Ni-20Cr+10Al COATING

The oxide layer on the Ni-20Cr+10 wt.% Al coating that underwent cyclic oxidation at 1010 °C for 1218.3 h (1462 cycles) was studied using TEM. Two typical electron micrographs of the oxide scale are shown in Fig. IV.1. The grain size of the oxide layer varies from a small value up to about 400 nm. EDS analysis showed that the oxide layer contains predominantly Al and O elements in the scale even though Cr was present in a minor quantity. Investigations are currently n progress to determine the nature of this secondary phase.

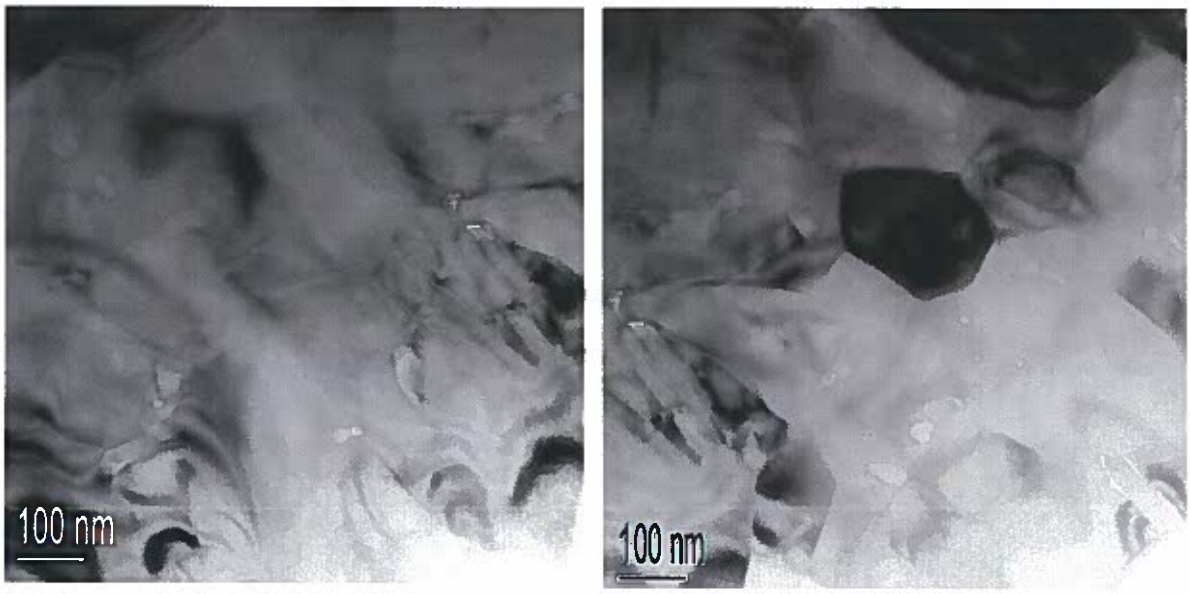

Fig. IV.1 Bright-field electron micrographs of the Ni-20Cr+10 wt.% Al oxide layer containing predominantly Al_2O_3 particles. The oxide grain size is typically about 400 nm.

Structural Characterization of Ni-20Cr-yAl (y = 0, 3, 7 and 10 wt.% Al) Coatings

A report submitted by

By

Prof. C. Suryanarayana
Department of Mechanical, Materials and Aerospace Engineering
University of Central Florida
Orlando, FL. 32816-2450
Tel: 407-823-6662; e-mail: csuryana@mail.ucf.edu

To

Dr. N.S. Cheruvu
Southwest Research Institute
San Antonio, TX 78238
Tel: 210-522-2492; e-mail: nscheruvu@swri.org

EXECUTIVE SUMMARY

Ni-20Cr (Haynes 230) alloy samples were coated with Ni-20Cr containing different amounts of Al (0, 3, 7, and 10 wt.% Al). The coatings were characterized for their crystal structure and microstructural features using a variety of techniques including X-ray diffraction (XRD), transmission electron microscopy (TEM), and three-dimensional atom probe (3DAP). All the deposited coatings had predominantly an FCC structure representing the Ni-solid solution phase, with a small amount of elemental Cr or Cr-solid solution appearing to be present in the high Al content coatings. Microstructurally, all the coatings exhibited columnar grains and in each of the columnar grains there was a multilayer structure. The multilayer structure had two different thicknesses – one about 15 nm in width and the other only about 3 nm in width. With the help of energy-filtered TEM and 3DAP studies, it could be unambiguously shown that the thicker layer was Ni-Cr rich while the thinner layer was Al-rich. Formation of this multilayered structure was explained on the basis of the conditions prevalent during the magnetron sputtering deposition of the coating material.

I. INTRODUCTION

I.1. Surface Coatings for Oxidation Resistance & High Temperature Applications

The increasing demand for advanced materials with enhanced performance characteristics in different types of environments has resulted in the development of new materials that possess near-surface properties different from their bulk properties. Coatings and surface modification treatments are mostly used for this purpose.

The major goal of the project is the improve oxidation and corrosion resistance of P 91 steel, 304 SS and Ni-base super alloys with deposition of coatings containing Al to form a protective alumina (Al_2O_3) scale. Conventional austenitic stainless steels rely on chromia (Cr_2O_3) scales for oxidation protection. But, chromia scales are not always stable in oxidizing environments, especially when they also contain water vapor, when they will suffer from accelerated oxidation attack. Water vapor is present in all combustion environments and therefore this is a significant issue for hot components in energy conversion systems. Alumina scales exhibit an order of magnitude lower oxidation rates than those of chromia in air (Fig. 1), and therefore remain stable in water vapor environments in the 600 °C to 800 °C temperature range of interest.

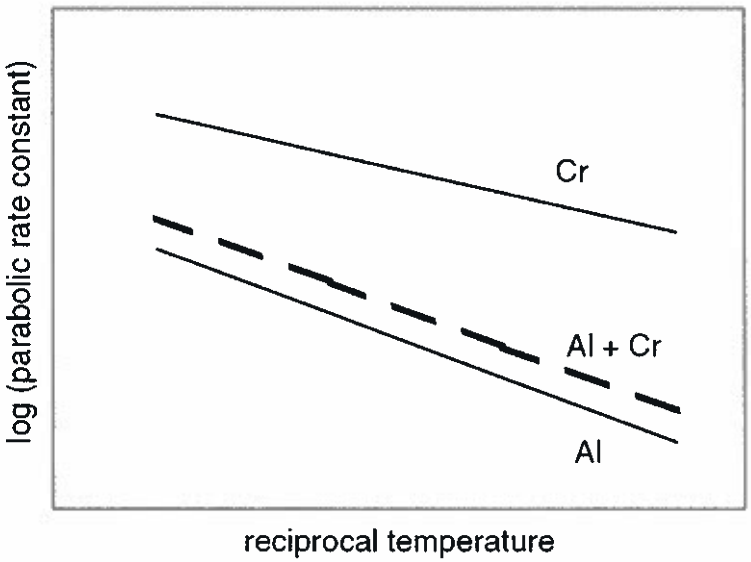

Fig. 1. Schematic Arrhenius plot of log parabolic rate constant against reciprocal of temperature for oxidation of alloys containing Al, Cr, and Cr+Al. It is clear from the plot that alloys containing Al exhibit much higher oxidation resistance than those containing Cr.

I.2. Why Fe-based and Ni-based coatings?

As seen from the above discussion, addition of Al provides better oxidation resistance to steel. Hence, the idea is to add Al to some base metals which have good Al solid solubility. Traditionally Fe and Ni are the principal components of superalloys. Both of them have exhibit good solubility of Al in them. While Fe can dissolve up to 38 wt.% Al, Ni can dissolve up to 18 wt.% of Al. Also, both Fe and Ni form the ordered intermetallics with Al, such as FeAl, NiAl, Fe3Al, Ni_3Al etc. In other words and Fe and Ni store Al in their matrix even if they form intermetallics and they are expected to provide Al to the oxidizing surface in a controlled manner. Further advantages with the present choice of stainless steels

1. They are 3-5 times cheaper than superalloys
2. The coefficients of thermal expansion (CTE) of the base metal (SS304) and coating materials (SS304+Al) are similar, so spallation is minimized

I.3. Objectives of the study

The goal of this project was to characterize the alloy coatings structurally. This involves, crystallographic study using X-ray diffraction (XRD) and metallographic study using transmission electron microscopy (TEM) and relating the structural and microstructural features to their oxidation behavior. The charge of the present contract was to determine the grain size and nature of the different phases present through TEM investigations. Since the microstructure affects the properties of materials, the information gathered in this project should prove valuable in exploring the potential of the alloy coatings to resist oxidation and provide competitive life cycle similar to that of superalloys. Thus, we had characterized the crystal structure and morphology of SS304+xAl coatings on SS304 substrates and Ni-20Cr+yAl alloy coatings on Ni-20Cr substrates. However, in this Report we will only describe the results obtained on the crystal structure and morphology of the Ni-20Cr+yAl alloy coatings on Ni-20Cr substrates.

The Ni-20Cr-yAl (y = 0, 3, 7, and 10 wt.%) coatings deposited on the Haynes 230 substrate were received from the Southwest Research Institute (SwRI), San Antonio, TX.

II. EXPERIMENTAL PROCEDURE

Surface coatings of Ni-20Cr-yAl on Ni-20 Cr(Haynes 230) alloy substrate with y = 0, 3, 7, and 10 wt% Al have been characterized in this project with a number of different techniques to obtain crystal structure and microstructural information. While the X-ray and electron diffraction methods were employed to obtain crystal structure information, Optical microscopy (OM), Scanning electron microscopy (SEM), TEM, and 3-dimensional atom probe (3DAP) techniques were used to obtain microstructural information as well as chemical composition.

II.1 Plasma-Enhanced Magnetron Sputtering (PEMS)

The coatings characterized in this investigation were deposited using the plasma-enhanced magnetron sputtering (PEMS) method. This is a non-equilibrium processing technique where the required elements are sputtered by high energy ions of Ar (or other inert gaseous elements) and consequently deposited on to the substrate material. Magnetrons are used to pullout the secondary electrons to a side inside the sputtering chamber so that only ions can interact with the target, increasing the efficiency of the sputtering process.

Two targets, viz., Ni-20Cr and Al, were used to produce the Ni-20Cr-yAl coatings. The Al content in the coating was varied by varying the bias voltage between the Al target and the substrate. Three different Al contents of 3, 7, and 10 wt.% were obtained this way. For comparison purposes, the Ni-20Cr coating without any Al content was also deposited on the Ni-20Cr substrate.

II.2 Characterization

All the coatings were characterized using different metallographic techniques for their crystal structure and microstructural details. Characterization involved the use of XRD, optical microscopy (OM), SEM, TEM (Philips Tecnai F30, operated at 300 kV), and Three-Dimensional Atom Probe (3DAP). The samples for TEM and 3DAP study were prepared by Focused Ion Beam (FIB) technique. XRD was used for primary phase identification before going on to TEM investigations.

Sample Preparation for 3DAP

Needle-shaped samples with about 50-100 nm tip radius are required for the atom probe study. The most common techniques to prepare needle/wire samples are electropolishing and focused ion beam (FIB). Both these methods were tried but only the sample produced by the FIB method succeeded in giving a good number of atom count (> 2 million) in atom probe. The needle preparation for 3DAP is somewhat similar to In-situ FIB sample preparation for TEM investigations. However, fine tuning was required for the atom probe sample as it is very easy to damage or destroy the tiny sample with ion beam. Also, Ga contamination is another issue while preparing the needle sample. Though Ga contamination cannot be avoided completely, it can be minimized by experience. Use of very low energy ion beam is essential in the final stages of sample preparation.

Soon after its preparation, the needle sample was immediately transferred to a vacuum chamber that is attached to the 3DAP microscope. Eventually, the sample was taken to the main chamber where the actual probing was done. The low temperature (-80° C) main chamber has suitable sized slots as sample holders. A high voltage was applied on to the 50 to 100 nm radius tip of the sample and high electrostatic field was created. This results in field ionization and a photograph is obtained when these ions eventually reach the detector screen. After millions of such collisions, it is possible to identify the elements present in the sample by analyzing the peaks in the plot of number of collisions vs. mass/charge ratio. Based on peak fitting in the plot, the position of each atom can be back calculated and finally a 3-dimensional reconstruction can be obtained for all the elements using the POSAP software.

III. RESULTS

The Ni-based coatings being characterized in this study and the Fe-based coatings characterized earlier share some common structural features such as columnar or lath grains, and the presence of multilayers. However, they have a very significant structural difference, i.e., the presence of ordering. The results of 304+xAl coatings clearly showed evidence for the presence of an ordered phase; but such an ordering behavior was not observed in the Ni-based alloy coatings.

Since all the Ni-based coatings containing 3, 7, and 10 wt.% Al exhibited very similar structural and microstructural features, the results are merged into one section to simplify the explanation.

III.1. XRD of Ni-20Cr-yAl Coatings

XRD patterns of the Ni-based coatings i.e., Ni-20Cr+yAl, where y = 0, 3, 7 and 10 wt% Al are shown in Fig.2. Table.1 shows the phases identified from Fig.2 for the Ni-based coatings and their structural details. Before phase identification, the K_β peaks (for example at $2\theta \sim 40°$) have been ignored. In the coatings with y = 0 and y = 3, only one phase is present that has been identified as an FCC Ni-based solid solution (γ phase). In the remaining two coatings with y = 7 and y = 10, two different phases were identified. They are (i) the FCC Ni-based solid solution (γ phase) and (ii) the elemental Cr or the Cr solid solution phase. All the coatings have a [111] preferred texture. Further, the γ (111) peak is noted to be very broad, i.e., the full width at half maximum (FWHM) is about 1.2° with the 2θ values ranging from 43.6° to 44.8°. This peak broadening could be due to (i) the extremely small crystallite size of the γ phase, (ii) strain in the γ phase due to the deposition conditions, (iii) presence of hidden peaks of an Al-based phase, or (iv) continuous variation of the Ni lattice parameter by the dissolution of Al in Ni at the interface of Ni/Al multilayers.

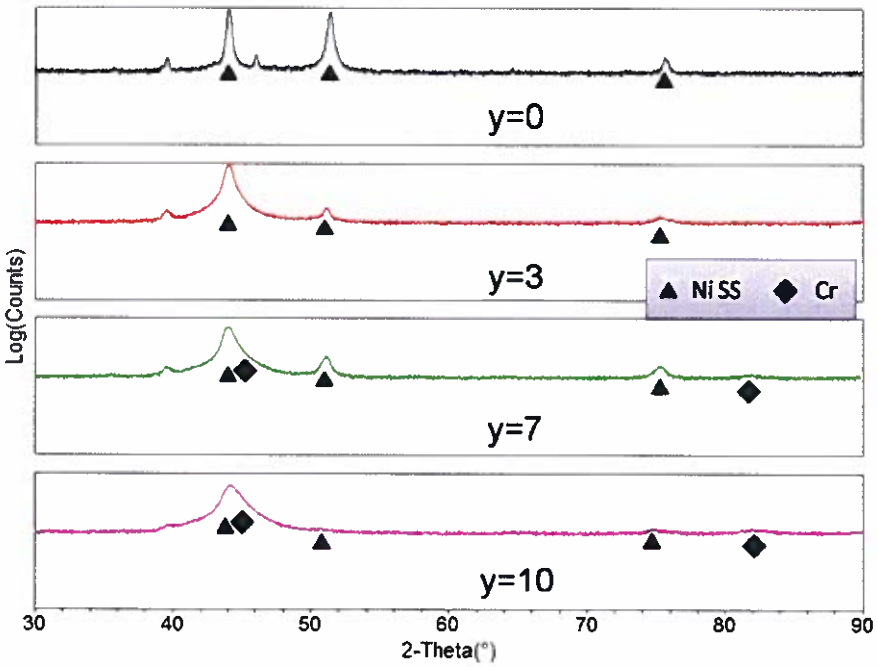

Fig. 2. XRD patterns of Ni-20Cr+yAl coatings (y = 0, 3, 7, and 10 wt.%). While the coatings with y= 0 and 3 contain only the Ni-based solid solution, the coatings with y = 7 and 10 contain the Ni-based solid solution and either elemental Cr or a Cr-based solid solution phase.

Table.1 Summary of results of crystal structures and lattice parameters of the different Ni-20Cr-based coatings with different Al contents as identified from their X-ray diffraction patterns.

Sample	Designation	Wt.% Al	Phase	Crystal Structure	Lattice parameter *a* (nm)
1	Ni-20Cr + 0Al	0	γ	FCC	0.3551
2	Ni-20Cr + 3Al	3	γ	FCC	0.3564
3	Ni-20Cr + 7Al	7	γ (major)	FCC	0.3568
			Cr (minor)	BCC	0.2882
4	Ni-20Cr + 10Al	10	γ (major)	FCC	0.3587
			Cr (minor)	BCC	0.2864

III.2. Transmission Electron Microscopy

In this section we will present results of transmission electron microscopy investigations on the Ni-20Cr-yAl coatings with y = 3, 7, and 10 wt.% Al.

Fig. 3shows the bright-field images of the three coatings containing 3, 7, and 10 wt.% Al. It may be noted that a lath structure is clearly visible in the coatings with 3 and 10 wt.% Al (Fig. 3(a) and 3(c), respectively). The microstructure shown in Fig. 3(b) also appears to indicate the presence of laths, but the lath boundaries are not clear. The average lath width of in the 3%Al coating was 440 nm while that in the 10%Al coating was 510 nm. From these values, it appears that the average lath widths were smaller in the N-based alloy coatings in comparison to those in the SS304+Al coatings. The corresponding values in the SS304 + 3 and 10 wt.% Al were 600 and 1200 nm, respectively.

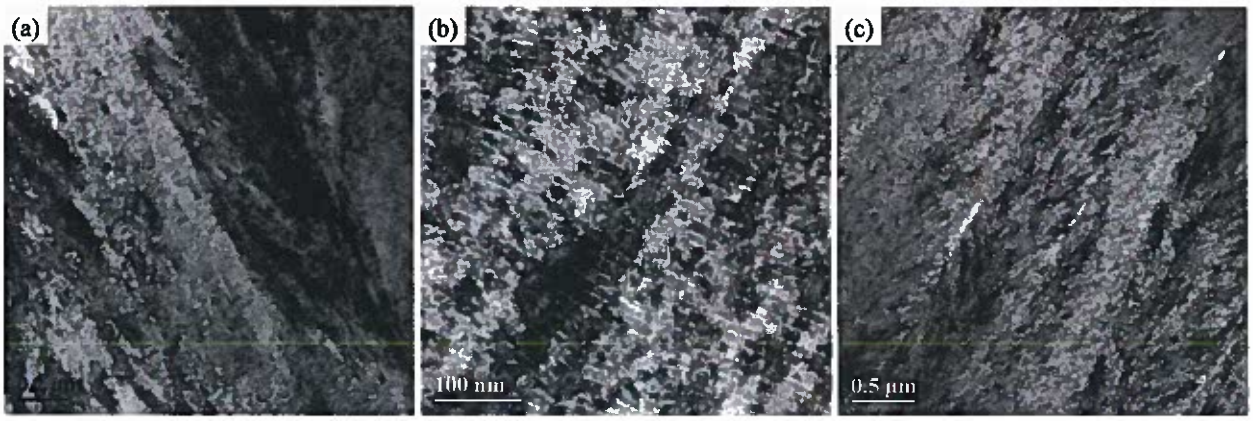

Fig. 3. Bright-field transmission electron micrographs of Ni-20Cr+yAl coatings with (a) y = 3, (b) y=7 (b), and (c) y=10 wt.% showing the overall microstructure at different magnifications. While the lath structure is clearly seen in the coatings with 3 and 10 wt.% Al, it is not very clear in the coating with 7 wt.% Al, even though there are indications of its presence.

III.2.1 Multilayer structure

In the microstructure of the Ni-based coatings, wavy and modulated structures of approximately 13 nm in thickness were observed. They were mostly oriented normal to the direction of deposition, i.e., across the laths. A thorough analysis of this multilayer structure was undertaken using different modes in the TEM, viz., bright field (BF), selected area diffraction (SAP), scanning transmission electron microscopy (STEM), energy dispersive spectroscopy (EDS), and Elemental Mapping in electron energy loss spectroscopy (EELS) to characterize the

modulated/lamellar structure. These analyses were then correlated with XRD results. In addition to these investigations, the multilayers were also characterized using 3-dimensional atom probe (3DAP) studies to obtain chemical composition on an atomic scale and also to determine whether the different layers have different distribution of the constituent elements.

III.2.2. *Bright Field and Selected Area Diffraction (SAD) Patterns*

Fig.4 shows the bright field electron micrographs of the Ni-20Cr-yAl alloy coatings with y = 3, 7, and 10 wt.% Al. All the three compositions show very similar structures with two types of bands in them. One type of the bands has a grey contrast with a width of about 13 nm, and the other band has a white contrast and a width of about 2 nm width. The lamellar structure is present in all the coatings, but appears to be particularly prominent in the coating with 10 wt.% Al.

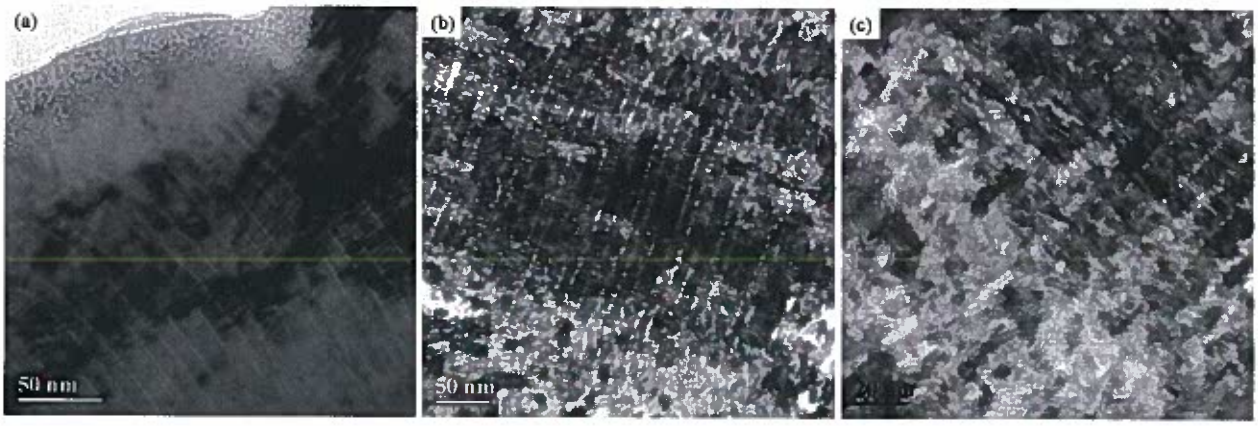

Fig.4. Bright field transmission electron micrographs showing the multilayered structure in the Ni-20Cr-yAl alloy coatings with (a) y=3, (b) y=7, and (c) y=10 wt.% Al. .

Electron diffraction patterns from the thin samples of Ni-20Cr-yAl coatings are shown in Fig. 5. All the diffraction patterns show ring patterns characteristic of fine grained polycrystalline material. The sequence of diffraction rings is characteristic of an FCC structure

from which the lattice parameter was calculated to be a = 0.356 nm. This value should be

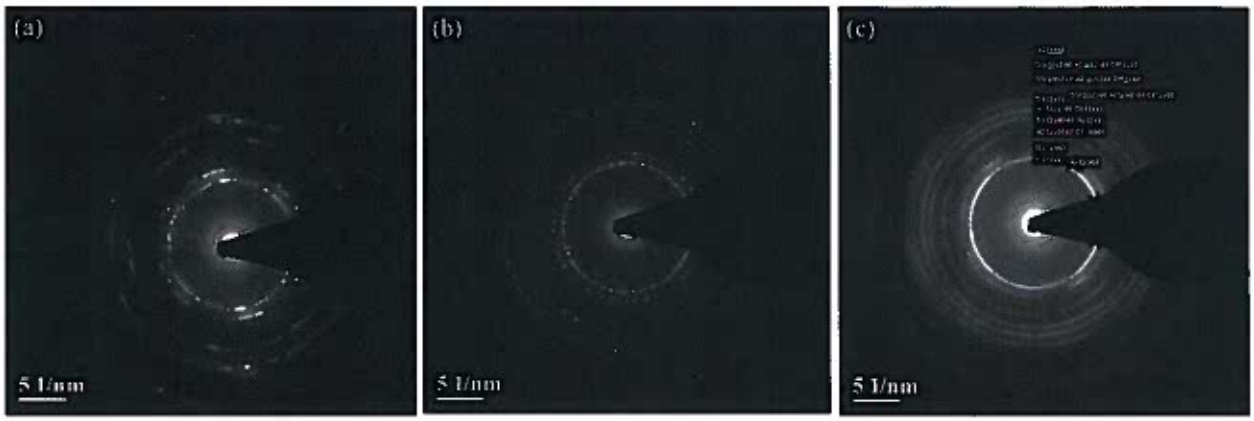

Fig. 5. Electron diffraction patterns from the Ni-20Cr-yAl alloy coatings with (a) y=3, (b) y=7, and (c) y=10 wt.% Al. . The diffraction patterns were indexed on the basis of an FCC γ-phase.

compared with the lattice parameter of pure Ni which is 0.357 nm. These two lattice parameters are very close to each other suggesting that what we are dealing with here is the Ni solid solution in the coatings. Some differences are also noted in the diffraction patterns. While a combination of both rings and spots is seen in the coatings containing 3 and 7 wt.% Al, only a ring pattern is observed in the coating containing 10 wt.% Al. All the diffraction patterns were indexed to be having essentially one phase – the FCC γ phase. The presence of a slight amount of Cr (or a Cr-based solid solution observed in the XRD patterns) could not be initially confirmed. Experiments are in progress for a more thorough characterization of the coatings with 7 and 10 wt.% Al.

III.2.3 *Scanning Transmission Electron Microscopy (STEM) and Energy Dispersive Spectroscopy (EDS)*

The layers (bands) are much more clearly revealed in the STEM mode than in the bright-field electron micrographs. Fig. 6 shows a high-magnification STEM micrograph of the band structure from a Ni-20Cr-3Al coating and the corresponding line profile analysis using Ni-Kα, Cr-Kα and Al-Kα. It can be clearly seen from the micrograph that there are two different types of bands in the wavelength span of about 15 nm. These are (i) Ni-rich Ni-Cr layers of about 12 nm width and (ii) Al layer of about 3 nm width. The Ni-rich layer further exhibits 3 different thicknesses of typically ~14, 12 and 10 nm, while the Al layer has a fixed thickness of about 3

nm. Since the band structure contains two types of layers with different compositions, this structure will be referred to as a multilayer structure. Very similar microstructures were observed in the 7 and 10 wt.% Al coatings also, shown in Fig. 7 and Fig. 8, respectively.

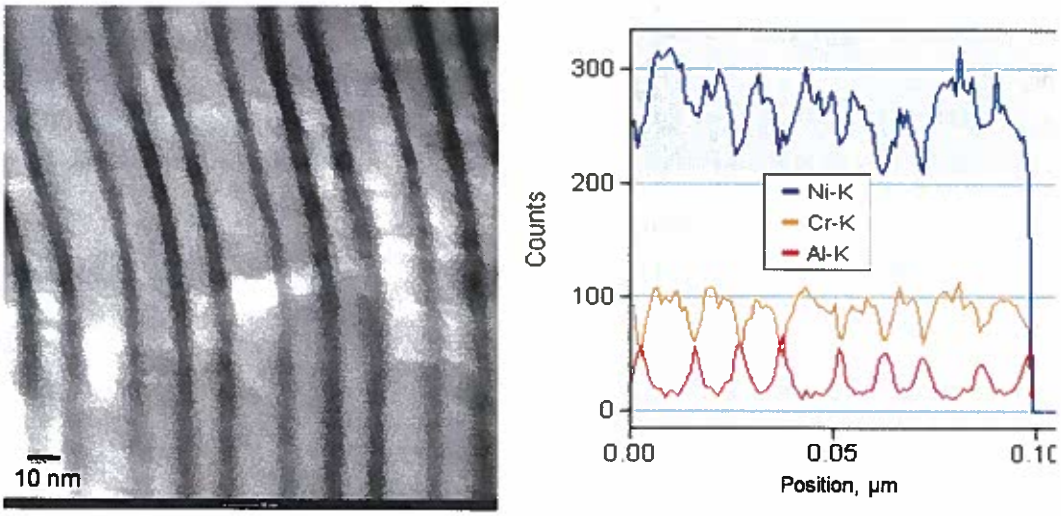

Fig. 6 Typical STEM micrograph of the Ni-20Cr-3Al coating and the corresponding line profile across the bands.

Fig. 7. Typical STEM micrograph of the Ni-20Cr-7Al coating at low and high magnifications.

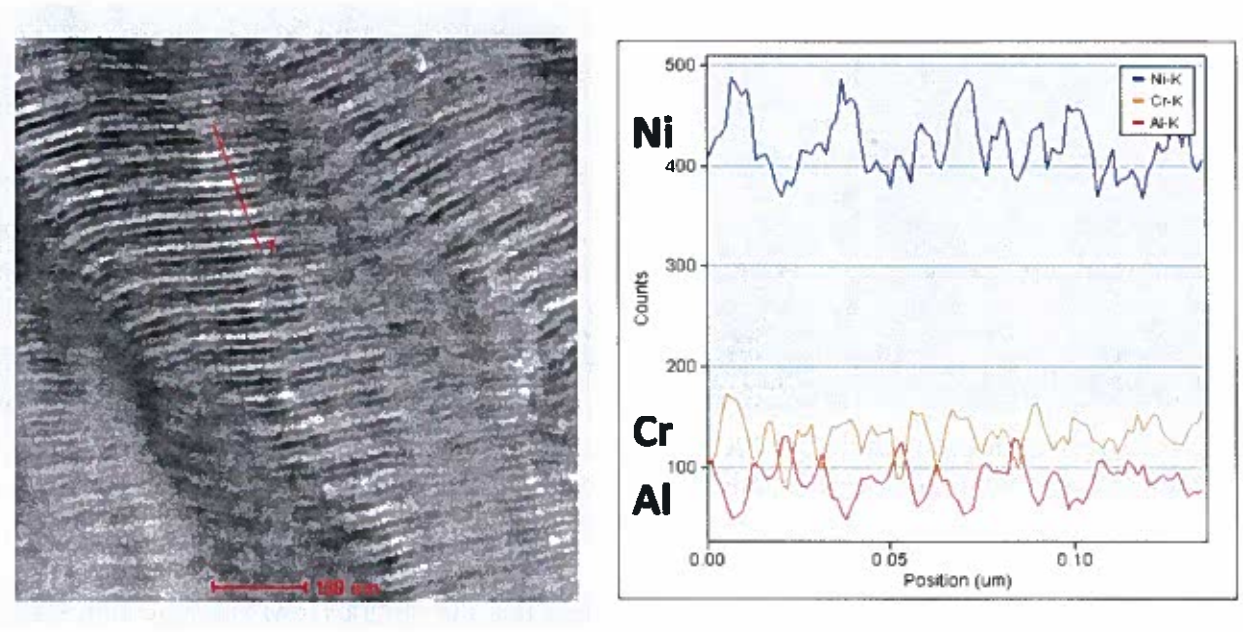

Fig. 8. A typical STEM micrograph of the Ni-20Cr-10Al coating and the corresponding line profile across the bands.

III.2.4 *Energy-Filtered TEM (EFTEM))*

Energy filtering is a valuable tool for materials characterization and can be used to solve different problems: (i) **Zero-loss filtering** - By using only the zero-loss beam, all inelastically scattered electrons are omitted (reduction of noise). That leads to increased contrast in the TEM images (especially important for specimens with low contrast, e.g. biological specimens) or in diffraction patterns. (ii) **Electron spectroscopic imaging** - By using electrons with a well-defined energy loss (ionization edge), elemental distribution maps can be generated. In the present case, since the coating contained three elements, viz., Ni, Cr, and Al, mapping for these three metals was done. The selected edges were Ni-Kα, Cr-Kα and Al-Lα. Fig. 9 shows the elemental mapping of the multilayer structure in the Ni-20Cr-3Al coating. From these three maps, it can be unequivocally concluded that the wide bands (about 14, 12, 10 nm in width) belong to Ni-Cr solid solution (γ phase) and the narrow bands (2-4 nm) belong to Al. The band structure repeats at about 14 nm on average. That is like, 14, 3, 12, 3, 10, 3, 14, 3, 12,....etc.

Fig. 9 Elemental mapping of the Ni-20Cr-3Al coating using Ni, Cr, and Al ionization edges. It becomes clear from these images that the thin bands are Al-rich and that the thick bands are Ni-Cr-rich.

From the above observations, it becomes clear that the Ni-20Cr-yAl coatings with y =3, 7, and 10 wt.% Al, contain a multilayer structure with two types of bands. The thicker of the bands has three different widths which are about 14, 12, and 10 nm.

To explore the multilayer structure further, we worked in collaboration with NIMS, Japan. 3 dimensional atom probe (3DAP) was performed on y = 10 sample to explore the details of the layered structure.

III.4. Three-Dimensional Atom Probe (3DAP)

Figures 10, 11, and 12 show reconstructed 3-dimensional images (henceforth called micrographs) for the elements Ni, Cr and Al from the Ni-20Cr-10Al coating. All the three micrographs show layered structures in confirmation of the earlier TEM studies. From a selected area, the composition profile of all the three elements is plotted in Fig. 13. The pattern of composition variation is similar to that of TEM (Fig. 6). It shows two different layers; one layer is enriched in Ni and Cr and depleted in Al. The neighboring layer is enriched in Al but depleted in Ni and Cr. This kind of composition variation could be attributed to the sputtering conditions and will be discussed in a later section.

In addition to the layers, the 3DAP uniquely identified the presence of Cr clusters (Fig. 9) of about 10 nm in size. The origin of these clusters is not clear at the moment. It is possible that a phase separation is occurring in the system.

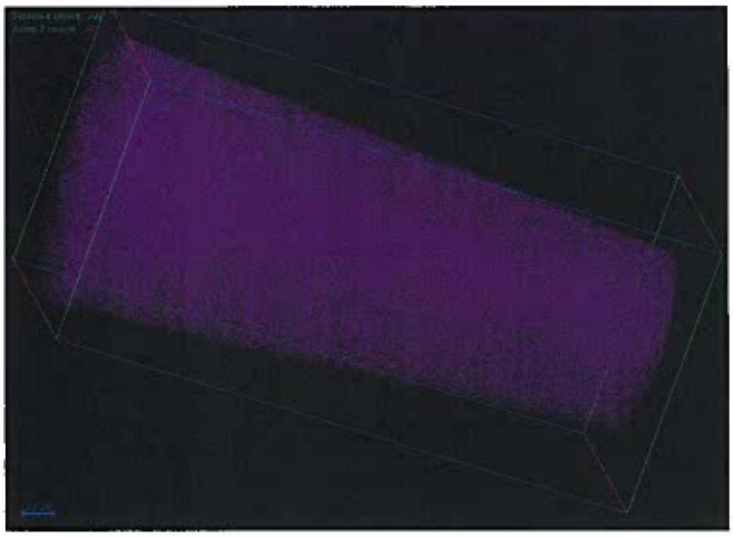

Fig. 10. Reconstructed Ni map from the 3DAP results on the Ni-20Cr-10Al coating.

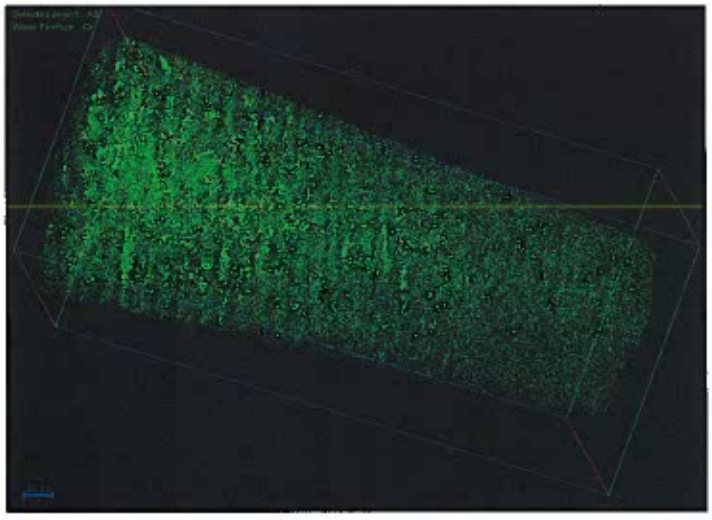

Fig. 11. Reconstructed Cr map from the 3DAP results on the Ni-20Cr-10Al coating.

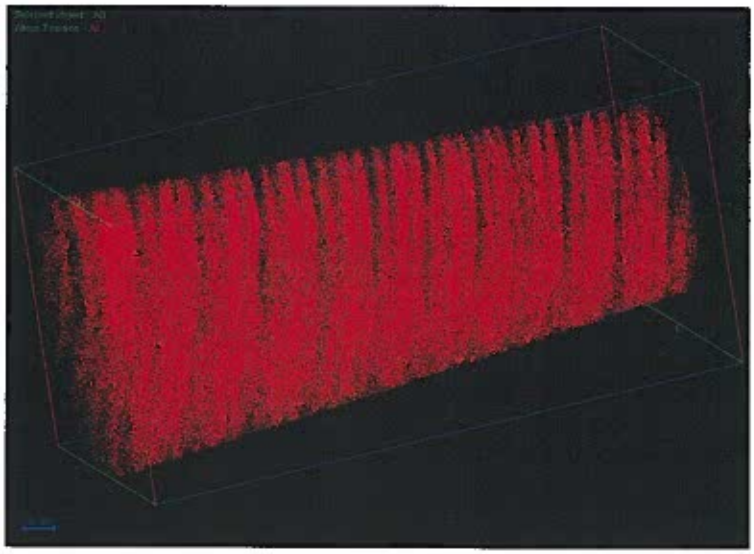

Fig. 12 Reconstructed Al map from the 3DAP results on the Ni-20Cr-10Al coating.

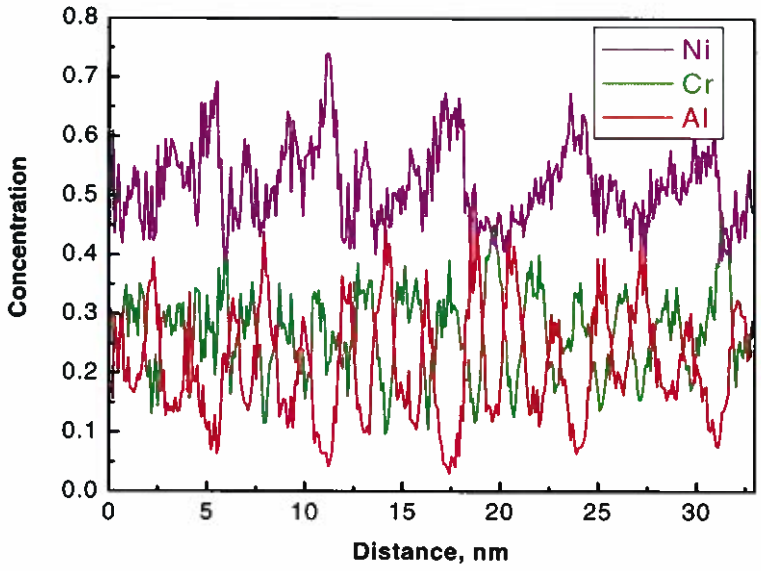

Fig. 13. Composition profile from the 3DAP results on the Ni-20Cr-10Al coating.

IV. DISCUSSION

Briefly summarizing the above results on Ni-20Cr-yAl coatings with y = 3, 7, and 10 wt.% Al, we note that the coatings exhibit columnar grains. These are very clear in coatings with 3 and 10 wt.% Al, but there are only indications of that in the coating with 7 wt.% Al. Instead of Al going into the matrix of Ni-20Cr, Al forms a separate layer, leading to the formation of a multilayer structure of Ni-Cr (γ) of about 12±2 nm, and Al of 3±1 nm. The multilayer structure is more prominent at higher Al contents. However, there is not much change in the layer width either in the γ phase layers or in the Al layers.

The reason for the formation of the multilayer-structure can be understood when we realize that two different targets were used during magnetron sputtering – one was the Ni-20Cr coating and the other of Al. Further, these two targets were positioned at 180° from each other as shown in Fig. 14. Consequently, the Ni-20Cr and Al were deposited alternately whenever the substrate was directly in front of the target. Therefore, it is fair to assume that homogeneous mixing can be obtained if both the targets are on the same side in the PEMS chamber.

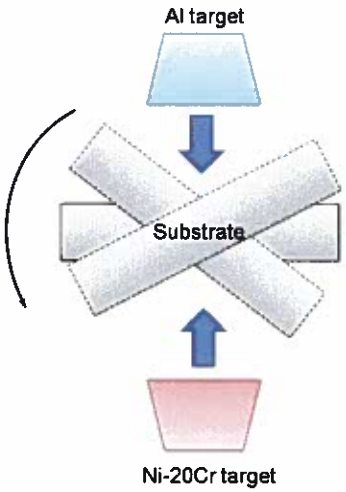

Fig.14 A pictorial representation of the deposition process

During sputtering, the substrate in the deposition chamber is maintained such that it follows a planetary motion, rotating around itself and about another center. Such rotation of the substrate orients it at different angles with respect to the targets as shown in Fig.14. The maximum amount of deposition is possible when the target is at 90° to the substrate. But, as the substrate rotates, it

creates a steep angle and another shallow angle and this leads to the three layers in one cycle or one complete rotation of the substrate. This is the probable reason why different thicknesses were observed in the thick coating.

Research Report

Submitted to
South West Research Institute

Submitted by
Advanced Coatings and Surface Engineering Laboratory (ACSEL)
Metallurgical and Materials Engineering Department
Colorado School of Mines
Golden, CO, 80401

Development of thick MCrAl/TiN multilayer coatings for high temperature applications using dc and pulse dc magnetron sputtering

Principal Investigator:
Prof. John J Moore: Professor and Center Director
Advanced Coatings and Surface Engineering Laboratory (ACSEL)
Metallurgical and Materials Engineering Department
(303-273-3771)
jjmoore@mines.edu

Co-Principal Investigator:
Dr. Jianliang Lin: Assistant Research Professor
Advanced Coatings and Surface Engineering Laboratory (ACSEL)
Metallurgical and Materials Engineering Department
(303-273-3178)
jlin@mines.edu

Previous Research Work:

The work conducted in the second stage has demonstrated that three MCrAl coating architectures as proposed by SWRI can be successfully deposited using PMS at CSM with the coating thickness in the range of 16 to 22 μm. The coatings exhibited a dense superlattice microstructure. The coatings deposited without the TiN interlayer (CSM-5, CSM-6 and CSM-7) exhibited improved adhesion strength to the substrates, and a decrease in the surface defects as compared to the coatings deposited with a TiN interlayer (CSM-1, CSM-2 and CSM-3) and the coatings deposited in the first stage work as well.

Current Research Work:

During the month of Jan 2011, we have deposited 10 MCrAl thick coatings with two different coating architectures on Haynes and AISI 304 stainless steel substrates: (1) Architecture II: a MCrAl multilayer structure and (2) Architecture III: a MCrAl-Al multilayer structure. Five depositions were carried out for each architecture, in which only one deposition contains a TiN interlayer. The thickness of the TiN interlayer has been reduced to 1~1.2 μm. The architecture II and III of the coatings has been described in details in a previous report (*12-6-2010*). The purposes of the current work are:

1) Perform a quality control of the as-deposited thick MCrAl coatings using the optimized coating architectures from previous research work. The quality control of the coatings was based on 5 repeated depositions on a large number of AISI and Haynes substrates (10 for each deposition) for two different architectures.
2) One of fifth of each coating architecture deposition contains a TiN interlayer. The thickness of the TiN interlayer has been reduced to 1 μm in an effort to achieve good adhesion of the TiN/MCrAl coating to the substrate.
3) Study using TEM the grain size and microstructure evolution of the as-deposited SW3-MCrAl-#5 coating and after thermal cycled at 1010°C for 500 and 1007 cycles.

Table 1 Sample description and properties of the MCrAl thick coatings

Architecture	Sample ID	TiN layer	# of sub	Thickness [μm]	Surface defects [number and size, (s-small, L-large)]
II: Multilayer (using plasma etching)	SW3-MCrAl-1	-	10	17	5L, 2s
	SW3-MCrAl-2	-	10	17	3L, 6s
	SW3-MCrAl-3	-	10	18	2L, 2s
	SW3-MCrAl-4	-	10	18	2L, 3s
	SW3-MCrAl-5	Yes	10	18	5L, >30s
III: MCrAl-Al Multilayer	SW3-MCrAl-6	-	10	19	5L, 1s
	SW3-MCrAl-7	-	10	19	1L, 1s
	SW3-MCrAl-8	-	10	18	2s
	SW3-MCrAl-9	-	10	19	3s
	SW3-MCrAl-10	Yes	10	20	3L, >15s

Experimental Details:

The substrates are AISI 304 stainless steel coupons from ACSEL and the coupons (AISI 304 stainless steel and Haynes alloy coupons) provided by SWRI. The substrates were ultrasonically cleaned in denatured acetone and alcohol for 20 minutes respectively. The substrates were wired down from the rotation holder in the chamber with a distance to the target surface of 152 mm. In general, a base pressure less than $1.5x10^{-6}$ Torr was achieved prior to all coating depositions. Ar plasma etching process was used to further clean the substrate surface for improving the coating adhesion. The etching process was carried out at a pressure of 8 mTorr with a pulsed dc bias of -500 V (200 kHz and 1.0 μs) for 40 mins, which generated a 370 W power and 0.8 A current on the substrates.

The targets were powered by two Advanced Energy Pinnacle Plus Power supplies. The pulsing power supply can be operated under either DC or pulsing mode. The pulsing parameters used for the depositions were 200 kHz and 1.0 μs, which correspond to an 80% duty cycle (The duty cycle is defined as the negative pulse time divided by the time of the pulsing cycle). The working pressure was 0.47 Pa. The Ar flow rate was maintained at 45 sccm. A -60 V dc substrate bias was used for all depositions.

The crystal structure of the coatings was determined by XRD using a SIEMENS X-ray diffractometer (Model KRISTALLOFLEX-810) operated with K-alpha Cu radiation in the conventional Bragg-Bentano mode. The cross-sectional microstructure of the coatings were characterized using a JSM-7000F field emission scanning electron microscopy (FESEM) operated at a 5 kV accelerating voltage. The thickness of the coatings was measured using a Dektak profilometer and checked using the cross-sectional SEM. The surface defects of the coatings were examined using an optical microscope at different locations to provide an evaluation of the worst and best surface morphologies of the coatings.

Results and Discussion:

Figure 1 shows the XRD patterns of the SW3-MCrAl coatings deposited with two different architectures and with/without a TiN interlayer. The SW3-MCrAl-#4 and SW3-MCrAl-#5 coatings, which were deposited using the architecture II, exhibited a strong FCC (111) peak centered at 43.7° and (200) and (220) centered at 50.9° and 74.8° (Figure 1a and 1b). The SW3-MCrAl-#9 and SW3-MCrAl-#10 coatings, which were deposited using the architecture III, also exhibited a polycrystalline FCC structure with (111), (200) and (220) peaks (Figure 1c and 1d). However, the intensity of the (111) reflection decreased compared to the coatings deposited using architecture II (Figure 1a and 1b).

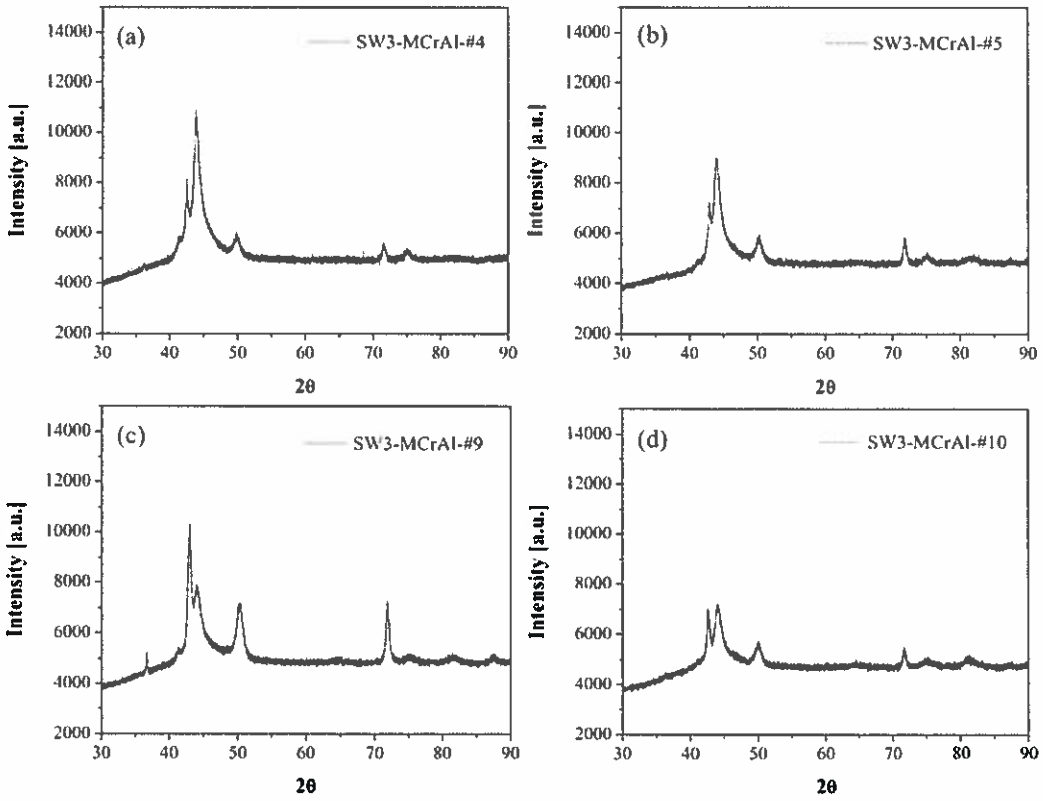

Figure 1. XRD patterns of the SW3-MCrAl coatings: Architecture II (a) SW3-MCrAl-#4, (b) SW3-MCrAl-#5 (with a TiN interlayer), and Architecture III (c) SW3-MCrAl-#9, and (d) SW3-MCrAl-#10 (with a TiN interlayer).

Figure 2 shows the cross-sectional SEM micrographs of the SW3-MCrAl coatings deposited with two different architectures and with/without a TiN interlayer. As shown in Figure 2a and 2b, the SW3-MCrAl-#4 coating (*without a TiN interlayer*) showed a dense multilayer structure. As shown in Figure 2c and 2c, the SW3-MCrAl-#5 coating (*with a TiN interlayer*) also showed a dense multilayer structure, which contains a 1.2 μm TiN interlayer between the substrate and the MCrAl coating, as labeled in Figure 2c.

As shown in Figure 2e to 2h, the SW3-MCrAl-#9 and SW3-MCrAl-#10 coatings deposited using architecture III exhibited a multilayered structure with the alternating growth of MCrAl and Al layers from the bottom to the top. The thicknesses of the MCrAl layers and the Al layers are about 1 μm and 200 nm, respectively. The SW3-MCrAl-#10 coating contains a 1.2 μm TiN interlayer between the substrate and the MCrAl coating.

The MCrAl layers in the All thick coatings exhibited a superlattice structure with the small variation of the bilayer period in the range of 22-30 nm, as shown in Figure 2b, 2d, 2f, and 2h. In the current study, it was identified that the incorporation of a thin TiN interlayer with a thickness of about 1~1.2 μm will not be detrimental to the adhesion of the thick MCrAl coatings. No coating delamilation was observed.

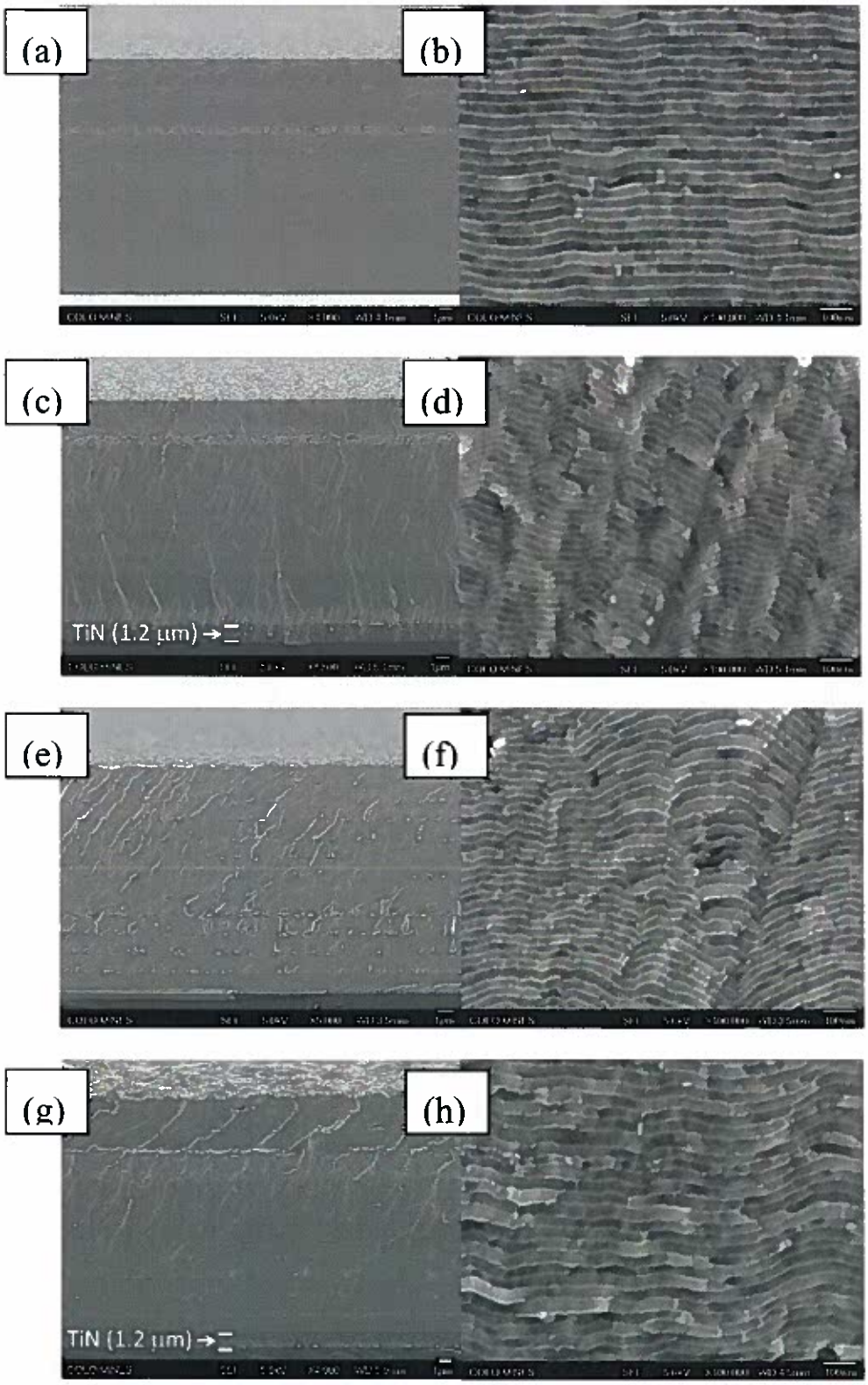

Figure 2. (a) Cross-sectional SEM micrographs showing the architecture of the SW3-MCrAl coatings: Architecture II (a) and (b) SW3-MCrAl-#4, (c) and (d) SW3-MCrAl-#5 (with a TiN interlayer), and Architecture III (e) and (f) SW3-MCrAl-#9, and (g) and (h) SW3-MCrAl-#10 (with a TiN interlayer).

The surface morphology and defects of the SW3-MCrAl coatings were examined using an optical microscope. Overall, the SW3-MCrAl coating exhibited smooth surface with a small number of defects. Figure 3 shows the images taken at different surface locations of the SW3-MCrAl coatings, which showed a high defect density. For each coating, four images were taken at different locations, as shown in Figure 3. The observations can be summarized as:

1) The SW3-MCrAl coatings deposited using architecture III (#6 to #10) exhibited less surface defects and improved surface quality than the coatings deposited using architecture II (#1 to #5).
2) The SW3-MCrAl coatings deposited with a 1.2 μm TiN interlayer (#5 and #10) exhibited a larger defect density than other coatings deposited without a TiN interlayer.
3) The defect format of the SW3-MCrAl coatings is mainly pits and imbedded macroparticles.

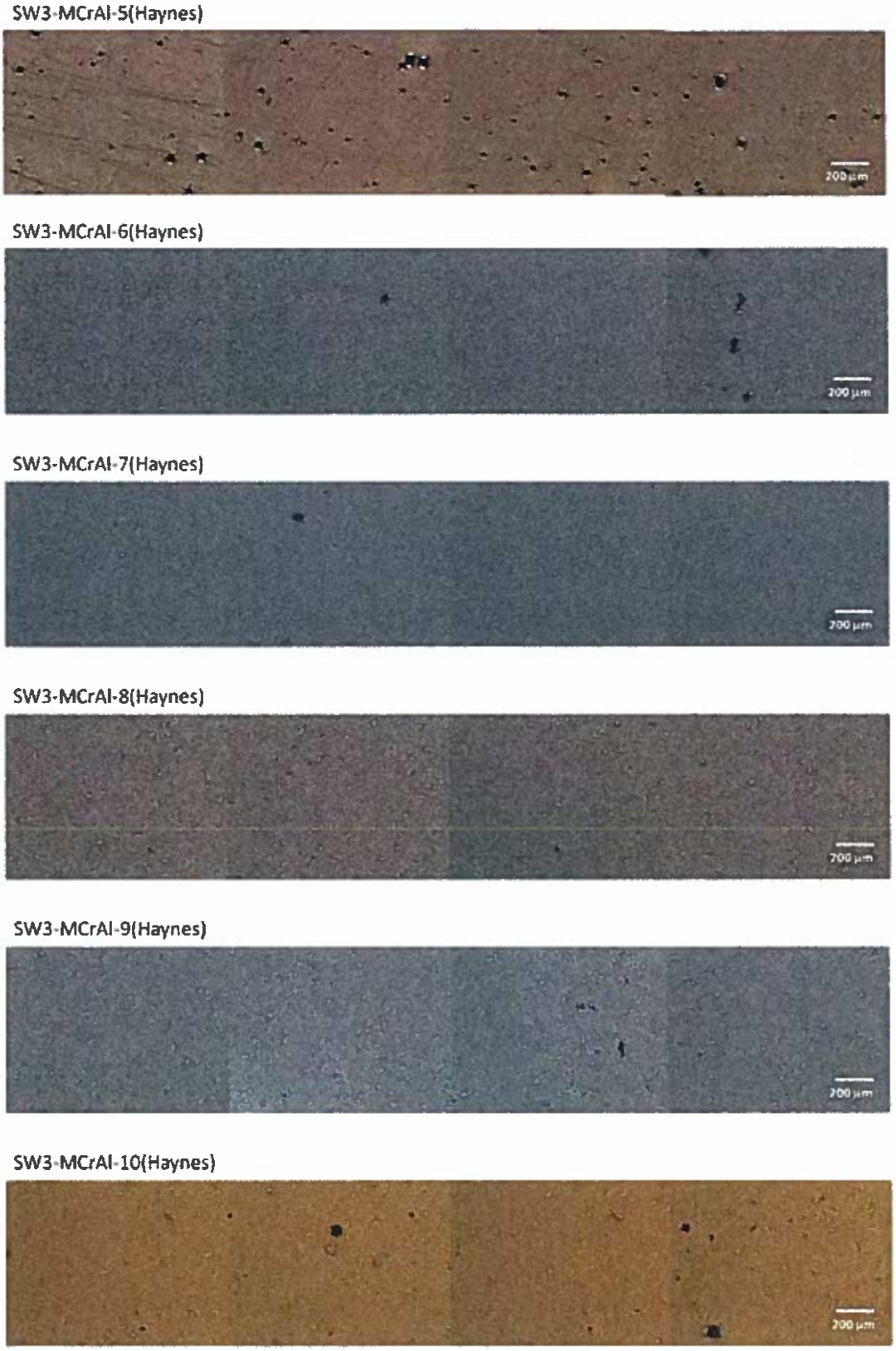

Figure 3. OM images of the thick SW3-MCrAl coatings deposited by PMS taken at four different locations on the as-deposited coating surface (including the worst surface defects observed on the coating surface).

Based on the results obtained in the second stage work, we can draw the following conclusions:

1) Ten thick MCrAl coatings (~20 μm) were successfully deposited on Haynes and AISI 304 stainless steel substrates using the previous optimized deposition parameters and architectures for a quality control purpose.
2) All coatings exhibited a dense superlattice microstructure and good adhesion. No coating delamilation was observed for the as-deposited samples.
3) The surface defects (pits and macroparticles) were examined using an optical microscope. Overall, all SW3-MCrAl coatings showed good surface quality. small amount of surface defect in the forms of pits and macroparticles were identified in the coatings. The SW3-MCrAl coatings deposited with a 1.2 μm TiN interlayer (#5 and #10) exhibited a larger defect density than other coatings deposited without a TiN interlayer

Respectfully submitted,

John J Moore, Ph.D.
Professor and Center Director
ACSEL, Colorado School of Mines

Jianliang Lin. Ph.D.
Assistant Research Professor
ACSEL, Colorado School of Mines

Research Report

Submitted to
South West Research Institute

Submitted by
Advanced Coatings and Surface Engineering Laboratory (ACSEL)
Metallurgical and Materials Engineering Department
Colorado School of Mines
Golden, CO, 80401

Title

Development of thick MCrAl/TiN multilayer coatings for high temperature applications using dc and pulse dc magnetron sputtering

Principal Investigator:
Prof. John J Moore: Professor and Center Director
Advanced Coatings and Surface Engineering Laboratory (ACSEL)
Metallurgical and Materials Engineering Department
(303-273-3771)
jjmoore@mines.edu

Co-Principal Investigator:
Dr. Jianliang Lin: Assistant Research Professor
Advanced Coatings and Surface Engineering Laboratory (ACSEL)
Metallurgical and Materials Engineering Department
(303-273-3178)
jlin@mines.edu

An industry-university consortium at the Colorado School of Mines

Advanced Coatings and Surface Engineering Laboratory (ACSEL),
Department of Metallurgical & Materials Engineering,
Colorado School of Mines

The work conducted in the first stage has demonstrated that the MCrAl coatings deposited by pulsed dc magnetron sputtering (PMS) exhibited improved coating density and finer grain size as compared to the coatings deposited by dcMS. However, the PMS sputtered thick MCrAl coatings (with the thickness up to 30 μm) also exhibited extensive surface defects in the forms of cauliflower pits and macro particles.

In the current work, we have deposited TiN-MCrAl thick coatings with different coating architectures using PMS. The work conducted in this stage includes:

1) The deposition rate was increased by decreasing the substrate to target distance from 235 mm (which was used in earlier depositions) to 152 mm. In addition, it is also possible to deposit more substrates in one deposition batch with the new rotation configuration in the deposition chamber.
2) Three coating architectures were proposed by SWRI in an effort to reduce the surface defects and improve the density of the thick MCrAl coatings.
3) The adhesion strength and surface quality of the MCrAl coatings with and without the TiN interlayer were compared.

As shown in Figure. 1, the proposed three coating architectures include

1) A TiN interlayer (2 μm) and the top single layer MCrAl coating (20 μm).
2) A TiN interlayer (2 μm) and the top multilayer MCrAl coating (20 μm). The top multilayer MCrAl coating was deposited with the following approach. The deposition process was stopped every 80 min, and then the substrate was plasma cleaned at a -500 V negative bias and an 8 mTorr working pressure in pure Ar for 5 mins.
3) A TiN interlayer (2 μm) and the top multilayer MCrAl-Al coating. The top multilayer MCrAl-Al architecture was formed by alternately depositing the MCrAl (1μm) and Al layers (200 nm) by switching off the MCr targets after every 20 mins and maintaining the power on the Al target for 1 min.

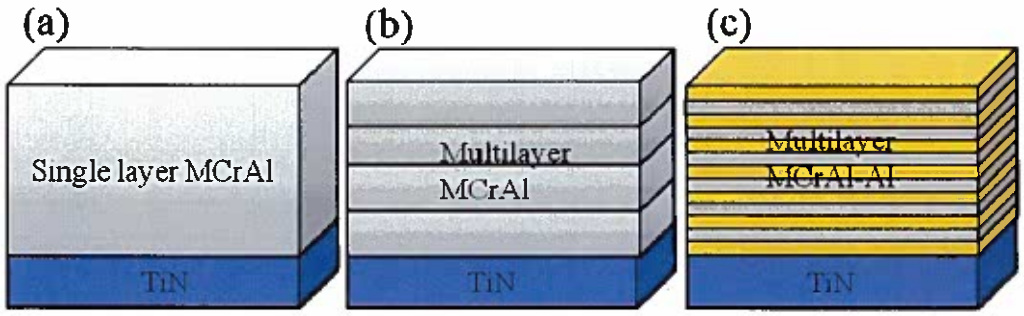

Figure 1. Different coating architectures deposited in the study: (a) a TiN interlayer+ a MCrAl single layer; (b) a TiN interlayer+ a MCrAl multi layer; (c) a TiN interlayer+ a MCrAl-Al multilayer;

The substrates are AISI 304 stainless steel coupons from ACSEL and the coupons (AISI 304 stainless steel and Haynes alloy coupons) provided by SWRI. The substrates were ultrasonically cleaned in denatured acetone and alcohol for 20 minutes respectively. The substrates were wired down from the rotation holder in the chamber with a distance to the target surface of 152 mm. In general, a base pressure less than $1.5x10^{-6}$ Torr was achieved prior to all coating depositions. Ar plasma etching process was used to further clean the substrate surface for improving the coating adhesion. The etching process was carried out at a pressure of 8 mTorr with a pulsed dc bias of -500 V (200 kHz and 1.0 μs) for 40 mins, which generated a 370 W power and 0.8 A current on the substrates.

The targets were powered by two Advanced Energy Pinnacle Plus Power supplies. The pulsing power supply can be operated under either DC or pulsing mode. The pulsing parameters used for the depositions were 200 kHz and 1.0 μs, which correspond to an 80% duty cycle (The duty cycle is defined as the negative pulse time divided by the time of the pulsing cycle). A -60 V dc substrate bias was used for all depositions. Other detailed deposition parameters for all depositions were summarized in Table 1. All coatings contain a 2 μm TiN barrier layer which was deposited by the following parameters: Ti target power=2 kW, working pressure= 3 mTorr, Ar to N_2 flow ratio = 85:15, negative substrate bias=- 60 V,

Table 1 summarizes the deposition conditions for the proposed three TiN-MCrAl coatings.

Sample ID	Target power		Pulsing parameters	Substrate bias [V]	Working pressure [mTorr]	Ar flow [sccm]	Total Deposition time [min]
	Two MCr targets [W]	One Al target [W]					
CSM-1	2000	1200	200 kHz and 1 μs reverse time	-60	3.5	45	300
CSM-2	2000	1200	200 kHz and 1 μs reverse time	-60	3.5	45	320
CSM-3	2000	1200	200 kHz and 1 μs reverse time	-60	3.5	45	320

Some of the characterization work has been conducted in ACSEL. The crystal structure of the coatings was determined by XRD using a SIEMENS X-ray

diffractometer (Model KRISTALLOFLEX-810) operated with K-alpha Cu radiation in the conventional Bragg-Bentano mode. The thickness, surface morphology and cross-sectional microstructure of the coatings were characterized using a JSM-7000F field-emission scanning electron microscopy (FESEM) operated at a 5 kV accelerating voltage.

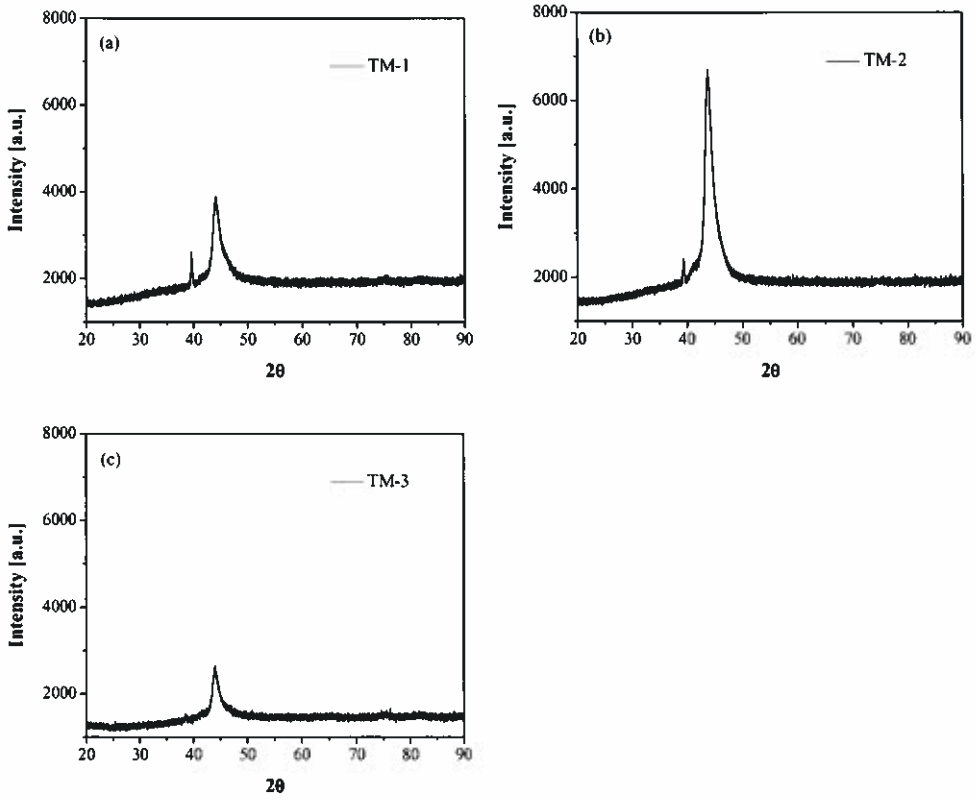

Figure 2. XRD patterns of the TiN-MCrAl coatings deposited on the Haynes substrate (a) CSM-1, (b) CSM-2, and (c) CSM-3.

Figure 2 shows the XRD patterns of three TiN-MCrAl coatings with different architectures. It can be seen that all coatings exhibited a single MCrAl phase. The CSM-2 coating exhibited the highest diffraction intensity, indicating a larger grain size and well developed crystalline in the coating. The CSM-3 coating exhibited a relatively wide diffraction peak, indicating a possible smaller grain size in the coating due to the multilayer structure.

Figure 3. (a) Cross-sectional SEM micrographs showing the architecture of the CSM-3 coating; (b) superlattice structure with Λ=24 nm observed in the MCrAl layers.

Figure 3 shows the cross-sectional SEM micrographs of the CSM-3 coating. As shown in Figure 3a, the CSM-3 coating showed a multilayered structure, in which the MCrAl and Al layers grew alternately from the bottom to the top. The thicknesses of the MCrAl layers and the Al layers are about 1 μm and 200 nm, respectively. It is also interesting to observe that the MCrAl layers in the CSM-3 coating actually exhibited a superlattice structure with a bilayer period of 24 nm, as shown in Figure 3b. The formation of the superlattice structure is probably due to the configuration and the slow rotation speed of the rotation system used in the deposition. It is also evident that no typical columnar structure can be observed in the CSM-3 coating with the development of the multilayer and superlattice structure.

The microstructure of the coatings was further characterized in SWRI using SEM, as shown in Figure 4. All three coatings exhibited dense and desired microstructure, which contains a 2 μm TiN interlayer and the top MCrAl (CSM-1 and CSM-2) or MCrAl-Al (CSM-3) multilayer. However, it is evident that these coatings (CSM-1 to CSM-3) showed the coating delamilation at the interface between the substrate and the TiN layer after the metallurgical sample preparation. All three coatings also exhibited certain numbers of surface defects in the forms of pits and macro particles as evident in Figure 5.

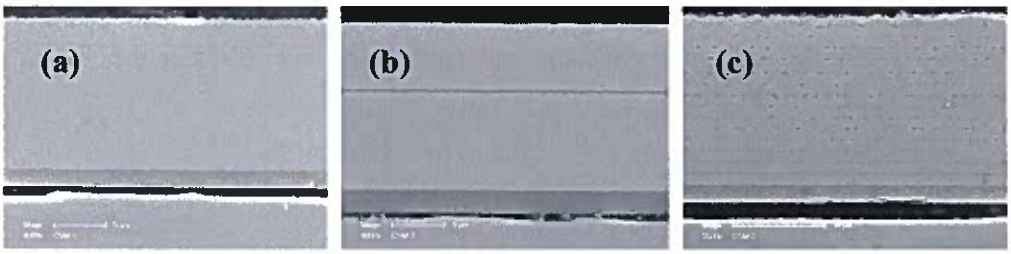

Figure 4. Cross-sectional SEM micrographs of three coating architectures deposited by PMS: (a) CSM-1, (b) CSM-2, and (C) CSM-3.

Figure 5. Top view SEM micrographs of three coating architectures deposited by PMS: (a) CSM-1, (b) CSM-2, and (C) CSM-3.

Since the coating delamilation was taken place at the interface between the TiN layer and the substrate, we assume that the thickness of the TiN layer is critical for the adhesion strength of the entire coating system. Therefore, one new coating (CSM-5) with the same architecture to CSM-1 (a single layer MCrAl coating) was deposited without the TiN interlayer. The other deposition conditions were kept the same.

As shown in Figure 6a, the CSM-5 coating exhibited superior adhesion strength as compared to the CSM-1 coating which contains a 2 μm TiN layer (Figure 4a). No coating delamilation was observed in CSM-5. The coating exhibited a dense microstructure. As shown in Figure 6b, the CSM-5 coating also showed an improved surface quality, which contains much less surface defect as compared to the previous CSM-1, CSM-2 and CSM-3 coatings.

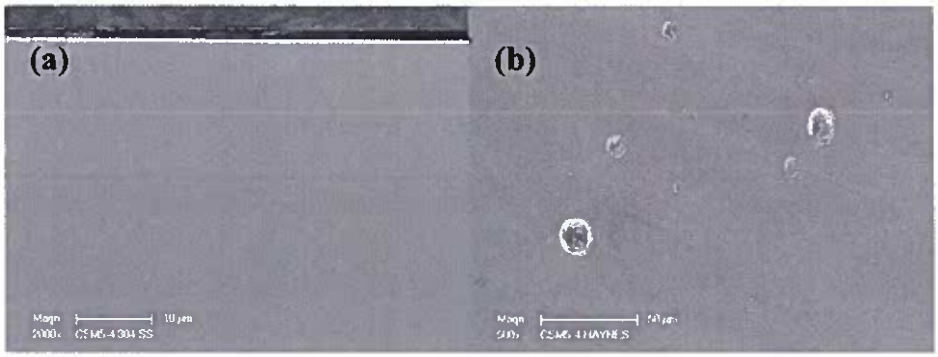

Figure 6. (a) Cross-sectional SEM micrograph and (b) top-view SEM micrograph of the CSM-5 coating deposited by PMS without the TiN interlayer.

Based on the results obtained in the second stage work, we can draw the following conclusions:

1) Three TiN-MCrAl coating architectures as proposed by SWRI have been successfully deposited using PMS at CSM with the coating thickness in the range of 16 to 22 μm. The coatings exhibited a dense superlattice microstructure.
2) As the substrate to target distance was decreased, the coatings deposited with a 2μm TiN interlayer (CSM-1, CSM-2 and CSM-3) exhibited decreased adhesion

strength as compared to the coatings deposited in the first stage work since the coating delamination was observed between the TiN interlayer and the substrate.

3) The coating deposited without the TiN interlayer (CSM-5) exhibited good adhesion strength to the AISI 304 stainless steel and the Haynes substrates.
4) The coating deposited without the TiN interlayer also exhibited a decrease in the surface defects as compared to the coatings deposited with a TiN interlayer and the coatings deposited in the first stage work as well.

For the future work, we believe it is important to optimize the thickness of the TiN interlayer between the substrates and the top MCrAl layer to achieve good adhesion strength in the overall coating system.

Respectfully submitted,

John J Moore, Ph.D.
Professor and Center Director
ACSEL, Colorado School of Mines

Jianliang Lin. Ph.D.
Assistant Research Professor
ACSEL, Colorado School of Mines

Research Report

Submitted to
South West Research Institute

Submitted by
Advanced Coatings and Surface Engineering Laboratory (ACSEL)
Metallurgical and Materials Engineering Department
Colorado School of Mines
Golden, CO, 80401

Title

Development of thick MCrAl/TiN multilayer coatings for high temperature applications using dc and pulse dc magnetron sputtering

Principal Investigator:
Prof. John J Moore: Professor and Center Director
Advanced Coatings and Surface Engineering Laboratory (ACSEL)
Metallurgical and Materials Engineering Department
(303-273-3771)
jjmoore@mines.edu

Co-Principal Investigator:
Dr. Jianliang Lin: Assistant Research Professor
Advanced Coatings and Surface Engineering Laboratory (ACSEL)
Metallurgical and Materials Engineering Department
(303-273-3178)
jlin@mines.edu

Research background and objective were submitted in the research proposal.

1. Deposition system and experimental details.

All coating depositions were carried out in a closed field unbalanced magnetron sputtering system (CFUBMS) in ACSEL. Fig. 1 shows the photo and the schematic drawing of the configuration of the system. The system contains four rectangular unbalanced magnetrons (308 mm×106 mm) (Teer, Coatings LTD.) of reversed magnetic polarities installed at 90-degree to each other around the cylinder chamber wall. For the TiN/MCrAl coating deposition, two MCr target were installed oppositely with a distance of 470 mm (the diameter of the chamber), while the Al and Ti targets were also installed oppositely in the system, as shown in Fig. 1b.

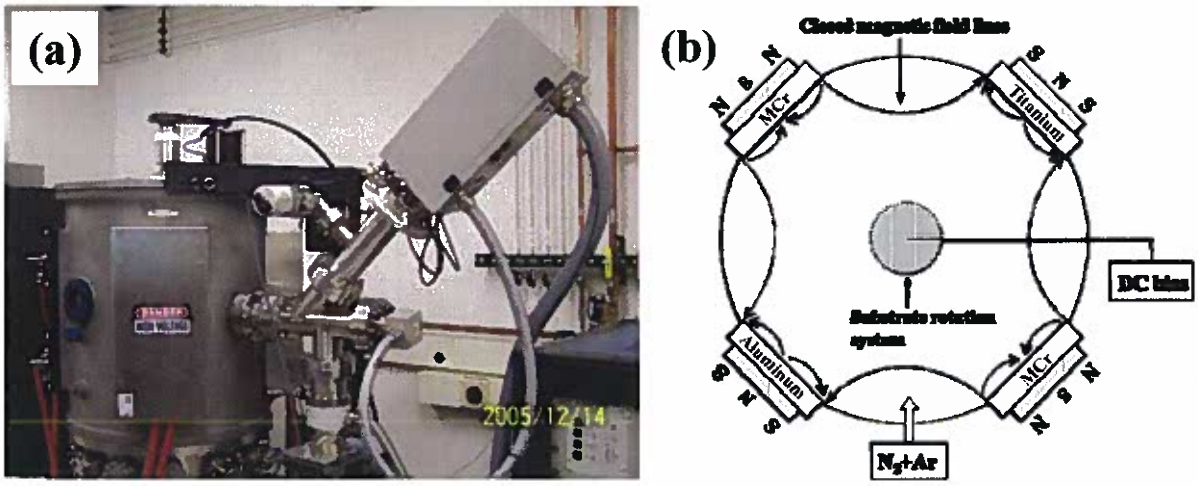

Fig. 1 (a) Photo of the CFUBMS system in ACSEL, and (b) schematic drawing showing the target and substrate configurations in the system

The substrates are AISI 304 stainless steel coupons from ACSEL and the coupons (AISI 304 stainless steel and Haynes alloy coupons) provided by SWRI. The substrates were ultrasonically cleaned in denatured acetone and alcohol for 20 minutes respectively. The substrates were wired down from the center holder in the chamber with a distance to the target surface of 235 mm. The substrates were rotated continuously with a speed of 20 rpm in the chamber by a rotation device (Fig. 1).

In general, a base pressure less than 1.5×10^{-6} Torr was achieved prior to all coating depositions. Ar plasma etching process was used to further clean the substrate surface for improving the coating adhesion. The etching process was carried out at a pressure of 8 mTorr with a pulsed dc bias of -500 V (200 kHz and 1.0 μs) for 40 mins, which generated a 370 W power and 0.8 A current on the substrates.

The targets were powered by using two Advanced Energy Pinnacle Plus Power supplies. The pulsing power supply can be operated under either DC or pulsing mode. The pulsing parameters used for PMS depositions were 100 kHz and 2.5 μs, which correspond to a 75% duty cycle (The duty cycle is defined as the negative pulse time divided by the time of the pulsing cycle). A -50 V dc substrate bias was used for all depositions. Other detailed deposition parameters for all depositions were summarized in Table 1.

Table 1. Deposition parameters of TiN and MCrAl coatings

ID		Power	Pulsing parameter	pressure [mTorr]	Ar flow [sccm]	N_2 flow [sccm]	Time [hr]	Thickness [μm]	Deposition rate [μm/hr]
TiN-2	dc	P_{Ti}=2 kW	N/A	3.0	36	4	2	1.7	0.85
TiN-3	PMS	P_{Ti}=2 kW	100 kHz,/1.0 μs	3.0	36	4	2	1.5-1.6	0.8
MCrAl-1	PMS	P_{MCr}=2 kW P_{Al}=1.0 kW	100 kHz/2.5 μs	3.0	46	N/A	2	6.7	3.3
MCrAl-4	dc	P_{MCr}=2 kW P_{Al}=1.5 kW	N/A	3.0	45	N/A	2	8.5-9	4.5
MCrAl-5	PMS	P_{MCr}=2 kW P_{Al}=1.5 kW	100 kHz/2.5 μs	3.0	46	N/A	2	7.5	3.7
MCrAl-6* (304)	dc	P_{MCr}=2 kW P_{Al}=1.5 kW	N/A	3.1	45	N/A	7	32-34	4.6-4.8
MCrAl-7* (304)	PMS	P_{MCr}=2 kW P_{Al}=1.5 kW	100 kHz/2.5 μs	3.0	46	N/A	8	28-30	3.5-3.7
MCrAl-8* (Haynes)	dc	P_{MCr}=2 kW P_{Al}=1.5 kW	N/A	3.1	45	N/A	6.5	28-30	4.3-4.6
MCrAl-9* (Haynes)	PMS	P_{MCr}=2 kW P_{Al}=1.5 kW	100 kHz/2.5 μs	3.0	46	N/A	7.5	26-28	3.5-3.7

* These long MCrAl coatings were deposited on a 1.5 μm TiN interlayer.

A series of characterization techniques was conducted at ACSEL in an effort to give a comparison of the structure and properties of the MCrAl/TiN coatings deposited using dcMS and PMS techniques:

1) The crystal structure of the coatings was determined by XRD using a SIEMENS X-ray diffractometer (Model KRISTALLOFLEX-810) operated with K-alpha Cu radiation in the conventional Bragg-Bentano mode.

2) The thickness, surface morphology and cross-sectional microstructure of the coatings were characterized using a JSM-7000F field-emission scanning electron microscopy (FESEM) operated at a 5 kV accelerating voltage.

3) The chemical composition of the coatings was using an energy dispersive spectrometer (EDS) attached in the SEM using atomic number (Z), absorption (A) and fluorescence (F) (ZAF) corrections. The EDS measurements were performed on the flat coating surface (no tilt) with the

following constant parameters: a 10 kV accelerating voltage, a 10 A probe current and a fixed 10 mm working distance.

4) The hardness and Young's modulus of the coatings were measured using a nanoindenter (NanoIndenter XPTM, MTS Systems Corporation) equipped with a Berkovich diamond indenter.

2. Results and discussion

2.1 dcMS and PMS deposited TiN coatings (interlayer)

As can be seen in Table 1, PMS sputtered TiN coating (TiN-3) exhibited a slight decrease in the deposition rate than that of the dcMS TiN coating (TiN-2). Fig. 2 shows the XRD patterns of TiN-2 and TiN-3 coatings. Both coatings exhibit a polycrystalline NaCl type face center cubic (fcc) structure with (111), (200) and (220) and (311) reflections. Nevertheless, the PMS TiN-3 coating exhibited broaden diffraction peaks compared to the dcMS TiN-2 coating, indicating a smaller grain size or a higher internal stress in the coating. The mechanical properties of all TiN and MCrAl coatings were summarized in Table 2. It can be seen that the PMS TiN-3 coating exhibited a higher hardness (32.8 GPa) and Young's modulus (423 GPa) than those of the dcMS TiN-2 coating.

Fig. 3 shows the cross-sectional SEM micrograph of the TiN-3 coating. The TiN-3 coatings exhibited a dense microstructure free of porosities. The coating also exhibited fine grain size in the nanometer range. Unfortunately, we did not obtain a SEM micrograph for the TiN-2 coating, because no TiN-2 coating was deposited on the Si wafer.

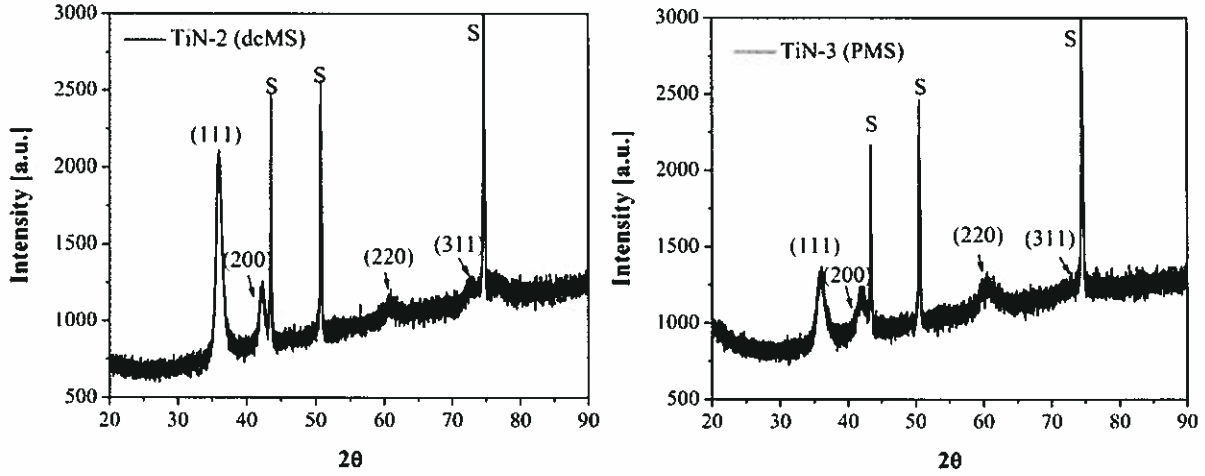

Fig. 2 XRD patterns of (a) TiN-2 (dcMS) and (b) TiN-3 (PMS) coatings

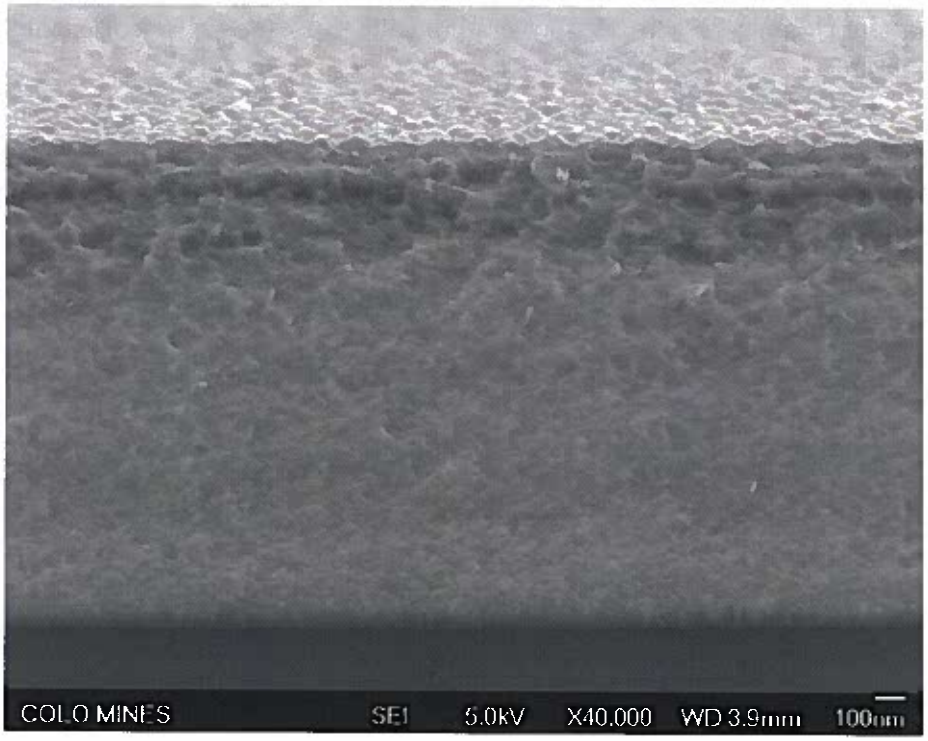

Fig. 3 Cross-sectional SEM micrograph of the PMS TiN-3 coating

Table 2 Summary of the Al concentration and the mechanical properties of dcMS and PMS deposited TiN and MCrAl coatings

Coating	Deposition	Al Composition [wt%]	Hardness [GPa]	Young's modulus [GPa]
TiN-2	dc	N/A	27.3±1.2	410±16
TiN-3	PMS	N/A	32.8±1.1	423±13
MCrAl-1	PMS	6.82	13.5±0.4	235±4.6
MCrAl-4	dc	8.46	10.9±1	207±11.2
MCrAl-5	PMS	8.95	13.7±0.5	230±6.8
MCrAl-6* (304)	dc	8.78	8.0±0.9	155±12
MCrAl-7* (304)	PMS	9.47	9.86±0.8	212±15
MCrAl-8* (Haynes)	dc	8.84	7.2±0.7	161±17
MCrAl-9* (Haynes)	PMS	9.89	8.7±0.7	202±10

2.2 dcMS and PMS deposited MCrAl coatings (2 hr deposition)

Single layer MCrAl coatings (without TiN interlayer) were deposited using dcMS and PMS in CFUBMS system for 2 hours in an effort to determine the deposition rate. The coatings were labeled as MCrAl-1, MCrAl-4, and MCrAl-5 in Table 1. For the same deposition time (2 hours), The dcMS MCrAl-4 coating exhibited higher deposition rate than the PMS MCrAl-1 and MCrAl-5 coatings. The MCrAl-1 coating exhibited the lowest deposition rate because a lower Al target power was used.

Fig. 4 shows the XRD patterns of MCrAl-4 (dcMS) and MCrAl-5 (PMS) coatings. The dcMS MCrAl-4 coating showed strong fcc diffraction peaks of (111) and (222). On the other hand, the PMS MCrAl-5 coating exhibited very broader diffraction peaks, suggesting finer grain structure, confirming the development of nanocrystallines in the coating.

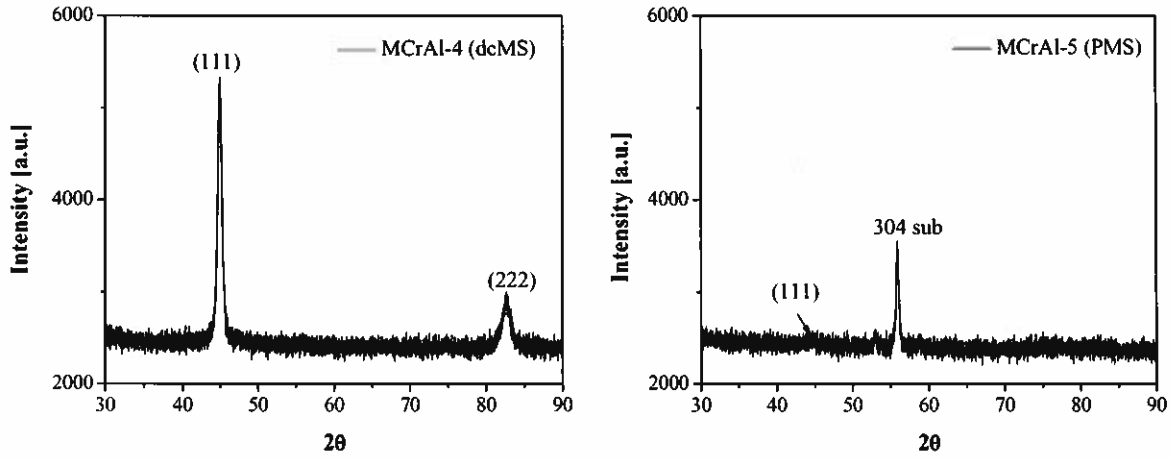

Fig. 4 XRD patterns of MCrAl-4 (dcMS) and MCrAl-5 (PMS) coatings

Fig. 5 shows the cross-sectional SEM micrographs of MCrAl-4 (dcMS) and MCrAl-5 (PMS) coatings. As shown in Fig. 5a, the dcMS MCrAl-4 coating exhibited a typical columnar grain structure. The width of the top of the columnar gains was estimated to be 400-500 nm. To the country, the width of the top of the columnar gains was reduced to 200-300 nm in the PMS MCrAl-5 coating (Fig. 5b). In addition, the MCrAl-5 coating exhibited a denser microstructure and smoother surface roughness as compared to the MCrAl-4 coating, as shown in Fig. 5.

The Al concentrations of the MCrAl-4 and MCrAl-5 coatings are 8.46 and 8.95, respectively, as revealed by EDS (Table 2). An important observation is that the PMS MCrAl-5 coating showed a high hardness of 14 GPa, while the dcMS MCrAl-4 coating exhibited a lower hardness of 10 GPa (Table 2). It is believed that the improved hardness of the MCrAl-5 coating is related to its finer grain size and denser microstructure as revealed in Fig. 4 and Fig 5.

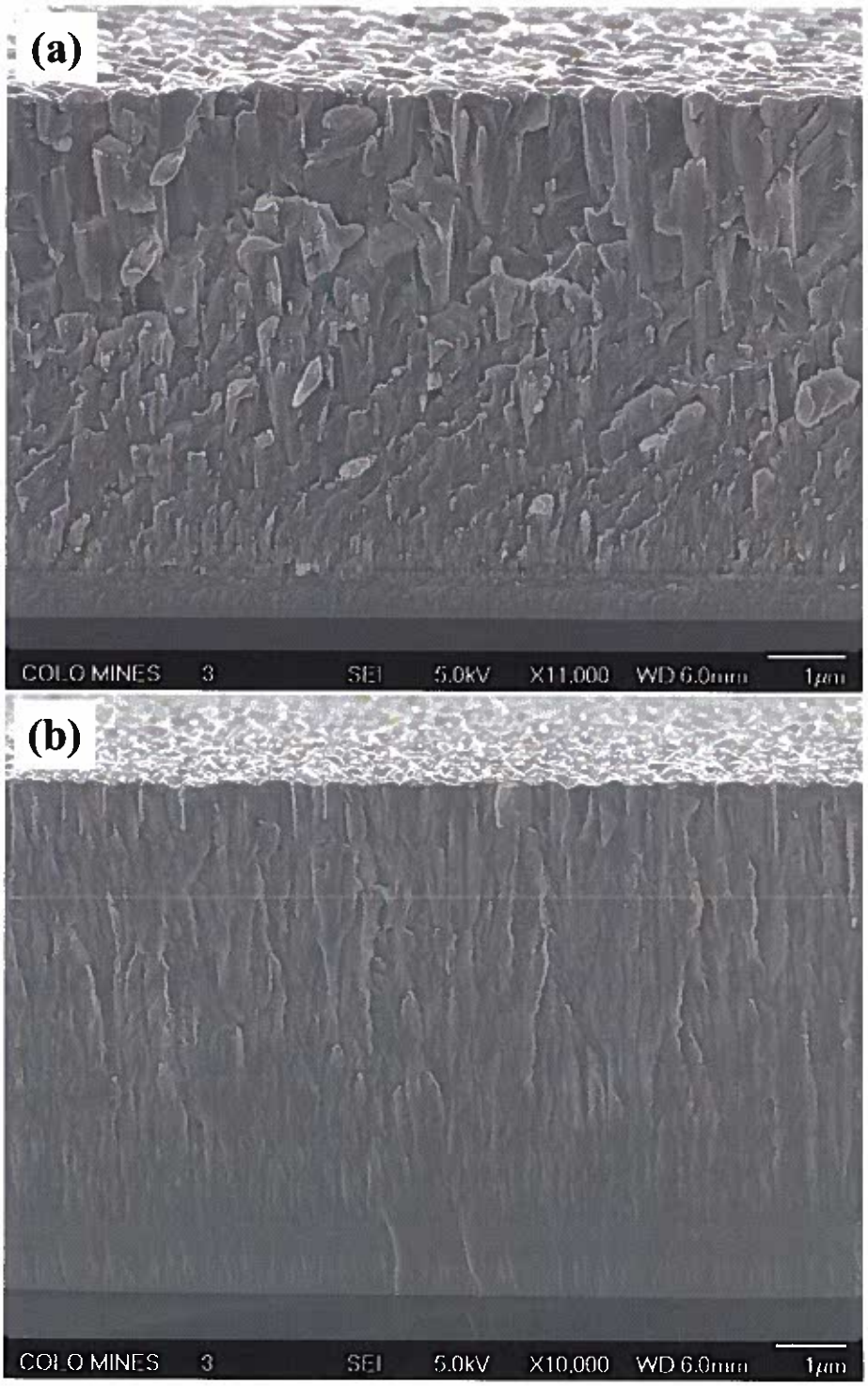

Fig. 5 Cross-sectional SEM micrographs of (a) MCrAl-4 (dcMS) and (b) MCrAl-5 (PMS) coatings

2.3 Thick MCrAl coatings on 304 and Haynes substrates.

In this section, we will mainly use MCrAl coatings deposited on AISI 304 stainless steel substrate as examples to compare the structure and properties of thick dcMS and PMS sputtered MCrAl coatings.

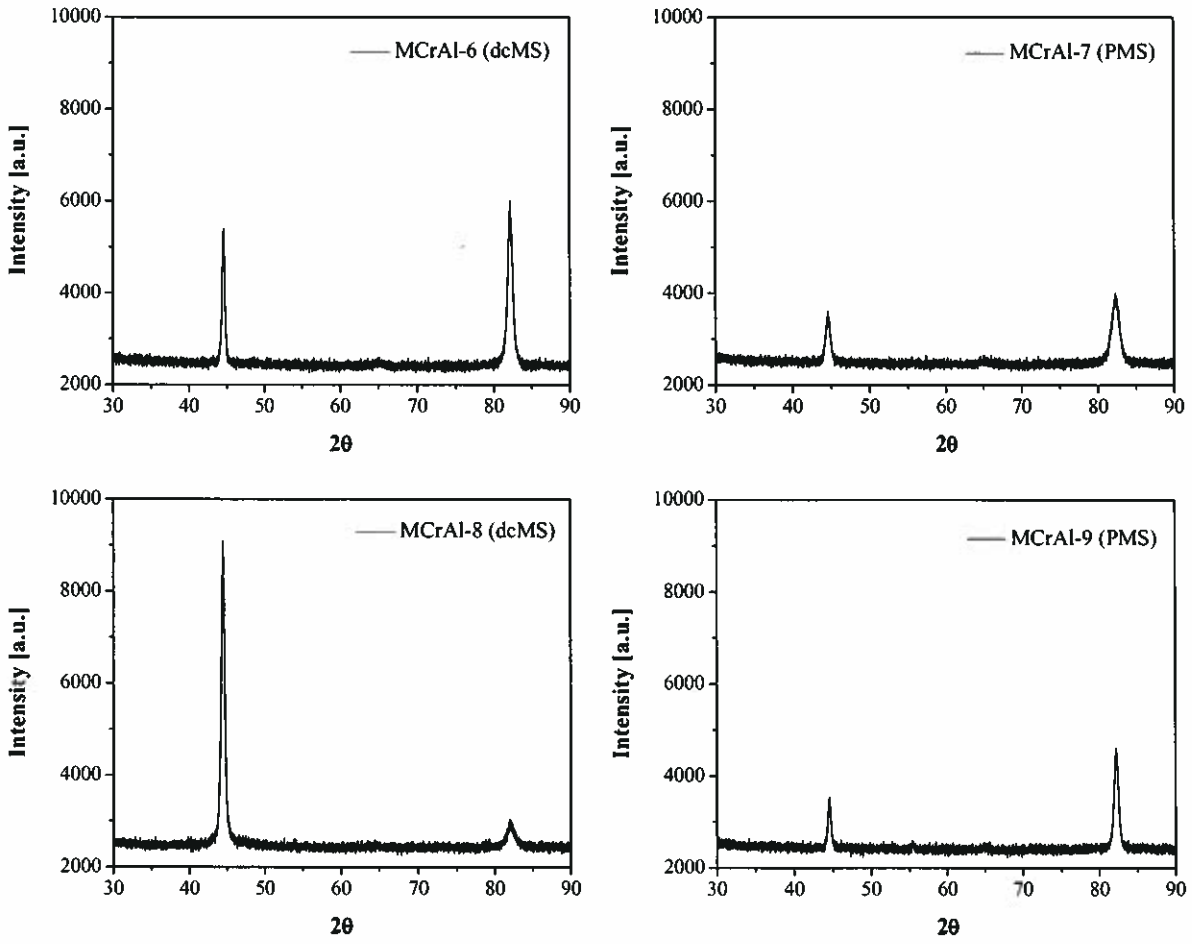

Fig. 6 XRD patterns of thick MCrAl-6 (dcMS) and MCrAl-7 (PMS) coatings deposited on AISI 304 stainless steel substrate, and thick MCrAl-8 (dcMS) and MCrAl-9 (PMS) coatings deposited on Haynes alloy substrate.

Fig. 6 shows the XRD patterns of thick MCrAl-6 (dcMS) and MCrAl-7 (PMS) coatings deposited on AISI 304 stainless steel substrate, and thick MCrAl-8 (dcMS) and MCrAl-9 (PMS) coatings deposited on Haynes alloy substrate. It can be seen that the diffraction peaks in the PMS sputtered MCrAl coatings (MCrAl-7 and MCrAl-9) are broader and exhibit lower intensity than the dcMS coating (MCrAl-6 and MCrAl-8), again suggesting a smaller grain size and/or higher residual stress in the PMS deposited MCrAl coatings.

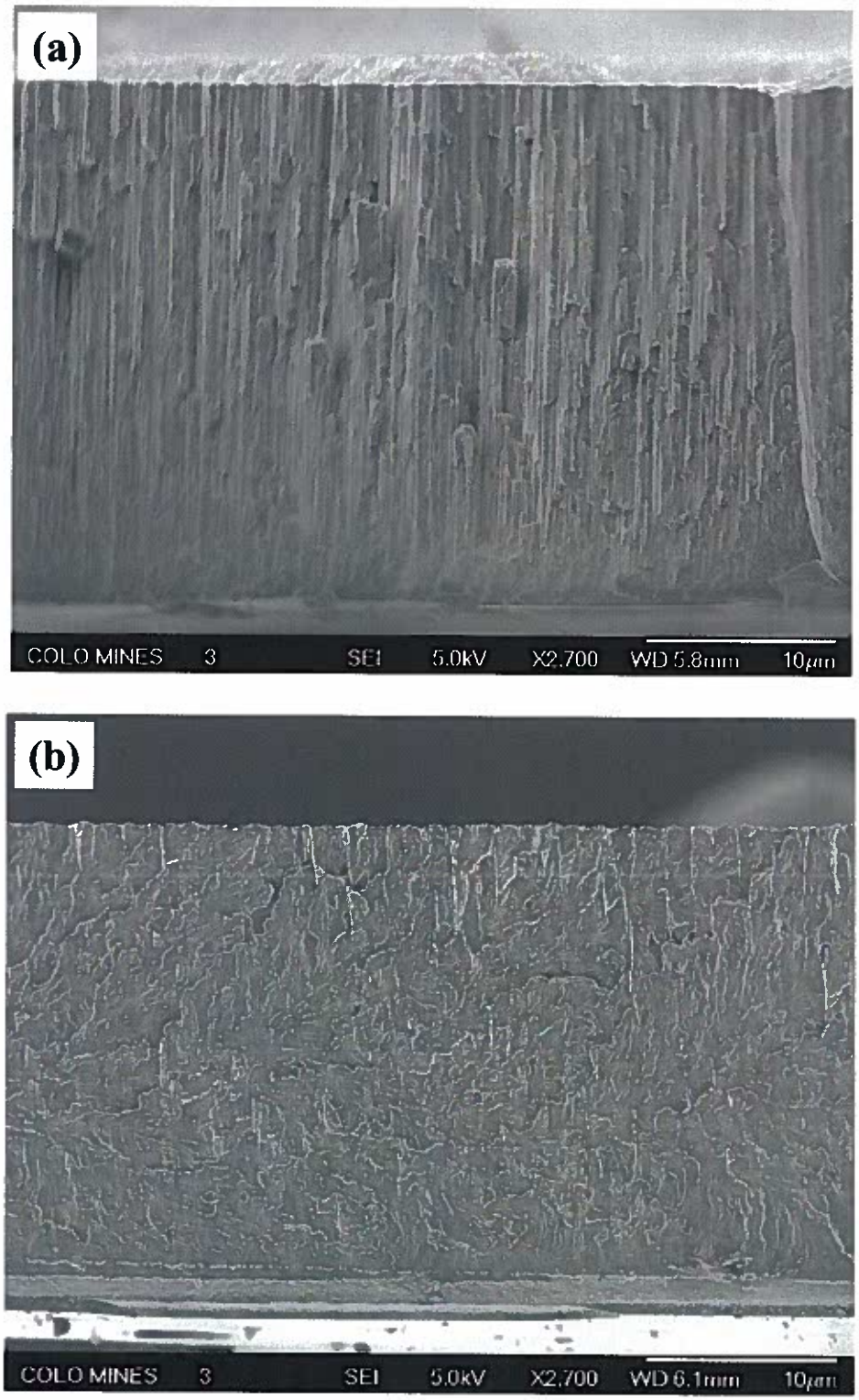

Fig. 7 Cross-sectional SEM micrographs of (a) MCrAl-6 (dcMS) and (b) MCrAl-7 (PMS) coatings

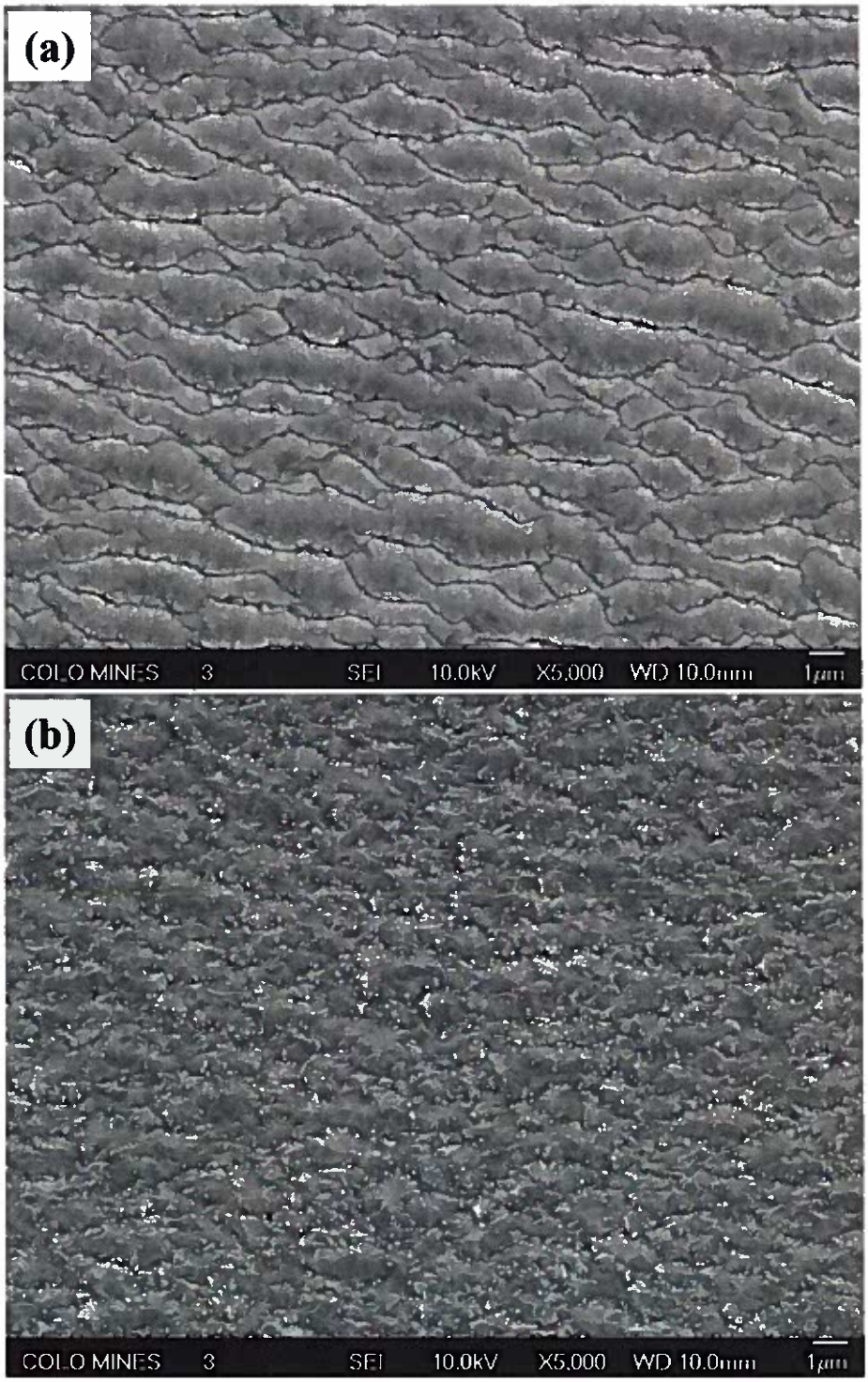

Fig. 8 Top view SEM micrographs of (a) MCrAl-6 (dcMS) and (b) MCrAl-7 (PMS) coatings

Fig. 7 and Fig. 8 show the cross-sectional and top view SEM micrographs of the MCrAl-6 and MCrAl-7 coatings, respectively. The thick dcMS MCrAl-6 coating exhibited typical large columnar grain growth, whereas the thick PMS MCrAl-7 coating showed a denser microstructure with a much less pronounced columnar grain feature and finer grain size, which are consistent with the previous observation from the 2 hour deposited coatings (Fig. 5).

As shown in Fig. 8, the surface morphology of the MCrAl-6 coating also confirmed the larger top grain size as compared to the MCrAl-7 coating. Additionally, net shaped boundaries/cracks can be clearly identified on the surface of the MCrAl-6 coating (Fig. 8a), which are probably related to the release of the thermal residual stress accumulated during the thick coating deposition. The surface of the MCrAl-7 coating also showed a small amount of boundaries/cracks (Fig. 8b). However, the size of the grains is much smaller and the coating is denser as compared to the MCrAl-6 coating.

As summarized in Table 2, the Al concentrations in the MCrAl-6 and MCrAl-7 coatings are 8.78 and 9.47, respectively, as revealed by EDS. Both thick MCrAl-6 and MCrAl-7 coatings exhibited lower hardness values than the coatings deposited for 2 hours (MCrAl-4 and MCrAl-5). However, the thick PMS MCrAl-7 coating still showed a higher hardness value than the thick dcMS MCrAl-6 coating (Table 2). The thick MCrAl coatings deposited on the Haynes alloy substrate (MCrAl-8 and MCrAl-9) showed similar hardness values to the coatings deposited on AISI 304 stainless steel.

2.3 Summaries

Based on the above results, we can draw the conclusion that the MCrAl coatings deposited by using PMS exhibited finer grain size, denser microstructure and higher hardness than those of the dcMS coatings for the same deposition time.

However, we also observed that the surface roughness of the thick PMS MCrAl coatings increased significantly as compared to the coatings deposited for 2 hours. There are a large amount of pits was visualized from the thick coating surface. We believe that the formation of the pits was due to the incorporation of the micro-particles and the release of the high thermal stress in the coating as the deposition time was increased.

Therefore, for the future work, we will aim at depositing MCrAl coatings as a function of the deposition time using the PMS technique, in an effort to determine the optimized deposition time/ coating thickness for the PMS MCrAl coating deposition in ACSEL CFUBMS system.

An industry-university consortium at the Colorado School of Mines

Advanced Coatings and Surface Engineering Laboratory (ACSEL),
Department of Metallurgical & Materials Engineering,
Colorado School of Mines

Research Report

Submitted to
South West Research Institute

Submitted by
Advanced Coatings and Surface Engineering Laboratory (ACSEL)
Metallurgical and Materials Engineering Department
Colorado School of Mines
Golden, CO, 80401

Title

Development of thick MCrAl/TiN multilayer coatings for high temperature applications using dc and pulse dc magnetron sputtering

4/30/2011

Principal Investigator:
Prof. John J Moore: Professor and Center Director
Advanced Coatings and Surface Engineering Laboratory (ACSEL)
Metallurgical and Materials Engineering Department
(303-273-3771)
jjmoore@mines.edu

Co-Principal Investigator:
Dr. Jianliang Lin: Assistant Research Professor
Advanced Coatings and Surface Engineering Laboratory (ACSEL)
Metallurgical and Materials Engineering Department
(303-273-3178)
jlin@mines.edu

Current research work:

From March to April 2011, we have studied the microstructure evolution of the SW3-MCrAl-#5 coating (see previous report 2-10-2011) after thermally cycled at 1010 ^{o}C for 500 and 1007 cycles using TEM.

Experimental details:

The SW3-MCrAl-#5 coating was thermally annealed at 1010 ^{o}C for 500 and 1007 cycles in SWRI. Cross-sectional TEM samples were prepared by focused ion beam (FIB) technique to electron transparency. A Philips/FEI CM200 transmission electron microscope (TEM) operated at 200 kV was used to examine the sample cross-section.

Results and discussion:

Figure 1 shows the TEM micrographs of the as-deposited SW3-MCrAl-#5 coating. The coating can be characterized as a columnar grain structure with a superlattice structure formed within the columnar grains, as shown in Figure 1a. The width of the top columnar grain is about 800 nm. As shown in Figure 1b, the dark layer is the MCr rich layer and the bright layer is the Al rich layer. The bilayer period of the superlattice structure is about 25 nm. The selected area electron diffraction (SAED) pattern of the coating exhibited a continuous ring pattern, which matches with an fcc polycrystalline structure with (111), (200), (220) and (311) diffractions (Figure. 1c). The continuous SAED ring pattern of the coating indicates that the coating contains fine grain size. As shown in a HRTEM image (Figure 1d), nanocrystalline grains with a grain size less than 10 nm were identified by the lattice fringe pattern in the MCr rich layer.

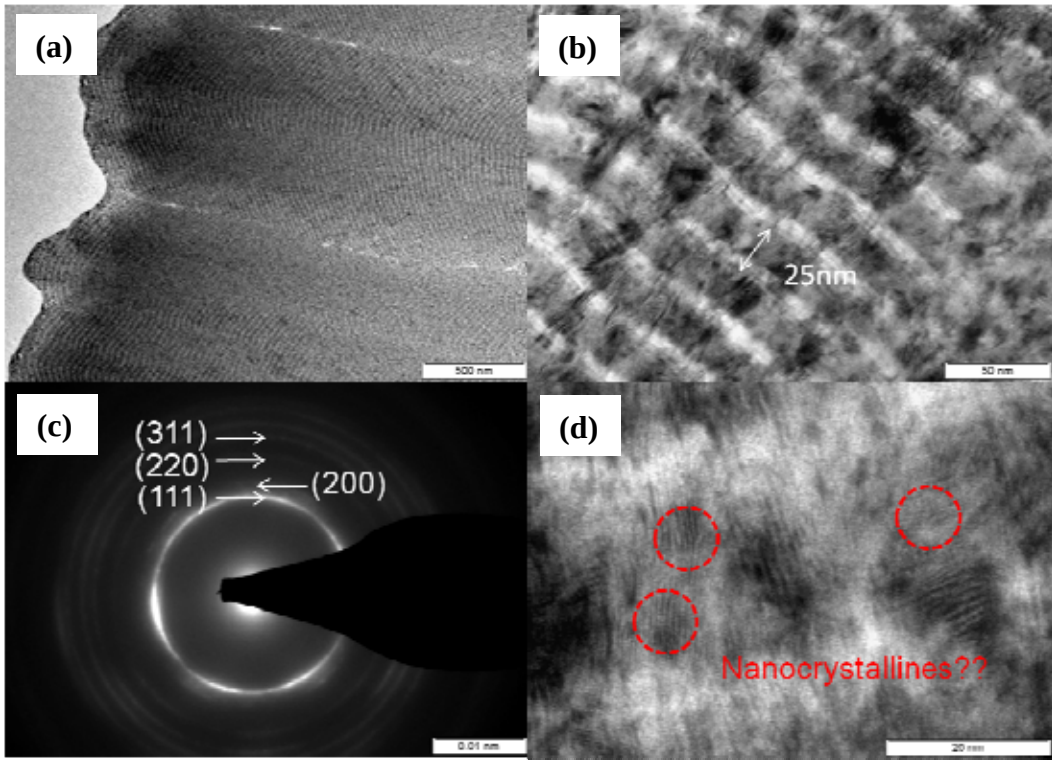

Figure 1. (a) TEM micrograph of the as-deposited SW3-MCrAl-#5 coating; (b) TEM micrograph showing the superlattice structure, (c) the SAED pattern, and (d) high resolution TEM image of the SW3-MCrAl-#5 coating showing nanocrystallines grains with a grain size less than 10 nm.

Figure 2 shows the BF and DF TEM micrographs and the SAED patterns of the SW3-MCrAl-#5 coating after 500 thermal cycles at 1010 ^{o}C. It is evident that a 1 μm thick oxide layer has been developed on the coating surface. The structure of the oxide layer is dense as shown from the BF TEM micrograph (Figure 2a). The typical oxide grain size is about 300-500 nm as revealed in the DF TEM micrograph (Figure 2b). The underlay MCrAl coating still exhibited a dense structure. However, it can be seen that the superlattice structure of the MCrAl coating vanished after the 500 thermal cycling treatment. The SAED pattern taken from the outer oxide layer showed a polycrystalline α-Al_2O_3 phase, whereas the SAED pattern taken from the inner coating layer showed a FCC structure similar to the as-deposited MCrAlN coatings. In another TEM image as shown in Figure 2e, it is evident that the columnar grain width of the SW3-MCrAl-#5 coating after 500 thermal cycles at 1010 ^{o}C is in the range of 500-800 nm, which is similar to that of the as-deposition coating.

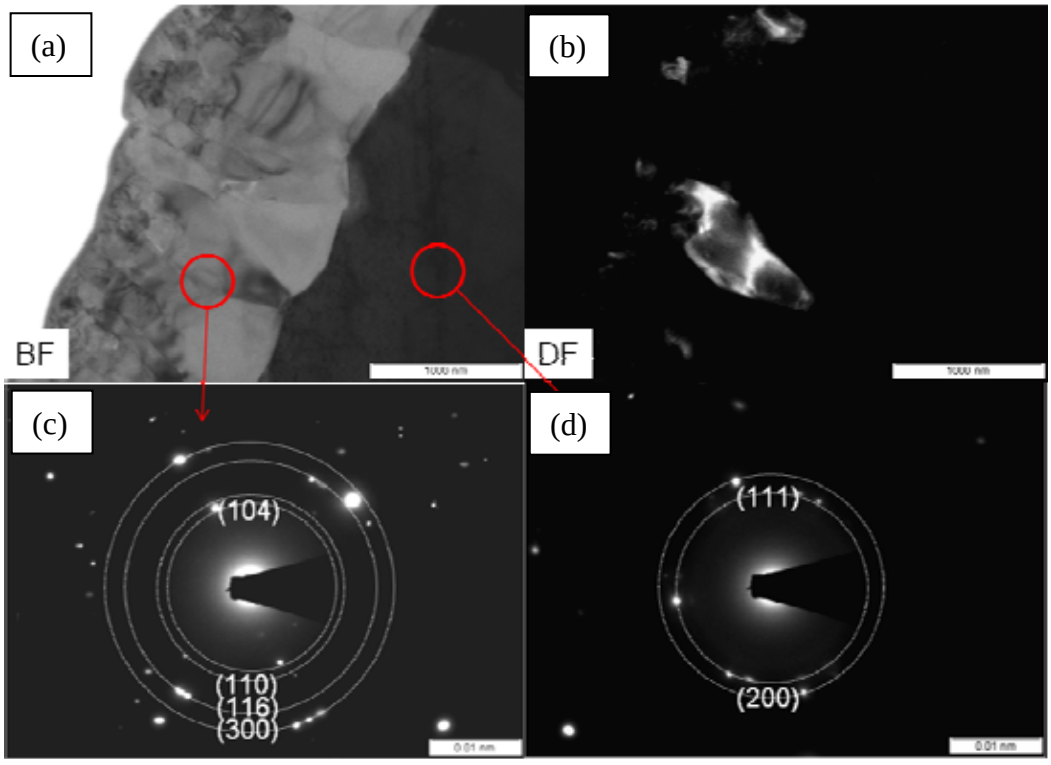

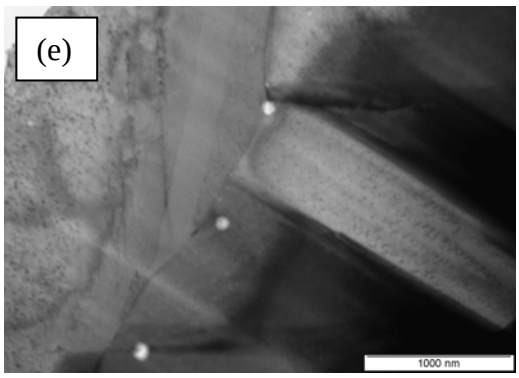

Figure 2. (a) BF TEM micrograph of the 500 thermal cycled coating; (b) DF TEM micrograph of the 500 thermal cycled coating, (c) the SAED pattern of the outer oxide layer, (d) the SAED pattern of the inner MCrAl coating, and (e) BF TEM micrograph of the 500 thermal cycled coating showing the width of the columnar grains is in the range of 500-800 nm.

Figure 3 shows the BF and DF TEM micrographs of the SW3-MCrAl-#5 coating after 500 thermal cycles at 1010 ^{o}C. It is evident that a large amount of dark precipitates were formed in the annealed coating (Figure. 3b). The DF TEM micrograph shown in Figure 3c demonstrated the size of the precipitates is less than 10 nm. Energy dispersive spectroscopy (EDS) analysis was carried out at three locations along the coating cross-section (Figure 3a): (1) outer oxide layer; (2) precipitates rich region; and (3) MCrAl coating. As shown in Figure 4, the EDS analysis showed the outer oxide layer (#1) contains Al and O elements. The dark precipitates rich region (#2) exhibited a higher Ni and Cr content than the MCrAl region (#3). The Cu element observed in the EDS spectra is from the reflection peak of the Cu grids.

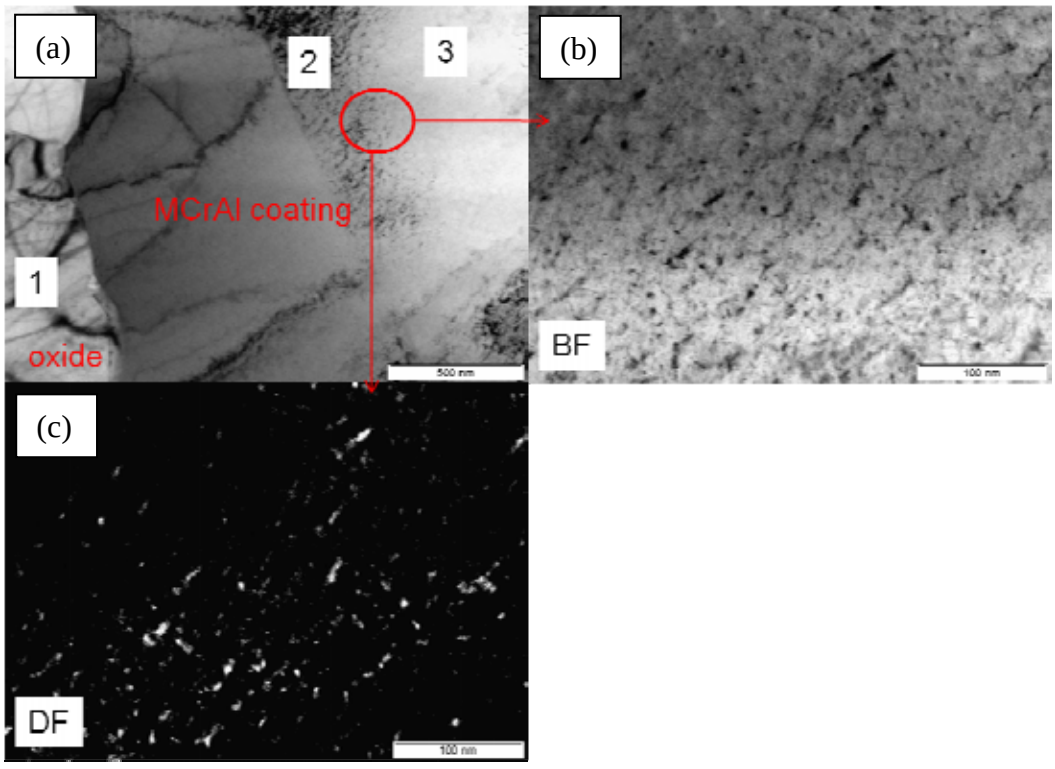

Figure 3. (a) TEM micrograph of the 500 thermal cycled coating; (b) BF TEM micrograph of the cycled region, (c) DF TEM micrograph of the cycled region, and (d) HRTEM image of the inner MCrAl coating showing 5-10 nm nanocrystallines.

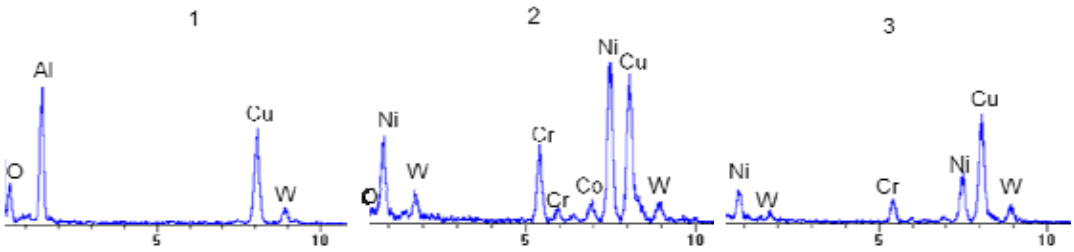

Figure 4. EDS analysis of three areas labeled in Figure. 3 (1) oxide layer, (2) dark precipitates, and (3) MCrAl coating

Figure. 5 shows a HRTEM micrograph obtained at the cross-section of the 500 thermal cycled MCrAl coating under the outer oxide layer. 5-10 nm Nanocrystalline grains are clearly seen by the lattice fringe pattern in the coating cross-section.

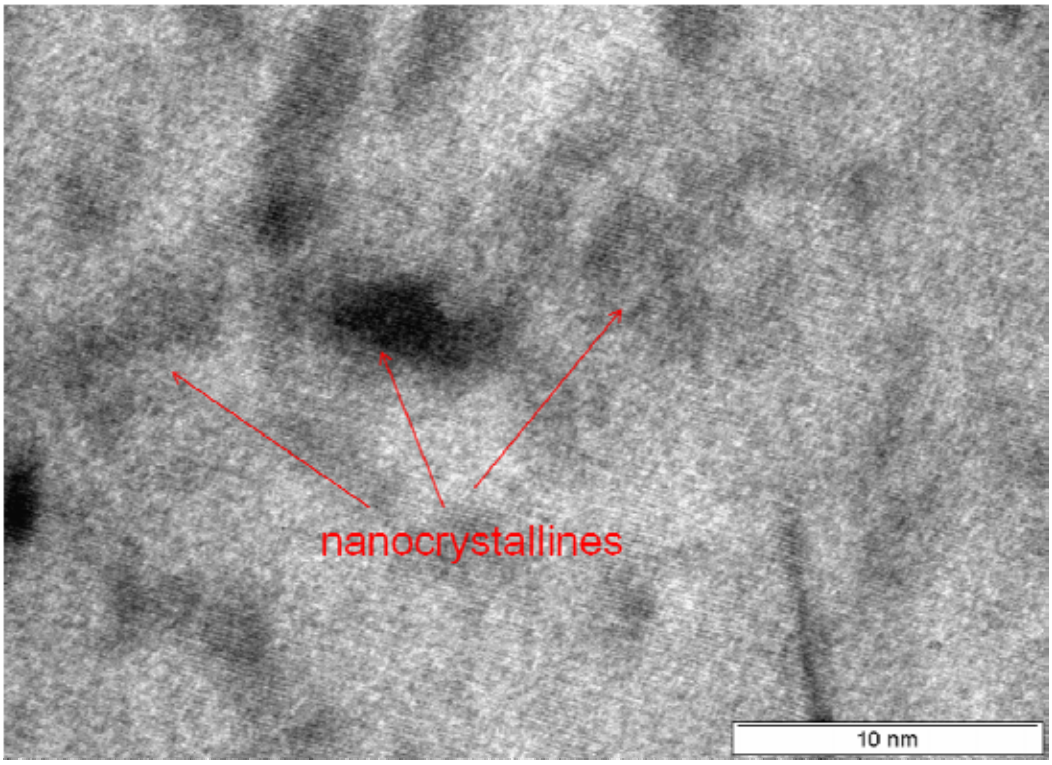

Figure 5. HRTEM micrograph showing 5-10 nm nanocrystallines in the 500 thermal cycled SW3-MCrAl-#5 coating

Figure 6 shows the BF and DF TEM micrographs and the SAED patterns of the SW3-MCrAl-#5 coating after 1007 thermal cycles at 1010 ^{o}C. A dense oxide layer has been developed on the coating surface (Figure 6a). The thickness of the oxide layer is about 1 μm, which is similar to the 500 thermal cycled coating (Figure 2a). The typical oxide grain size is about 700-800 nm as revealed in the DF TEM

micrograph (Figure 6b), which is larger than that of the 500 thermal cycled coating (Figure 2b). The underlay MCrAl coating still exhibits a dense columnar grain structure. As shown in Figure 6a, the columnar grain width of the underlay MCrAl coating is in the range of 800-1000 nm, which is comparable to the grain size of the as-deposited and 500 thermal cycled MCrAl coatings (Figure. 1a and Figure 2a). This result demonstrated that the grain size of the MCrAl coating only exhibited a slightly change after 1007 thermal cycles at 1010 ^{o}C. The SAED pattern taken from the outer oxide layer showed a polycrystalline α-Al_2O_3 phase, whereas the SAED pattern taken from the inner coating layer showed a FCC structure similar to the as-deposited and the 500 thermal cycled MCrAlN coatings.

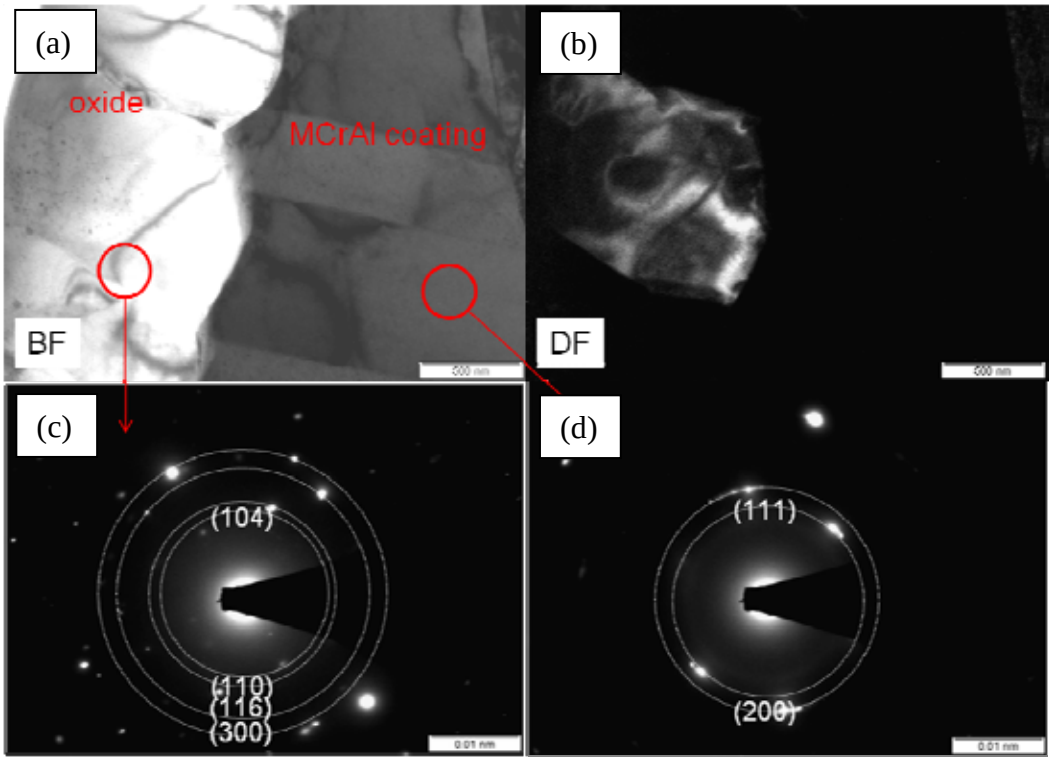

Figure 6. (a) BF TEM micrograph of the 1000 thermal cycled coating; (b) DF TEM micrograph of the 1000 thermal cycled coating, (c) the SAED pattern of the outer oxide layer, and (d) the SAED pattern of the inner MCrAl coating.

Figure 7 shows the BF and DF TEM micrographs of the SW3-MCrAl-#5 coating after 1007 thermal cycles at 1010 ^{o}C. Similar to the observations for the film annealed after 500 cycles, it is evident that a large amount of dark precipitates were formed in the annealed coating (Figure. 7a and 7b). The DF TEM micrograph shown in Figure 7c demonstrated the size of the precipitates is less than 10 nm. EDS analysis was carried out at three locations along the coating cross-section (Figure 7a): (1) outer oxide layer; (2) precipitates rich region; and (3) MCrAl coating. As shown in Figure 8, the EDS analysis showed the outer oxide layer (#1) contains Al and O elements. The dark

precipitates rich region (#2) exhibited a higher Ni and Cr content than the MCrAl region (#3). The Cu element observed in the EDS spectra is from the reflection peak of the Cu grids.

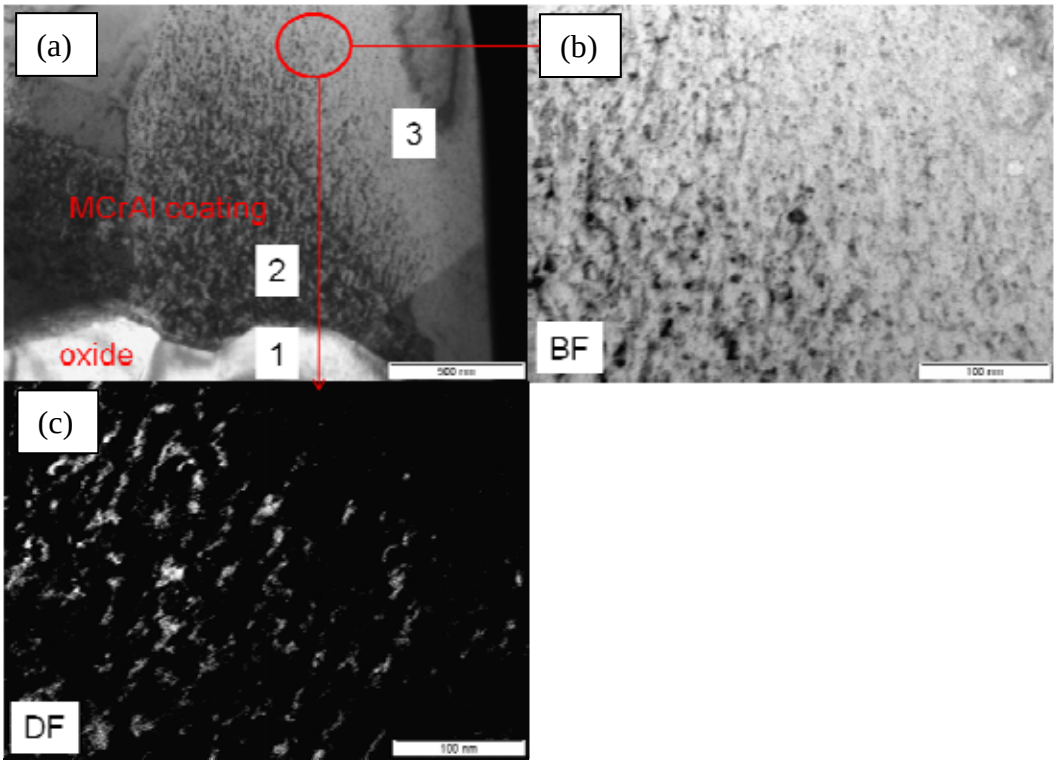

Figure 7. (a) TEM micrograph of the 1000 thermal cycled coating; (b) BF TEM micrograph of the cycled region, (c) DF TEM micrograph of the cycled region, and (d) HRTEM image of the inner MCrAl coating showing 5-10 nm nanocrystallines.

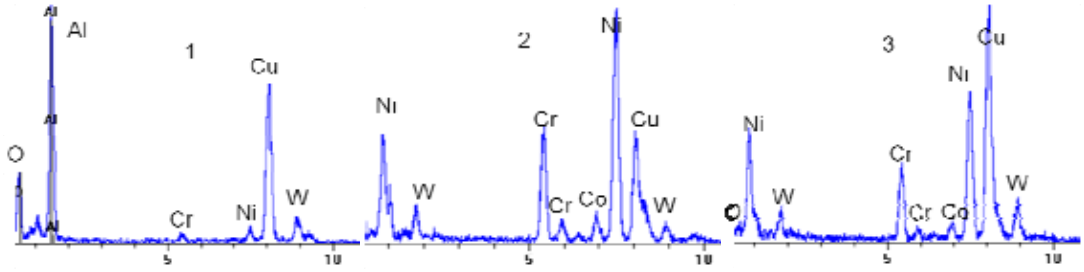

Figure. 8 EDS analysis of three areas labeled in Figure. 6 (1) oxide layer, (2) dark precipitates, and (3) MCrAl coating

Figure.9 shows a HRTEM micrograph obtained at the cross-section of the 1000 thermal cycled MCrAl coating under the outer oxide layer. Again, nanocrystalline

grains with a grain size less than 10 nm are clearly seen by the lattice fringe pattern in the coating cross-section.

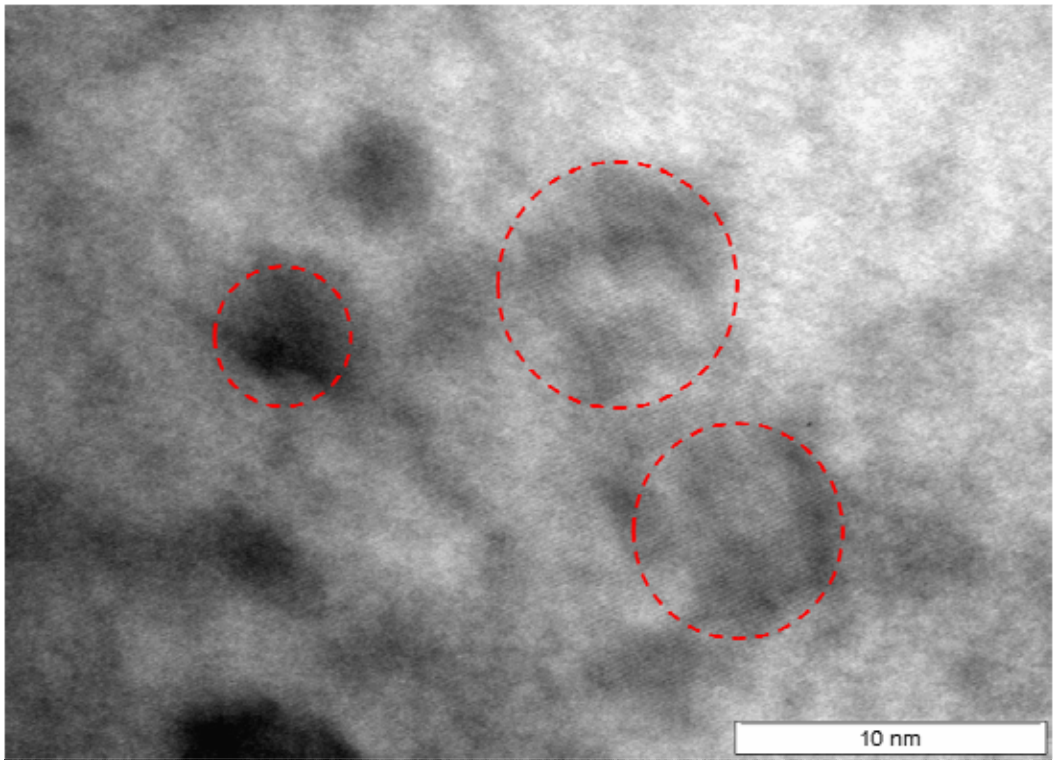

Figure 9. HRTEM micrograph showing 5-10 nm nanocrystallines in the 1000 thermal cycled SW3-MCrAl-#5 coating

Based on the TEM results, we can draw the following conclusions:

1) The as-deposited MCrAlN coating exhibited a columnar structure. The top columnar width was as wide as 800 nm. However, a superlattice structure with nanocrystallines (<10 nm) has been identified in the DF and HRTEM images.
2) After annealing at 1050 ^{o}C for 500 and 1000 cycles, a 1 μm thick and dense Al_2O_3 layer was formed on the coating surface. The underlay MCrAl coating still exhibited a dense columnar structure. The columnar grain width for both annealed coatings is comparable to the as-deposited MCrAl coating (less than 800 nm). A large amount of dark precipitates was observed in the MCrAl coating near the surface region, which contains high Ni and Cr contents compared to the other MCrAl coating regions without the dark precipitates.

Respectfully submitted,

John J Moore, Ph.D.
Professor and Center Director
ACSEL, Colorado School of Mines

Jianliang Lin. Ph.D.
Assistant Research Professor
ACSEL, Colorado School of Mines